



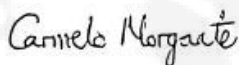
UNIVERSITÀ DEGLI STUDI DI PALERMO

PhD Course in Chemical, Environmental, Biomedical, Hydraulic and
Materials Engineering

**VALORISATION OF WASTE BRINES FROM THE
DESALINATION INDUSTRY THROUGH CIRCULAR
ECONOMY APPROACHES**

PhD candidate:

Carmelo Morgante



Supervisor:

Prof. Alessandro Tamburini



PhD course coordinator:

Prof. Giorgio Micale

Co-supervisors:

Dr. Fabrizio Vassallo
Dr. Julio Lopez Rodriguez
Prof. Vittorio Boffa
Prof. Jose Luis Cortina Pallas

XXXVI Cycle

GRADUATION YEAR 2024

ACKNOWLEDGEMENTS

First, I would like to express my sincere gratitude to the EU-funded projects “Zero Brine” and “Water Mining”, thanks to which many of the activities carried out during my PhD study were possible. Collaborating and exchanging ideas with the various EU partners helped me grow academically and allowed me to work with many great minds of the scientific community.

I am extremely grateful to my supervisor, Prof. Alessandro Tamburini, and PhD course coordinator, Prof. Giorgio Micale, for their invaluable advice, continuous support and patience during my PhD study. I cannot say otherwise also for the professors who supervised me during my studies abroad: Prof. Vittorio Boffa (Aalborg University, Denmark) and Prof. Jose Luis Cortina (Universitat Politècnica de Catalunya, Spain). Both their immense intelligence and kindness have made them an inspiration for me for the type of researcher I would like to be in the academic world.

Among the several colleagues of my research group in Palermo, a special thanks goes to Nunzio, Marta, Abdullah, Mimma and Luigi for both their moral and technical support throughout my PhD. However, there is just one colleague to whom I necessarily have to thank the most of all: Fabrizio Vassallo.

Fabrizio has been by my side every step of the way. Starting as a simple colleague who supervised me during the preparation of my master’s degree thesis, he continued to help throughout all the years we have known each other. Not only is he the most intelligent person I know but I also admire him for his immense goodness. He has been both a best friend and a brother to me, always being there both in my work and in my private life. There are no other words to describe the great admiration I feel for him. I hope my friendship with him can last a lifetime. Thank you for all the great moments. I wish you all the best Fabrizio!

*A special thanks to the Danish gang from Aalborg University: Giacomo, Max, Rasmus, Morten, Bastian, Zhencai, Xinxin, Lana, Dario, Samuel, Natasha and Peam. They are the craziest and coolest people I have ever met. Without them, my period abroad in Denmark would have never been the once-in-a-lifetime experience it was. **Tak for al jeres støtte, jeg ønsker jer al held og lykke!***

I extend a heartfelt thank you to my second family, my Spanish family in Barcelona: Karina, Mariana, Johannes, Tanaz, Dani, Oscar, Sonia, Double, Tamara, Elena, Marc, Monica, Victor, Tatiana and Sergi. Not only they were my colleagues I spent my days with during my six months in Spain, but they became genuine and sincere friends. They are, without a doubt, the kindest people I know. However, this family could not be complete without two other special individuals: my “abuelos”! Julio and Alexandra have been much more than just two colleagues. They welcomed me

Acknowledgements

*into their beautiful home and made me feel like actual family. All my amigos supported me throughout my last year of PhD both in my ups and downs and have continued to be there ever since. I will forever cherish all the great moments I have shared with my “familia”, and I truly consider myself fortunate to have met such exceptional people. **Os deseo lo mejor, os quiero amigos mios!***

Thank you to my long-life friends, Noemi and Lorena, who I have known for more than 15 years. During my PhD, regardless the fact we have been in opposite parts of Europe, distance has never been an issue. They have always been there, supporting me every time I have needed them.

Last but not the least I would like to thank the most important people of all in my life: my parents and sisters. Without their love and moral support not only it would have been impossible to reach this important goal of my life but also I would not be the person I am today. Their wisdom has always guided me, and they are the ultimate role models of my life.

PREFACE

The question of what the future holds has become increasingly prevalent in the 21st century, as we grapple with the exponential rise in global population and environmental pollution. This surge has given rise to critical issues like climate change, water scarcity, and the challenge of sustaining a consistent resource supply. Over the past decades, numerous approaches and subsequent technological advancements have been implemented to tackle such issues, with the primary aim of fostering a more sustainable and economically friendly future.

The establishment of desalination plants worldwide since the 1960s has been one significant solution to freshwater scarcity. These plants extract freshwater from seawater or other natural water bodies like rivers and lakes. Technological progress over time has led to the development of more efficient desalination plants. This evolution includes a shift from thermal-based evaporative technologies, such as Multi-Stage Flash (MSF) and Multi-Effect Distillation (MED), with water recoveries around 20-30%, to membrane-based technologies like Reverse Osmosis (RO), achieving higher recoveries of up to 50%. However, regardless of the technology used, desalinating water unavoidably produces a concentrated by-product known as "brine," which is often discharged back into natural water bodies, raising environmental concerns.

Another pressing global issue is the depletion of land-based mining resources. To meet the growing demand for raw materials, finding alternatives can be increasingly challenging and expensive. Seawater mining has emerged as a promising solution, particularly in the form of desalination brine mining. In the last decade, several schemes have been proposed in literature, integrating desalination plants with various downstream technologies (i.e., membrane-based processes, crystallization, and evaporative processes), adopting a Minimum Liquid Discharge (MLD) or Zero Liquid Discharge (ZLD) concept. The goal is threefold: (i) overcome freshwater

scarcity by producing drinking water, (ii) recover high-value minerals from brines, and (iii) reduce the volume of brines discharged into the environment, thereby diminishing treatment costs and the related environmental impact. Therefore, exploiting this waste as a source of raw materials, allows to shift from a linear economy model to a circular one. It is worth mentioning that MLD targets a water recovery around 80% meanwhile ZLD achieves values of recovery typically between 95-99%. Whilst these concepts seem promising, several challenges unfortunately persist. More specifically, seawater and desalination brine have low mineral concentrations, and the components in major quantity present the lowest market value. Consequently, generating sufficient revenue to offset the substantial capital and operating costs of MLD/ZLD schemes becomes a critical consideration. Therefore, it is crucial to select carefully the technologies of the scheme and the minerals to recover to ensure economic feasibility.

Within this context, the focus of this PhD thesis is the investigation of viable strategies for valorising seawater and desalination brine through an MLD approach in the remote small islands of Sicily, Italy. These islands heavily rely on seawater desalination as their primary source of freshwater. The PhD thesis initially considered two distinct valorisation chains: (i) an MLD process for seawater reverse osmosis (SWRO) brine from Pantelleria Island and (ii) an MLD process for the direct valorisation of seawater in Lampedusa Island.

The first chain underwent a meticulous techno-economic analysis at a potential industrial scale, leveraging multi-scale modelling tools integrated into an innovative advanced simulation platform. Parametric and sensitivity analyses were carried out to identify optimal operating conditions for each integrated unit within the chain, in order to target economic feasibility. The second MLD chain, evolving from the first, was actually developed at a large pilot scale and subjected to experimental testing in Lampedusa Island. It is worth mentioning that the second MLD chain represented the first large-scale demonstration plant in history for the recovery of multiple high-quality resources from seawater. A comprehensive circularity assessment was further

performed to evaluate the technical advantages of MLD over conventional linear desalination processes.

From the investigation of the two proposed MLD processes, magnesium recovery emerged as a pivotal factor for economic feasibility, given its unique combination of high concentration and market value. The imperative was therefore to maximize both magnesium recovery and purity. To this purpose, the focus turned to optimizing the performance of a novel magnesium reactive crystallizer known as the "Multiple Feed – Plug Flow Reactor" (MF-PFR). The MF-PFR is a reactor in which the direct mixing between the feed solution and an alkaline reactant (a sodium hydroxide NaOH solution) promotes the precipitation of magnesium under the form of magnesium hydroxide $Mg(OH)_2$. Different operational strategies of the reactor were investigated, aiming to enhance the properties of $Mg(OH)_2$ (i.e., sedimentation rate, filtration rate, particle size, purity). Furthermore, the nature of the feed solution to the reactor was also important for magnesium purity and recovery, depending on the performances of the upstream pre-treatment step of the MLD schemes.

Nanofiltration (NF) technology was chosen as the pre-treatment step for both MLD schemes due to its selective separation capabilities, particularly for multivalent ions like magnesium. An innovative positively charged NF membrane was synthesized to enhance magnesium production. Its properties were thoroughly characterized, and the novel membrane was tested with synthetic seawater and desalination brine solutions. Performances were compared with those of current commercial NF membranes, demonstrating higher magnesium selectivity. The performances of the same commercial NF membranes were assessed in different operating conditions at a small pilot scale. Collected results were used to identify optimal operating conditions and the most effective NF membrane available on the market. A multi-scale mathematical model for NF technology facilitated a techno-economic analysis to optimize the operating conditions of a potential industrial NF plant, maximizing the revenue from $Mg(OH)_2$ produced from seawater and desalination brine.

The successful outcomes of the entire PhD project were incorporated into a final proposed MLD scheme at industrial scale. A thorough economic analysis underscored the economic feasibility of this MLD process for brine valorisation, affirming the substantial potential of MLD as a sustainable alternative for minerals and water recovery.

The present PhD thesis is organized in seven chapters, grouped in four main sections, as illustrated in Figure 1:

SECTION 1

Chapter 1 provides the techno-economic perspectives of a first potential industrial-scale MLD process that valorises the brine produced by the Sataria desalination plant of Pantelleria (Italy).

Chapter 2 presents the results of the experimental campaign of the second MLD process at pilot-scale in Lampedusa (Italy) for seawater valorisation. Results of a circularity and integration assessment are also reported.

SECTION 2

Chapter 3 focuses on the experimental activities to enhance the properties of $Mg(OH)_2$ recovered from seawater/brine. Different operational strategies of the MF-PFR are investigated at the Brine Excellence Centre (BEC) of the University of Palermo, using synthetic solutions that mimic a wide range of brines.

SECTION 3

Chapter 4 reports the synthesis, characterization and selectivity performances of a novel positively charged NF membrane, aimed at maximizing magnesium selectivity.

Chapter 5 presents a vast comparative study of 5 current commercial NF membranes, evaluating their rejection performances of major and minor components in seawater/brine at different operating pressure.

Chapter 6 focuses on the evaluation of two specific commercial NF membranes (NFX and VNF1) at different permeate recoveries. Results of their characterization,

experimental testing and modelling are accompanied by an in-depth techno-economic assessment, focused on maximizing magnesium revenue.

SECTION 4

Chapter 7 provides the economic perspectives of a final proposed MLD chain, incorporating the outcomes achieved throughout the PhD project.

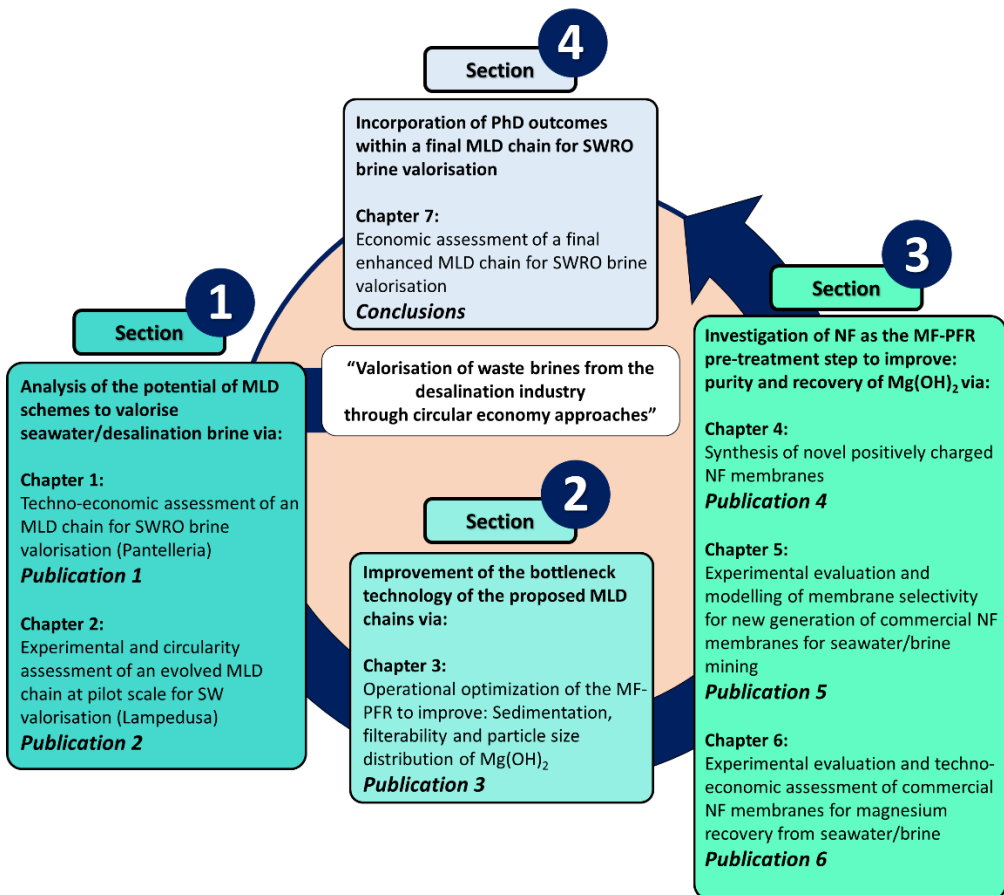


Figure 1: Structure of the PhD thesis

CONTENTS

***ACKNOWLEDGEMENTS*..... i**
***PREFACE*..... iii**
***CONTENTS*..... 1**

***SECTION 1: Resource recovery from seawater and desalination brines via a Circular Economy approach*..... 5**
***Literature review*..... 5**

***1“Valorisation of SWRO brines in a remote island through a circular approach: Techno-economic analysis and perspectives”*..... 14**

1.1 Pantelleria Case Study: Brine valorisation chain description14
 1.1.1 Nanofiltration (NF).....17
 1.1.2 Magnesium Reactive Crystallizer (MRC)18
 1.1.3 Multiple-Effect Distillation (MED).....19
 1.1.4 NaCl Thermal Crystallizer (NTC).....20
1.2 Technical Models description.....20
1.3 Economic Models description24
1.4 Simulation Approach27
1.5 Results and Discussion.....28
 1.5.1 Feasibility analysis of NF membrane rejections and NaCl recovery.....28
 1.5.2 Economic analysis35
 1.5.2.1 Analysis of the Base Case scenario35
 1.5.2.2 Economic comparison with other brine treatment concepts38
 1.5.2.3 MED influence on the economics of the MLD scheme.....40
 1.5.2.4 Parametric analysis and Tornado diagram of the main factors affecting the BTSC41
1.6 Conclusions.....45

***2“Pioneering Minimum Liquid Discharge desalination: a pilot study in Lampedusa island”*.....47**

2.1 The Sea-Mining case study in Lampedusa island (Italy).....47
2.2 Pilot facilities and operational procedure49
 2.2.1 Nanofiltration (NF).....50
 2.2.2 Multiple Feed – Plug Flow Reactor (MF-PFR).....52
 2.2.3 ElectroDialysis with Bipolar Membranes (EDBM)54
 2.2.4 Multi-Effect Distillation (MED).....57
 2.2.5 Evaporative ponds (EPs)60
 2.2.6 Operating conditions and analytical procedure62

| | | |
|----------------------------------------------------------------------------------------------------------------------------------------------|----------------------------------------------------------------------------------------|------------|
| 2.2.7 | Circularity assessment..... | 65 |
| 2.3 | Results and discussion | 66 |
| 2.3.1 | DPNF pre-treatment stage performances | 67 |
| 2.3.2 | Purity and recovery of products/chemicals | 68 |
| 2.3.3 | Energy performances of pilot units | 70 |
| 2.3.4 | Specific performances of the MED unit..... | 72 |
| 2.3.5 | Stability of pilot plants | 72 |
| 2.3.5.1 | NF | 73 |
| 2.3.5.2 | MF-PFR..... | 74 |
| 2.3.5.3 | EDBM..... | 76 |
| 2.3.5.4 | MED | 77 |
| 2.3.6 | Integration and circularity assessment..... | 78 |
| 2.4 | Conclusions..... | 81 |
| <i>SECTION 2: Magnesium recovery from seawater/brines via a novel Multiple Feed –Plug Flow Reactor (MF-PFR).....</i> | | |
| | | 83 |
| <i>Literature review.....</i> | | |
| | | 83 |
| <i>3“Influence of Operational Strategies for the Recovery of Magnesium Hydroxide from Brines at a Pilot Scale”</i> | | |
| | | 89 |
| 3.1 | Concept of Magnesium Hydroxide recovery via a novel reactive crystallizer | 89 |
| 3.2 | Materials and methods | 94 |
| 3.2.1 | Overview of the experimental campaign..... | 94 |
| 3.3 | Experimental procedure..... | 96 |
| 3.3.1 | Preparation of feed and reactant solution | 96 |
| 3.3.2 | Sampling procedure..... | 96 |
| 3.3.3 | Analytical procedure | 97 |
| 3.3.4 | Definition of performance parameters..... | 99 |
| 3.4 | Results and discussion | 101 |
| 3.4.1 | Effect of Mg ²⁺ brine concentration (Configuration A) | 101 |
| 3.4.2 | Effect of brine flow rate (Configuration A)..... | 104 |
| 3.4.3 | Effect of the hydrodynamic asset (Configurations A vs. B) | 106 |
| 3.4.4 | Effect of Mg(OH) ₂ suspension recirculation (Configuration C) ... | 108 |
| 3.4.5 | Effect of brine flow rate (Configuration C)..... | 110 |
| 3.5 | Conclusions..... | 112 |
| <i>SECTION 3: Nanofiltration, a pre-treatment step to enhance magnesium purity and recovery.....</i> | | |
| | | 114 |
| <i>Literature review.....</i> | | |
| | | 114 |
| <i>4“Metal-Organic-Framework-based nanofiltration membranes for selective multi-cationic recovery from seawater and brines”</i> | | |
| | | 125 |

| | | |
|------------|-----------------------------------------------------------------------------------------------------------------------------------------------------------------------------------------------------|-------------------|
| 4.1 | Experimental | 125 |
| 4.1.1 | Materials | 125 |
| 4.1.2 | MOF synthesis..... | 126 |
| 4.1.3 | Membrane fabrication | 126 |
| 4.1.4 | Membrane Characterization | 128 |
| 4.1.5 | Filtration tests | 129 |
| 4.2 | Results and Discussion..... | 132 |
| 4.2.1 | Characterization of the membrane materials | 132 |
| 4.2.1.1 | MOF and ZnO nanoparticles..... | 132 |
| 4.2.1.2 | CMZ nanoparticles | 135 |
| 4.2.2 | Characterization of nanocomposite membranes..... | 137 |
| 4.2.3 | Filtration of single salt solutions | 142 |
| 4.2.4 | Filtration of real seawater and desalination brine..... | 146 |
| 4.3 | Conclusions..... | 148 |
| | | |
| | <i>5“New generation of commercial nanofiltration membranes for seawater/brine mining: Experimental evaluation and modelling of membrane selectivity for major and trace elements”</i> | <i>150</i> |
| 5.1 | Experimental | 150 |
| 5.1.1 | NF membranes and Synthetic solutions | 150 |
| 5.1.2 | NF Experimental set-up and procedure | 152 |
| 5.1.3 | Analytical procedure | 154 |
| 5.1.4 | Membrane performance indicators | 155 |
| 5.1.5 | Ion transport descriptions by means of the SEDF model | 155 |
| 5.2 | Results and Discussion..... | 158 |
| 5.2.1 | Effect of transmembrane pressure on permeate flux | 158 |
| 5.2.2 | Effect of transmembrane pressure on rejections for seawater | 160 |
| 5.2.4 | Membrane permeances to species through the SEDF model | 170 |
| 5.2.5 | Selectivity of the NF membranes | 171 |
| 5.3 | Conclusions..... | 175 |
| | | |
| | <i>6“Evaluation of enhanced nanofiltration membranes for improving magnesium recovery schemes from seawater/brine: integrating experimental data with a techno-economic assessment”.....</i> | <i>177</i> |
| 6.1 | Materials and methods | 177 |
| 6.1.1 | Membranes and characterization procedure | 177 |
| 6.1.2 | Preparation of synthetic solutions | 178 |
| 6.1.3 | Pilot set-up description | 179 |
| 6.1.4 | Experimental testing..... | 180 |
| 6.1.5 | Analytical procedure and data analysis of samples | 181 |
| 6.2 | Modelling | 183 |

| | | |
|------------|---------------------------------------------------------|------------|
| 6.2.1 | NF multi-scale technical model..... | 183 |
| 6.2.2 | MRC technical model..... | 183 |
| 6.2.3 | NF Economic model description..... | 184 |
| 6.2.4 | Technical and Economic performance indicators..... | 185 |
| 6.3 | Results and Discussion..... | 186 |
| 6.3.1 | NFX and VNF1: membrane characterization..... | 186 |
| 6.3.2 | Mass transfer model validation..... | 189 |
| 6.3.2.1 | NFX treating seawater..... | 190 |
| 6.3.2.2 | NFX treating desalination brine..... | 193 |
| 6.3.2.3 | VNF1 treating seawater..... | 196 |
| 6.3.2.4 | VNF1 treating desalination brine..... | 199 |
| 6.3.3 | Techno-economic assessment..... | 202 |
| 6.3.3.1 | NFX treating seawater..... | 202 |
| 6.3.3.2 | NFX treating SWRO brine..... | 205 |
| 6.3.3.3 | VNF1 treating seawater..... | 206 |
| 6.3.3.4 | VNF1 treating desalination brine..... | 208 |
| 6.3.4 | Global techno-economic overview of the 4 scenarios..... | 209 |
| 6.4 | Conclusions..... | 210 |

| | |
|-------------------------------------------------------------------------------------------------|------------|
| <i>SECTION 4: Economic perspectives of a final MLD process for SWRO brine valorisation.....</i> | <i>213</i> |
|-------------------------------------------------------------------------------------------------|------------|

| | |
|-------------------------------------------------------------------------------------|------------|
| <i>SUMMARY & FINAL REMARKS.....</i> | <i>221</i> |
| <i>NOMENCLATURE.....</i> | <i>228</i> |
| <i>APPENDIX A.....</i> | <i>232</i> |
| <i>APPENDIX B.....</i> | <i>243</i> |
| <i>APPENDIX C.....</i> | <i>248</i> |
| <i>REFERENCES.....</i> | <i>257</i> |
| <i>LIST OF ISI PUBLICATIONS AND PRESENTATIONS AT INTERNATIONAL CONFERENCES.....</i> | <i>276</i> |
| <i>AWARDS.....</i> | <i>279</i> |

SECTION 1: Resource recovery from seawater and desalination brines via a Circular Economy approach

Literature review

In our contemporary era, critical issues once perceived as concerns for future generations are now emerging with a sense of immediacy. Climate change, water scarcity, and the depletion of land resources are compelling the global economy to embrace a more sustainable vision for the future [1].

Efforts to combat freshwater scarcity have primarily revolved around the installation of numerous desalination plants worldwide. Presently, there are approximately 19,000 such plants [2,3], producing about 100 million m³ of freshwater daily [2]. Notably, more than half of this output (65.5 million m³ daily) derives from RO [4]. However, desalination is accompanied by two main drawbacks which are: (i) its energy demand and (ii) the production of an effluent called “brine” [4–7]. Despite substantial progress in reducing energy consumption for seawater reverse osmosis (SWRO) from around 16 kWh/m³ in the 1970s to about 3 kWh/m³ [2] in 2020, the production of brine remains a significant challenge.

Brine is a solution that presents large amounts of total dissolved salts (TDS), and that must be necessarily treated before its discharge into the environment according to strict regulations [8]. When discharged, brine can be harmful to the environment due to its salinity, temperature and chemical substances (used for pre-treatment/membrane cleaning). More specifically, brine salinity can be 1.6–2 times higher than that of seawater (35 g/L) [9] reaching up to 70 g/l in the case of SWRO [10]. Global estimates indicate a daily brine production of about 142 million m³, requiring careful treatment before discharge due to its high TDS content [11].

Conventional methods for managing brine are: (i) ocean disposal [12], (ii) surface water discharge [13] (the least expensive among the brine disposal methods [14]),

(iii) sewer disposal [15], (iv) deep-well injection [16], and (v) evaporation ponds [17]. The choice of the disposal method to employ depends on several factors such as the quality, the volume, the location of the discharge point of the brine and the cost which typically lies within the range 5-33% of the total cost of the desalination process [18]. Such disposal methods, however, often incur high capital costs and environmental impacts. Consequently, there is a pressing need for cost-effective and sustainable alternatives [19].

Beyond freshwater scarcity, land mining deficiency represents another current global issue to tackle. With specific respect to several raw materials, (i) gradual higher costs for both extraction and environmental mitigation [10] and (ii) geographical availability have placed the European Union (EU) in a position of significant dependence from other countries, urging the need to find innovative solutions.

To address the aforementioned challenges in a sustainable manner, it appears essential to find a “limitless” source for freshwater, on one side, and minerals, on the other, to be exploited with ideally zero environmental impact. Within this context, the concept of seawater/brine mining with MLD and ZLD processes emerges as a potential solution.

Seawater and desalination brine contain several valuable elements [20]. Some in the highest concentration range are sodium, magnesium, calcium and potassium, which are already commercially extracted as chlorides, sulphates, and carbonates, meanwhile magnesium is usually extracted as hydroxide [21]. Other more valuable elements present in seawater, such as lithium, however are much less concentrated and a bit more difficult to extract [22]. Seawater mining offers several advantages compared to terrestrial mining, including access to inexhaustible ocean water volumes, consistent seawater composition, the ocean natural dilution capacity for treated waste streams, and a stable and fixed mining operation footprint [23].

MLD/ZLD processes aim to minimize or eliminate liquid effluent discharge, transforming waste into a manageable solid form suitable for landfill disposal.

Whereas ZLD processes consist of technologies integrated in such a manner to reach a water recovery of 95-99%, MLD processes concern the integration of thermal and/or membrane-based processes reaching water recoveries around 80% [24]. Moreover, modern MLD and ZLD systems have evolved to not only recover freshwater but also extract valuable minerals from seawater brines. This approach presents a comprehensive solution that simultaneously addresses issues related to freshwater scarcity, the environmental and economic impact of brine discharge, and land mining depletion.

In conclusion, seawater/brine mining, coupled with advanced ZLD and MLD processes, has the potential to revolutionize resource management, offering a sustainable path forward in the face of pressing global challenges.

Within this context, a growing body of literature is emerging. Table 1 reports an overview of all the freshwater/minerals recovery schemes proposed in the existing literature for seawater and desalination brine. It is noteworthy that the majority of these studies are based on conceptual ideas, analysed from a techno-economic perspective via process modelling and software tools.

Among the simulative studies on MLD/ZLD, Panagopoulos proposed several process schemes [25,26]. Initially, an elementary ZLD scheme was examined, featuring RO, a Brine Concentrator (BC), and a Brine Crystallizer (BCr). The results of an economic analysis revealed a remarkable 99.36% water recovery, accompanied by a treatment cost of 1.04 \$/m³ of freshwater produced. The same author further explored variations to the initial ZLD scheme, such as the introduction of a Forward Osmosis (FO) unit [27], substituting RO with High Pressure Reverse Osmosis (HPRO) [28], or replacing the BCr with Wind Aided Intensified Evaporation (WAIV) [29].

Table 1: Comparison between MLD/ZLD chains for seawater/brine valorisation present in the literature. The yellow section incorporates all works based on proposed concepts, the salmon section includes all works at lab-scale and the brown section concerns all works at pilot scale.

| Author | Ref. | Feed | MLD/ZLD chain | Application Scale | | | Additional info | | | | |
|-----------------------------|---------|------------|-------------------------------------------------|-------------------|-----|-------|-------------------------------------------|-------------------|-----------------------------------|--------|------------------------------------------------------------------------------------------------------------------------------------------|
| | | | | Conc. | Lab | Pilot | Recovery of multiple high purity minerals | Economic Analysis | Levelized costs of minerals/water | BTSC * | Other info |
| Panagopoulos, 2021 (a), (b) | [25,26] | SW | RO-BC-BC | ✓ | - | - | ✗ | ✓ | ✓ | ✗ | Capacity = 100 m ³ /day Water recovery = 99.36% Energy = 2240.4 kWh Water cost = 1.04 \$/m ³ |
| Panagopoulos, 2022 (c) | [27] | SW | RO-FO-BC-BC | ✓ | - | - | ✗ | ✓ | ✓ | ✗ | Capacity = 100 m ³ /day Water recovery = 98.88% Energy = 1024.6 kWh Water cost = 0.79 \$/m ³ |
| Panagopoulos, 2022 (d) | [28] | SW | HPRO-BC-BCr | ✓ | - | - | ✗ | ✓ | ✓ | ✗ | Capacity = 100 m ³ /day Water recovery = 99.19% Energy = 2006.2 kWh Water cost = 1.02 \$/m ³ |
| Panagopoulos, 2022 (e) | [29] | SW | RO-BC-WAIV | ✓ | - | - | ✗ | ✓ | ✓ | ✗ | Capacity = 100 m ³ /day Water recovery = 85.75% Energy = 1.3 MWh/m ³ Water cost = 1.01 \$/m ³ |
| El-Zanati et al., 2007 | [30] | SW | NF-SWRO-MD | ✓ | - | - | ✗ | ✗ | ✗ | ✗ | Capacity = 100 m ³ /d Water recovery = 76.2% Energy = --- Water cost = 0.92 \$/m ³ |
| Tahir et al., 2022 | [31] | SW | MED-HDH-Ev | ✓ | - | - | ✗ | ✗ | ✗ | ✗ | MED water prod. = 1 kg/s HDH water rec. = 40% SEC = 720-820 kJ/kg |
| Poirier et al., 2022 | [32] | SWRO brine | multi-crystallization system with heat recovery | ✓ | - | - | ✓ | ✓ | ✓ | ✗ | Capacity = 1000 kg/h Water recovery = 99.2% NaCl recovery = 91.6% Energy = 60.7 kWh/ton Water cost = 13.79 \$/m ³ |

Section 1

| | | | | | | | | | | | |
|-------------------------------------------|-----------|---------------|----------------------------------|---|---|---|---|---|---|---|----------------------------------------------------------------------------------------------------|
| Al Bazed et al., 2014 | [33] | SWNF brine | Cr-MCr | ✓ | - | - | ✗ | ✓ | ✓ | ✗ | Capacity = 1000 m ³ /d Water recovery = 92% Water cost = 2.82 \$/m ³ |
| Von Eiff et al., 2021 | [34] | Brine | MD-MSF-C | ✓ | ✓ | - | ✗ | ✓ | ✗ | ✓ | Water recovery = 89% Water cost = 0.62 \$/m ³ Brine cost = 1.24 \$/m ³ |
| Chen et al., 2021 | [35] | SWRO brine | MED-Cr | ✓ | - | - | ✗ | ✓ | ✗ | ✓ | Thermal energy = 600- 1000 kJ Brine cost = 4.17 \$/m ³ |
| Van Wyk et al., 2018, 2020 | [11,36] | SW | SCWD | ✓ | ✓ | - | ✗ | ✓ | ✗ | ✓ | Feed Capacity = 8 kg/h Water recovery = 91% Brine cost = 1.16 \$/m ³ |
| Tufa et al., 2015 | [37] | SW | MD-RED | - | ✓ | - | ✗ | ✗ | ✗ | ✗ | Water recovery = 92% Gross power density = 2.4 W/m ² |
| Zhang et al., 2017 | [38] | SWRO brine | Cr-SED-EDBM | - | ✓ | - | ✓ | ✓ | ✗ | ✗ | NaOH (85% pure) HCl (95% pure) coarse salt (92 % pure) |
| Ji et al., 2009 | [39] | SWRO brine | MD-Cr | - | ✓ | - | ✗ | ✗ | ✗ | ✗ | Water recovery = 90% NaCl recovery = 17 kg/m ³ |
| Kieselbach et al., 2020 | [40] | Brine | NF-ED-Ev-Cr- MD | - | ✓ | ✓ | ✗ | ✓ | ✗ | ✓ | Capacity = 1.5 m ³ /h Water recovery = 65% Brine cost = 0.5 €/m ³ |
| Xevgenos et al. 2014, 2015, 2016 | [5,41,42] | SWRO Brine | Ev-Cr | - | - | ✓ | ✗ | ✗ | ✗ | ✗ | Capacity = 2 m ³ /day 90% water recovery Powered by solar energy |
| Al-Amoudi et al. 2023 | [43] | SW | NF-(RO-HPRO- 2 OARO)- OARO | - | - | ✓ | ✗ | ✓ | ✓ | ✗ | Capacity = 16 m ³ /day Water recovery = 65.2% No salts are recovered |

**All acronyms of technologies that comprise the MLD/ZLD schemes are reported in the "Nomenclature" section*

***BTSC = Brine Treatment specific Cost*

Despite yielding slightly lower water recoveries—98.88%, 99.19%, and 85.75%, respectively, the economic feasibility of these adaptations was demonstrated. However, on the other hand, in all of the previous schemes, no information concerning the purity of the recovered products was reported. Chen et al. [35] simulated the integration between a Multi-Effect distillation unit and a crystallizer to recover salt and water from desalination brine. Results revealed that a brine treatment cost of 4.17 $\$/\text{m}^3$ could be achieved when waste heat was employed. Furthermore, in literature it was also possible to find proposed MLD/ZLD schemes capable of recovering several salts other than NaCl. Al Bazed et al. [33] identified an innovative scheme for resource recovery from brines, employing a two-step process involving chemical precipitation and membrane crystallization (MCR). Sodium carbonate (NaCO_3) was introduced in the chemical precipitation step to facilitate the recovery of calcium carbonate (CaCO_3), while membrane crystallization yielded sodium chloride (NaCl), magnesium sulphate (MgSO_4), and water. The results demonstrated a daily water production of over 234 m^3 , generating a substantial annual revenue of \$241,408. This meant that a water specific production cost of 2.82 $\$/\text{m}^3$ could be obtained. Furthermore, the process garnered additional revenues from the sale of other recovered products. However, it is worth noting that the information provided lacked details on the purity of the final products and their potential applications. Von Eiff et al. [34] integrated membrane distillation (MD), Multi Stage Flash (MSF) and Crystallization. By selling freshwater and pure Na_2SO_4 , a low brine disposal cost (0.08 $\$/\text{m}^3$) was achieved.

Very few were the studies in literature that presented experimental work at bench-scale/laboratory level. Tufa et al. [37] conducted a study aimed at harnessing energy from seawater brines via a lab-scale membrane-based MD-RED (Membrane Distillation-Reverse ElectroDialysis) system. The main experimental findings were the achievement of a 92% freshwater recovery and a gross power density equal to 2.4 W/m^2 .

Zhang et al. [38] conducted a comprehensive investigation into the performance of integrating chemical precipitation, selectrodialysis (SED), and electrodialysis with bipolar membranes (EDBM). This multifaceted approach resulted in the production of chemicals such as NaOH (85% purity) and HCl (95% purity), along with coarse salt at a purity level of 92%. Ji et al. [39] explored the treatment of seawater reverse osmosis (SWRO) brines using a combination of a membrane distillation unit (MD) and a crystallizer (Cr). Their approach yielded high water recoveries of up to 90%.

As far as MLD/ZLD schemes implemented at a larger scale (i.e., pilot-scale) were concerned, only three works could be found. Among them, Kieselbach et al. [40] reported a large-scale plant within the framework of the Highcon research project. More precisely, the demonstration plant consisted of RO, NF, ED and MD with a feed capacity of 1.5 m³/h. The chain produced sodium hydrogen carbonate NaHCO₃ at a purity of 90%, achieving a low brine disposal cost of 0.5 €/m³. However, NaHCO₃ was recovered via evaporation and crystallization at lab-scale, thus resulting in a hybrid plant between the lab and pilot scale. Within the framework of the European-funded project SOL-BRINE, a solar-driven evaporator-crystallizer process was developed by Xevgenos et al. to recover 90% of water and dry mixed salts in Tinos Island (Greece) [5,41,42]. The project aimed at reducing brine discharge by exploiting solar energy as the only energy source for the system.

Furthermore, in Ummlujj, Saudi Arabia, Al-Amoudi et al. [43] presented a larger demonstration plant designed for water desalination. The plant featured a nanofiltration (NF) unit with a robust feed capacity of 16 m³/h, specifically tailored for the separation of monovalent and multivalent ions. The process presented two concentration steps. The first concentration step involved a combination of reverse osmosis (RO), high-pressure reverse osmosis (HPRO), and a 2-stage OARO (Osmotically Assisted Reverse Osmosis) process. This step resulted in the production of freshwater. The second concentration step utilized OARO, fed by the NF retentate, generating two distinct concentrated streams: a monovalent-rich stream with a salinity of 130 g/L and a bivalent-rich stream with a salinity of 83 g/L. To

enhance the pilot plant performance, upgrades were implemented, incorporating more selective NF membranes, a second NF stage, and an additional stage of OARO. Despite these improvements, it is noteworthy that the concentrated streams did not yield pure salts or minerals. The focus remained on freshwater production and concentration rather than the recovery of specific mineral components.

Overall, in examining the extensive body of literature on MLD/ZLD schemes for seawater/brine valorisation (as summarized in Table 1), two main conclusions emerged, shedding light on crucial gaps in the existing research:

- (i) Numerous schemes proposed in the literature lacked demonstrated profitability, primarily due to the absence of a detailed economic analysis. In addition, for those cases in which an economic evaluation had been conducted, the schemes were capable of recovering water with a mixture of salts or one/two low purity salts. Consequently, the pricing of the recovered salts is constrained to be low, and the range of applications and target markets for these salts is markedly limited;
- (ii) As of the current moment, there is a notable absence of studies presenting results from a large-scale demonstration of an integrated seawater valorisation system capable of simultaneously recovering multiple high-purity resources.

The present PhD project therefore aimed at filling these missing gaps to demonstrate the techno-economic feasibility of high valuable resource recovery from seawater/SWRO brine via an MLD approach.

To such end, a first innovative and versatile brine valorisation chain was proposed, capable of recovering high purity products: H_2O (TDS < 10 ppm), $\text{Mg}(\text{OH})_2$ (>90%), $\text{Ca}(\text{OH})_2$ (>90%) and NaCl (97%). The rationale behind targeting these particular products stems from the fact that, among the several potentially recoverable products, they stand out as being among the few that can be recovered in significant quantities due to the chemical composition of desalination brine. Therefore, for the

first chain, specific technologies were selected to recover the aforementioned high purity products. A detailed analysis of this first proposed MLD chain was performed in order to verify its techno-economic feasibility. By achieving high purities, the products of the chain could target a much broader market than other ZLD/MLD schemes present in literature. Furthermore, among the recovered resources, Magnesium is one of the Critical Raw Materials (CRMs) defined by the EU. Therefore, both an economic benefit (recovery of high valuable minerals and water, lower cost for brine disposal) and an environmental one (reduction of brine discharge) could be achieved. Both the description of the MLD chain along with the results of the vast simulative campaign are reported in Chapter 1 (entirely supported by **Publication 1** [44]).

Subsequently, a second MLD chain, considered as an evolution of the first chain was developed at a large demonstration scale and experimentally tested in Lampedusa island (Italy). The evolution mainly consisted in the possibility of in-situ chemical production to reduce the overall chemical demand of the first chain by adding a fifth technology. This work aimed at filling the second gap by presenting for the first time in literature the results of an integrated system of 5 technologies that:

- (i) operates at a large demonstration level, i.e. feed capacity of 2.46 m³/h;
- (ii) is highly versatile, producing chemicals (NaOH, HCl), high valuable salts (Mg(OH)₂, Ca(OH)₂, NaCl) and high-quality water;
- (iii) employs waste heat generated by a power station, therefore reducing the energy footprint of the system.

The description of the second MLD chain along with the experimental results achieved are reported in Chapter 2 (entirely supported by **Publication 2** [45]).

1 “Valorisation of SWRO brines in a remote island through a circular approach: Techno-economic analysis and perspectives”

In the context of the EU-funded project “Zero Brine,” an innovative brine management chain was meticulously examined adopting an MLD approach. The focus of this investigation was both technical and economic, with a specific case study involving the treatment of Seawater Reverse Osmosis (SWRO) brine generated on the minor Sicilian island of Pantelleria, Italy. The overarching objective was to propose a versatile brine treatment chain that could serve as inspiration for industrial-scale implementation. To achieve this, a comprehensive techno-economic analysis was conducted using the advanced modelling platform RCE [46]. This platform integrated mathematical models to simulate the treatment technologies of the chain. Additionally, the analyses were complemented by a thermodynamic equilibrium study using PHREEQC [47]. The results derived from these analyses played a crucial role in identifying optimal operating conditions that could enhance the techno-economic feasibility and sustainability of the proposed MLD chain.

1.1 Pantelleria Case Study: Brine valorisation chain description

A seawater desalination plant situated in Pantelleria (Italy) was taken into consideration, with a specific focus on the brine produced by the “Sataria” seawater desalination plant [48]. Figure 2 illustrates the pressure vessels and high-pressure equipment of the RO plant.



Figure 2: Sataria SWRO Plant, Pantelleria (Italy).

The facility consists of four RO units, each boasting a capacity of 1250 m³/d for freshwater production and a typical water recovery of 45%. However, only three out of the four RO units operate simultaneously, resulting in a daily average total capacity of approximately 3750 m³/d. As previously mentioned, the production of freshwater via desalination is accompanied by the generation of a by-product called “brine”: a notable economic and environmental concern. In the specific case of SWRO, the generated brine typically presents a total dissolved salts (TDS) of 70 g/L. Table 2 provides the ionic concentration values of the brine produced by the Sataria plant.

Table 2: Ions concentrations of the brine produced by Sataria desalination plant obtained via Ionic Chromatography

| Ionic species | Na ⁺ | Ca ²⁺ | Mg ²⁺ | K ⁺ | Cl ⁻ | SO ₄ ²⁻ | HCO ₃ ⁻ |
|----------------------------|-----------------|------------------|------------------|----------------|-----------------|-------------------------------|-------------------------------|
| Concentration [g/l] | 21.4 | 0.88 | 2.70 | 0.78 | 39.0 | 5.50 | 0.18 |

The primary objective of this study is to introduce an innovative and sustainable treatment chain, termed the MLD chain, to effectively utilize approximately 50% of the total brine generated by the three operational RO units of the "Sataria" plant. The proposed treatment chain, depicted in Figure 3, comprises four key units: (i) Nanofiltration (NF), (ii) Mg Reactive Crystallizer (MRC), (iii) Multi-Effect Distillation (MED), and (iv) NaCl Thermal Crystallizer (NTC). Such technologies were carefully selected in order to specifically recover high purity products in large quantities (i.e., Mg(OH)₂, Ca(OH)₂, NaCl, H₂O), thus potentially enhancing the overall mineral revenue from brines.

In the initial stage, the SWRO brine undergoes nanofiltration (NF), resulting in the creation of two distinct streams: a retentate enriched with bivalent ions like SO₄²⁻, Ca²⁺, and Mg²⁺, and a permeate exhibiting significantly lower concentrations of these ions. Subsequently, the retentate is directed to the Mg Reactive Crystallizer (MRC), where a chemical reaction with an alkaline reactant facilitates the recovery of magnesium and calcium in the form of hydroxide precipitates.

The effluent remaining from the MRC is combined with the NF permeate and introduced into the Multi-Effect Distillation (MED) unit. Within the MED, the brine undergoes concentration through evaporation in multiple effects, yielding a distillate. Simultaneously, the MED reduces the brine volume, exiting the unit with a salt concentration near saturation.

The outlet brine from the MED is then directed to the final NaCl Thermal Crystallizer (NTC). In this stage, sodium chloride (NaCl) precipitates, resulting in the formation of a solid crystal product. The process also produces a distillate and a residual brine.

The key attractiveness of this treatment chain lies in its ability to transform waste brine into a valuable resource. By systematically reducing its volume, the chain effectively mitigates environmental impact while simultaneously generating multiple valuable products, including magnesium hydroxide ($Mg(OH)_2$), calcium hydroxide ($Ca(OH)_2$), drinking water, and sodium chloride (NaCl). This integrated approach showcases a sustainable and economically viable solution for brine management in the context of SWRO plants.

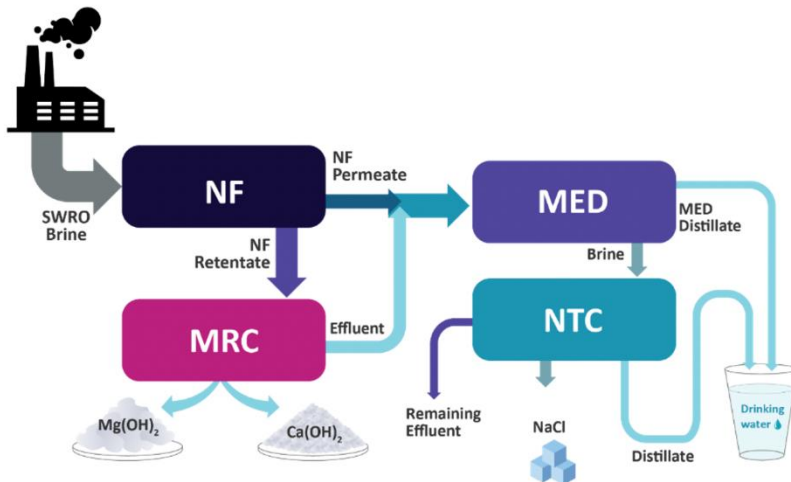


Figure 3: Conceptual scheme of the proposed MLD system.

To gain a deeper understanding of (i) the fundamental principles central to the operation of each technology and (ii) the rationale behind the consideration of these specific technologies, details of each unit are provided in the subsequent sections.

1.1.1 Nanofiltration (NF)

Nanofiltration (NF) stands out as a pivotal pressure-driven membrane-based process, predominantly employed as a pre-treatment technology in contemporary desalination practices [49]. The membrane utilized in this process exhibits characteristics that bridge the attributes of Reverse Osmosis (RO) and Ultrafiltration (UF) [34], boasting pore sizes ranging from 1-2 nm [50]. Operating within the range of 5-40 bar pressure [51] and achieving permeate recoveries of up to 80% [52], NF surpasses RO in water fluxes and outperforms UF in small solute rejections [53]. One of its distinctive features lies in its capability to selectively reject bivalent ions, such as Mg^{2+} , Ca^{2+} , and SO_4^{2-} (with rejection rates ranging from 60% to 99%) [54], exhibiting a notably higher selectivity compared to monovalent ions like Na^+ and Cl^- (0-50% rejection) [55]. The efficacy of NF is attributed to its transport mechanisms embedded within the membrane, governed by steric hindrance (size-based exclusion), dielectric exclusion (resistance attributed to solute hydration shedding), and Donnan exclusion (rejection/attraction influenced by membrane potential) [49]. While membrane fouling remains a ubiquitous challenge in membrane processes, NF has undergone extensive testing in prolonged operational scenarios, demonstrating stability and enhancing the overall performance of conventional desalination technologies like RO, MSF, and MED. Notably, the Saline Water Conversion Corporation (SWCC) showcased remarkable outcomes, including a 30% increase in water recovery and a substantial reduction in energy consumption for NF-SWRO and NF-MSF/MED applications [51]. Moreover, the presence of NF proved instrumental in diminishing scaling potential within MSF and MED, enabling operations at elevated temperatures of up to 120-130°C [56]. In comparison to traditional pre-treatment methods like chemical precipitation, which demand

substantial chemical inputs [57] and exhibit vulnerability to fluctuations in brine concentrations, NF emerges as a robust alternative. When compared with other membrane processes such as RO and FO (Forward Osmosis), the higher energy consumption of the former and the elevated membrane cost of the latter position led to choose NF as the optimal technology for the initial phase of the proposed MLD process.

1.1.2 Magnesium Reactive Crystallizer (MRC)

The Magnesium Reactive Crystallizer (MRC) operates through a direct mixing process, where brine directly interacts with an alkaline solution (NaOH). In this interaction, magnesium ions in the brine react with hydroxyl ions from the alkaline solution, leading to the precipitation of $Mg(OH)_2$ crystals. Notably, this chemical reaction occurs at a specific pH value of 10.35. Achieving this pH requires a precise adjustment of the alkaline flow rate relative to the specific brine flow rate. Beyond magnesium recovery, the MRC offers the potential for calcium recovery as $Ca(OH)_2$ in a subsequent stage. However, this secondary reaction occurs at a higher pH of 13. Subsequent to the recovery of magnesium and calcium from the initial waste brine, a neutralization step takes place through the addition of HCl to restore the brine initial pH. The choice of NaOH as the alkaline reactant is crucial to ensure the high purity of $Mg(OH)_2$ crystals. Extensive testing in the past has confirmed the efficacy of NaOH in mineral recovery, producing products of superior purity [58]. In contrast, alternative alkaline compounds such as $Ca(OH)_2$ or lime have been found to induce co-precipitation of by-products (e.g., calcium sulphates, carbonates, and hydroxides), thereby diminishing the purity of $Mg(OH)_2$ [59]. The operational principles of the MRC closely resemble those of the pilot-scale plant "Multiple Feed - Plug Flow Reactor," developed and tested by Vassallo et al. in real conditions. The experimental results from previous works of Vassallo et al. have demonstrated high purity levels exceeding 90% for both $Mg(OH)_2$ and $Ca(OH)_2$ [60,61]. Finally, a Drum filter is employed to recover magnesium and calcium hydroxide crystals from the outlet suspension of the MRC.

1.1.3 Multiple-Effect Distillation (MED)

Multi-effect distillation (MED) stands out as a thermal-based technology extensively utilized in the desalination industry, particularly for treating high salinity feeds. Despite being the oldest method [62], it remains the least energy-consuming among other thermal-based technologies like Multiple-Stage Flash Distillation (MSF) [63], boasting energy consumption values ranging from 145-230 MJ/m³ of thermal energy [64]. The MED process involves a sequence of evaporators, referred to as effects, operating at progressively decreasing pressures and temperatures from the initial effect to the final one [65]. This stepwise pressure reduction allows the temperature of evaporation to decrease accordingly. Each effect comprises a tube bundle where vapour flows, transferring energy, and the feed is sprayed onto its surface. Partial evaporation takes place, yielding vapour for the subsequent effect and residual brine, which then advances to the next stage. The vapour produced in the last effect is condensed to yield the final distillate. In industrial-scale MED, the number of effects can vary from 2 to 16, depending on several factors, and in some instances, it may even reach 20 [64]. The Top Brine Temperature (TBT), representing the maximum brine temperature within the first effect, is constrained to 60-90°C due to scaling formation on tube surfaces [66]. The incorporation of NF can bring the TBT up to 120-130°C. Higher temperatures translate to more effects and, consequently, a greater quantity of distillate. However, the number of effects is limited by the necessity to maintain minimum temperature differences between consecutive stages. Several different MED configurations exist, including Backward feed, Forward feed, Parallel feed, and Parallel/cross feed. For the purposes of techno-economic analysis, a forward feed configuration is considered to achieve higher concentrations [67]. A pilot-scale MED process was developed and demonstrated within the SOL-BRINE project [41]. Results from this project indicated that the Total Dissolved Solids (TDS) of the brine effluent could be increased up to the saturation point (26% sodium chloride), simultaneously recovering water of demineralized quality [42]. However, in scenarios of such high concentration ratios, the number of effects is limited compared to conventional MED desalination systems, with 5-10 effects being a more

realistic range [68]. Among the acknowledged advantages of MED are the production of high-quality freshwater (TDS < 10 ppm), large capacity, the ability to handle high salinity feeds, concentration potential, and overall robustness. Despite certain drawbacks, such as low thermal efficiency [69], these are mitigated in the Pantelleria case study by utilizing waste heat supplied by a nearby diesel power plant.

1.1.4 NaCl Thermal Crystallizer (NTC)

In the context of NaCl production, an evaporative crystallizer was chosen: a straightforward and widely employed technology. This method has been proven to be effective in concentrating salt up to saturation, facilitating NaCl precipitation through thermal energy. Simultaneously, it yields both a distillate and residual brine. Extensive research, as documented in literature, underscores the superior advantages of the coupling MED-evaporator over emerging alternatives like Membrane Distillation (MD) [35]. Several advantages such as its capacity for handling large volumes and its adaptability to utilize low-grade or waste heat led to opt for the evaporative crystallizer. This strategic choice aligns with the goal of achieving optimal NaCl production efficiency. Via a parametric analysis of the upstream technologies of the proposed MLD system (see Paragraph 1.5.1), the NTC could produce high purity NaCl (97%), suitable for food purposes.

1.2 Technical Models description

To assess the techno-economic viability of the proposed treatment chain to be potentially implemented at an industrial scale, a thorough assessment was performed. To such end, firstly, technical models capable of simulating the functioning of the technologies were essential and implemented in Python.

Regarding the simulation of the NF unit, a comprehensive multi-scale model was employed, spanning three distinct scales. First, a small-scale model utilized a 1-D discretization of the NF membrane, employing the Donnan Steric Pore Model with

Dielectric Exclusion (DSPM-DE). One important assumption of this specific model was that the membrane is considered as a charged porous structure, for which specific membrane properties were required as inputs: the pore radius r_{pore} [nm], the active layer membrane thickness δ_m [μm], the dielectric constant ϵ_{pore} [-] and the charge density X_d [mol/m^3]. Such properties presented the following values for the membrane NF270 (employed in this work): $r_{\text{pore}} = 0.45$ nm, $\delta_m = 3$ μm , $\epsilon_{\text{pore}} = 56.5$, charge density $X_d = 40$ mol/m^3 [70]. This model, widely acknowledged in the scientific community, employed the extended Nernst-Planck equation to describe the ionic transmembrane phenomena, taking into account convection, diffusion, and electro-migration of the ions through the membrane. Simultaneously, the Hagen Poiseuille equation was applied to compute the solvent flux across the NF membrane. It is to be noted that the model was able to consider the phenomenon of concentration polarization: an important phenomenon that influences the single ion fluxes across the membrane. The small-scale model was subsequently integrated into a medium-scale model representing a single NF unit. The length of the NF element was discretized into intervals, with average values of ionic concentrations, flow rates, and pressure estimated for each interval. Key variables, such as osmotic pressure and bulk mass transfer coefficient within the NF element, were calculated based on these averages. The small-scale model facilitated the computation of ion rejections and solvent flux. Outlet concentrations and flow rates for each discretized interval were determined using mass balance equations. The large-scale model aimed at calculating the total number of vessels required to achieve a specific recovery value through an iterative approach. The NF technical model had been previously introduced by Micari et al. [70], with validation for similar brine compositions and operating conditions. For brevity, all equations of the NF technical model are provided in Appendix A.

As far as the MRC unit is concerned, it is noteworthy that no pre-existing model had been developed at the time of this study. The MRC operates through two consecutive precipitation steps: (i) the precipitation of $\text{Mg}(\text{OH})_2$ and (ii) the precipitation of $\text{Ca}(\text{OH})_2$. Specifically, literature lacks information concerning the kinetics of the

chemical precipitation of $\text{Mg}(\text{OH})_2$. For this reason, a simplified process model was developed, incorporating mass balance equations and assuming an instantaneous reaction between magnesium (present in the feed stream) and hydroxyl ions (present in the alkaline stream). The mass balance equations played a crucial role in estimating the NaOH flow rate needed to attain pH values of 10.4 and 13 for $\text{Mg}(\text{OH})_2$ and $\text{Ca}(\text{OH})_2$ precipitation, respectively. These equations also considered typical conversion factors for magnesium and calcium into their respective hydroxides, drawing from experimental data outlined in [61]. Additionally, the model estimated the required flow rate of HCl for neutralizing the MRC effluent. Regarding the specific geometry of the MRC unit considered in the techno-economic analysis, it mirrored that of the pilot-scaled magnesium crystallizer previously developed by Vassallo et al. [61]. For a detailed presentation of all equations related to the MRC technical model, refer to Appendix A.

In contrast, the simulation of the MED unit leveraged a comprehensive mathematical model, previously introduced by Micari et al. [67]. The model considered a Forward Feed configuration, where both the feed and vapour progressed in the same direction. Each effect of the MED unit involved the computation of mass flow rates, temperature, and pressure profiles through the application of mass and energy balance equations. The MED model differentiated between three classes of effects, namely: (i) the first effect, (ii) the intermediate effects, and (iii) the last effect with the end condenser. For the sake of brevity, all equations of the MED technical model are available in Appendix A. Notably, the first effect was unique as it received heat from an external source, and the feed stream passed through all the preheaters. In this effect, the feed was sprayed onto a tube bundle while external heat circulated within the tubes. Vapour generated by partial evaporation of the feed stream crossed the demister and the first preheater, partially condensing before being directed to the next effect as the heating source. The remaining brine from the first effect was also fed to the next effect, sprayed on the external tube bundle. The modelling approach for the intermediate effects differed slightly, involving two energy balances on the preheater and heat exchanger to calculate condensed and evaporated fractions,

respectively. The last effect, lacking a preheater, sent all vapour directly to the end condenser, where complete condensation occurred. Mathematically, this translated into different energy balances on the effect and the last flashing box, as the total vapour in the last effect condensed in the end condenser and collected in the flash box. The brine exiting the last effect constituted the final brine of the entire MED plant, while the condensate from the flash box served as the ultimate distillate. Both outlets had to necessarily respect the global mass balance equations. Regarding the end condenser, its feed was utilized to condense vapour. The total required cooling water flow rate was determined through heat balance, with any surplus cooled down and reused in the system.

Finally, a simplified process model for the NTC was developed, relying on both mass and enthalpy balance equations (refer to Appendix A for details). Given a desired value of the global NaCl recovery from the combined "evaporative technologies" (MED + NTC), mass balance equations facilitated the computation of mass flow rates for NaCl, brine, and distillate. Simultaneously, simple enthalpy balance equations were employed to estimate the thermal energy required for evaporation, accounting for sensible and latent heat, as well as the operating temperatures of the crystallizer. To assess the purity of the produced NaCl, logical conditions were embedded within the technical model equations. These conditions considered the precipitation of potential by-products that could compromise the final purity of NaCl based on the desired NaCl recovery and operating parameters, such as operating temperature. The incorporation of these logical conditions was made feasible through data obtained from PHREEQC software. Specifically, by inputting the ionic composition of the NTC feed at specific pressure and temperature conditions into PHREEQC, the software identified compounds prone to precipitation at those operating conditions and returned their solubility using the thermodynamic Pitzer model. Results from PHREEQC simulations informed the introduction of logical conditions within the model, accounting for the precipitation of by-products that could impact the purity of the produced NaCl.

In summary, Table 3 provides a comprehensive overview of the technical models, presenting input parameters and key outputs for each model.

Table 3: Main inputs and outputs of the technical model of each unit in the MLD system

| Technology | Main Input parameters (Technical model) | Main Outputs (Technical model) |
|----------------------------------------------------------|------------------------------------------------------------------------------------------------------------------------------------------------------------------------------------------------------------------------------------------------------------------------------------------------------------------------------|---------------------------------------------------------------------------------------------------------------------------------------------------------------------------------------------------------------------------------------------------------------------------------------------------------------------------------------------------------------------------------------------|
| Nanofiltration (NF) | <ul style="list-style-type: none"> • Inlet flow rate [m³/d] • Inlet ions concentrations [g/L] • Membrane ions rejections [-] • Operating pressure [bar] • Permeate recovery [%] • Specific membrane properties | <ul style="list-style-type: none"> • NF retentate flow rate [m³/d] • NF permeate flow rate [m³/d] • Retentate ions concentrations [g/L] • Permeate ions concentrations [g/L] • Total number of vessels[-] • Electricity demand [kWh_{el}] |
| Magnesium Reactive Crystallizer (MRC) | <ul style="list-style-type: none"> • Inlet flow rate [m³/d] • Inlet ions concentrations [g/L] • NaOH concentration (1st/2nd stage) [g/L] • Mg conversion factor 1st stage [%] • Ca conversion factor 2nd stage [%] | <ul style="list-style-type: none"> • Flow rate of produced hydroxides [kg/d] • Flow rate of alkaline solution [m³/d] • Effluent flow rate [m³/d] • Outlet effluent ions concentrations [g/L] • Electricity demand [kWh_{el}] |
| Multi-Effect Distillation (MED) | <ul style="list-style-type: none"> • Inlet flow rate [m³/d] • Inlet NaCl concentration [g/L] • Steam Temperature [°C] • Outlet NaCl concentration [g/L] • Number of effects [-] | <ul style="list-style-type: none"> • Distillate flow rate [m³/d] • Outlet brine flow rate [m³/d] • Outlet brine ions concentration [g/L] • Area of heat exchangers [m²] • Heat demand [kWh_{th}] • Electricity demand [kWh_{el}] |
| NaCl Thermal Crystallizer (NTC) | <ul style="list-style-type: none"> • Inlet flow rate [m³/d] • Inlet ions concentrations [g/L] • Inlet feed temperature [°C] • Operating temperature [°C] • NF membrane rejection correction factor [-] • Total NaCl recovery (MED+NaCl Cryst) [%] | <ul style="list-style-type: none"> • Distillate flow rate [m³/d] • Outlet effluent flow rate [m³/d] • Outlet effluent ions concentration [g/L] • Outlet flow rate of NaCl produced [kg/d] • Purity of NaCl produced [%] • Heat demand [kWh_{th}] • Electricity demand [kWh_{el}] |

1.3 Economic Models description

To assess the economic viability of each technology, each process model was integrated with an economic one, with the main outputs of the technical models serving as inputs for their corresponding economic models. Similar to the technical models, the economic models were implemented using Python.

For the NF unit, the economic model adopted the Verberne cost model [56], drawing on practical data provided by NF unit suppliers [56]. Capital costs were computed based on four components: (i) building construction, (ii) pumps, filters, and piping, (iii) energy supply systems, and (iv) investment in membrane modules. Each capital expenditure (capEX) component was updated using the chemical engineering price index CEPCI (referenced to the year 2021). A straight-line depreciation was applied to each capEX contribution, considering depreciation periods of 30 years for buildings, 15 years for piping, pumps, and energy systems, and 5 years for membrane modules. A discount rate of 6% was employed, aligning with typical values for desalination plants [57]. Operating costs included expenses for electrical energy consumption, chemical usage, maintenance, quality control, and daily operation, assuming a plant availability of 8000 working hours per year. For brevity, equations of the NF economic model can be found in Appendix B.

The economic models for the MRC, MED, and NTC units employed the Bare Module Cost Technique for capital cost estimation [58], a widely accepted tool in chemical plant economic assessments. Capital costs were expressed as functions of the purchased cost of equipment, which was initially estimated as the purchase cost in standard conditions (C_p^0 [€]). This value was a function of the actual equipment size, adjusted using the *CEPCI* index and a global correction factor (F_{BM}) to account for direct and indirect costs, as well as non-standard operating conditions. The calculated values (C_{BM} [€]) were then adjusted for contingency and fee factors ($\alpha_{\text{cont}} = 15\%$ and $\alpha_{\text{fee}} = 5\%$ of the total C_{BM} , respectively). The total module cost (C_{TM} [€]) was depreciated over 20 years with a discount rate (i) of 6%. Refer to Appendix B for capEX details for the MRC, MED, and NTC.

Operating costs for the MRC encompassed energy consumption for pumping and drum filtration, reaction chemicals (NaOH solution for the first and second stage), and chemicals for neutralization (HCl solution to restore the pH of the final brine). The MED unit operating costs included electric energy consumption, thermal energy consumption, and chemical consumption for cleaning, anti-scaling, and anti-foaming

purposes. NTC unit operating costs considered electric energy consumption for pumping, thermal energy for NaCl crystal precipitation, and disposal costs for the final brine. Additionally, the least expensive conventional brine treatment method, surface water discharge (0.2905 €/m³ of brine), was integrated into the NTC operating costs. Detailed operating cost equations for the MRC, MED, and NTC can be found in Appendix B. The economic analysis of the proposed MLD process was performed considering the main specific costs/prices of chemicals and energy sources reported in Table 4:

Table 4: Specific costs/prices of chemicals and energetic sources employed in the economic analysis

| Specific Cost* | | |
|---------------------|--------|-----------------------|
| Mg(OH) ₂ | 1000 | €/ton [71,72] |
| Ca(OH) ₂ | 125 | €/ton [73] |
| Water | 0.83 | €/m ³ [71] |
| NaOH | 330 | €/ton [74] |
| HCl | 125 | €/ton [75] |
| NaCl | 66 | €/ton [76] |
| Electricity | 0.2 | €/kWh ** |
| Waste Heat | 0.0083 | €/kWh*** [67] |

**All specific costs expressed in \$ in the quoted references were converted in € considering a currency conversion factor (April 2021) equal to 0.83€/§*

***The specific cost of electricity refers to industrial user' cost in Pantelleria, Italy*

****The specific cost of waste heat is assumed to account also for the depreciation costs of equipment (e.g. heat exchangers) needed to valorise it.*

These specific costs, identified as the primary inputs for the economic analysis, played a pivotal role in evaluating the economics of the MLD chain. In the context of the Pantelleria case study, typical electricity and waste heat costs prevalent on the island were incorporated into the analysis. Notably, waste heat was used in the study as, currently, renewable energy sources are constrained by elevated capital costs. All operating costs were estimated, taking into account an assumed annual plant availability of 8000 working hours per year.

1.4 Simulation Approach

To comprehensively assess the overall performance of the entire treatment chain, both technical and economic models for all technologies were integrated into a unified workflow using RCE (Reusable Component-based Environment) software. RCE, an innovative tool developed by the German Aerospace Centre (DLR), was chosen for its unique capabilities, detailed in [46]. The distinct features of RCE made it an ideal solution for effortlessly incorporating multiple models and conducting a thorough techno-economic analysis. Within the RCE framework, each technology was represented as a block, within which both technical and economic models, implemented in Python, were invoked. Each technology block had external inputs, and the process outputs of one model became the process inputs for the subsequent model in the treatment chain. Between successive models, additional scripts were implemented based on simple mass balance equations to account for the mixing of multiple streams, such as the blending of NF permeate and MRC effluent. The economic feasibility of the entire treatment chain was then evaluated through five key global parameters. Four of these were: (i) Levelized cost of water ($LCOW_{\text{ater}}$), (ii) Levelized cost of $Mg(OH)_2$ ($LCOM_{g(OH)_2}$), (iii) Levelized cost of $Ca(OH)_2$ ($LCOC_{a(OH)_2}$) and (iv) Levelized cost of $NaCl$ ($LCOS_{\text{alt}}$). The Levelized Cost, in general terms, represents the selling price of a particular product (e.g., water, salt) required to achieve the break-even point over a specified plant lifetime. Under the assumption that the produced flow rate of a specific product and the operating costs remain consistent across each year of the plant lifetime, the levelized cost (LC) for the i^{th} product can be calculated using the following formula:

$$LCO_i^{th} = \frac{\sum_{\text{units}} capEX + \sum_{\text{units}} opEX - (\sum_{\text{units}} REV - (REV_{i^{th}}))}{Q_{i^{th}} \text{ (or } V_{i^{th}}) * N_{oper, hours}} \quad (1)$$

Where the $LOCI^{th}$ was the Levelized Cost of the i^{th} product [$\text{€}/\text{ton}$ or $\text{€}/\text{m}^3$ (according to the units in which the product quantity was expressed)], $capEX$ were the depreciated capital costs of each unit/technology within the treatment chain

[€/year], $opEX$ were the operating costs of each unit [€/year], REV was the revenue of each technology [€/year] and $Q_{i^{th}}$ (or $V_{i^{th}}$) was the annual quantity of the specific product produced [ton/h or m³/h]. The last main parameter was the Brine Treatment Specific Cost (BTSC) defined as:

$$BTSC = \frac{\sum_{units} capEX + \sum_{units} opEX}{V_{Brine\ feed} * N_{oper, hours}} \quad (2)$$

Where the $BTSC$ was expressed in €/m³ of brine fed and $V_{Brine\ feed}$ was the annual brine fed to the treatment chain [m³/h].

1.5 Results and Discussion

The analysis conducted in this study was fundamentally divided into two distinct parts:

- (i) a technical analysis with the scope to investigate the impact of specific parameters (i.e., the ionic rejection of the NF membrane) on the performances of the treatment chain and properties of the selling products;
- (ii) an economic analysis dedicated to identifying the primary contributors to the overall economic feasibility of the proposed MLD chain. This involved varying characteristics of individual technologies (e.g., changing the number of MED effects) or adjusting specific costs (e.g., electricity costs) to understand their influence on the economic viability of the chain.

1.5.1 Feasibility analysis of NF membrane rejections and NaCl recovery

For the technical analysis (and also for the economic analysis), the brine composition detailed in Table 2 was utilized, with a fixed inlet brine flow rate of 2280 m³/d

(equivalent to 50% of the total brine produced by three out of the four operating RO units at the Sataria desalination plant).

Concerning the NF plant, which served as the pre-treatment step and the first stage of the MLD system, the study considered spiral-wound elements. Each element comprised five membrane leaves wound together, and, in line with large-scale industrial practices, six elements were arranged in series within a pressure vessel. Within each pressure vessel, the retentate from one element became the feed for the subsequent element, and the permeates from all elements within the same pressure vessel were mixed together. Additionally, a number of pressure vessels were arranged in parallel to achieve a specified permeate recovery. The chosen operating conditions for the NF plant reflected typical parameters in the brine management field: a permeate recovery of 60% at an operating pressure of 20 bar.

To establish realistic membrane ion rejections, a comprehensive review of existing literature on NF rejections was conducted. It was observed that the NF270 membrane (Filmtec) was predominantly employed in treating desalination brines. Considering various rejection values reported in literature under similar operating conditions and brine compositions (e.g., [77–79]), an average rejection value for each ion was considered. The set of ion rejection values is presented in Table 5.

Table 5: Set of ion rejections of the NF membrane (operating conditions: Permeate recovery = 60%; Pressure = 20 bar).

| Ionic Species | Na^+ | Ca^{2+} | Mg^{2+} | K^+ | Cl^- | SO_4^{2-} | HCO_3^- |
|-------------------------------|--------|-----------|-----------|-------|--------|-------------|-----------|
| Membrane rejection [%] | 6 | 50 | 71 | 5 | 12 | 91 | 45 |

As shown in Table 5, the NF270 membrane performance was not optimal, particularly in terms of calcium and magnesium rejections. Notably, only 50% of calcium was rejected, leading to significant adverse effects on the subsequent stages of the treatment chain. This limitation had two main consequences: (i) only 50% of calcium was recovered as calcium hydroxide, resulting in reduced total revenue, and (ii) the 50% of calcium that permeated through had the potential to induce scaling in

the Multi-Effect Distillation (MED) unit and compromise the purity of the final NaCl product. The impact was even more pronounced for magnesium, considering its higher selling price compared to calcium hydroxide.

Achieving food-grade salt (NaCl) quality, with a required final purity of at least 97% according to the Codex Alimentarius [80], was a critical objective. Therefore, a technical analysis was performed to understand the influence of NF ion rejections on the NaCl purity. More specifically, this involved a theoretical analysis in which two fictitious correction factors, α and β , were introduced to understand to what extent the single ion rejections of the NF membrane had to be increased in order to achieve a certain NaCl purity at the end of the proposed MLD chain

The introduced correction factors were indeed two to account for ions with similar transport behaviour across the NF membrane, ensuring a consistent correction for rejections. Specifically, rejections of Mg^{2+} , Ca^{2+} , and SO_4^{2-} (which share similar transport characteristics [81]) were corrected by the same factor α . Similarly, HCO_3^- and Cl^- , characterized by comparable behaviour, were corrected by β . Meanwhile, the rejections of Na^+ and K^+ (which typically have low and stable values at various operating conditions) were considered constant. It is to be noted that the origin of the two correction factors derives from empirical observations of the NF membrane behaviour, concerning the general set of transport phenomena mechanisms and not only one specific transport mechanism. For instance, if the correction factors were to have only considered Donnan Exclusion, most certainly the ions would have been grouped differently. This would have meant that an increase of the positive surface of the NF membrane for example would have only increased the membrane rejections of the cations, leading to a contemporarily decrease of the anionic rejections. Therefore, considering all transport phenomena mechanisms in the case of this specific work, all ion rejections increase with the correction factors but at different rates. Equations (3) and (4) outlined how the bivalent and monovalent ions varied with α and β , respectively.

$$R_{i^{th}}^{NEW} = R_{i^{th}}^{\circ} + \alpha * (1 - R_{i^{th}}^{\circ}) \quad (3)$$

$$R_{j^{th}}^{NEW} = R_{j^{th}}^{\circ} + \beta * (1 - R_{j^{th}}^{\circ}) \quad (4)$$

Where i^{th} and j^{th} are the bivalent ion (Mg^{2+} , Ca^{2+} and SO_4^{2-}) and monovalent ion (Cl^{-} and HCO_3^{-}), respectively. R° and R^{NEW} are the initial rejection value (**Error! Reference source not found.**) and the updated rejection value. α and β are the bivalent and monovalent ions correction factors, respectively.

In the detailed parametric analysis, the variation of the parameter α was explored within a range of 0 to 1 at fixed intervals of 0.1. When α equalled 0, the rejection value (R^{NEW}) was equivalent to the original rejection value (R°), while for α equal to 1, R^{NEW} equalled 100%. For each specific α value, β was calculated to maintain the electro-neutrality of the solution, considering both the NF permeate and NF retentate. The results of this analysis are depicted in Figure 4a) and 3b), where the rejection of a specific ion is plotted and compared against the typical rejection values of commercial NF membranes (represented by the coloured areas). These commercial membranes have been extensively tested and applied in the treatment of seawater brines, as documented in previous studies [77–79].

Observations from the analysis revealed that values of α exceeding 0.8 led to unrealistic sets of rejections, with single ion rejections falling outside the so-called "real and commercial" range. Consequently, $\alpha=0.8$ was identified as a critical scenario, while $\alpha=0.7$ was adopted in all simulations as an optimistic yet realistic value. This choice was justified by the fact that $\alpha=0.7$ resulted in a set of rejections that remained within the typical ranges observed in real-world commercial applications.

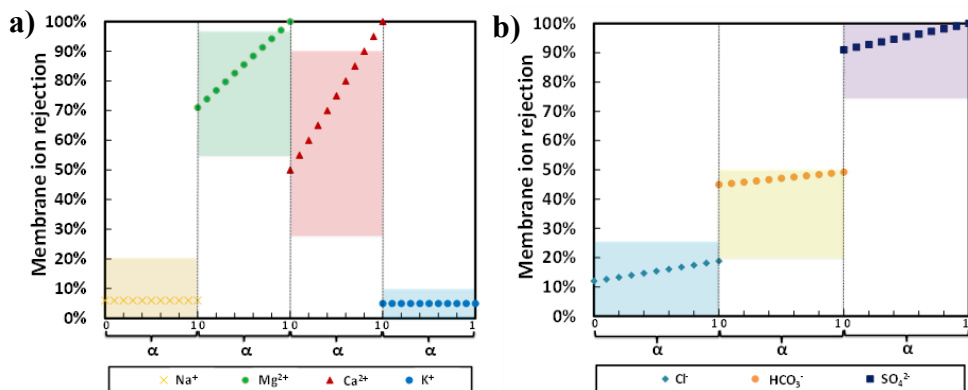


Figure 4: a) Trend of membrane rejection of cations with α (ranging from 0 to 1); b) Trend of membrane rejection of anions with α (ranging from 0 to 1). Coloured areas for each ion indicate the typical rejection values of commercial NF membranes.

However, the primary objective of the analysis was to identify the minimum value of the correction factor α that guaranteed a minimum NaCl purity of 97%, meeting the criteria for sale as a food-grade product. To achieve this, PHREEQC software, known for its reliability in similar applications as demonstrated in past works [47], was employed.

For the simulations, treating the MED and NTC as a unified unit, MED inlet concentrations were required as inputs. These concentrations resulted from the mixing of the NF permeate and the MRC effluent. To maintain the integrity of the analyses across different values of α , all parameters of the MRC, including geometrical and operating conditions, were fixed and kept constant. Experimental values were applied for the concentration of NaOH (1 mol/L) and conversion factors of Mg^{2+} (95%) and Ca^{2+} (97%) for the first and second stages, respectively. These conditions remained consistent throughout the analyses.

Within the PHREEQC simulations, the quantity of water to be evaporated was fixed to ensure a specific NaCl recovery. Subsequently, based on the precipitated products, the purity of NaCl produced was calculated.

For each α value, the purity was evaluated at three different NaCl recovery levels: 30%, 50%, and 75%. The results of these analyses are illustrated in Figure 5a).

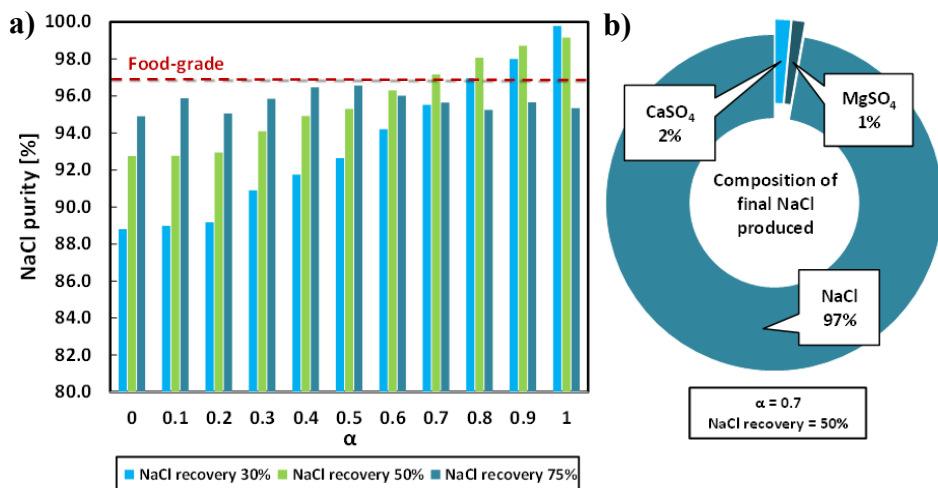


Figure 5: a) Trend of purity of NaCl produced at different values of α and NaCl recovery; b) Composition of the final NaCl produced at food-grade obtained with $\alpha=0.7$ and NaCl recovery = 50%.

The results depicted in Figure 5a) reveal an increase in purity with α at low recoveries (30%) of NaCl. This trend is primarily attributed to the greater rejection of magnesium and calcium by the NF membrane, leading to their enhanced recovery as hydroxides in the MRC. Consequently, smaller quantities of these impurities were available to precipitate, thereby preserving the purity of the final product. A similar trend was observed at a NaCl recovery of 50%, although the increase in purity exhibited a diminished slope. This can be attributed to the fact that as more NaCl is recovered (through increased water evaporation), a greater amount of impurities tends to precipitate, counteracting the positive impact on purity.

At very high NaCl recoveries (75%), purity did not exhibit a net increase with α , fluctuating around an average value. Notably, this average value remained below the 97% threshold required for the food-grade target. The optimal conditions for achieving the target purity were identified at a NaCl recovery of 50% with α equal to 0.7. Importantly, this value of α (0.7) still ensured operation within a realistic range of NF membrane ion rejections.

In Figure 5b), the percentage of impurities in the final NaCl product is presented. Specifically, CaSO₄ and MgSO₄ were the main compounds that precipitated with NaCl, constituting 2% and 1% of the total solid product, respectively.

Moreover, considering α equal to 0.7, Table 6 lists the ionic composition and flow rates of the main streams in the MLD process. Notably, only 6% of the initial SWRO brine was discharged back into the environment, characterizing the MLD process as an "almost-ZLD" (Zero Liquid Discharge) process. Table 7, furthermore, provides the flow rates of the products achieved with the MLD process.

Table 6: Ionic composition and flow rates of the main streams of the MLD process.

| | NF feed | NF retentate | NF permeate | MED feed | MED brine | Discharge |
|----------------------------------|---------------------|-----------------|----------------|-------------|--------------|-----------|
| Ion | Concentration [g/L] | | | | | |
| Na ⁺ | 21.4 | 20.7 | 20.9 | 21.2 | 107 | 5.90 |
| Mg ²⁺ | 2.70 | 5.98 | 0.37 | 0.21 | 1.08 | 0.13 |
| Ca ²⁺ | 0.88 | 1.84 | 0.20 | 0.13 | 0.65 | 0.04 |
| K ⁺ | 0.78 | 0.79 | 0.74 | 0.63 | 3.15 | 0.24 |
| Cl ⁻ | 39.0 | 43.9 | 34.3 | 31.4 | 158 | 6.45 |
| SO ₄ ²⁻ | 5.50 | 12.9 | 0.24 | 3.18 | 16.0 | 0.02 |
| HCO ₃ ⁻ | 0.18 | 0.19 | 0.08 | 0.05 | 0.25 | 0.02 |
| Flow rate [m ³ /d] | 2280 | 950 | 1330 | 2330 | 398 | 135 |

Table 7: Flow rates of the products of the MLD process.

| Product | Mg(OH) ₂ | Ca(OH) ₂ | Water (MED) | NaCl | Water (NTC) |
|-----------|---------------------|---------------------|------------------------|-------------|-----------------------|
| Flow rate | 12,956 kg/d | 2923 kg/d | 1932 m ³ /d | 64,992 kg/d | 252 m ³ /d |

1.5.2 Economic analysis

1.5.2.1 Analysis of the Base Case scenario

Once the optimal value of α required for achieving 97% purity of NaCl was identified, a comprehensive economic analysis of the proposed MLD system was conducted to assess its feasibility. It is essential to emphasize that the compositions and flow rates considered for the MLD system were based on the values listed in Tables 6 and 7.

Up to this point, specific information regarding the operating conditions of the MED and NTC units had not been provided. The previous technical analysis treated the MED unit and the NTC unit as a unified entity without delving into specific operating conditions. More precisely, to understand which salts could potentially precipitate after concentrating the NF permeate and retentate compromising the purity of produced NaCl, the PHREEQC software only required a fixed overall water recovery given by the MED and NTC. No other inputs were required. However, for the economic analysis, defining the specific operating conditions of both technologies was necessary.

Concerning the MED, 10 effects were considered, a typical industrial value, operating at a TBT of 110°C. This temperature choice was possible thanks to the NF unit upstream. For the NTC, 5 effects were considered with a maximum operating temperature of 100°C. Both the MED and NTC units utilized waste heat sourced from flue gases produced in a nearby power plant. This approach contributed to reducing operating costs for the energy-intensive technologies within the treatment chain. The techno-economic analysis results, presented in Figure 6, indicated that the MED was one of these technologies (ranking third in electricity consumption).

In terms of thermal energy consumption, the MED unit consumed more than twice the amount of heat compared to the NTC. Additionally, it is noteworthy that the

specific electric consumption of the MRC unit was the highest. This was attributed to the Drum filter employed for the recovery of hydroxide solids from the produced slurry. These insights provided a detailed understanding of the energy and economic dynamics within the MLD system, guiding further considerations for process optimization and economic sustainability.

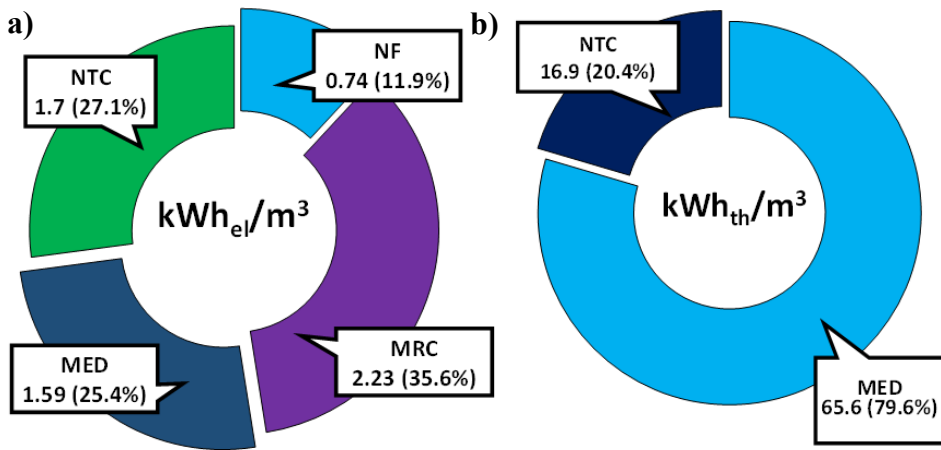


Figure 6: Distribution of the electrical and thermal energy consumption per m³ of intake brine in the MLD system.

Anyhow, energy consumed by the units was only one of the contributions to the total cost of the SWRO brine valorisation chain. Results of the global economics of the entire process are provided in **Error! Reference source not found.**

In Figure 7, it is evident that the total capital costs were significantly lower than the total operating costs. Notably, NF and MED units contributed the majority to capital costs. NF contribution was attributed to its membranes, while MED capital costs were associated with its multiple effects and numerous heat exchangers. On the other hand, the MRC unit played a pivotal role in driving overall high operating costs. This was primarily due to the consumption of substantial amounts of expensive alkaline reactants (such as NaOH) and subsequent chemical usage (HCl) for the final neutralization step. Despite the high overall costs, the total revenue generated by the

MLD system exceeded both capital and operating costs. This was primarily facilitated by the high selling price of $\text{Mg}(\text{OH})_2$, coupled with the substantial quantities of NaCl produced.

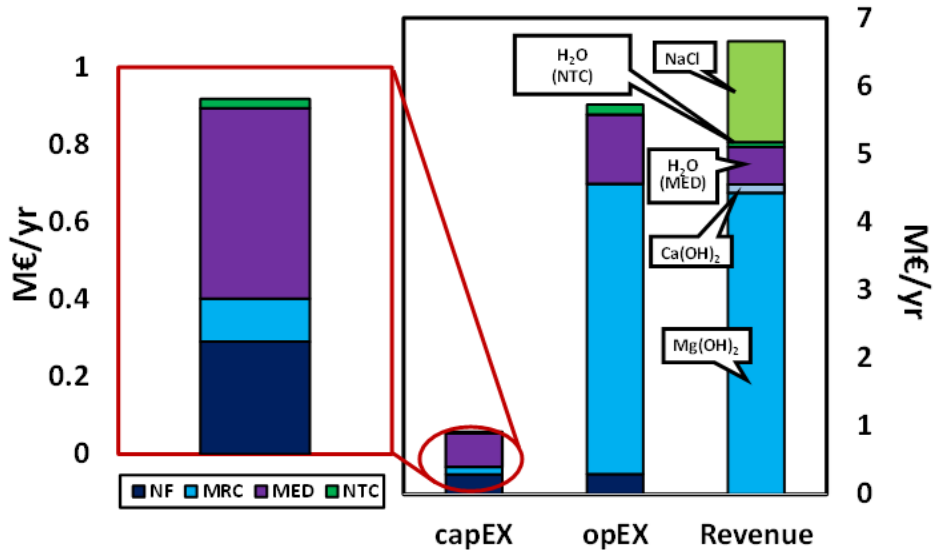


Figure 7: Global economics of the proposed MLD system expressed in million (M) euros per year. CapEX and opEX bars refer to the 4 technologies according to the same legend shown in the inset.

As a result of the higher revenues compared to the sum of capital and operating costs, the Levelized Costs of the valuable products obtained from the chain were lower than their selling price. Figure 8 provides a detailed breakdown of all Levelized Costs. Notably, only the Levelized Cost of salt (LCOS_{alt}) equalled the typical market price (i.e., 66 €/ton), affirming the competitive nature of the treatment chain for salt production. All in all, the low Levelized Costs underscored the economic viability and attractiveness of the integrated technology for the production of various valuable products.

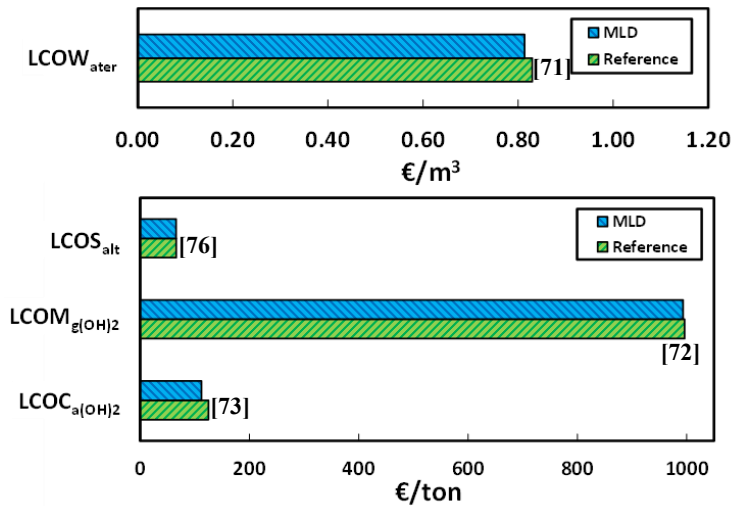


Figure 8: Levelized costs of valuable products ($LCOW_{ater}$ = Levelized Cost of Water; $LCOS_{alt}$ = Levelized Cost of Salt; $LCOM_{g(OH)_2}$ = Levelized Cost of $Mg(OH)_2$; $LCOC_{a(OH)_2}$ = Levelized Cost of $Ca(OH)_2$) compared to their actual market prices.

1.5.2.2 Economic comparison with other brine treatment concepts

The economic feasibility of the entire treatment chain was further assessed by examining the Brine Treatment Specific Cost (BTSC), as defined in Section 1.4. Figure 9 provides a comparative analysis of the brine treatment cost of the proposed MLD system with conventional brine disposal methods and recently proposed brine valorisation schemes found in the literature. When considering only capital and operating costs, neglecting any revenue (Figure 9), the MLD system appeared less attractive compared to existing brine disposal methods. Specifically, the BTSC was calculated to be 8.49 €/m³, considerably higher than the 4.65 €/m³ required with conventional evaporation ponds. However, when factoring in the sale of all the valuable products recovered by the integrated chain, the BTSC approached zero, much lower than both conventional methods and recent proposals in the literature (Figure 9).

It is noteworthy that the brine treatment costs associated with schemes presented in the literature (e.g., 0.5 €/m³ [40], 0.96 €/m³ [35], 0.06 €/m³ [34], 0.96 €/m³ [11])

already accounted for the revenue generated from the sale of valuable goods. Particularly, the BTSC of the proposed treatment chain, calculated at -0.02 €/m^3 , assumed a negative value. This negative BTSC reflects that the sum of capital expenditures (capEXs) and operating expenditures (opEXs) for the treatment chain was lower than the overall revenue achieved. The negative BTSC indicates that the proposed treatment chain is not only cost-effective but potentially represents a net saving. This outcome suggests that the treatment chain is market-competitive, where brine treatment is no longer a cost but a source of economic gain.

It is important to note that these results should be interpreted with consideration for current market conditions for the products involved. Changes in market conditions upon the large-scale implementation of the proposed chain may impact the economic outcomes.

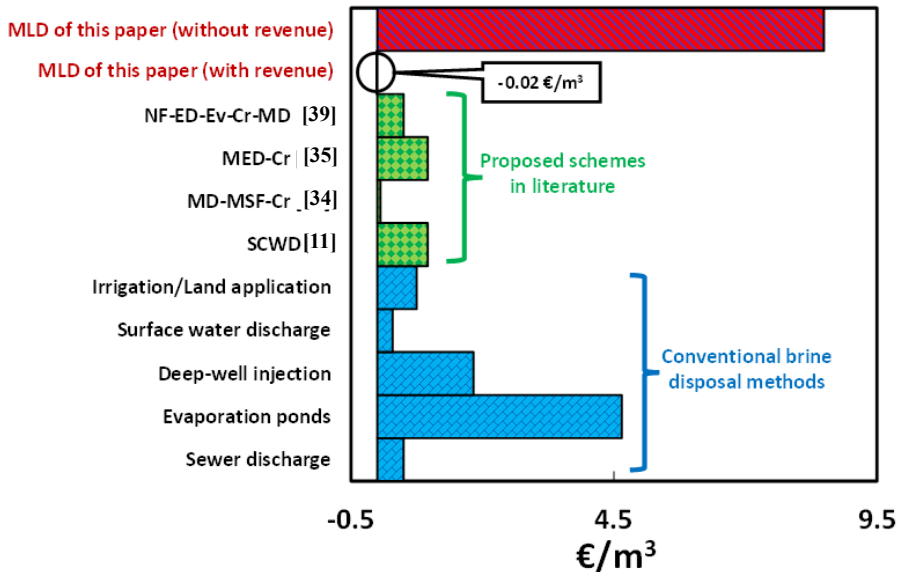


Figure 9: Comparison between conventional methods costs [76], proposed schemes in literature and BTSC of the proposed MLD with and without accounting for the revenues.

1.5.2.3 MED influence on the economics of the MLD scheme

The comprehensive techno-economic analysis successfully established and demonstrated the economic viability of the MLD system, applied as a hybrid technology to achieve brine volume minimization, mineral recovery, and water production. However, these findings were specific to a treatment chain that included an MED unit with a defined technical design, specifically with 10 effects. Therefore, it was interesting to explore how the total costs and the BTSC might be influenced by varying the number of MED effects.

Figure 10 illustrates the trend of total capital expenditures (capEXs), total operating expenditures (opEXs), and the BTSC of the treatment chain in relation to the number of effects. Considering a range of effects between 5 and 15, it is noteworthy that capEXs and opEXs exhibited opposite trends as the number of MED effects increased. This resulted in an overall minimum value of the BTSC, precisely when 8 effects were reached. The augmentation of capital costs was primarily attributed to the increase in units, leading to a higher number of heat exchangers and condensers, among other components. In contrast, operating costs predominantly decreased due to the reduction in thermal energy consumption required by the MED.

While the increase in operating costs prevailed at low numbers of effects, and the increase in capital costs was prominent at higher numbers of effects, the existence of a minimum value for the BTSC was justified. Notably, the minimum value of the BTSC was negative. This negative value stemmed from the fact that the sum of total capEXs and opEXs was lower than the total revenue obtained from the sale of all valuable goods produced. This outcome highlights the economic efficiency and competitiveness of the treatment chain, particularly emphasizing its potential for net economic gain.

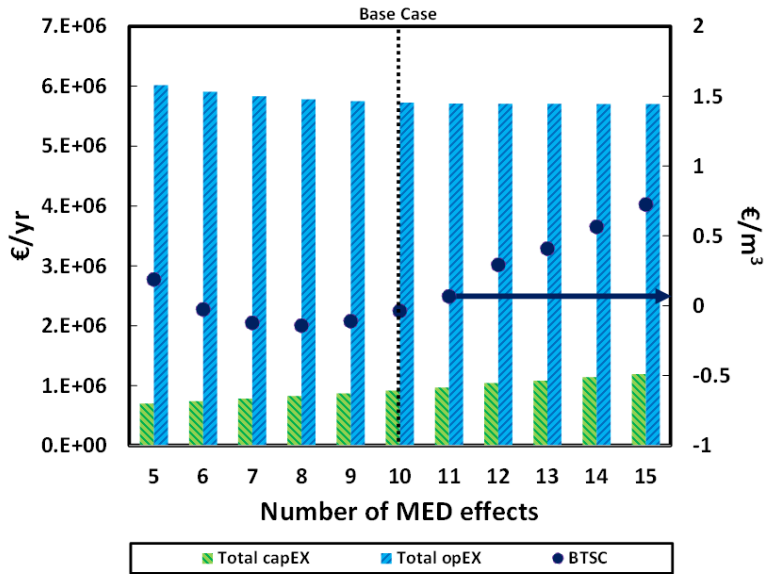


Figure 10: Trend of total capEXs, total opEXs and BTSC of the entire treatment chain with the number of MED effects. The polynomial curve that links the BTSC at different numbers of MED effects has also been represented.

1.5.2.4 Parametric analysis and Tornado diagram of the main factors affecting the BTSC

After identifying an optimal design for the MED technology, a final parametric economic analysis was conducted to assess the impact of specific costs of chemicals or electricity on the overall economics of the proposed MLD system. The specific costs (or prices) were varied within reasonable ranges to understand how changes in these parameters could affect the global economic feasibility of the MLD system.

Table 8 provides the typical ranges considered for the parametric analysis, representing the variations in the cost (or price) of a specific chemical or electricity. It is important to note that the minimum and maximum values in each range correspond to those observed in the year 2021 in Europe.

Table 8: Range of specific prices/costs of chemicals and energetic sources employed in the parametric analysis.

| | Typical range of specific price/cost* | |
|---------------------|------------------------------------------|-----------------------|
| Mg(OH) ₂ | 580 - 1162 | €/ton ** |
| Ca(OH) ₂ | 42 - 208 | €/ton [73] |
| Water | 0.42 - 1.66 | €/m ³ [82] |
| NaOH | 166 - 498 | €/ton [74] |
| HCl | 83 - 250 | €/ton [83] |
| NaCl | 42 - 125 | €/ton [76] |
| Electricity | 0.08 - 0.25 | €/kWh [84] |

**All specific prices/costs were converted in € considering a currency conversion factor April 2021 equal to 0.83€/€*

***Range of the specific price of Magnesium Hydroxide derives from an internal economic analysis carried out by UNIPA*

Figure 11 presents a Tornado diagram depicting the variation of the Brine Treatment Specific Cost (BTSC) concerning the parametric costs (or prices), such as the specific costs (or prices) of chemicals (NaOH, HCl, Mg(OH)₂, NaCl, Ca(OH)₂) and electricity. This analytical representation highlights the maximum and minimum values reached by the BTSC when the cost of a specific chemical or electricity is at its minimum or maximum within the considered ranges. Notably, the diagram illustrates that the higher the selling prices of the recovered products (Mg(OH)₂, NaCl, Ca(OH)₂, and H₂O), the lower the BTSC, as the former contributes to an overall increase in revenue for the treatment chain. Conversely, high costs of NaOH, HCl, and electricity lead to increased operating costs, resulting in a higher BTSC. Additionally, the diagram emphasizes the substantial influence of cost (or price) variations in NaOH, Mg(OH)₂, and NaCl on the BTSC compared to other factors. Specifically, when NaOH is purchased at a very high price (e.g., 498 €/ton) or Mg(OH)₂ and NaCl are sold at their lowest prices (e.g., 580 €/ton and 42 €/ton, respectively), the BTSC may surpass conventional brine treatment costs, potentially impacting the competitiveness of the proposed MLD system. This concern is not as

pronounced when electricity reaches its highest cost or when $\text{Ca}(\text{OH})_2$ and H_2O are sold at their lowest prices.

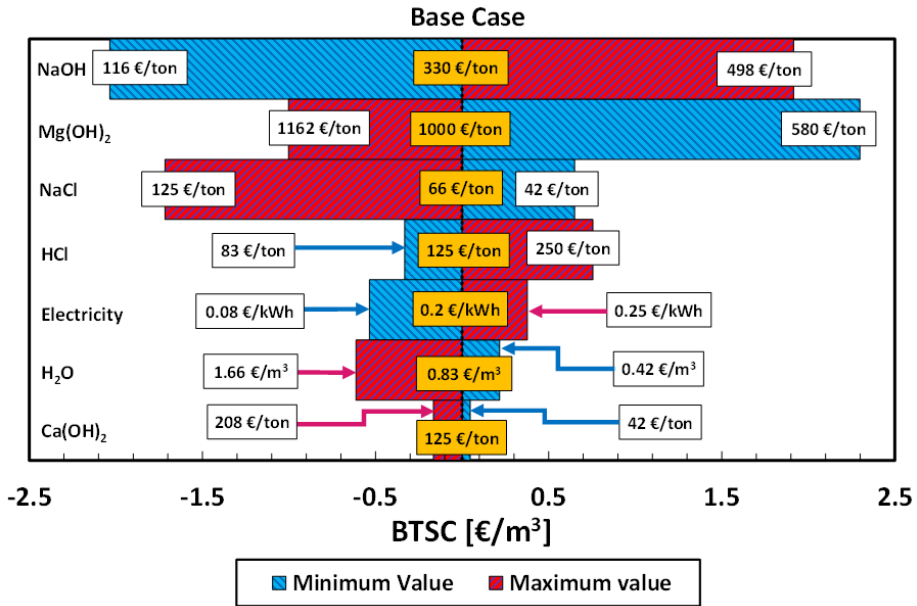


Figure 11: Trend of the BTSC at minimum and maximum commercial values of different chemical compounds and electricity. The specific costs in the white boxes are the minimum and maximum values of the ranges whereas those in the yellow boxes are referred to the base case.

Figure 12 clearly demonstrates the substantial impact of NaOH on the overall opEX of the treatment chain, surpassing the influence of other chemicals. Specifically, the graph illustrates that the most significant fluctuations in operating costs occur when the cost of NaOH varies within a reasonable range from its minimum to maximum value. In contrast, variations in the cost of H_2O result in minimal changes to the operating costs compared to the base case value. This underscores the critical role that NaOH costs play in shaping the economic viability of the proposed treatment chain.

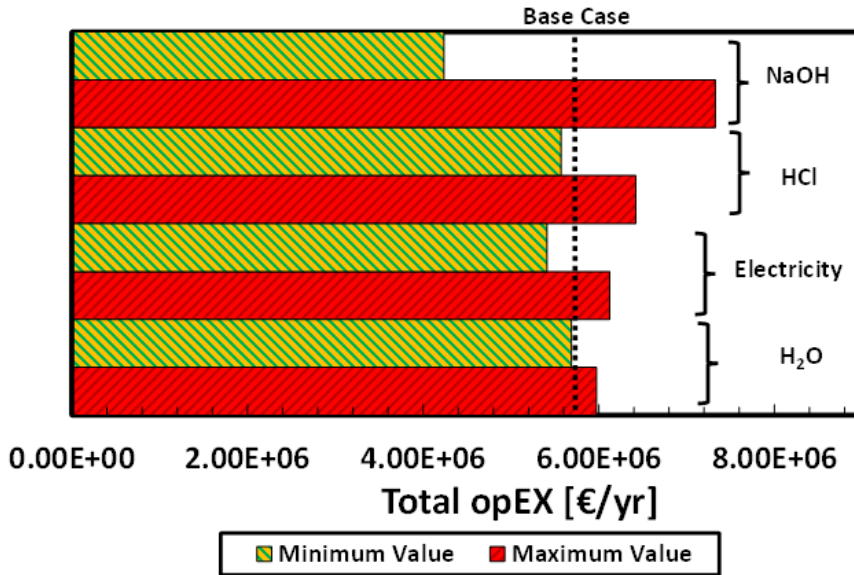


Figure 12: Trend of the opEXs of the entire treatment chain at minimum and maximum commercial values of different chemical compounds and electricity.

The sensitivity analysis presented in Figure 11 and Figure 12 underscores the significant influence of the Magnesium Reactive Crystallizer (MRC) on the overall economics of the proposed MLD system. Specifically, the cost of the alkaline reactant (NaOH) and the selling price of Magnesium Hydroxide ($\text{Mg}(\text{OH})_2$) were identified as key factors for the economic feasibility of the MLD process. Across a broad range of NaOH costs and $\text{Mg}(\text{OH})_2$ selling prices, the treatment chain demonstrated economic viability. The system is economically attractive unless extreme conditions, such as very high NaOH costs and very low $\text{Mg}(\text{OH})_2$ selling prices were encountered.

Additionally, to assess the robustness of the proposed MLD system under different scenarios, two extreme cases were examined (see Figure 13): a best-case scenario where all costs were set to their lowest values and product selling prices to their highest values, and a worst-case scenario where the opposite was applied. The best-

case scenario resulted in extremely low Levelized Cost of Magnesium Hydroxide ($LCOM_{g(OH)_2}$) and negative values for all other levelized costs and the Brine Treatment Specific Cost (BTSC), indicating a highly competitive technology for magnesium hydroxide production. On the contrary, the worst-case scenario led to very high levelized costs, making the proposed treatment economically infeasible.

In summary, the proposed MLD system offers an attractive alternative for seawater brine management, particularly when considering a range of realistic conditions. It demonstrates economic competitiveness and provides a net saving, surpassing conventional disposal methods and recent schemes proposed in literature. The sensitivity analysis highlights the importance of NaOH costs and $Mg(OH)_2$ selling prices in influencing the economic feasibility of the treatment chain.

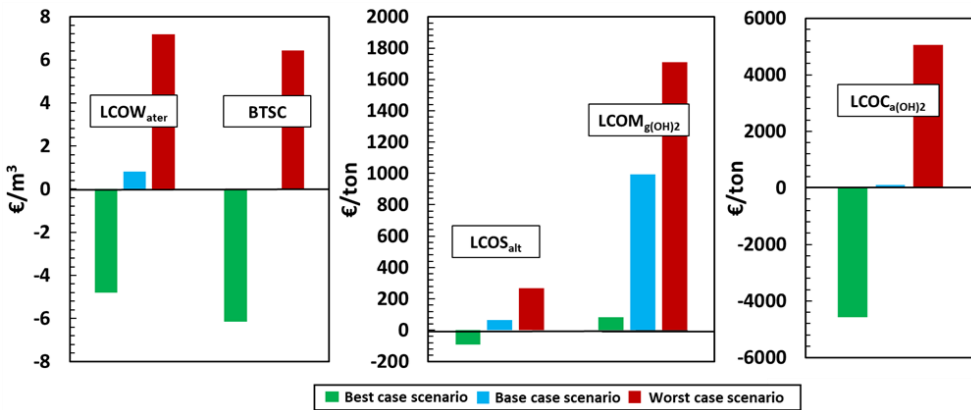


Figure 13: Comparison between the best case, base case and worst-case scenario for a) Levelized cost of water and BTSC, b) Levelized cost of salt and magnesium hydroxide and c) Levelized cost of calcium hydroxide.

1.6 Conclusions

In this first chapter a novel MLD process brine disposal and mineral recovery in the context of seawater reverse osmosis (SWRO) brines was presented. The proposed system combined several technologies, including NF, an MRC, MED, and NTC,

targeting the recovery of magnesium hydroxide, calcium hydroxide, water, and sodium chloride.

The technical analysis highlighted the feasibility of achieving food-grade sodium chloride in the final crystallizer by selecting appropriate NF rejection values, which fall within the range of those exhibited by current commercial NF membranes.

In the economic analysis of the base case scenario, it was observed that operational expenditures (opEXs) dominated the cost structure, surpassing capital expenditures (capEXs) by about five times. The high opEXs are attributed to the use of expensive chemicals in the magnesium crystallizer. However, the overall revenue generated by the treatment chain, particularly from the sale of magnesium hydroxide, outweighed the sum of capEXs and opEXs. The economic sustainability of the MLD system was further demonstrated through the Levelized Cost Index, where the computed values for all products were lower or equal to their current market prices.

An investigation into the influence of the number of MED effects on the global economics identified a minimum value of the Brine Treatment Specific Cost (BTSC) at 8 MED effects. The analysis indicated that significant variations in the costs of sodium hydroxide (NaOH) and prices of magnesium hydroxide ($\text{Mg}(\text{OH})_2$) could potentially compromise the economic feasibility of the proposed MLD system, with the MRC technology identified as the bottleneck of the treatment chain.

In a comparison with conventional brine disposal methods and recently proposed treatment chains, the proposed MLD scheme exhibited lower BTSC under current market conditions, establishing its economic viability as a competitive alternative for brine management. The study provides valuable insights into the integration of various technologies for efficient brine disposal, mineral recovery, and water production.

2 “Pioneering Minimum Liquid Discharge desalination: a pilot study in Lampedusa island”

Within the context of the EU-funded project “Water Mining”, focused on developing large demo systems that are of pre-industrial scale seawater/wastewater valorisation, a novel demonstration plant was developed and experimentally tested on the minor Sicilian island of Lampedusa (Italy). The MLD chain represented a significant advancement of the first proposed MLD chain reported in Chapter 1. The primary objective of the novel demonstration plant was to showcase a competitive and circular desalination process. This included:

- (i) Maximizing water production.*
- (ii) Producing multiple high-quality, valuable salts.*
- (iii) Achieving low-energy consumption through the utilization of waste heat.*
- (iv) Implementing in-situ chemicals production and internal re-use.*
- (v) Reducing the volume of desalination brine discharged into water bodies.*

Such aspects could reduce the overall environmental impact of desalination related to brine discharge and enable a more circular production of resources compared to traditional land-mining within the EU.

2.1 The Sea-Mining case study in Lampedusa island (Italy)

The MLD demo plant (based on an evolved concept of the MLD chain proposed in Chapter 1) was installed in Lampedusa, Italy, in close proximity to the desalination plant and power station of the island. It incorporated five distinct technologies: (i) Nanofiltration (NF), (ii) Magnesium and Calcium Multiple Feed – Plug Flow Reactor (MF-PFR), (iii) ElectroDialysis with Bipolar Membranes (EDBM), (iv) Multi-Effect Distillation (MED), and (v) Evaporation Ponds (EPs). More specifically, this plant presented an extra technology (EDBM) compared to the MLD chain of Chapter 1 in order to provide in-situ chemical production. Furthermore, the NTC of the first proposed chain was substituted by evaporation ponds due to financial matters of the EU-funded WATER MINING project. The schematic representation of the integrated process is depicted in Figure 14.

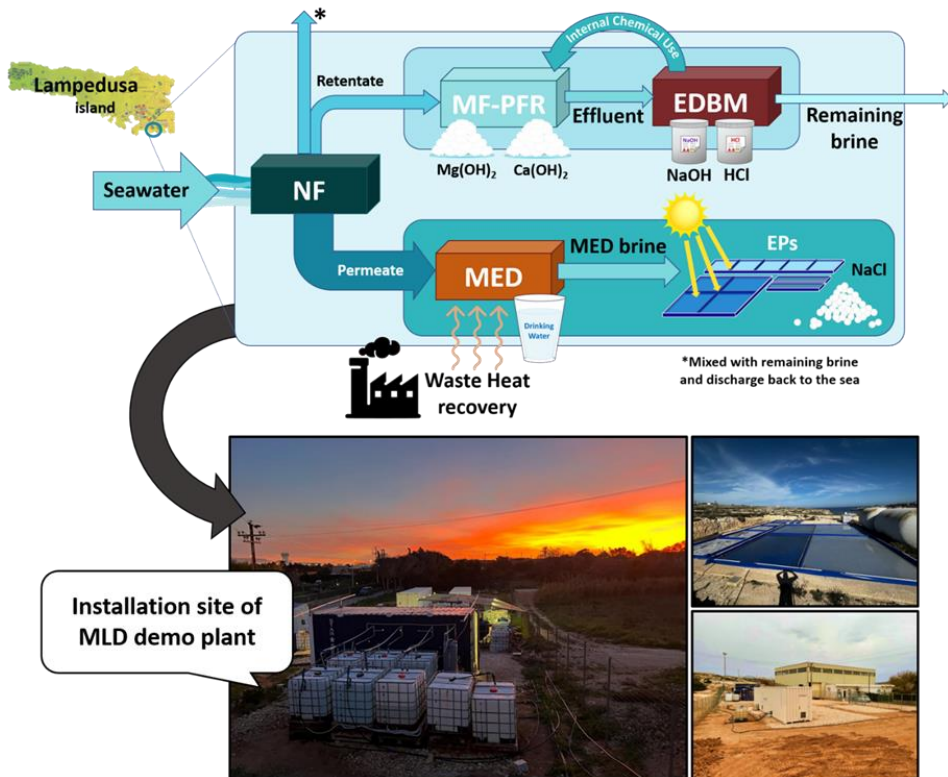


Figure 14: Conceptual scheme of the seawater valorisation chain in Lampedusa, Italy.

As illustrated in Figure 14, seawater was introduced into a double-pass NF plant, generating two concentrated streams: (i) an NF retentate, enriched with divalent ions like magnesium, calcium, and sulphates, and (ii) an NF permeate, enriched with monovalent ions such as sodium and chlorides. The NF retentate was subsequently valorised by the MF-PFR, where, through two sequential steps at a controlled reaction pH, magnesium and calcium were selectively recovered as hydroxides by adding a sodium hydroxide (NaOH) solution. The clarified effluent from the MF-PFR, devoid of magnesium and calcium, was then conveyed to an EDBM plant, producing two chemicals: (i) NaOH solution, usable as the alkaline reactant for the MF-PFR, and (ii) HCl solution, suitable for cleaning purposes throughout the integrated process and in the nearby desalination facility on the island. The

valorisation chain of the NF permeate incorporated more conventional technologies compared to those of the retentate stream. Initially, an MED plant harnessed the waste heat from the Lampedusa Power plant to produce high-quality water. The resulting brine was subsequently directed to a series of evaporation ponds to recover NaCl (table salt grade).

It is important to note that the capacities of the downstream units (such as MF-PFR, EDBM, and EPs) subsequent to the NF and MED pilots did not align with the full capacity required to treat the effluent streams from NF and MED. This discrepancy was attributed to practical and financial limitations during the construction of the pilot plants within the Water Mining project. Nonetheless, despite these constraints, the sizes of all downstream units could be fully representative in terms of (i) product characterization, (ii) recovery efficiency, and (iii) stability assessment, particularly within the context of pre-industrial applications. Section 2.3.6, however, provides an assessment of integration and circularity within a fully integrated system.

2.2 Pilot facilities and operational procedure

The individual technologies integrated into the MLD demonstration plant were deliberately chosen to extract valuable resources from the primary elements found in seawater. To comprehensively assess both (i) the production efficiency of the overall integrated plant and (ii) the functionality of each technology, detailed technical information on each pilot unit is presented in the subsequent sections. Performance parameters for each technology are also outlined, serving as benchmarks for evaluating the quality of the recovered products under specific operating conditions for each technology. These conditions are elucidated alongside the analytical procedure used to determine the performance parameters, offering an initial insight into the economic feasibility of the demonstration plant. Lastly, four specific indicators are introduced to assess the circularity of the seawater valorisation chain, particularly in the context of full integration among the units.

2.2.1 Nanofiltration (NF)

NF was the first technology of the MLD process. In the outlined scheme, seawater was sourced from a beach well, underwent filtration using a multi-media filter (MMF) to eliminate residual suspended solids, and then directed to a Double Pass Nanofiltration (DPNF) system comprising two passes: NF1 and NF2. It is to be noted that the DPNF plant was constructed by Lenntech BV. Figures 15a) and 15b) provide an image of the pilot plant and a simplified process flow diagram, respectively.

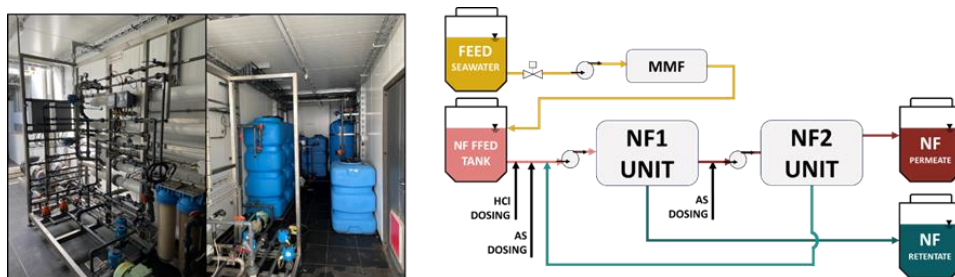


Figure 15: a) Image of the NF pilot plant; b) Process flow diagram of the NF unit adopted.

As depicted in Figure 15b), the filtered seawater underwent two key treatments: (i) acid (HCl) dosing for pH reduction and (ii) anti-scalant (AS) dosing (Kurita Vitec 7000) to mitigate inorganic scaling on the membrane surface. The anti-scalant was dosed at 1.5 mg/L and 1 mg/L before NF1 and NF2, respectively. High-pressure pumps were employed to generate the necessary pressure (up to a maximum of 40 bar) for permeating water through the NF1 and NF2 membranes. The two passes of the DPNF system comprised 12 and 10 Synder NFX membranes (4040), with a combined membrane area of 97 and 81 m², respectively.

Following dosing, seawater underwent separation into NF1 permeate and NF1 concentrate. The NF1 permeate was subsequently divided into NF2 permeate and NF2 concentrate. While the NF2 permeate served as the final permeate stream directed to the downstream MED unit, the NF2 concentrate was recirculated to NF1

and mixed with seawater to form the NF1 feed. The NF1 retentate was directed to the MF-PFR pilot for valorisation.

In summary, the DPNF system processed a feed flow rate of 2.46 m³/h with a total permeate recovery of 69%. Consequently, the NF2 permeate had a flow rate of 1.70 m³/h, and the NF1 concentrate had a flow rate of 0.76 m³/h. To facilitate automatic and continuous operation, as well as data logging, the DPNF system was equipped with pressure transmitters, flow transmitters, electrical conductivity (EC) sensors, temperature sensors, pH sensors, and electrical valves.

To assess the performance and stability of the DPNF plant, the following performance parameters were calculated and recorded throughout the operation:

- Permeate recovery $R_{p,(s.p \text{ or } DPNF)}$ of single pass (or DPNF plant), which represents the quantity of permeate from the single pass (or NF2) in relation to the feed solution of the single pass (or global feed solution), calculated according to Equation 5:

$$R_{p,(s.p \text{ or } DPNF)} = \frac{Q_{p,(s.p \text{ or } NF2)}}{Q_{f,(s.p \text{ or } DPNF)}} * 100 \quad (5)$$

Where $R_{p,(s.p \text{ or } DPNF)}$ is the permeate recovery of the single pass (or DPNF plant) [%], $Q_{p,(s.p \text{ or } NF2)}$ is the permeate flow rate of the single pass (or NF2) [m³/h] and $Q_{f,(s.p \text{ or } DPNF)}$ is the feed flow rate of the single pass (or the DPNF plant) [m³/h].

- Ionic rejection $r_{i,(s.p \text{ or } DPNF)}$ of the single pass (or DPNF plant) calculated as the difference in ion concentration between the feed of the single pass (or DPNF plant) and the permeate of the single pass (or NF2) divided by the concentration of the ion in the feed solution of the single pass (or DPNF plant) (see Equation 6).

$$r_{i,(s.p \text{ or } DPNF)} = \frac{C_{i,f,(s.p \text{ or } DPNF)} - C_{i,p,(s.p \text{ or } DPNF)}}{C_{i,f,(s.p \text{ or } DPNF)}} * 100 \quad (6)$$

Where $r_{i,(s.p \text{ or } DPNF)}$ is the ionic rejection [%] of ion i concerning the single pass (or DPNF plant), $C_{i,f,(s.p \text{ or } DPNF)}$ is the feed ion concentration of the single pass (or DPNF plant) [mg/L] and $C_{i,p,(s.p \text{ or } DPNF)}$ is the permeate ion concentration of the single pass (or NF2) [mg/L].

- Membrane permeability K , computed as the permeate flow rate divided by transmembrane area and transmembrane pressure (Equation 7):

$$K = \frac{Q_{p,NFn}/A_{m,NFn}}{TMP} \quad (7)$$

Where K is the membrane permeability [L/m²/h/bar], $Q_{p,NFn}$ is the permeate flow rate of NF1 or NF2 [m³/h], $A_{m,NFn}$ is the membrane area of NF1 or NF2 [m²] and TMP is the trans-membrane pressure of NF1 or NF2 [bar].

2.2.2 Multiple Feed – Plug Flow Reactor (MF-PFR)

The initial phase of the NF retentate valorisation line involved the Multiple Feed – Plug Flow Reactor (MF-PFR): a specialized reactive crystallization process designed to reclaim Magnesium and Calcium in the form of hydroxides. This was achieved through the controlled addition of an alkaline reactant (NaOH solution) at a specific reaction pH. The pilot plant comprised (i) a patented reactive crystallizer [61,85], coupled with (ii) a drum filter for the retrieval of solids, and (iii) a neutralization step to balance the final clarified solution, making it suitable for supplying the EDBM unit. For a visual representation of the pilot plant and an outline of the Mg and Ca recovery process, refer to Figures 16a) and 16b), respectively. It is to be noted that the MF-PFR was developed by the University of Palermo (more precisely, Carmelo Morgante and Fabrizio Vassallo).

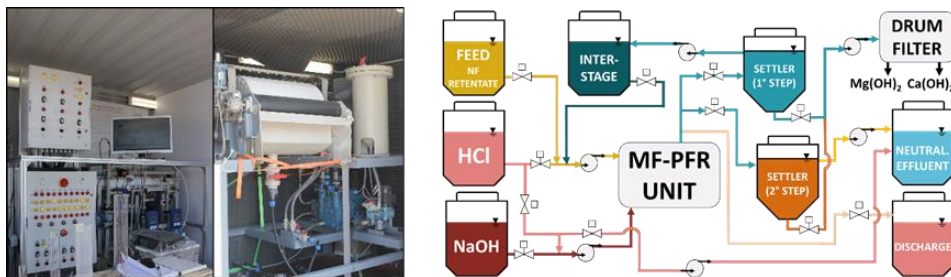


Figure 16: a) Image of the MF-PFR (left) and Drum filter (right) pilot plants; b) Process flow diagram of the Mg/Ca precipitation process implemented within the MF-PFR pilot plant.

At the heart of the pilot was the reactor, where the feed solution (DPNF retentate) was intricately mixed with a NaOH solution through multiple nozzles positioned along the entire length of a cylindrical vessel containing the alkaline reactant. The strategic placement and orientation of the nozzles facilitated rapid mixing of both reactants. Notably, $Mg(OH)_2$ precipitation occurs at pH 10.6, while $Ca(OH)_2$ precipitates at pH 13. Therefore, continuous monitoring of the feed solutions' conductivity, reaction pH, and reactant solution flow rates was essential, facilitated by sensors (KROHNE). To ensure operation at a specific pH value, thereby promoting the precipitation of either Mg or Ca, the feed flow rates were regulated through a PLC implemented in the LabVIEW® environment.

After the initial precipitation of $Mg(OH)_2$ (1° precipitation step), the resulting slurry was directed to a settling tank. The clarified solution obtained was pumped to an inter-stage tank for further treatment by the MF-PFR to recover $Ca(OH)_2$ (2° precipitation step), while the concentrated slurry was subjected to the filtration step. Following the second precipitation step, where $Ca(OH)_2$ precipitated at a reaction pH of 13, the resulting slurry was directed to a separate settling tank. The concentrated slurry was then pumped to the drum filter, while the final clarified solution underwent a neutralization step through HCl dosing. The pH of the neutralized brine was monitored using an in-line pH meter (KROHNE, PH8320). A semi-industrial scale drum filter was employed for recovering magnesium hydroxide and calcium hydroxide from their respective concentrated slurries, with

technical details of the filtration section provided in a previous study by Vassallo et al. [61].

To evaluate the production efficiency and the quality of products achieved by the MF-PFR unit, two performance indicators were considered:

- Recovery, which indicates the total amount of magnesium (or calcium) recovered in relation to the total amount of magnesium (or calcium) present in the feed solution (calculated according to Equation 8).

$$R_j = \frac{n_j^\circ - n_j}{n_j} * 100 \quad (8)$$

Where n is the molar flow-rate [mol/min], the apex $^\circ$ refers to the inlet molar flow rate, while the subscript j refers to a specific cation (i.e. magnesium).

- Purity of solid, calculated as the amount of magnesium (or calcium), relative to the total amount of cations measured via Ionic Chromatography (IC) or titration (see Equation 9).

$$Purity_{Mg^{2+}(or\ Ca^{2+})} = \frac{C_{Mg^{2+}(or\ Ca^{2+})}}{\sum_{i=1}^n C_i} * 100 \quad (9)$$

Where C_i is the molar concentration [mol/L] of the i^{th} ion.

2.2.3 ElectroDialysis with Bipolar Membranes (EDBM)

The neutralized effluent exiting the MF-PFR was directed to the ElectroDialysis with Bipolar Membranes (EDBM) unit. EDBM is an electro-membrane process that facilitates the production of chemical reagents, such as acid and base, from a saline solution using electrical energy [86,87]. This technology employs three types of ion exchange membranes (IEXs): cationic (CEM), anionic (AEM), and bipolar membrane (BPM). The BPM consists of a cationic and an anionic membrane welded together. The sequence of a CEM, AEM and BPM form a repeating unit known as a triplet. When an electric field is applied through the cell pack, cations migrate

towards the cathode (negative electrode), while anions migrate towards the anode (positive cathode). Once migrated, the cations encounter hydroxyl ions from the BPMs, producing a base solution. On the other hand, anions, interacting with protons from BPMs, generate an acidic solution.

It is worth mentioning that the EDBM pilot plant was developed by the University of Palermo (more specifically, Calogero Cassaro and Giovanni Virruso).

In the pilot plant, a large-scale EDBM stack was utilized to specifically produce sodium hydroxide (NaOH) and hydrochloric acid (HCl). The pilot plant comprised two main parts: the EDBM stack and the pumping station with measuring/control instruments, as depicted in Figure 17a).

The EDBM stack (FuMA-Tech GmbH, model: FT-ED1600-3) consisted of 40 triplets divided into two sections of 20 triplets each, resulting in a total membrane area of 19.2 m². The unit utilized the following ionic exchange membranes (IEXs): FUMASEP® FAB-PK anion exchange membranes (PET reinforced with PK, 130 µm thick), FUMASEP® FKB cation exchange membranes (PK reinforced with PK, 130 µm thick), and FUMASEP® FBM bipolar membranes (composite membrane reinforced with woven PEEK, approximately 160 µm thick). The anode and cathode were made of DSA and stainless steel, respectively. Concerning the hydraulic circuit, four lines were designed, one for each electrolytic solution (refer to Figure 17b)). The monitoring of main variables in the process involved the use of magnetic flowmeters, conductivity meters, pH meters, and pressure transducers. For process control and data acquisition, National Instrument® hardware and LabVIEW software were employed. Additional technical details on the design and construction of the EDBM pilot plant can be found in [88].

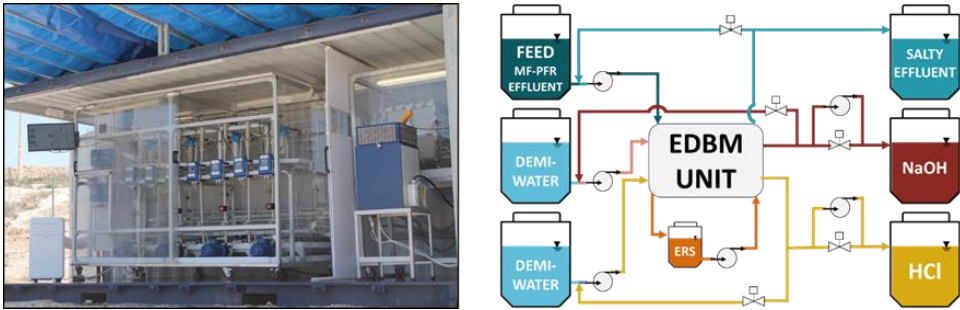


Figure 17: a) Image of the EDBM pilot plant (pumping station and measuring/control instruments on the left, DC drive and EDBM stack on the right); b) Process flow diagram of the Feed&Bleed configuration adopted.

The EDBM unit operated in a continuous mode, employing a Feed&Bleed configuration (depicted in Figure 17b)). This configuration allowed for the attainment of various product targets by adjusting the outlet flow rate of acid and base streams, thereby meeting diverse concentration requirements.

To assess the performance of the EDBM unit, two primary indicators were utilized:

- Current efficiency (CE, %), which accounts for the quantity of electric charges introduced into the system that are successfully converted into the production of protons or hydroxide ions (computed according to Equation 10):

$$CE = \frac{Q_{p,out}(C_{p,out}-C_{p,in})F}{60 N_{tr} i A_m} * 100 \quad (10)$$

Where $Q_{p,out}$ is the outlet flowrate of product [L/min], $C_{p,out}$ and $C_{p,in}$ are the outlet and the inlet product concentration [mol/L], respectively, F is Faraday's constant (i.e., 96,485 C/mol), N_{tr} is the triplet number, A_m is the membrane active area [m²] and i [A/m²] is the electric current density provided to the stack.

- Specific Energy Consumption (SEC) [kWh/kg], which represents the energy consumed to produce 1 kg of the desired product (calculated according to Equation 11):

$$SEC = \frac{U i A_m}{60 Q_{p,out}(C_{p,out}-C_{p,in}) M_p} \quad (11)$$

Where U is the electric potential (V) applied to the stack, and M_p is the molecular weight of the desired product [g/mol].

2.2.4 Multi-Effect Distillation (MED)

Concerning the valorisation chain of NF permeate, the initial stage involved the utilization of a Multi-Effect Distillation (MED) unit. The MED process is based on thermal principles, harnessing heat to generate high-quality water through the evaporation of saline solutions, such as seawater [67,89]. This process exploits evaporative chambers known as effects, each featuring a heat transfer surface facilitating the exchange of heat between the untreated water and condensing steam. The primary steam originates from a heat source with a temperature typically below 100°C under saturation conditions. During condensation, it releases latent heat, driving the evaporation of the untreated water. The condensation-evaporation cycle is sustained effect-by-effect, owing to varying saturation conditions of the two streams ensured by a vacuum system (comprising vacuum pumps or steam ejectors) and a diminishing pressure profile across the effects.

From the original raw water, two streams emerge: (i) vapor (secondary steam) and (ii) concentrated water (brine). The generated steam serves as the heat source for the subsequent evaporation effect, eventually condensing by exchanging heat with untreated water at a lower temperature and pressure. Meanwhile, the brine flows to the next effect, combining with the newly produced brine. This cycle repeats across all the effects of the evaporator, optimizing thermal energy recovery for the unit.

The steam produced in the final effect undergoes condensation in a concluding condenser, where all distillate streams are amalgamated into a single flow. Likewise, the numerous concentrated brine streams generated in each effect are consolidated into a single stream for discharge.

In the process configuration, the MED pilot unit was fed by the NF permeate, yielding (i) high-quality water and (ii) highly concentrated brine directed to solar evaporating ponds for NaCl recovery. Figures 18a) and 18b) provide a visual representation of the installed MED plant and the process flow diagram of the pilot unit. The pilot was developed and provided by Sofinter S.p.A and Thermossol Steam Boilers S.A.

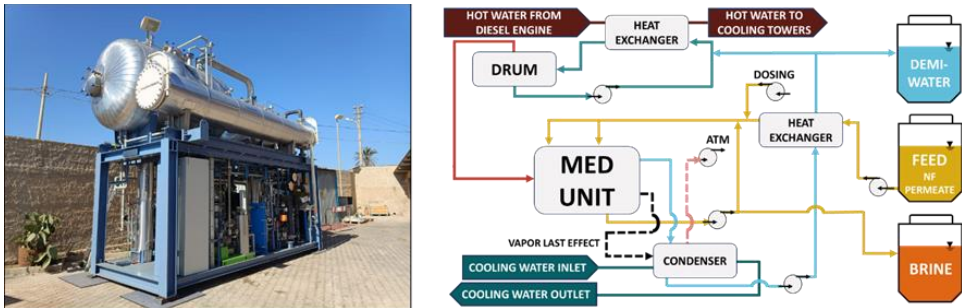


Figure 18: a) Picture of the MED pilot plant; b) Process flow diagram of the MED unit.

More precisely, the installed MED pilot in Lampedusa comprised the following components:

- (i) A heat input section (steam generation section) arranged as a closed-loop circuit of demineralized water to generate "primary steam." Through a heat exchanger, "waste" heat from the power plant cooling circuit was recovered and transferred to a secondary stream of demineralized water. This stream was directed into a drum where vapor was produced through flash evaporation;
- (ii) A heat recovery section (MED evaporator), where, heat exchange, the heat input was given in each effect, resulting in the production of distilled water;
- (iii) A heat reject section (final condenser), where the thermal energy was ultimately released at a lower temperature (condenser) into cooling water circuit, thus completing the heat balance;

- (iv) Auxiliary systems, including a vacuum generation unit and a chemicals dosing unit.

To evaluate the system performance, the following operating parameters were considered:

- Concentration Factor (CF): represents the molar concentration of sodium chloride (equivalent) in the outlet brine divided by the concentration in the inlet brine.

$$CF = \frac{C_{NaCl,out,brine}}{C_{NaCl,in,brine}} \quad (12)$$

Where $C_{NaCl,out,brine}$ is the brine outlet molar concentration of NaCl [mol/L] and $C_{NaCl,in,brine}$ is the brine inlet molar concentration of NaCl [mol/L].

- "Specific Electric Energy Consumption" (SEEC): indicates the electrical energy consumption per cubic meter of produced distilled water, calculate as the ratio between electrical energy and the total amount of distilled water:

$$SEEC = \frac{Power_{el}}{\dot{m}_{dist}} \quad (13)$$

- Gain Output Ratio (GOR): expresses the conversion of primary vapour into distillate water. It is calculated as the ratio between the mass flowrate of produced distillate \dot{m}_{dist} [kg/h] and mass flowrate of the produced primary vapour \dot{m}_{steam} [kg/h]:

$$GOR_{gross} = \frac{\dot{m}_{dist}}{\dot{m}_{steam}} \quad (14)$$

2.2.5 Evaporative ponds (EPs)

The final technology of the treatment chain was composed of Evaporative Ponds (EPs). They were constructed with the purpose of recovering pure Sodium Chloride (NaCl), mirroring the traditional approach of natural saltworks. This involves producing table salt through fractional precipitation in multiple shallow basins. Figures 19a) and 19b) illustrate the ponds, providing an image and a schematic diagram, respectively. The ponds were provided by the University of Palermo. They were built using wood planks for the border and a cloth in PVC covering a layer of sand placed on the concrete platform. A depth of 10 cm was adopted as computed during the design phase.

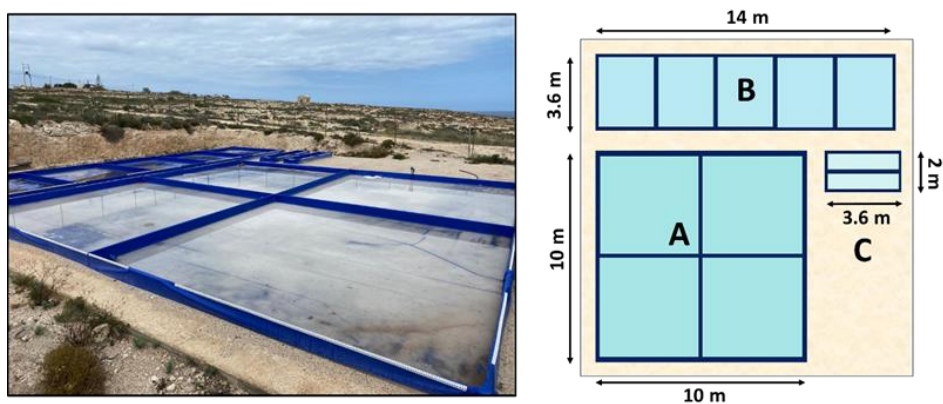


Figure 19: a) Image of Evaporation Ponds; b) Footprint of the evaporation ponds employed.

To elaborate, Pond A, subdivided into four smaller ponds, served as the "hot" pond where the outlet solution from the MED unit was collected. Within this pond, the NaCl concentration increased until reaching the saturation point. Pond B, segmented into six smaller ponds, functioned as the "crystallizing" pond where NaCl solid crystals precipitated. Finally, Pond C, divided into two smaller sections, allowed for the collection of the depleted solution, i.e., the final exhausted bittern.

The design of the ponds and the determination of inlet/outlet brine flow rates involved using the Penman equation to estimate the evaporation rate [90], and the PHREEQC software, employing the Pitzer thermodynamic package, was utilized to simulate salt precipitation [91]. In detail, the evaporation rate E (mm/day) was estimated on the basis of a value of the net solar radiation calculated by a correlation developed by ENEA, the Italian “National Agency for New Technologies, Energy and Sustainable Economic Development” [92]. A value of 25 MJ/m²/day was assumed for May, considering the geographical coordinates of Lampedusa. The other parameters were assumed as the following: wind speed 5m/s, humidity 77% and temperature 19.7°C.

The results of the design are shown in Table 9, where the composition and flow rates from/to each pond are listed. Of course, values for the outlet of pond A are the inlet for pond B and the same applies for the outlet of pond B and the inlet for pond C.

Table 9: Inlet mean ions composition in the ponds.

| | Inlet Composition [g/L] | | | | | | | Flow rate,IN (L/h) |
|---------------|-------------------------|----------------|------------------|------------------|-----------------|-----|------|-----------------------|
| | Na ⁺ | K ⁺ | Ca ²⁺ | Mg ²⁺ | Cl ⁻ | TDS | NaCl | |
| Pond A | 69.5 | 2.102 | 0.13 | 0.13 | 125 | 197 | 177 | 180 |
| Pond B | 123 | 3.55 | 0.24 | 0.24 | 194 | 321 | 311 | 147 |
| Pond C | 101 | 45.9 | 3.07 | 3.07 | 211 | 367 | 253 | 117 |

The purity of NaCl was calculated as the amount of sodium (as sodium chloride) with respect to the total amount of salts in the samples. All the species present in the samples were detected via Ionic Chromatography (IC) analysis. The purity of NaCl was assessed using the following equation:

$$Purity_{NaCl} = \frac{M_{NaCl_{real}}}{M_{salt}} * 100 \quad (15)$$

where $M_{NaCl_{real}}$ is the measured mass of NaCl in the solid sample and M_{salt} is the total salt mass.

2.2.6 Operating conditions and analytical procedure

The technologies involved in the proposed MLD process scheme operated in accordance with the specified operating conditions detailed in Table 10 (main flow rates) and Table 11 (inlet composition), encompassing specific parameters for each technology. Table 10 indicates that the recovery rates for NF1 and NF2 were set at 71% and 92%, respectively, to achieve a permeate flow rate of 1.70 m³/h and a retentate flow rate of 0.76 m³/h. The NF plant maintained an operational duration of 8 hours per day, with daily sampling of the feed, NF1 retentate, and NF2 permeate. In contrast, the MF-PFR, operating at a smaller scale than NF, displayed distinct flow rates (Table 10). For the 1st and 2nd precipitation steps, a 1 mol/L NaOH solution from the EDBM unit required NaOH flow rates of 0.85 L/min and 1 L/min, respectively, to attain pH values of 10.6 for Mg(OH)₂ precipitation and 13 for Ca(OH)₂ precipitation. The MF-PFR also operated for 8 hours per day in the 1st step (5 hours per day in the 2nd step), with collected samples of Mg(OH)₂ and Ca(OH)₂ slurry. The EDBM, similar in scale to the MF-PFR, utilized a current density of 400 A/m² and a 55 V applied voltage, along with a 0.25 mol/L Na₂SO₄ solution for the ERS electrodes. The EDBM stack acid and base compartments were fed with permeate from a SWRO (conductivity of 400 μS/cm), producing industrial water. During 5 hours of daily operation, samples of acid and base solutions were collected. The MED pilot plant operated similarly to other units, relying on various parameters, including utility availability and temperature (primarily hot water from a diesel engine cooling circuit). The condenser pressure, determining the distillation effects' operating pressure, was typically set at 70 mbar. The estimated hot water flow rate was 25 m³/h, averaging 80°C with fluctuations of ±5°C, while cooling water for the cold utility was at an average temperature of 25 °C. Distillate and brine samples were taken during the 4 operating hours per day for subsequent analysis.

The brine recirculation flow rate was fixed at 6.5 m³/h to ensure effective tube bundle wettability at low feed flow rates and maintain adequate residence time within the MED, facilitating brine concentration. As for the Evaporation ponds, the feed flow

rate was nominally set at 180 L/h, though pond capacity varied with weather conditions, resulting in practical semi-batch operations. The crystallized product was collected for purity analyses.

Regarding aqueous sample analysis:

- Na^+ , K^+ , Ca^{2+} , Mg^{2+} , and SO_4^{2-} concentrations were measured using Inductively Coupled Plasma-Optical Emission Spectrometry (ICP-OES) or Ion Chromatography analysis (Metrohm 882 Compact Ion Chromatography).
- Cl^- concentration was determined through discrete Skalar analyses.
- HCO_3^- concentration was measured via titration.

For determining the purity of recovered solids, a meticulous procedure was followed. The wet solid underwent filtration and washing with demineralized water (for $\text{Mg}(\text{OH})_2$ and $\text{Ca}(\text{OH})_2$) or a saturated NaCl solution (for NaCl). A weighed quantity was dried at 120 °C for 24 hours, and after cooling to room temperature, weight detection was repeated to estimate initial humidity content. To analyse anion and cation concentrations in the solid, the dried sample was dissolved in deionized water and analysed via Ionic Chromatography (IC) using a Metrohm 882 Compact IC equipped with anion-exchange Metrosep® A Supp 5 and cation-exchange Metrosep® C4 columns. The mobile phase for anions detection was a solution of Na_2CO_3 3.2 mM and NaHCO_3 1 mM at a flux of 0.7 mL/min, while the cations used a 5.5 mmol/L H_3PO_4 solution.

Table 10: Main flow rates and specific operating parameters of each technology comprising the proposed MLD process.

| Technology | Stream | Flow rate | Additional specific parameters |
|------------|-------------|---------------------------|-------------------------------------------------------------------------------------------------------------------------------------------------------------------------------------------------------------------------------------|
| NF | Feed | 2.46 m ³ /h | NF1 recovery = 71% NF2 recovery = 92% |
| | Permeate | 1.7 m ³ /h | |
| | Retentate | 0.76 m ³ /h | |
| MF-PFR | 1° Brine | 2.5 L/min | 1° step pH = 10.6 |
| | 1° Alkaline | 0.85 L/min | 2° step pH = 13 |
| | 2° Brine | 1.5 L/min | C _{NaOH} (1° step) = 1 mol/L |
| | 2° Alkaline | 1 L/min | C _{NaOH} (2° step) = 1 mol/L Total capacity Mg(OH) ₂ = 14.4 ton/y |
| EDBM | Salt | 1.8 L/min | Current density = 400 A/m ² Voltage = 55 V C _{EERS} = 0.25 mol/L H ₂ O employed as feed for acid and base channels Total capacity NaOH = 21.23 ton/y Total capacity HCl = 15-16 ton/y |
| | Acid | 1.35 L/min | |
| | Base | 1.1 L/min | |
| | ERS | 20 L/min | |
| MED | Feed | 1.75 m ³ /h | Pressure condenser = 70 mbar Heat source T* = 80°C Cooling water T = 20°C |
| | Distillate | 1.5-1.6 m ³ /h | |
| | Rec. Brine | 6.5 m ³ /h | |
| | Cold water | 20 m ³ /h | |
| EPs | Brine | 0.2-0.3 m ³ /h | - |
| | Feed | 180 L/h | |

*The heat source supplied into the MED was cooling water coming from a diesel engine used as a power generator.

Table 11: Inlet composition of each technology comprising the proposed MLD process.

| Technology | Inlet Composition [mg/L] | | | | | | |
|------------|--------------------------|----------------|------------------|------------------|-----------------|-------------------------------|-------------------------------|
| | Na ⁺ | K ⁺ | Ca ²⁺ | Mg ²⁺ | Cl ⁻ | SO ₄ ²⁻ | HCO ₃ ⁻ |
| NF | 12,960 | 438 | 425 | 1,300 | 21,090 | 3,230 | 183 |
| MF-PFR | 15,590 | 669 | 1,400 | 4,650 | 30,565 | 10,460 | 315 |
| EDBM | 17,000 | 303 | - | - | 19,600 | 5,010 | 2,730 |
| MED | 11,100 | 423 | 15 | 12 | 17,143 | 5 | 79 |
| EPs | 69,510 | 2,102 | 219 | 94 | 110,126 | 0 | - |

2.2.7 Circularity assessment

After evaluating the technical feasibility and stability of the system, it became important to identify circular opportunities and linear risks to enhance the system durability and resilience. To achieve this goal, the following indicators were developed. In assessing the circularity of the system, the initial step involved quantifying the waste reduction attributable to circularity measures. In the study of this specific MLD process, the reduction in brine from the proposed circular system was measured in comparison to a linear reverse osmosis (RO) desalination plant. The Total Waste Reduction (TWP) [93] was calculated using the following equation:

$$TWP = \frac{\text{Volume of SWRO brine (non circular)}\left[\frac{m^3}{h}\right] - \text{Volume of brine from a circular system}\left[\frac{m^3}{h}\right]}{\text{Volume of SWRO brine (non circular)}\left[\frac{m^3}{h}\right]} * 100 \quad (16)$$

The volume of SWRO brine (non-circular) was estimated based on a 40% efficiency assumption for the RO plant, while the volume of brine from the circular system was considered to be the outlet salt stream from the EDBM unit.

Resource efficiency (RE) [94] highlighted the effectiveness of recovering valuable products from seawater within the framework of a circular economy. RE was defined as the ratio of useful material output to input, and it was determined using the following equation:

$$RE = \frac{\text{Mass of useful materials output}\left[\frac{kg}{h}\right]}{\text{Mass of useful materials input}\left[\frac{kg}{h}\right]} * 100 \quad (17)$$

Since the capacity of each unit varied, RE was assessed for each product based on the capacity of the required technology.

Regarding the circularity of resources, the chemicals and water needed were internally produced from seawater brine. Circular Chemical Inflow (CCI) [95] assessed the circularity of chemicals used in the process, specifically HCl and NaOH. CCI was determined using the equation:

$$CCI = 1 - \frac{\text{Volume of chemical inflow from non circular sources } [\frac{m^3}{h}]}{\text{Total volume of chemical inflow (circular and non circular)} [\frac{m^3}{h}]} * 100 \quad (18)$$

Here, the volume of chemical inflow from circular and non-circular sources referred to HCl and NaOH used in the MF-PFR unit.

Finally, the proposed system aimed at low-energy consumption through waste heat utilization. Waste heat was employed to meet the thermal energy requirements in the MED unit and to harness solar energy for recovering NaCl salt from the evaporation ponds. Thus, measuring the energy self-sufficiency of the system became crucial. The Energy Self-Sufficiency (ESS) [95] was computed using the following equation:

$$ESS = \frac{\text{Sustainable Energy in kWh produced and utilised on site}}{\text{Total energy demand of the system [kWh]}} * 100 \quad (19)$$

Here, thermal energy requirements were converted to electricity requirements, assuming a 30% efficiency of the diesel engine based on the fuel used.

2.3 Results and discussion

The overall technical viability of the proposed pilot-scale MLD chain was assessed through two key methods: (i) analysing samples collected from each recovered product and (ii) calculating specific performance indicators, as previously specified for each pilot plant within the chain. Additionally, to showcase the robustness of the proposed treatment chain in achieving products with consistent specific characteristics, the stability of the principal operating parameters for each technology was examined during their daily operational cycles. It is worth mentioning that each unit was operated for a different amount of hours, due to the different nominal capacity of each of the pilot units, which in fact required the installation of buffer tanks in order to interconnect the different units and fully operate the integrated chain. Finally, the results of the integration and circularity assessment were

documented. It is worth mentioning that the results were achieved by the author of the present PhD thesis with the aid of Fabrizio Vassallo, Calogero Cassaro and Giovanni Virruso (for the EDBM unit) and Giuseppe Scelfo (for the MED unit).

2.3.1 DPNF pre-treatment stage performances

It is widely acknowledged in the literature that the performance of the pre-treatment step, specifically the DPNF in this case, plays a pivotal role in the overall efficiency of any seawater/brine mining scheme [23]. This significance stems from its capability to generate water streams with characteristics suitable for further processing, particularly those selectively enriched in monovalent or divalent ions in this context. An ensuing advantage of this capability is the successful recovery of resources with high purity and yield through subsequent crystallization steps. Consequently, it was important to investigate the DPNF ability to selectively separate ions.

As illustrated in Figure 20, the results demonstrated that the DPNF process achieved a rejection rate of over 97% for multivalent ions. More specifically, rejection values of 97%, 99%, and 100% were attained for Ca^{2+} , Mg^{2+} , and SO_4^{2-} , respectively. In contrast to the high rejection of multivalent ions, the rejection of monovalent ions Na^+ , K^+ , and Cl^- was more limited, at 14%, 3%, and 19%, respectively. Based on these findings, the DPNF process proved to be effective in selectively separating both monovalent and multivalent ions originally present in seawater.

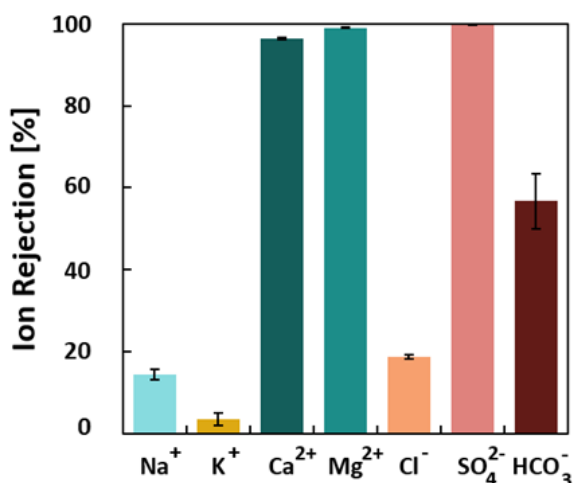


Figure 20: The ions rejections of the DPNF process (average values are presented, whereas the error bars show the deviation for the minimum and maximum values, considering two measurements).

2.3.2 Purity and recovery of products/chemicals

The brine valorisation lines, addressing the DPNF retentate and MED brine, yield various products ranging from $\text{Mg}(\text{OH})_2$ and a $\text{Ca}(\text{OH})_2$ and $\text{Mg}(\text{OH})_2$ mixture (in the second precipitation step) to chemicals generated in the EDBM, culminating in high-purity NaCl crystallized in evaporative ponds. Product purities varied with operating conditions, and Figure 21a) presents the average purities of all recovered solids based on measurements during the experimental assessment of each technology.

Figures 21b) and 21c) depict the recovery of each product and the concentration of the acid/alkaline streams produced, respectively. It is worth mentioning that such values changed with variable operating conditions during the experimental campaign, for each experiment a couple of samples were taken when the stationary condition was achieved. Thus, an average value is reported with error bars indicating the variability of each parameter.

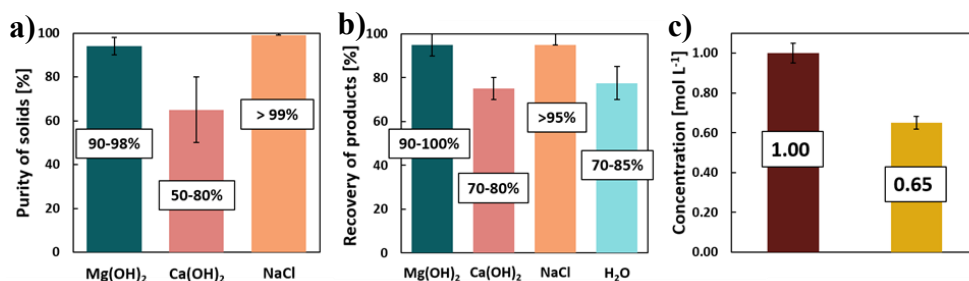


Figure 21: a) Purity of recovered solids; b) Recovery of solids and H₂O (MED distillate); c) Concentration of chemicals produced by the EDBM unit. The average value is reported, with error bars indicating the variability of each parameter along the pilot experimental campaign.

Product analysis results revealed that the MF-PFR produced Mg(OH)₂ with an average purity of approximately 94%. As detailed in previous works by Vassallo et al. [60,61], the purity of Mg(OH)₂ was influenced by carbonate/bicarbonate presence in the feed, leading to calcium co-precipitation as calcium carbonate — an insoluble species under MF-PFR operating conditions (pH around 10.6 and 20-25°C). Moreover, the recovery of this hydroxide during the 1st precipitation step exceeded 90%, with possibilities for further enhancement by increasing the outlet pH through increased alkaline flow rates.

In the 2nd precipitation step, designed to eliminate all bivalent cations (magnesium and calcium), IC analysis of the solid revealed an average Ca(OH)₂ purity exceeding 60%. The co-precipitation of magnesium as hydroxide, stemming from incomplete magnesium removal during the 1st precipitation step, affected purity. Calcium removal efficiency ranged between 70-80%, while magnesium was entirely precipitated due to the elevated pH (about 13).

Notably, NaCl produced via evaporation ponds exhibited excellent results with a purity surpassing 99%, well above the required minimum purity limit for food applications (97%) [80]. Recovery approached 100%, as seen in Figure 21b). In particular, four samples were withdrawn from four of the sub-ponds obtaining an average for the NaCl purity of 99.1% ±1.9.

The MED unit achieved substantial freshwater recovery, reaching values up to 85%, considering a single MED unit with concentration factors in the brine reaching up to 7.

Finally, Figure 21c) underscores the EDBM success in producing a 1M NaOH solution (utilized as the alkaline reactant for the MF-PFR) and a 0.65 M HCl solution, serving for neutralization and cleaning purposes.

2.3.3 Energy performances of pilot units

Table 12 presents the energy consumption of each pilot plant along with specific energy performance indicators for the EDBM unit. In Table 12, NF consumed 5.7 kW, accounting for the energy used by two high-pressure pumps, the booster pump, and the circulation pumps for MMF and outlet streams (NF permeate and retentate). For the MF-PFR, 1.94 kW was calculated, including the drum filter. Of this, 0.98 kW was consumed by the main electrically-driven parts of the reactor (pumps), assuming that auxiliaries (sensors and controllers) accounted for 20% of the total consumption of major items. The remaining 0.96 kW of the drum filter considered a utilization factor of 10% and auxiliaries power consumption equal to 20% of the total filter consumption.

Table 12: Energy performances of the pilot plants.

| Technology | kW | Specific Energetic indicators | |
|------------|------|-------------------------------|---------|
| NF | 5.7 | | |
| MF-PFR | 1.94 | | - |
| EDBM | 8.78 | CE_{HCl} [%] | 50-70 |
| | | CE_{NaOH} [%] | 65-85 |
| | | SEC_{HCl} [kWh/kg] | 3.0-4.0 |
| | | SEC_{NaOH} [kWh/kg] | 2.0-3.0 |
| MED | 9.08 | $SEEC$ [kWh/m ³] | 6.0-7.0 |

Concerning the electrical energy consumption of the MED plant, 9.08 kW were used, with only 4.34 kW necessary for plant operation, accounting for the energy

consumed by distillate and brine circulation pumps and the recycling pump of the brine stream. The remaining 4.74 kW relates to the vacuum generator, that was an oversized liquid ring vacuum pump (chosen to speed up the start-up of the plant). As a matter of fact, it is to be noted that the liquid ring vacuum pump could have been substituted, for example, by a steam driven vacuum system, where the required steam could be potentially produced by recovering waste heat from the stack of the power plant. The specific electrical energy consumption (SEEC) of the MED pilot plant ranged from 6-7 kWh/m³, consistent with other pilot plants with only 2 effects reported in the literature [96,97]. However, lower values, closer to 2-3 kWh/m³ (typical for water production by seawater desalination), are possible for optimized industrial-scale plants with properly sized pumps and configurations.

For the EDBM, an energy consumption of 8.78 kW was recorded, mainly attributed to the DC drive for generating the electric field in the EDBM stack, with a small portion used by circulation pumps (about 25% of the total). In this case, auxiliaries' power consumption was assumed to be 20% of the total energy consumed for the EDBM unit. The EDBM system performance was evaluated in terms of current efficiency and specific energy consumption, with acid and base production having current efficiencies ranging between 50-70% and 65-85%, respectively. The lower current efficiency of the acid stream was attributed to proton diffusion through the AEM towards the salt compartment, resulting in an acidified salt solution at the stack outlet. Specific energy consumption for acid and base fell within the range of 3-4 and 2-3 kWh/kg, respectively, with the higher SEC of the acid related to the lower current efficiency recorded for this solution. The obtained values of SEC were compared with values published in literature for similar concentrations of chemicals [98,99]. In the present case the salt solution has a significant lower concentration compared to those employed in previous studies (at least 1 M of NaCl).

2.3.4 Specific performances of the MED unit

To further evaluate the performance of the MED pilot plant, specific parameters were considered: (i) the concentration factor of NaCl and (ii) the gross GOR (GOR_{Gross}). As indicated in Table 13, the concentration factor of NaCl achieved a maximum value of 7. It is important to note that this result was obtained by producing a distillate with a conductivity lower than 30 $\mu\text{S}/\text{cm}$ and without encountering any scaling issues in the effects.

Table 13: Specific performances of the MED pilot plant.

| MED specific performance indicators | |
|-------------------------------------|---------|
| Gross GOR [-] | 1.5-2.0 |
| CF [-] | 4.0-7.0 |

Regarding the gross GOR, its value is tied to the number of effects in the MED unit. Specifically, as the number of effects increases, the quantity of produced distillate increases, all while relying on a single inlet steam at the first effect. In this particular case, the MED unit has 2 evaporative effects, and the average gross GOR value ranged between 1.5 and 2.

2.3.5 Stability of pilot plants

As mentioned earlier, the subsequent paragraphs provide an evaluation of the stability of the main operating parameters for each technology throughout their daily operational runs.

Moreover, the total amount of working hours for each technology of the treatment chain is reported as follows:

- Nano Filtration, total working hours 670;
- Multiple Feed Plug Flow Reactor, total working hours 480;
- Multi Effect Distillation, total working hours 70;

- Electro Dialysis with Bipolar Membrane, total working hours 880;
- Evaporative ponds, total working hours 5090.

2.3.5.1 NF

To ensure consistent feeding conditions for the downstream units in the demonstration plant, the operational stability of the NF plant was evaluated. This assessment involved monitoring the trends of four key parameters: feed temperature (depicted in Figure 22a), NF pass recovery (Figure 22b), EC (Figure 22c), and NF membrane permeability (Figure 22d).

As illustrated in Figure 22a), the seawater temperature experienced a moderate increase over the operational run of 8 hours per day. However, the conductivity of the feed seawater remained stable, maintaining an EC value of 52 mS/cm. Regarding the NF1 and NF2 recovery rates, Figure 22b) demonstrates that the DPNF system consistently maintained them at 71% and 92%, respectively. In Figure 22c), further demonstration of the stability of the NF process over time can be observed by the electrical conductivity EC for the NF1 permeate and NF2 permeate. More specifically, whilst the EC of NF1 permeate was 45.3 mS/cm over the entire operational run, the EC of NF2 permeate reached a lower value of 41.6 mS/cm. Such difference was due to the lower feed concentration of NF2.

Turning to membrane permeability (Figure 22d)), a pattern similar to that of the feed temperature was observed. As seawater temperature increased, membranes became more permeable, requiring less pressure to produce a fixed permeate amount. Notably, NF2 exhibited higher permeability than NF1, attributed to the differing ion rejection in the two passes.

The variance in membrane permeability is linked to the rejected ions, with NF1 handling a stream rich in multivalent ions, resulting in a higher osmotic pressure difference. Consequently, higher applied pressure was needed to overcome this osmotic pressure difference and produce permeate.

In summary, the DPNF system demonstrated stable operation, as evidenced by the consistent trends in permeate recovery and EC rejection throughout the operational period.

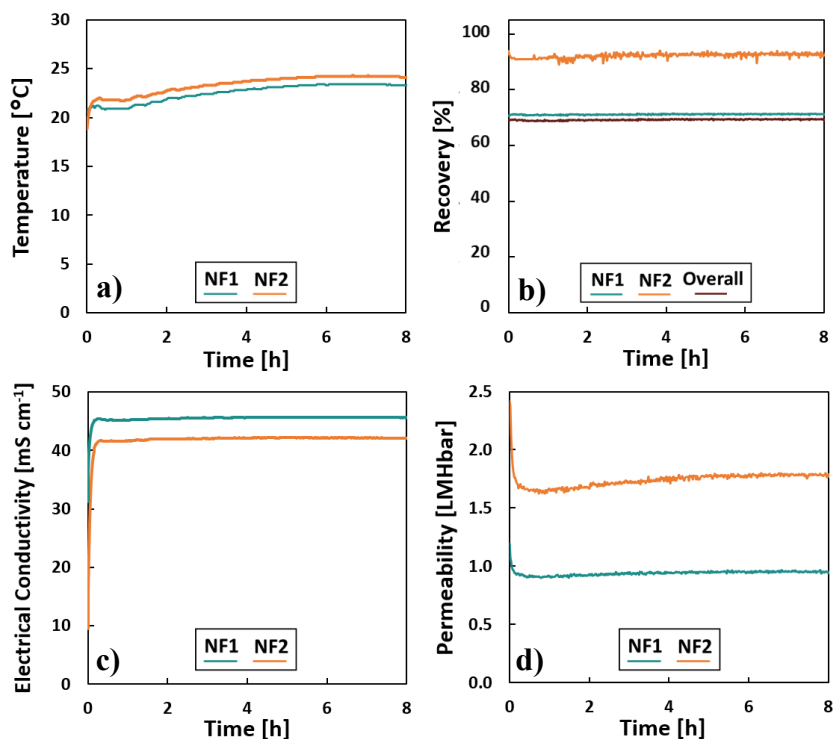


Figure 22: a) The temperature of the feed streams, b) the permeate recovery, c) the electrical conductivity of NF1 and NF2 permeates and d) the membrane permeability of NF1, NF2 and/or the overall DPNF process, throughout the operation.

2.3.5.2 MF-PFR

As detailed in Paragraph 2.2.2, the MF-PFR underwent two consecutive precipitation steps for the recovery of $\text{Mg}(\text{OH})_2$ and $\text{Ca}(\text{OH})_2$. Each step, conducted for 8 hours/day in the 1st stage and 5 hours/day in the 2nd stage, involved recording and plotting pertinent operational parameters such as pH, brine flow rates, and alkaline flow rates over time. This monitoring aimed to evaluate the system stability,

recognizing that sustained pH and flow rates would ensure consistent recovery and purity of the hydroxides.

Figure 23 depicts the temporal variations of these parameters during the magnesium precipitation step (Figure 23a) and the calcium precipitation step (Figure 23b)). As observed in both Figures 23a) and 23b), the outlet reaction pH and brine flow rate remained stable throughout the experiments. It is noteworthy that stability could potentially be compromised by pressure drops resulting from nozzle scaling or minor fluctuations in the magnesium (or calcium) content of the inlet brine.

The slight increase in alkaline flow rate over time, as explained, could be attributed to the variations in the magnesium content of the inlet brine. However, it is crucial to highlight that the implemented control system was meticulously designed to mitigate such disturbances effectively. Consequently, it successfully managed to uphold stability in the system, ensuring the reliable and consistent accomplishment of the task at hand.

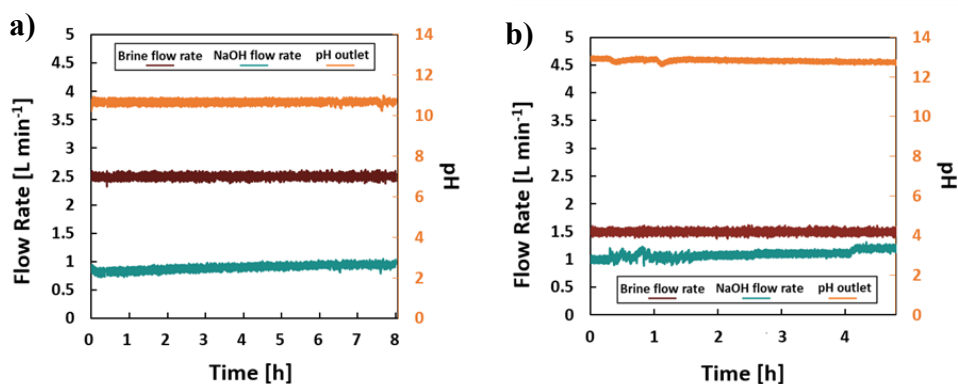


Figure 23: Variation of pH and both flow rates during the operational run of a) the first precipitation step for $Mg(OH)_2$ production and b) the second precipitation step for $Ca(OH)_2$ production.

2.3.5.3 EDBM

To ensure both a continuous supply of a targeted 1M NaOH solution to the MF-PFR and the consistent production of an HCl solution within a narrow concentration range, it was important to assess the stability of the EDBM pilot plant. The key parameters monitored over time included: (i) the concentrations of HCl and NaOH (Figure 24a)), (ii) the applied voltage of the pilot system (Figure 24b)), (iii) the calculated specific energy consumption (SEC) related to HCl and NaOH (Figure 24c)), and (iv) the current efficiency (CE) of the system concerning HCl and NaOH (Figure 24d)).

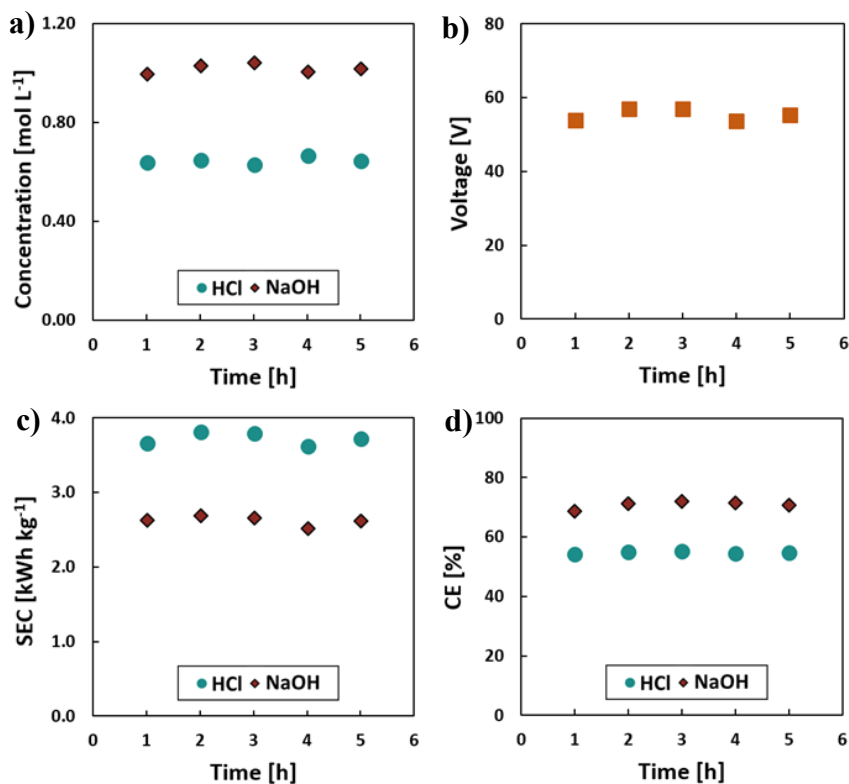


Figure 24: a) trend of HCl and NaOH concentration, b) trend of voltage, c) trend of Specific Energy consumption referred to HCl and NaOH produced, d) trend of current efficiency referred to HCl and NaOH during operation.

As depicted in Figure 24a), the concentrations of NaOH and HCl were consistently maintained at 1 mol/L and 0.65 mol/L, respectively. The implementation of an advanced control system, as detailed in reference [88], played a pivotal role in ensuring this stability. Despite the lower HCl concentration, observed factors, such as the diffusion and loss of proton ions into the salt and alkaline compartments and a slight increase in the outlet acid solution flow rate due to osmotic and electroosmotic water flux [86], were identified as contributing to this phenomenon. Figure 24b) illustrates that the resulting voltage of the EDBM stack exhibited minor fluctuations, remaining close to 55 V. This stability in voltage further reinforced the reliability of the system. Lastly, due to the consistent behaviour of the system, the calculated SEC and CE remained stable throughout the operational run, as evidenced in Figures 24c) and 24d). Overall, the EDBM pilot plant demonstrated reliability and stability, affirming its capacity to sustain continuous operations.

2.3.5.4 MED

In order to evaluate the operational stability of the MED pilot plant and assess its potential for freshwater production and NaCl recovery, crucial for downstream collection in the evaporation ponds, an examination was conducted. The focus was on monitoring the operating temperature and pressure trends of the 1st effect throughout a 4-hour operational run.

As depicted in Figure 25a), after the initial hour of plant start-up, both pressure and temperature exhibited remarkable stability, hovering around 50°C and 0.1 bar, respectively. This outcome held significant importance, given that the MED pilot utilized waste heat from the diesel engines of the local Lampedusa Power Plant, characterized by slight and unpredictable temperature variations.

Turning attention to the quality of the outlet streams, Figure 25b) illustrates the monitored conductivity of the brine and distillate during daily operational runs. Both maintained constant values at approximately 195 mS/cm and 20 μ S/cm, respectively. This successful outcome achieved two primary objectives: (i) the production of high-

quality water and (ii) maximized NaCl recovery. Overall, the MED pilot plant demonstrated robust operational stability, ensuring reliable performance and successful attainment of its key goals.

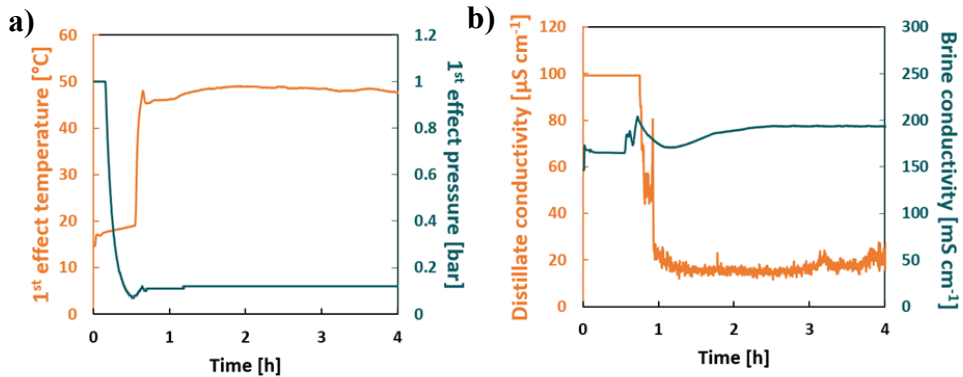


Figure 25: a) trend of 1st effect operating temperature and pressure in time; b) trend of distillate and brine conductivity in time.

2.3.6 Integration and circularity assessment

The integration and circularity assessment of the pilot plant provides invaluable insights for guiding future decisions and strategies. In this assessment, a full integration of the units was assumed. This meant that the capacity of the five different technologies perfectly match each other, eliminating discharge issues experienced in real pilot units due to practical constraints within the project. Figure 26 presents a detailed mass balance of the fully integrated system through a Sankey diagram. This visual representation vividly showcases the efficient recovery of valuable resources within the integrated system. Notably, the Sankey diagram illustrates a closed-loop system wherein chemicals like NaOH and HCl can be recirculated within the system (in MF-PFR) for the precipitation of $\text{Mg}(\text{OH})_2$ and $\text{Ca}(\text{OH})_2$. Additionally, the saline effluent from the EDBM can be looped back into the system (to the MED), potentially reducing the net freshwater requirement of the process to zero. Figure 26 serves as compelling evidence of substantial waste

reduction compared to linear desalination systems. In the fully integrated system, waste streams are minimized, and various materials are efficiently recycled and repurposed, as depicted by the loops and connections in the diagram. This comprehensive integration approach not only enhances resource recovery but also aligns with principles of sustainability and circularity in the context of desalination processes.

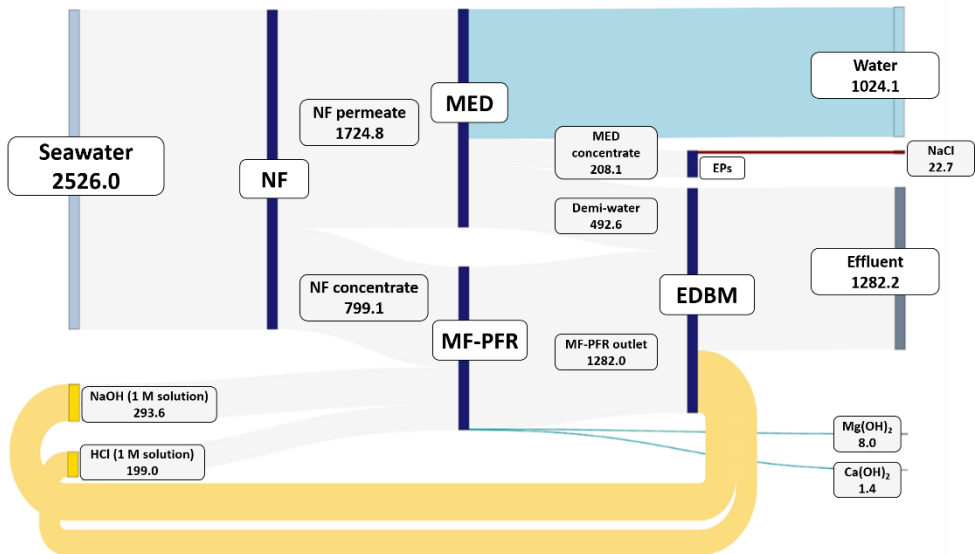


Figure 26: Mass balance [kg/h] of a fully integrated system. The recovered chemicals, NaOH and HCl, are recirculated in the system (MF-PFR). Saline effluent from the EDBM can be recycled back to the system (MED).

Table 14 provides a concise summary of the integration and circularity assessment results. The analysis highlighted an impressive 92.7% reduction in total brine, marking a substantial improvement compared to conventional linear desalination methods. This achievement signified an important step towards environmental enhancement, showcasing the effective recovery of resources from seawater brine. In terms of resource efficiency (RE), the results demonstrated a remarkably high recovery of all valuable materials that would typically be discharged in linear systems. A particular remark for the recovery of water, which indicates the system's advantage in terms of water availability when compared to linear systems. This

emphasized the potential for more sustainable resource management, as the pilot plant system excelled in efficiently recovering valuable materials and minimizing waste compared to traditional linear processes.

The circularity assessment revealed a Circular Economy Indicator (CCI) of 100%, indicating that all chemicals, such as HCl and NaOH, essential for the process, were internally produced from seawater brine. This not only supported internal production needs but also allowed for surplus production that can be marketed. This result is a noteworthy advancement in (i) reducing dependence on external sources and (ii) securing the supply chain for critical materials like magnesium.

Despite the system high energy requirements posing a challenge, potential opportunities exist for risk mitigation. Integrating the power station with the desalination plant could enhance the water-energy nexus, potentially reducing energy consumption and costs. Moreover, harnessing the energy gain from utilizing waste heat to meet thermal energy requirements could significantly enhance the system overall energy self-sufficiency. These considerations underscore the potential for further optimization and sustainable development in the pilot plant system.

Table 14: Circularity assessment results.

| Indicator | Percentage | |
|--------------------------------|------------|---|
| Total brine reduction (TBR) | 92.7% | ↑ |
| Resource Efficiency (RE) | | |
| Water | 79.7% | ↑ |
| Mg(OH) ₂ | 90-100% | ↑ |
| Ca(OH) ₂ | 50-80% | ↑ |
| NaCl | >95% | ↑ |
| HCl | 90-95% | ↑ |
| NaOH | 90-95% | ↑ |
| Circular Chemical Inflow (CCI) | 100% | ↑ |
| Energy Self-Sufficiency (ESS) | 85.4% | ↑ |

Overall, the impact of the results is evident in the practical advancements achieved, from substantial waste reduction to the establishment of a ZLD system and the potential for marketable salt and chemical production from integrated desalination and brine treatment plants. These findings not only contribute to the scientific

understanding of integrated desalination systems but also pave the way for transformative changes in environmental sustainability.

Regarding the environmental aspect, the proposed system significantly reduces the environmental impact on the marine ecosystem compared to conventional desalination due to the brine discharge elimination. Additionally, the achieved high energy self-sufficiency holds promise as a potential solution for energy-scarce regions, such as Lampedusa.

Therefore, this work stands as a catalyst for progressive change, providing a foundation for future discussions and actions in resource management.

2.4 Conclusions

In the framework of sustainable minerals production, recent attention within the scientific community has been directed towards the proposition of MLD/ZLD schemes for treating seawater/brine. These schemes aim to address both the depletion of land mining resources and the adverse environmental impacts associated with seawater desalination processes. However, many of the proposed schemes remain at the conceptual or laboratory scale. This work breaks new ground by presenting the results of a large-scale demonstrative plant for seawater valorisation, boasting a feed capacity of 2.46 m³/h. The plant was designed to recover various valuable resources while harnessing waste heat from the cooling circuits of a small island Power Plant in Lampedusa.

The seawater treatment chain encompassed five distinct technologies: (i) Nanofiltration, (ii) Multiple Feed – Plug Flow Reactor, (iii) ElectroDialysis with Bipolar Membranes, (iv) Multi-Effect Distillation, and (v) Evaporation Ponds. Results demonstrated that this treatment chain can successfully recover: (i) Three valuable resources: Mg(OH)₂ (purity: 90-98%), Ca(OH)₂, and NaCl (purity > 99%); (ii) High-quality freshwater (with recovery rates reaching up to 85% and freshwater conductivity below 30 μS/cm); (iii) Two chemicals utilized as reactants and for

cleaning/neutralizing purposes within the treatment chain (1M NaOH and 0.65M HCl solutions).

Moreover, the stability of each unit during daily operational runs was assessed and successfully achieved, confirming not only the technical feasibility of the proposed demo plant but also the viability of MLD as a sustainable alternative for minerals recovery.

In a concluding circularity assessment, the system demonstrated the potential to operate in a fully circular mode, requiring zero external chemical inputs and achieving extremely high recovery rates for water and chemicals generated in the process. This marks a significant stride towards circular minerals recovery practices.

SECTION 2: Magnesium recovery from seawater/brines via a novel Multiple Feed –Plug Flow Reactor (MF-PFR)

Drawing conclusions from the findings presented in Section 1, encompassing both Chapter 1 and Chapter 2, the importance of Magnesium recovery for the technical and economic viability of the proposed MLD treatment chains becomes evident. In Chapter 1, it became apparent that the only viable pathway to offset the total investment and operational costs of the first proposed MLD chain lay in the sale of $\text{Mg}(\text{OH})_2$. Meanwhile, Chapter 2 underscored the substantial quantity of chemicals required for the Magnesium reactor (MF-PFR) in the second proposed MLD chain. To enhance the techno-economic feasibility of the proposed MLD chains, a pivotal focus on improving the operational performance of the core technology, namely the MF-PFR, was deemed essential. This focal point constituted the primary emphasis of Section 2 and is robustly supported by the contents of **Publication 3** [100].

Literature review

Over the past few decades, the gradual depletion of minerals through land mining and the concurrent rise in demand have compelled the European Union to identify thirty "critical" raw materials (CRMs) [101,102]. Addressing the recovery of these materials has become a central objective of the EU Green Deal [103], an action plan focused on developing sustainable technological processes to mitigate environmental pollution and reduce economic dependence on other nations.

Magnesium, among the CRMs, has recently emerged as a focal point in the European economy. Notably, one of its primary compounds, $\text{Mg}(\text{OH})_2$, finds widespread use across various industrial sectors owing to its distinctive chemical-physical properties [104]. Applications span the pharmaceutical field, refractories, wastewater treatment

industry, and gas desulphurization [105–107]. Furthermore, $\text{Mg}(\text{OH})_2$ is employed in the calcination process for magnesium oxide production [108] and has garnered increased attention for its vital role in safety protection too [109]. Specifically, under fire conditions, it undergoes degradation at high temperatures (around 350°C), generating water vapor that forms a protective envelope around the flame, excluding air and diluting flammable gases. This characteristic renders $\text{Mg}(\text{OH})_2$ an optimal, non-toxic flame retardant in polymeric materials [110,111].

To meet the increasing global demand for $\text{Mg}(\text{OH})_2$, recent years have witnessed a transition from land mines to seawater as the primary source. This shift is primarily driven by the diminishing availability of easily accessible, high-grade mineral deposits, leaving lower-grade ore found deeper in the earth. As ore quality declines, production costs, including water and energy expenditures, tend to rise [112]. Compounded by issues such as water scarcity and the environmental impact of mining, the attractiveness of traditional mining methods diminishes even further [21,113]. Consequently, seawater has emerged as an increasingly viable alternative mineral source.

While it is not a groundbreaking revelation that seawater contains various elements from the periodic table, with magnesium (Mg^{2+}) being the second most abundant cation after sodium (Na^+), comprising approximately 15% of the total salt [114], its potential as an abundant source for magnesium recovery is noteworthy [20,109,115]. Seawater exploitation for magnesium recovery is not a new concept and has been practiced for decades [116–118]. Presently, several facilities worldwide, including those in Ireland, Japan, Norway, and the USA, produce magnesium-based compounds from seawater [114]. However, the relatively low concentrations and associated high extraction costs have limited mineral production from seawater.

A potential solution to overcome these challenges and promote more sustainable extraction techniques is the utilization of desalination brine, which contains higher Mg^{2+} concentrations [59,119–123]. This concept, known as "Brine Valorisation," not only ensures the production of valuable minerals but also reduces the cost of water produced by desalination plants and minimizes the environmental impact of brine

discharge [4,9,124,125]. This approach, grounded in the principles of circular economy, advocates for a more sustainable management of brine.

Moreover, extracting $\text{Mg}(\text{OH})_2$ from brines presents a win-win scenario. Beyond its aforementioned valuable applications, this process simultaneously removes a scaling compound that could compromise membrane-based evaporative desalination technologies and brine concentrators within MLD/ZLD systems [126–128].

Despite the diverse sources for magnesium recovery, various methods for producing $\text{Mg}(\text{OH})_2$ have been explored in scientific literature. These methods include the hydration of magnesium oxide (MgO), precipitation of salt with an alkaline solution, electrolysis of an aqueous magnesium salt solution [129], and the sol-gel technique [130]. However, a predominant focus in the literature lies on reactive chemical precipitation due to its simplicity, cost-effectiveness, and ease of commercialization [10].

Numerous alkaline reagents have been utilized to promote $\text{Mg}(\text{OH})_2$ precipitation, with ammonia being a common choice [119,131]. Mohammad et al. [119], for instance, successfully recovered magnesium from desalination reject brine using ammonium hydroxide, achieving >95% pure $\text{Mg}(\text{OH})_2$ products. However, challenges remain in achieving total magnesium conversion, with 97% being the highest recovery reported in these processes.

An alternative, safe, and cost-effective reactant is $\text{Ca}(\text{OH})_2$ or slaked lime. The Dow Chemical Company patented a process in 1943 for magnesium recovery from seawater through precipitation with lime due to the low cost of this reactant. Several studies [59,122,123,132] have explored the use of $\text{Ca}(\text{OH})_2$ or slaked lime, achieving high magnesium recoveries but often resulting in lower purities of the final product (typically below 80%, and up to 91% with lime screening operations). These impurities are attributed to contaminants present in the lime, such as carbonates or calcium ions in the magnesium source, leading to co-precipitation of calcium sulphates, calcium hydroxide, and calcium carbonate during $\text{Mg}(\text{OH})_2$ production.

In industrial settings, achieving the high purity of $\text{Mg}(\text{OH})_2$ necessary for producing MgO pure up to 97% [133] via calcination requires the use of low-impurity raw

stones and appropriate calcination conditions for highly pure lime solutions. Additionally, various pre-treatments are necessary for decarbonation or the removal of suspended particles in the magnesium source.

An innovative alternative was proposed by La Corte et al. [134] and Vassallo et al. [135], who introduced a novel membrane crystallizer called "CrIEM." In this system, brine came into contact with a low-cost reactant ($\text{Ca}(\text{OH})_2$) via an anionic exchange membrane, promoting the precipitation of high-purity $\text{Mg}(\text{OH})_2$ particles. However, whilst promising, this technology still remains at the laboratory scale and may face challenges in future industrial applications due to the use of expensive membranes, leading to higher capital costs.

The potential hazards associated with ammonia and the challenges posed by low purities using $\text{Ca}(\text{OH})_2$ have spurred extensive research into the precipitation performance of $\text{Mg}(\text{OH})_2$ through the use of NaOH. Casas et al. [120] demonstrated that using NaOH resulted in higher purities of $\text{Mg}(\text{OH})_2$ compared to when using sodium carbonate (Na_2CO_3). Song et al. [116,117] also achieved high-purity $\text{Mg}(\text{OH})_2$ particles from concentrated saline solutions. Utilizing a Mixed Suspension Mixed Product Removal crystallizer, they produced spherical particles with purities exceeding 99%, characterized by an average particle size distribution ranging from 6 to 30 μm . However, a drawback was the high tendency of particle agglomeration, forming gelatinous suspensions and making filtration challenging [136].

Turek and Gnot [137] recovered $\text{Mg}(\text{OH})_2$ as a by-product using NaOH from hard coal mine brine. The authors noted that maintaining an excess of hydroxide ions during crystallization resulted in slower sedimentation speed and more challenging filtration compared to an excess of Mg^{2+} ions. Sung-Woo and Jun-Heok [138] proposed a multi-step reactive process for recycling magnesium chloride from industrial brines. After adding sulfuric acid to precipitate calcium ions, NaOH was introduced to produce $\text{Mg}(\text{OH})_2$ with a purity of 98% and a hexagonal flat platelet structure. Additives such as carboxyl methyl cellulose and sodium stearate were incorporated, halving sedimentation times and achieving a crystal size of 0.5 μm , with a purity of 99.5%.

Henrist et al. [129] explored how the use of NaOH or ammonium hydroxide (NH_4OH) influenced the size, shape, and level of agglomeration of $\text{Mg}(\text{OH})_2$ crystals produced from artificial brines. NaOH led to cauliflower-shaped globular agglomerates at 60°C , while ammonia resulted in more resistant platelet-shaped particles, as also noted by Li et al. [139]. The latter study also examined the impact of operating temperature on the characteristics of the final product, revealing that higher temperatures led to smaller crystals that agglomerated more.

Recent work by Jarosinski et al. [140] introduced a novel method where the reaction with NaOH was followed by washing with a 25% ammonia solution and acetone. This procedure enabled the production of a product with a high specific surface area of $100 \text{ m}^2/\text{g}$, exceeding the requirements for flame retardant purposes ($< 10 \text{ m}^2/\text{g}$). Cipollina et al. [141] conducted an experimental campaign with semi-batch and continuous reactors, demonstrating that higher concentrations of alkaline reactant and magnesium ions led to the formation of larger particles, with purity ranging between 98% and 100% in most experimental runs.

Summarizing the advantages and disadvantages of potential reactants for $\text{Mg}(\text{OH})_2$ precipitation from the previous studies, it is possible to discern the following insights: (i) ammonium hydroxide yields highly pure hexagonal $\text{Mg}(\text{OH})_2$ particles but suffers from low Mg ion conversion and the generation of by-products, such as ammonia, which poses safety concerns in subsequent electrolytic processes [137]; (ii) lime usage results in the production of low-purity $\text{Mg}(\text{OH})_2$ despite its cost-effectiveness; (iii) NaOH facilitates the production of highly pure $\text{Mg}(\text{OH})_2$ with 100% conversion of Mg^{2+} [46]. However, NaOH is expensive and leads to the precipitation of gelatinous suspensions that are challenging to sediment and filter [141].

In light of these challenges associated with NaOH, Chapter 3 of the present PhD thesis sought to explore the impact of different operating conditions and process strategies on the $\text{Mg}(\text{OH})_2$ precipitation process using the novel MF-PFR. Developed by ResourSEAs srl and previously introduced by Vassallo et al. [61,142] at the Brine Excellence Centre of the University of Palermo, this is the first unstirred reactive

crystallizer at a pilot scale (in literature) designed to produce $\text{Mg}(\text{OH})_2$ from waste industrial brines. The MF-PFR, being a modular reactor, offers scalability advantages over classical batch stirred reactors, addressing issues related to large-scale reactor design as volume increases [143].

Initial testing of the MF-PFR by Vassallo et al. [61] focused on selectively recovering $\text{Mg}(\text{OH})_2$ and $\text{Ca}(\text{OH})_2$ at controlled pH values from spent brines in the water softening industry. Specifically, the MF-PFR treated the retentate of the nanofiltration unit processing the spent brine from the industrial water production plant of Evides Industriewater B.V. (Rotterdam). The authors conducted an extensive experimental campaign to demonstrate the stability and robustness of the prototype at different inlet flow rates and initial brine compositions. While the performances were evaluated based on $\text{Mg}(\text{OH})_2$ and $\text{Ca}(\text{OH})_2$ purity, the influence of these operating parameters on the properties of the produced slurries, such as sedimentation rate, filtration rate, and particle size distributions, was not assessed. Nevertheless, the results highlighted the potential for achieving high mineral recovery rates: 100% and 97% for magnesium and calcium hydroxides, respectively, with high product purity (> 98%) being another noteworthy achievement [60].

Overall, Chapter 3 (entirely supported by **Publication 3** [100]) tends to fill in the missing gap in literature, specifically providing valuable insights on the influence of different operational strategies of the MF-PFR on the sedimentation rate, filtration rate and particle size distribution of $\text{Mg}(\text{OH})_2$ crystals.

3 “Influence of Operational Strategies for the Recovery of Magnesium Hydroxide from Brines at a Pilot Scale”

This chapter is mainly focused on evaluating the impact of various operating conditions on the sedimentation rate, filtration rate, and granulometry characteristics of the final $Mg(OH)_2$ products. Experiments were conducted using the same MF-PFR presented by Vassallo et al. [61], examining the effects of (i) initial Mg^{2+} brine concentration, (ii) brine/NaOH flow rate at a constant initial Mg^{2+} concentration, and (iii) the potential for recycling a portion of the product to induce a seeded precipitation process.

Two distinct Mg^{2+} -containing brine scenarios were considered: (i) a brine simulating the Mg^{2+} concentration of a real brine exiting an NF unit treating seawater [144], and (ii) a brine mimicking the Mg^{2+} concentration of a real brine exiting a typical Mediterranean saltwork [145]. The two scenarios were able to cover a wide range of feed concentrations. Additionally, different reactor configurations were investigated. This comprehensive study aimed to provide crucial insights for the design of industrial $Mg(OH)_2$ reactors in circular economy schemes, addressing inherent challenges and offering innovative solutions. Collected results are particularly valuable in overcoming common issues related to sedimentation and filterability encountered in the precipitation of $Mg(OH)_2$ via NaOH solutions.

3.1 Concept of Magnesium Hydroxide recovery via a novel reactive crystallizer

The innovative reactive crystallizer examined was the MF-PFR, as introduced by Vassallo et al. [60,61]. Figure 27 shows: (a) an image of the developed MF-PFR pilot plant and (b) a simplified Piping and Instrumentation Diagram (P&ID) illustrating all the key features of the plant.

The experimental setup, as shown in Figures 27a) and 27b), comprised the MF-PFR pilot unit housed on an aluminium structural skid, incorporating the reactor along with its auxiliary components. Pumps P1 and P2 were used to feed the brine and NaOH solution, respectively, to the reactor from two 200 L upstream cylindrical tanks made of High-Density Polyethylene (HDPE), denoted as T1 and T2. Pressure, temperature, and flow rate along the two feed lines were measured for both solutions using pressure transducers P/S3-8 (OPTIBAR 1010C, KROHNE, and VEGABAR14, VEGA), temperature sensors T/S2-7 (TRA-C20, KROHNE), and

magnetic induction flow meters F/S1-6 (OPTIFLUX 4300 C, KROHNE). The conductivity of the alkaline solution was monitored by the conductivity meter C/S5 (IND1000, MAC100, KROHNE). The brine flow rate was regulated by adjusting the percentage of the opening section of the RV1 valve. To monitor the outlet slurry pH, a pH-Meter (PH 8320, KROHNE) was employed, and the pH was adjusted by varying the alkaline flow rate through a cascade control. The resulting $\text{Mg}(\text{OH})_2$ slurry was stored in a 500 L cylindrical HDPE tank labelled T3. Another tank (T4) was used for storing (i) the discharged cleaning solutions and (ii) the slurry produced during the startup of the pilot plant. Overall, a LabVIEW software-based control panel was developed to monitor and control the specified parameters of the prototype.

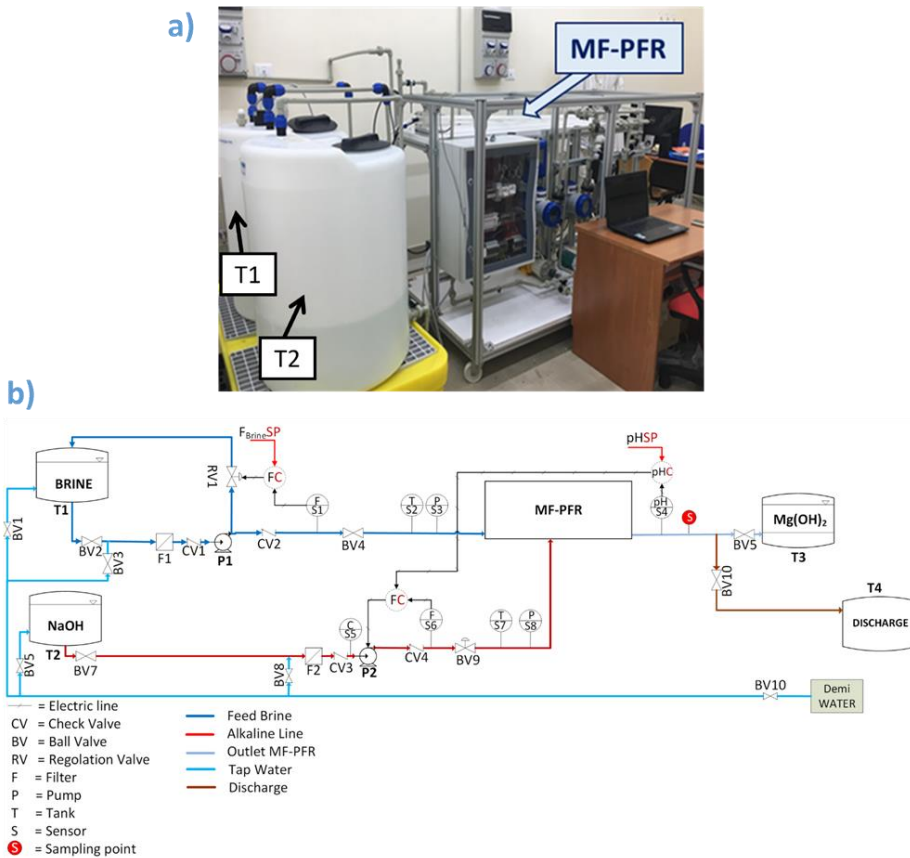
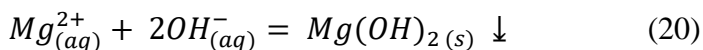


Figure 27: a) The MF-PFR prototype developed at the Brine Excellence Centre satellite laboratory of the University of Palermo and b) simplified P&ID of the MF-PFR prototype. Figure 27a) was adapted from Vassallo et al. [61].

As far as the MF-PFR reactor is concerned, it comprised two interconnected volumes: one compartment received the feed (a synthetic solution mimicking the Mg^{2+} concentration in waste brine), while the other compartment was supplied with an aqueous solution of NaOH. As depicted in Figure 28, the two feed streams came into contact through a multiple inlet arrangement, designed to enhance supersaturation homogenization across the reactor volume. Each inlet was equipped with nozzles specifically designed to facilitate rapid mixing of the two streams [61,142]. Both the distribution and number of nozzles are of fundamental importance due to the fact that they can influence the main parameters that govern the fast

reaction of $Mg(OH)_2$ such as mixing and supersaturation. More specifically, the limits of this fast reaction concern the particle size of the product. Fast reactions generally lead to very high nucleation rates and low growth rates, thus producing many small crystals. The growth of crystals is limited since all of the supersaturation has been employed for nucleation. It is therefore important, via the distribution of nozzles, to control the mixing and supersaturation to desirably achieve low nucleation rates and high growth rates. However, it is to be noted that specific technical details concerning the reactor equipment (e.g., reactor length, size, number and distribution of the nozzles) are not provided in the thesis since they are currently protected by a patent issued by ResourSEAs srl [85].

Nevertheless, it can be stated that when the reactants met in the MF-PFR, Magnesium (Mg^{2+}) ions in the feed solution (brine) reacted with Hydroxyl (OH^-) ions from the alkaline solution, leading to the precipitation of $Mg(OH)_2$ as indicated by the chemical reaction Equation 20:



This reaction results in a dense white suspension or slurry due to the colour of the precipitated particles.

In this study, the performance of the MF-PFR was evaluated using three different operating strategies, schematically illustrated in Figure 28. The objective was to investigate whether distributing the brine into the alkaline solution or vice versa could impact the final product—for example, producing nanoparticle-sized or microparticle-sized products, generating more or less easily filterable products, and so on. Figure 28a) represents the standard MF-PFR configuration, denoted as configuration A, where brine is injected into the alkaline solution. Configuration B (Figure 28b)) involves feeding NaOH into the brine solution. Finally, a third operating configuration (configuration C) was examined, illustrated in Figure 28c). In this case, the $Mg(OH)_2$ slurry exiting the reactor was partially mixed with fresh alkaline solution and recycled back to the reactor to induce seeded precipitation,

promoting total conversion of Mg ions in the reactor. It is important to note that no reaction takes place downstream of the reactor since the reaction is instantaneous.

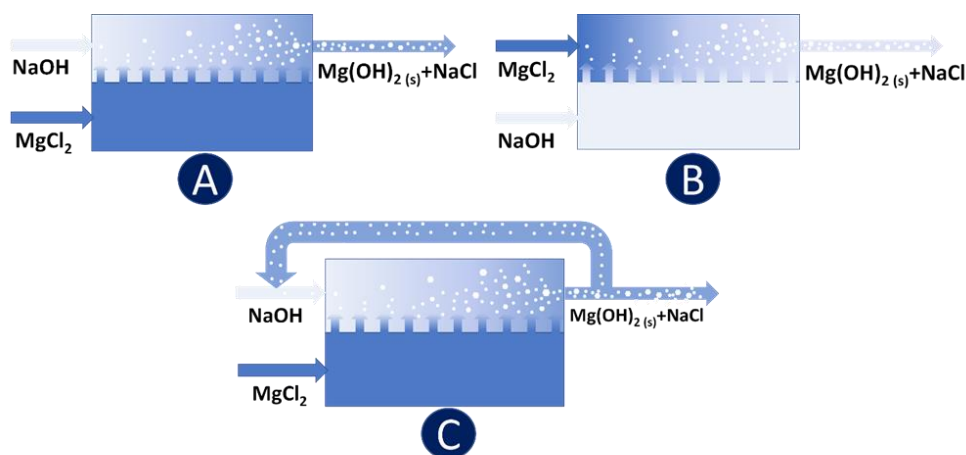


Figure 28: Conceptual schemes of Mg(OH)_2 precipitation within the MF-PFR made of two adjacent compartments: A) The brine solution is injected in the NaOH solution; B) The NaOH solution is injected into the brine; C) the same strategy as A but the Mg(OH)_2 slurry is recycled and partially mixed with fresh alkaline solution.

The MF-PFR prototype was meticulously designed to precisely control the reaction pH at which Mg(OH)_2 precipitation takes place. Specifically, the complete precipitation of Magnesium content in a Mg-containing brine is expected to occur quantitatively at the theoretical reaction equilibrium pH value of approximately 10.4 [135]. When pH values fall below 10.4, magnesium ions persist in the outlet stream due to incomplete conversion. Conversely, reaching pH values around 12.5-13.0 can lead to co-precipitation of additional ions, depending on the composition of the feed stream. For instance, in the presence of calcium ions, Ca(OH)_2 particles may precipitate. This co-precipitation poses a risk to the purity of the produced Mg(OH)_2 . Therefore, the choice of the ratio between the flow rates of the feed and alkaline reactant is critical to avoid low purities. The actual feasibility of conducting pH-controlled Mg(OH)_2 precipitation tests using the MF-PFR was documented in [61].

3.2 Materials and methods

3.2.1 Overview of the experimental campaign

To investigate the impact of operating conditions on the production of $\text{Mg}(\text{OH})_2$ in terms of particle size distribution, filterability, and sedimentation rate, an extensive experimental campaign was carried out. Six tests were performed, and their details are listed in Table 15. Synthetic brines containing only magnesium chloride were utilized for all tests. Additionally, the concentration of NaOH was consistently set to 1M across all cases for comparative purposes. However, the flow rate of the NaOH solution varied within a specified range (reported in Table 15) for each test, aiming to achieve a final $\text{Mg}(\text{OH})_2$ slurry pH values of 10.1, 10.4, and 12.

Table 15: Main nominal operating conditions of experimental tests.

| Test | Brine Concentration | | NaOH conc. [mol/L] | Brine Flow rate [L/min] | NaOH | Conf* | Comparison Test and purpose |
|------|---------------------|-----------------|--------------------------|-------------------------------|-------------------------------|-------|-------------------------------------------|
| | Mg ²⁺ | Cl ⁻ | | | solution | | |
| | mol/L | mol/L | | | Flow rate range [L/min] | | |
| 1 | 0.240±0.005 | 0.480±0.005 | 1.00±0.03 | 0.66±0.04 | 0.12±0.08 – 0.38±0.05 | A | - |
| 2 | 1.00±0.02 | 2.00±0.02 | 1.00±0.03 | 0.66±0.04 | 0.59±0.04 – 1.10±0.03 | A | Test 1. Initial Mg ²⁺ conc. |
| 3 | 0.240±0.005 | 0.480±0.005 | 1.00±0.03 | 2.00±0.08 | 0.38±0.06 – 0.80±0.03 | A | Test 1. Brine flow rate. |
| 4 | 0.240±0.005 | 0.480±0.005 | 1.00±0.03 | 2.00±0.08 | 0.29±0.08 – 0.78±0.03 | B | Test 3. Reactor conf. |
| 5 | 0.240±0.005 | 0.480±0.005 | 1.00±0.03 | 0.66±0.04 | 0.24±0.08 – 0.90±0.03 | C | Test 1. Reactor conf. |
| 6 | 0.240±0.005 | 0.480±0.005 | 1.00±0.03 | 2.00±0.08 | 0.8±0.03 – 1.20±0.03 | C | Test 5. Brine flow rate. |

*Configuration adopted. Letters A, B and C refer to Figure 28

The last column in Table 15 denotes the reference test case considered for comparison, with the only differing parameter between the two compared tests. Specifically, as mentioned in Paragraph 3.2.1, one primary objective of the

experiments was to assess the impact of the initial Mg^{2+} concentration on the characteristics of the final produced particles. In Test 1 and Test 2, two different concentrations of Mg^{2+} were tested, utilizing the same operating parameters for comparison purposes (e.g., brine flow rate of 0.66 L/min). The two investigated Mg^{2+} concentrations, 1 M and 0.24 M, were representative of a typical Mg^{2+} concentration in (i) saltwork brines (1 M), assessed with the European Horizon 2020 Project SEArcularMINE [145], and (ii) seawater NF retentate (0.24 M), produced within the second proposed MLD treatment chain of the present PhD thesis (WATER MINING Project [144]). The latter concentration was essential to analyse due to the growing interest in recent years towards Nanofiltration as a pre-treatment step for desalination technologies and/or MLD/ZLD systems [54,146]. Flow rate values were selected in accordance with the target prototype flow rates to be adopted in the WATER MINING and SEArcularMINE projects.

Test 3 aimed to explore the influence of the brine flow rates, specifically 0.66 L/min (Test 1) and 2.00 L/min (Test 3), on the resulting $\text{Mg}(\text{OH})_2$ final product at a fixed magnesium brine concentration of 0.24 M. Test 4 provided data for comparison with Test 3 to assess the impact of the A and B reactor configurations (see Figure 28) at a fixed Mg^{2+} concentration of 0.24 M and a brine flow rate of 2.00 L/min. Finally, Tests 5 and 6 were conducted by adopting the reactor configuration C. Data from Test 5 were compared with those of Test 1 to investigate the influence of the recycling strategy on the $\text{Mg}(\text{OH})_2$ product characteristics, treating a 0.24 M Mg^{2+} solution and adopting a brine flow rate of 0.66 L/min. Furthermore, the comparison between the results of Tests 5 and 6 aimed to determine the influence of the brine flow rates, namely 0.66 L/min (Test 5) and 2.00 L/min (Test 6), when a recycling strategy was adopted and 0.24 M Mg^{2+} solutions were treated.

3.3 Experimental procedure

3.3.1 Preparation of feed and reactant solution

The brine and alkaline solutions used in the experiments were prepared using deionized water with a conductivity below 15 $\mu\text{S}/\text{cm}$. The alkaline solution was prepared using technical-grade NaOH pellets (purity > 97%, Inovyn). For the brine solution, technical-grade magnesium chloride hexahydrate ($\text{MgCl}_2 \times 6\text{H}_2\text{O}$) pellets (purity > 97%, Chem-Lab, Belgium) were employed. Table 15 provides details of the brine and alkaline solutions prepared for each experimental test. The final composition of all brine solutions was verified using ion chromatography (Metrohm 882 compact IC plus), and the final compositions of the alkaline solutions were confirmed via titration.

3.3.2 Sampling procedure

For each experimental run, the reactor underwent a stability analysis during the initial stage, commonly referred to as the 'start-up stage.' Throughout this phase, known as the "start-up stage," the flow rates of the brine and NaOH solutions were set and monitored using the interfacial panel developed in LabVIEW software. Sampling commenced once these parameters stabilized or showed minimal variation (within approximately 2% of the target flow rate value). As outlined in Paragraph 3.2.1, the flow rate of the alkaline solution was increased during the experimental test to achieve the desired pH values of 10.1, 10.4, and 12.0 in the outlet $\text{Mg}(\text{OH})_2$ slurry.

For each alkaline solution flow rate, two 1-liter samples of the outlet stream ($\text{Mg}(\text{OH})_2$ slurry) were collected. One sample was dedicated to sedimentation and filtration analyses, including subsequent ion chromatographic analysis of the filtrate. The second sample was exclusively used for granulometric analyses. It is important to note that for Test 1 and 2, no sample at pH 10.4 was taken. This was primarily due

to difficulties encountered in fixing the operating conditions of the reactor, caused by the combination of low brine flow rates and the absence of a recycling strategy.

3.3.3 Analytical procedure

Figure 29 provides the conceptual scheme of the whole analytical procedure employed for each produced $\text{Mg}(\text{OH})_2$ suspension.

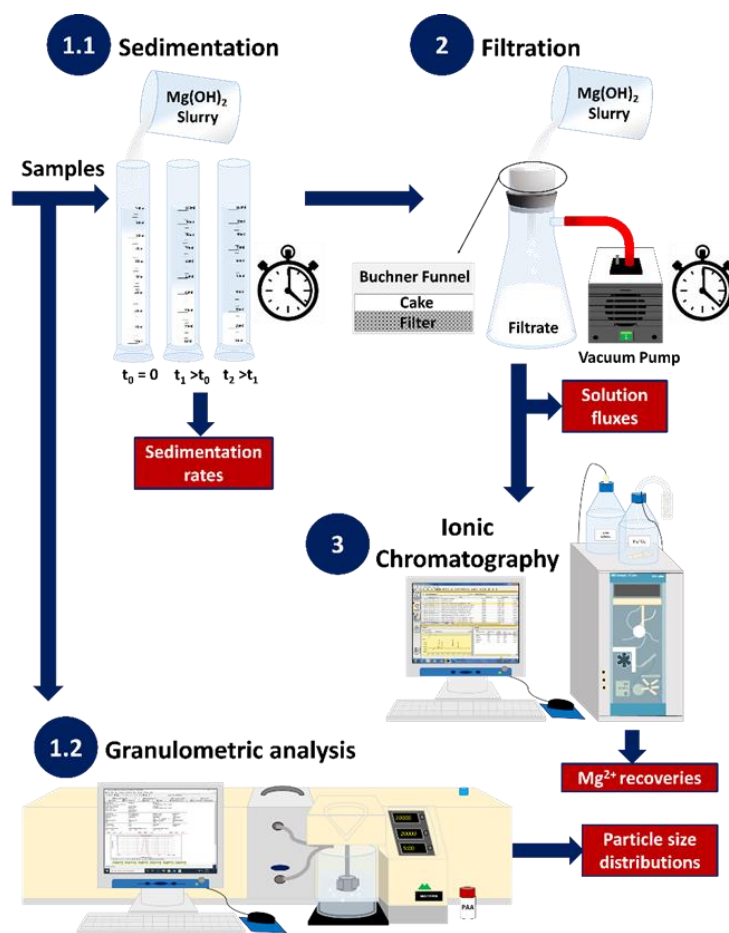


Figure 29: A conceptual scheme of the entire analytical procedure: (1.1) Analysis of sedimentation trends in time; (1.2) Granulometric analysis via the use of a Malvern Mastersizer 2000; (2) Analysis of filtration trends and (3) Analysis of Mg recovery via Ionic chromatography.

After the completion of each experimental run, sedimentation analyses were conducted for each $\text{Mg}(\text{OH})_2$ slurry with different pH values of 10.1, 10.4, and 12.0, corresponding to the various NaOH flow rates applied in the reactor. It is important to note that the final pH of the $\text{Mg}(\text{OH})_2$ slurry did not vary after collecting it from the reactor outlet. This analysis aimed to evaluate the sedimentation rate of solid $\text{Mg}(\text{OH})_2$. Each sample was vigorously agitated to ensure complete suspension of all solids in the sample holder. Subsequently, 100 ml of the sample was poured into a calibrated volumetric glass cylinder (Figure 29, point 1.1). The volume of sediment was recorded at regular time intervals, with measurements taken every 30 minutes initially and, as sedimentation rates decreased, every 1 or 2 hours. The duration of each analysis depended on the time required to reach a plateau in the sediment volume over time.

Following sedimentation analyses, samples were filtered after re-suspension (Figure 29, point 2). The filtration set-up included a vacuum pump (Buchi V-100), a 125 ml vacuum flask, an analogue glycerine-filled vacuum pressure gauge to monitor filtration pressure, a needle valve to adjust the pressure, a Büchner funnel, and glass microfiber filters with a diameter of 70 mm and a pore dimension of 1.6 microns (WhatmanTM GF/A grade, GE Healthcare Life Sciences), along with rubber rings to ensure a mechanical seal between the funnel and the flask. Filtration of 50 ml of the sample was carried out at a fixed pressure of 0.5 bar using the needle valve, and the time required for complete filtration was recorded. The solution flux of each sample was then calculated (see Section 3.2.4) to assess filterability.

The filtrate was analysed via Ionic Chromatography (882 Compact IC plus, Metrohm) to measure the Mg^{2+} content and assess magnesium recovery for each test (Figure 29, point 3).

The second remaining sample was dedicated to granulometric analyses to evaluate the size distribution of produced $\text{Mg}(\text{OH})_2$ agglomerates/aggregates (Figure 29, point 1.2). The static light scattering Malvern Mastersizer 2000 equipped with the Malvern Hydro 2000 MU for sample dispersion was employed for these analyses. For each experiment, poly(acrylic acid, sodium salt) droplets (PAA, MW 1200,

Sigma-Aldrich, Inc.) were added as a dispersant, and the stirring velocity was set to 2000 rpm. Granulometric analyses included the addition of Mg(OH)₂ sample to the water-filled beaker, sonication for up to 5 minutes, and the measurement of at least 5 particle size distributions (PSDs) to assess the assemblage state and fracture strength of Mg(OH)₂ particles. The use of a dispersant and sonication was necessary due to the high flocculation tendency of Mg(OH)₂ suspensions. Indeed, if they were not broken down, only agglomerates made of the actual Mg(OH)₂ particles would be measured [147].

3.3.4 Definition of performance parameters

To assess the behaviour and properties of the final produced Mg(OH)₂ slurry in each experiment, the following parameters were taken into account:

- Sedimentation trend: the profile of the normalized volume fraction of sedimented Mg(OH)₂ slurry over time with respect to the total initial volume;
- Cake permeability coefficient: The permeability of the solution across a specific filter cake area normalized with respect to the filter area itself, defined as:

$$\theta_{perm} = \frac{V_{sol}}{t_{filt.} * A_{filter} * P_{filt.}} * \delta_{cake} \quad (21)$$

where θ_{perm} is the permeability coefficient [$\frac{m^2}{min * bar}$], V_{sol} is the volume of solution permeated across the filter cake [L], $t_{filt.}$ is the time of complete filtration [min], A_{filter} is the area of the filter [m²], $P_{filt.}$ is the operating pressure during filtration [bar] and δ_{cake} is the thickness of cake formed during filtration [m] calculated as:

$$\delta_{cake} = \frac{V_{sol} * m_{Mg(OH)_2}}{\rho_{cake} * A_{filter}} \quad (22)$$

where $m_{Mg(OH)_2}$ is the magma density of $Mg(OH)_2$ slurry [g/L] and ρ_{cake} (assumed to be equal to the water density) is the density of the cake formed during filtration [g/m³];

- Magnesium recovery (Y) that accounts for the amount of Mg^{2+} ions recovered from the brine due to the precipitation. It is computed as the ratio between the difference of Mg^{2+} moles in the feed and those in the filtrate with respect to the magnesium moles in the feed [%];
- Magma density of $Mg(OH)_2$ slurry calculated as the ratio of the mass of $Mg(OH)_2$ solid present in the slurry over the volume of produced slurry [g/L];
- Particle Size Distributions (PSDs) without and with a treatment of the samples by sonication.

Additionally, to understand the impact of fluid dynamics on $Mg(OH)_2$ particles, the Reynolds number within (i) the nozzle and (ii) a section of the bulk mixing zone immediately after a nozzle were calculated for all investigated cases using the following equations:

$$Re_{nozzle} = \frac{\rho_{water} * (Q_{Nozzle}) * (D_{nozzle})}{\mu_{water} * \frac{\pi}{4} * (D_{nozzle}^2)} \quad (23)$$

$$Re_{bulk} = \frac{\rho_{water} * (Q_j + Q_{Nozzle}) * (D_{Mix})}{\mu_{water} * \frac{\pi}{4} * S_{MIX}} \quad (24)$$

where Re_{nozzle} and Re_{bulk} are the Reynolds number within the nozzle and the section of the bulk mixing zone, Q_j is the flow rate of the host solution receiving the injected one [m³/s], Q_{Nozzle} is the flow rate within the nozzle [m³/s], D_{Mix} is the characteristic diameter of the mixing zone [m], S_{MIX} is the cross section of the mixing zone [m²] and D_{nozzle} is the diameter of the nozzle [m]. For the sake of simplicity, the density ρ_{water} [kg/m³] and dynamic viscosity μ_{water} [Pa*s] of water (997 kg/m³ and 0.0082 Pa s, respectively, at 20 °C) were considered rather than those of the suspensions. Reynolds number within the nozzle and within the bulk mixing zone of the MF-PFR for all experimental tests are listed in Table 16.

Table 16: Nominal flow rates and values of Reynolds number in nozzle and in the bulk for experimental tests.

| Test | Slurry pH | Q_{brine} [L/min] | Q_{NaOH} [L/min] | Re_{nozzle} | Re_{bulk} |
|------|-----------|----------------------------|---------------------------|----------------------|--------------------|
| 1 | 10.1 | 0.66 | 0.12 | 880 | 210 |
| | 12 | | 0.38 | | 330 |
| 2 | 10.1 | 0.66 | 0.59 | 880 | 420 |
| | 12 | | 1.10 | | 660 |
| 3 | 10.1 | 2.00 | 0.38 | 2650 | 640 |
| | 10.4 | | 0.60 | | 740 |
| | 12 | | 0.80 | | 830 |
| 4 | 10.1 | 2.00 | 0.29 | 660 | 990 |
| | 10.4 | | 0.50 | | 1040 |
| | 12 | | 0.78 | | 1100 |
| 5 | 10.1 | 0.66 | 0.24 | 880 | 18610 |
| | 10.4 | | 0.44 | | |
| | 12 | | 0.90 | | |
| 6 | 10.1 | 2.00 | 0.80 | 2650 | 18920 |
| | 10.4 | | 0.90 | | |
| | 12 | | 1.20 | | |

3.4 Results and discussion

3.4.1 Effect of Mg^{2+} brine concentration (Configuration A)

In the initial phase, $\text{Mg}(\text{OH})_2$ suspensions generated in operating configuration A (refer to Figure 28) with varying initial concentrations of Mg^{2+} were examined. This comparison involved analysing the results of Test 1 and Test 2 (refer to Table 15). In Configuration A, brine was directed through distributed nozzles towards NaOH solutions flowing in the adjacent compartment. The solutions mixed as the brine was injected into the NaOH solution. As detailed in Paragraph 3.3.2, no samples were taken at pH 10.4 during Test 1 and Test 2 due to challenges encountered in stabilizing the reactor operating conditions, more specifically the reaction pH. It is important to anticipate that such challenges always occurred when the recycling strategy (configuration C) was not adopted. This was mainly due to the fact that recycling

part of the outlet stream allowed to improve the mixing of the solutions and homogenize the pH within the reactor.

Reynolds numbers were calculated for both tests within the bulk of the mixing zone Re_{bulk} and inside the nozzle Re_{nozzle} (see Table 16). The tests shared the same brine flow rate, resulting in identical Re_{nozzle} values. However, Re_{bulk} varied due to the higher NaOH flow rate (refer to Table 17) employed in the case of a 1M concentration. The higher NaOH flow rate was required to ensure a stoichiometric mole flow of Mg^{2+} and OH^- ions.

Figure 30a) provides the sedimentation trend of normalized volume of $Mg(OH)_2$ slurry over time ($V(t)/V_{initial}$) for Test 1 and Test 2 at two different pH values: 10.1 and 12.

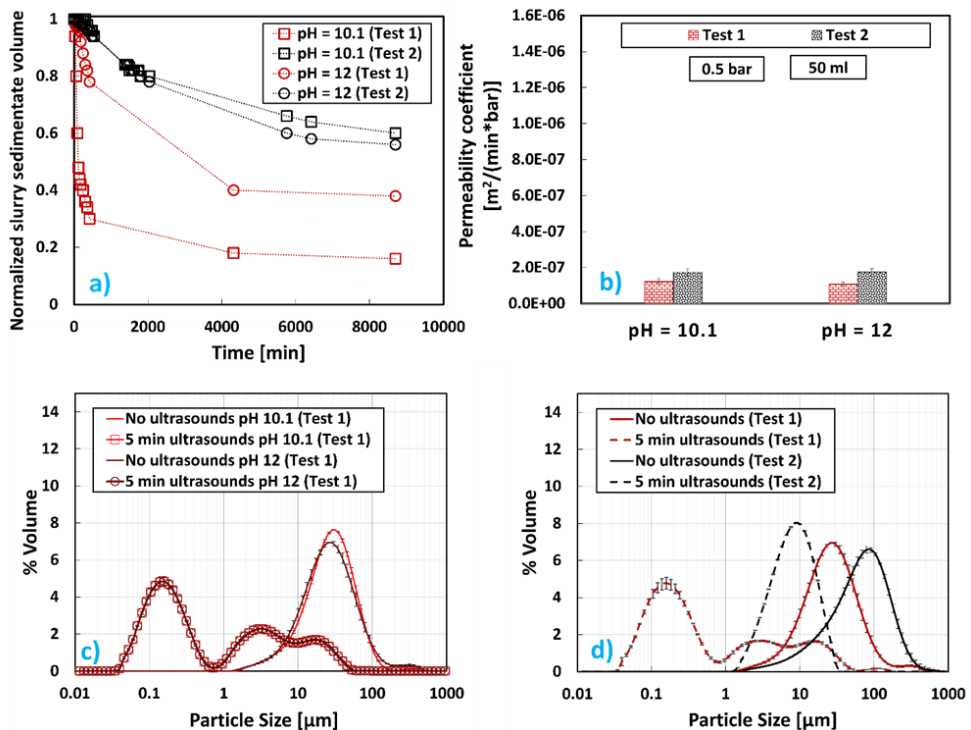


Figure 30: $Mg(OH)_2$ results at pH values 10.1 and 12 for initial Mg^{2+} concentrations of 0.24M (Test 1) and 1M (Test 2): a) sedimentation trend over time; b) Cake permeability coefficients; c) V-PSDs (effect of pH); d) V-PSDs (comparison between Tests 1 and 2 at pH =12).

It is clear from the observations that $\text{Mg}(\text{OH})_2$ suspensions generated from a lower Mg^{2+} feed concentration (Test 1, depicted by red lines and symbols in Figure 30a)) exhibited quicker sedimentation compared to those at higher concentrations (Test 2, represented by black lines and symbols in Figure 30a)). This outcome was due to the lower slurry magma density in Test 1 than in Test 2 (refer to Table 17). An additional contributing factor was the higher supersaturation achieved with a greater Mg^{2+} concentration. Specifically, heightened supersaturation leads to the formation of smaller particles that aggregate, entrapping more mother liquor and resulting in the production of more iso-dense particles. Consequently, this leads to slower sedimentation rates at 1M [137].

To assess the filterability of the product, the cake permeability coefficient (Equation 21) was calculated and compared between Test 1 and Test 2, as shown in Figure 30b). Notably, the initial difference in Mg^{2+} concentration did not significantly impact the cake permeability of the product. Lower Mg^{2+} concentrations showed slightly lower permeabilities due to the lower magma density of the filtered suspension. Additionally, a decrease in permeability was observed with an increase in slurry pH from 10.1 to 12. As expected, at pH 10.1, Mg^{2+} ions were only partially converted to $\text{Mg}(\text{OH})_2$. However, the extent of conversion was found to be dependent on the initial Mg^{2+} concentration, with magnesium recovery in Test 1 at 46.9% and 93.3%, and in Test 2 at 88.1% and 98.7% (at pH 10.1 and 12, respectively).

Figure 30c) presents the volume particle size distributions (V-PSDs) of $\text{Mg}(\text{OH})_2$ particles for Test 1 at different pH values (10.1 and 12) before and after sonication. Interestingly, slurry pH had no discernible influence on the V-PSDs, leading to the decision to compare V-PSDs of different tests at the same slurry pH (12) throughout the study. Figure 30d) shows the V-PSDs of $\text{Mg}(\text{OH})_2$ particles for Test 1 and Test 2 at pH 12 before and after sonication. Similar V-PSDs were obtained without sonication, with particle sizes ranging between 1-100 μm and 1-500 μm for Test 1 and 2, respectively. Significantly divergent V-PSDs emerged after sonication, revealing larger agglomerates (1-20 μm) for the high concentration (Test 2) compared to smaller aggregates/agglomerates observed for Test 1, predominantly in

the range of 0.08-1 μm . This disparity arose due to the lower concentration of the feed brine in Test 1, resulting in a more uniform distribution of local supersaturation. Indeed, the $\text{Mg}(\text{OH})_2$ precipitation process proceeded at a slower rate in Test 1, fostering the formation of weaker agglomerates of nanosized aggregates that can be easily disintegrated. In contrast, stronger agglomerates of nanosized aggregates formed in Test 2, requiring higher energy for breakdown, as discussed by Battaglia et al. [147].

Table 17: Re_{nozzle} , Magma density and Magnesium recovery for Tests 1 and 2.

| | Slurry pH | Q_{brine} [L/min] | Q_{NaOH} [L/min] | Re_{nozzle} | Magma density [g/L] | Mg^{2+} recovery [%] |
|----------|-----------|-------------------------------|------------------------------|---------------|---------------------------|-------------------------------------|
| 1 | 10.1 | 0.66 | 0.12 | 880 | 5.56 | 46.9 |
| | 12 | | 0.38 | | 9.65 | 93.3 |
| 2 | 10.1 | 0.66 | 0.59 | 880 | 27.1 | 88.1 |
| | 12 | | 1.10 | | 21.6 | 98.7 |

3.4.2 Effect of brine flow rate (Configuration A)

Utilizing the same operating configuration A outlined in Section 3.4.1 (Figure 28a)), the impact of the brine flow rate in the distribution section on the final product was explored. With a constant Mg^{2+} concentration of 0.24M, two distinct brine flow rates were investigated: 0.66 L/min and 2 L/min (Test 1 and Test 3, detailed in Table 15). These values resulted in different Re_{nozzle} values within the nozzle, as outlined in Table 18. As detailed in Paragraph 3.3.2, no sample was taken at pH 10.4 during Test 1 due to challenges encountered in stabilizing the reactor operating conditions. Figure 31a) depicts the sedimentation trends for Test 1 and Test 3 at two different pH values: 10.1 and 12.

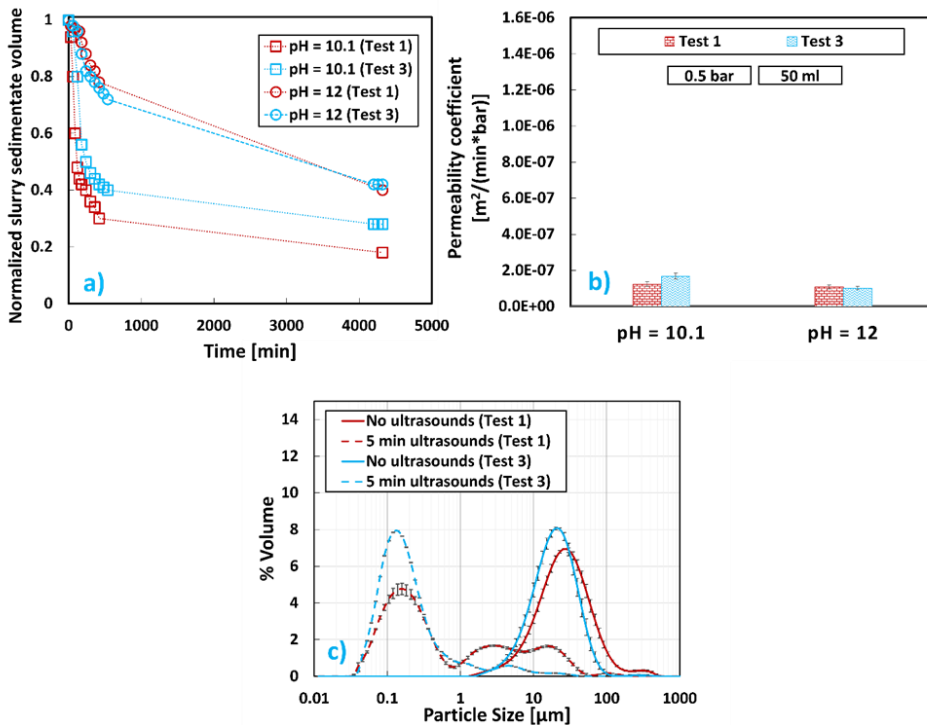


Figure 31: $Mg(OH)_2$ results at pH values 10.1 and 12.0 for brine flow rates equal to 0.66 L/min (Test 1) and 2 L/min (Test 3): a) sedimentation trend over time; b) Cake permeability coefficients; c) V-PSDs.

As observed, the brine flow rate had minimal influence on the sedimentation of the suspensions, with very similar trends noted. This similarity could be attributed to the $Mg(OH)_2$ suspensions being nearly identical, characterized by similar magma densities and nearly equal particle size distributions. Once again, suspensions at higher pH values exhibited slower sedimentation compared to those at lower pH. Regarding the filterability of the final product, comparable cake permeability coefficients were obtained at different operating brine flow rates. Similar to Paragraph 3.4.1, a decrease in permeability coefficient was observed with an increase in slurry pH. Notably, when comparing Test 1 with Test 3, the increased mixing in Test 3 had a noticeable effect only at the lowest pH of 10.1, resulting in slower settling but higher permeability (highlighting the opposite trend of these two parameters). Additionally, a higher magnesium recovery of 58.6% was achieved in

Test 3 compared to 46.9% in Test 1 at pH 10.1. However, negligible differences in all analysed parameters were observed during Test 1 and Test 3 at pH 12 (refer to Table 18).

Figure 31c) presents the Volume Particle Size Distribution (V-PSD), both before and after sonication, of the $Mg(OH)_2$ particles obtained for Tests 2 and 3 at a slurry pH of 12, as no significant differences in PSDs were observed at different pH values. Before sonication, varying brine flow rates did not lead to different initial V-PSDs, as they referred to $Mg(OH)_2$ agglomerates. Post-sonication, V-PSDs were centred around the order of magnitude of nanometres. Notably, lower brine flow rates in Test 1, resulting in lower Re_{bulk} values and a lower mixing degree in the reactor, led to a mixture of aggregates and agglomerates of particles characterized by diameters spanning from nanometres to micrometres. Conversely, in the higher mixing condition of Test 3, almost no micrometre-sized agglomerates were observed. Consequently, it can be concluded that operating at higher flow rates allows achieving a tighter, unimodal final Volume Particle Size Distribution of the product, centred more towards the order of magnitude of nanometres.

Table 18: Re_{nozzle} , Magma density and Magnesium recovery for Tests 1 and 3.

| | Slurry pH | Q_{brine} [L/min] | Q_{NaOH} [L/min] | Re_{nozzle} | Magma density [g/L] | Mg^{2+} recovery [%] |
|----------|-----------|------------------------|-----------------------|---------------|---------------------------|------------------------------|
| 1 | 10.1 | 0.66 | 0.12 | 880 | 5.56 | 46.9 |
| | 12 | | 0.38 | | 9.79 | 93.3 |
| 3 | 10.1 | 2.00 | 0.38 | 2650 | 6.89 | 58.6 |
| | 12 | | 0.80 | | 9.55 | 95.5 |

3.4.3 Effect of the hydrodynamic asset (Configurations A vs. B)

The MF-PFR was originally designed with the brine entering a distribution section and being injected into the alkaline solution in the adjacent section (configuration A as shown in Figure 28). To comprehensively explore the capabilities of the MF-PFR, tests were conducted to observe the effects on the final products when switching the positions of the brine and NaOH feeds (configuration B, as reported in Figure 28b)).

This arrangement involved injecting the alkaline reactant into the brine solution. A comparison of the produced $Mg(OH)_2$ suspensions was then performed, contrasting Test 3 and Test 4 (refer to Table 15). As depicted in Figures 32a) and 32b), switching the feed streams resulted in a corresponding change in sedimentation and filtration trends.

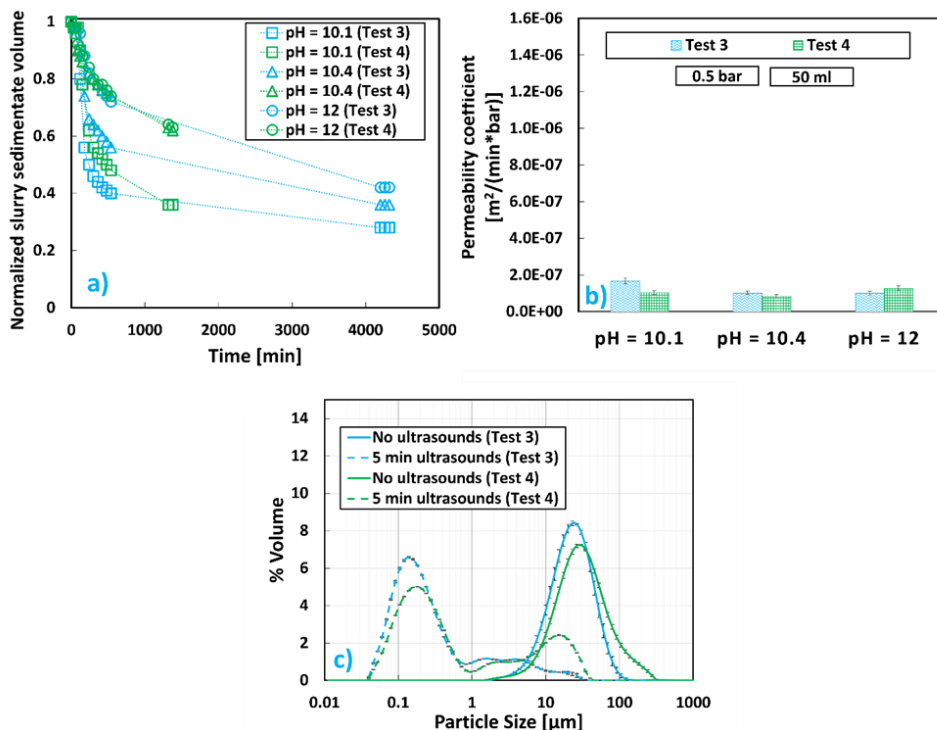


Figure 32: $Mg(OH)_2$ results at pH values 10.1, 10.4 and 12, brine flow rate equal to 2 L/min and initial Mg^{2+} concentration of 0.24 M for Configuration A (Test 3) and Configuration B (Test 4): a) sedimentation trend over time; b) cake permeability coefficients; c) V-PSDs.

This distinction was evident, particularly at the lowest pH value of 10.1, where the slower settling of Test 4 corresponded to a smaller cake permeability compared to Test 3. While at pH 10.4, the behaviour was relatively similar to that observed at pH 10.1, Test 4 outperformed Test 3 at pH 12 in both settling rate and cake permeability. This observation could be elucidated by examining the Reynolds numbers for both

bulk (refer to Table 16) and nozzle (refer to Table 19). The Re_{bulk} for Test 4 consistently exceeded that of Test 3, but it was only at pH 12 that the Re_{nozzle} for Test 4 became of the same order of magnitude as that of Test 3. The lower Re_{nozzle} for Test 4, attributed to less powerful jets injected into the host solution via the nozzles, resulted in poorer control of the final Volume Particle Size Distribution (V-PSD) for Configuration B (Test 4), as depicted in Figure 32c). This outcome could be attributed to an inhomogeneous supersaturation in the bulk, leading to the production of a more varied mixture of particle sizes. In fact, a narrower peak was achieved when applying ultrasound to the sample produced in Test 3.

Table 19: Re_{nozzle} , Magma density and Magnesium recovery for Tests 3 and 4.

| | Slurry pH | Q_{brine} [L/min] | Q_{NaOH} [L/min] | Re_{nozzle} | Magma density [g/L] | Mg^{2+} recovery [%] |
|----------|----------------------|-------------------------------------------|------------------------------------------|---------------------------------|------------------------------------|--------------------------------------------------|
| 3 | 10.1 | | 0.38 | | 6.89 | 58.6 |
| | 10.4 | 2.00 | 0.60 | 2650 | 8.31 | 77.2 |
| | 12 | | 0.80 | | 9.55 | 95.5 |
| 4 | 10.1 | | 0.29 | 390 | 6.30 | 51.6 |
| | 10.4 | 2.00 | 0.50 | 660 | 7.91 | 70.7 |
| | 12 | | 0.78 | 1040 | 9.42 | 93.6 |

3.4.4 Effect of $Mg(OH)_2$ suspension recirculation (Configuration C)

Configuration C (depicted in Figure 28c)) was also subjected to testing. This configuration involved partially mixing the $Mg(OH)_2$ slurry exiting the reactor with fresh alkaline solution and then redirecting it back to the inlet of the MF-PFR. As previously mentioned in Paragraph 3.3.2, no sample was taken during Test 1 at pH 10.4 due to challenges in stabilizing the reactor operating conditions. The recycling strategy significantly increased Re_{bulk} (refer to Table 16). Substantial differences were observed with this new configuration, as it can be seen in Figure 33.

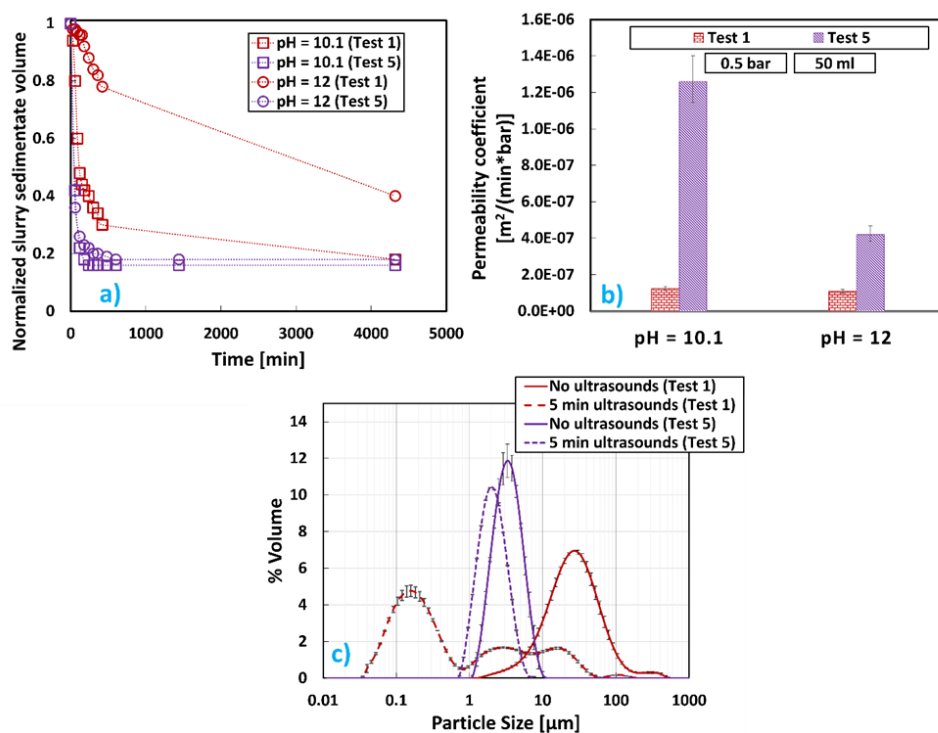


Figure 33: $Mg(OH)_2$ results at pH values 10.1 and 12.0, brine flow rate equal to 0.66 L/min and initial Mg^{2+} concentration of 0.24 M for Configuration A (Test 1) and Configuration C (Test 5): a) sedimentation trend over time; b) Cake permeability coefficients; c) V-PSDs.

$Mg(OH)_2$ suspensions, produced using the recycling strategy (Test 5), exhibited significantly faster sedimentation compared to cases where no recycling was employed (Test 1). Notably, for Test 5, there was no apparent pH influence on the sedimentation process of $Mg(OH)_2$ suspensions, in contrast to the trends observed in Paragraphs 3.4.1, 3.4.2, and 3.4.3. However, the impact of pH on cake permeability was evident, with the permeability at pH 12 being less than half that at pH 10.5 in Test 5, whereas this difference was barely appreciable for Test 1. Comparing the permeability of Test 5 with that of Test 1 revealed an increase of almost one order of magnitude when adopting the recirculation strategy, a noteworthy improvement for both sedimentation and filtration behaviours in industrial applications.

Moreover, as depicted in Figure 33c), the Volume Particle Size Distributions (V-PSDs) of Test 5 showed slight changes after ultrasound treatment, consistently

exhibiting a peak between 1-10 micrometres. This peak could be correlated with stronger agglomerates induced by the recycling strategy, confirming the faster sedimentation and filtration illustrated in Figures 33a) and 33b). Another notable advantage of the recycling strategy over Configuration A was evident: the ability to achieve 100% recovery at pH 12 (Test 5), surpassing the 93.3% recovery obtained with Test 1 (refer to Table 20).

Table 20: Re_{nozzle} , magma density and magnesium recovery for Tests 1 and 5.

| | Slurry pH | Q _{brine} [L/min] | Q _{NaOH} [L/min] | Re _{nozzle} | Magma density [g/L] | Mg ²⁺ recovery [%] |
|----------|-----------|-------------------------------|------------------------------|----------------------|---------------------------|-------------------------------------|
| 1 | 10.1 | 0.66 | 0.12 | 880 | 5.56 | 46.9 |
| | 12 | | 0.38 | | 9.79 | 93.3 |
| 5 | 10.1 | 0.66 | 0.24 | 880 | 6.75 | 65.8 |
| | 12 | | 0.90 | | 5.54 | 100 |

3.4.5 Effect of brine flow rate (Configuration C)

Utilizing the same recycling strategy outlined in Section 3.4.4, where the Mg(OH)₂ slurry produced is partially mixed with fresh alkaline solution and returned to the reactor, the impact of brine flow rate on the final product was assessed. Increasing the brine flow rate reaffirmed the previous observation, where the slower settling recorded in Test 6 corresponded to a larger permeability (refer to Figure 34). Once again, higher pH values were associated with lower permeability for both Test 5 and Test 6.

As mentioned earlier, the recycling strategy allowed for the control of the size distribution of the final product, yielding a Volume Particle Size Distribution (V-PSD) centred at 4-5 micrometres. Additionally, as reported in Table 21, the adoption of the recycling strategy had a significant influence on magnesium recovery at pH values of 10.4. Notably, a 100% recovery was achieved compared to the highest value of 77% obtained in Test 3 at the same pH value. This improvement was

attributed to the use of the recycle of the outlet stream and its mixing with fresh NaOH solution in the recycle stream.

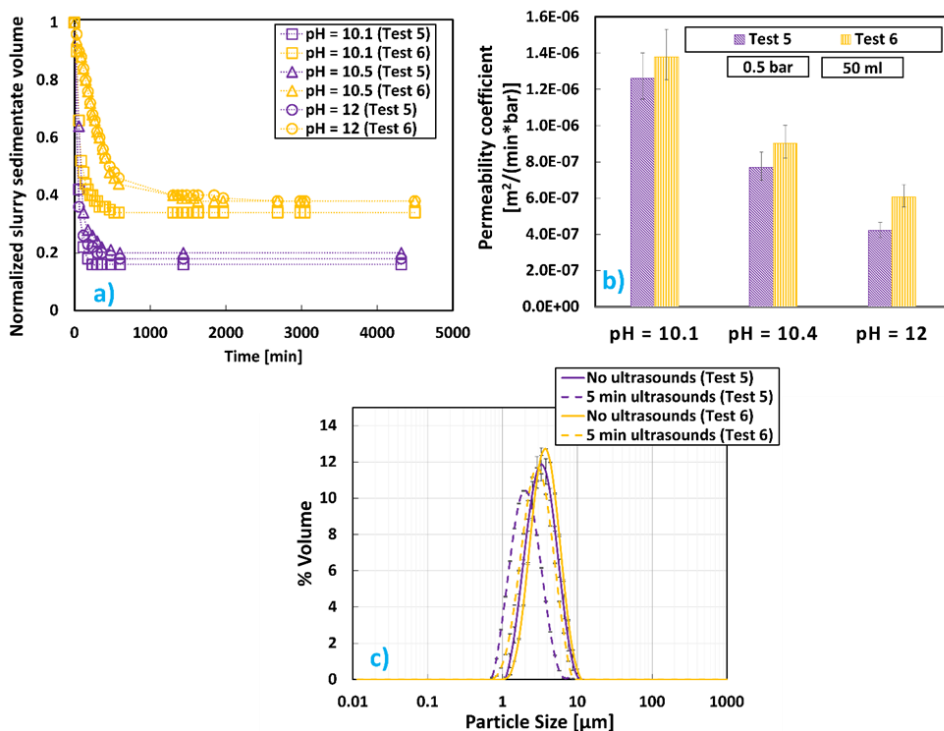


Figure 34: Mg(OH)₂ results at pH values 10.1, 10.4 and 12.0 for brine flow rates equal to 0.66 L/min (Test 5) and 2 L/min (Test 6): a) sedimentation trend over time; b) Cake filtration permeability coefficients; c) V-PSDs.

Table 21: Re_{nozzle} , Magma density and Magnesium recovery for Tests 5 and 6.

| | Slurry pH | Q_{brine} [L/min] | Q_{NaOH} [L/min] | Re_{nozzle} | Magma density [g/L] | Mg ²⁺ recovery [%] |
|---|-----------|---------------------|--------------------|---------------|---------------------|-------------------------------|
| 5 | 10.1 | 0.66 | 0.24 | 880 | 6.75 | 65.7 |
| | 10.4 | | 0.44 | | 7.60 | 100 |
| | 12 | | 0.90 | | 5.54 | 100 |
| 6 | 10.1 | 2.00 | 0.80 | 2650 | 8.52 | 85.2 |
| | 10.4 | | 0.90 | | 9.65 | 100 |
| | 12 | | 1.20 | | 8.75 | 100 |

3.5 Conclusions

The precipitation process of $\text{Mg}(\text{OH})_2$, from synthetic solutions was investigated using a novel MF-PFR crystallizer designed for pilot-scale $\text{Mg}(\text{OH})_2$ production. Various reactor parameters were explored to understand the impact of (i) initial Mg^{2+} concentrations, simulating those found in waste Mg-rich solutions from saltworks bitterns (Mg^{2+} 1.0 M) and desalination waste brines (Mg^{2+} 0.24 M); (ii) different reactant flow rates; and (iii) the implementation of a product recycling strategy (seeded crystallization). The main corresponding outcomes were:

(i) Higher initial Mg^{2+} concentration (1.0 M) in the feed brine resulted in the production of larger and more robust agglomerates of $\text{Mg}(\text{OH})_2$ particles compared to lower initial concentrations (0.24 M). Specifically, after applying ultrasounds and introducing a dispersant agent, micro-sized $\text{Mg}(\text{OH})_2$ agglomerates/aggregates were observed in the case of 1.0 M Mg^{2+} solutions, while nano-sized and micro-sized particles were detected for the 0.24 M case;

(ii) No significant influences were observed on sedimentation trends, filtration times, and granulometry of the final product when employing different reactant flow rates, irrespective of the reactor configurations. However, $\text{Mg}(\text{OH})_2$ suspensions produced with over-stoichiometric NaOH amounts, resulting in a final suspension pH of 12, exhibited lower sedimentation rates and cake permeability coefficient values in most cases;

(iii) A pivotal aspect was the adoption of a product recycling strategy favouring a seeded crystallization process. Specifically: (a) $\text{Mg}(\text{OH})_2$ suspensions sedimented up to 4 times faster than those produced without product recycling; (b) the cake permeability coefficient increased, reaching values up to one order of magnitude higher than those of suspensions produced without product recycling.

In summary, the recycling strategy (iii) emerges as a critical parameter with considerable importance in addressing filterability and sedimentation challenges in

large-scale $\text{Mg}(\text{OH})_2$ suspensions production, especially those precipitated using NaOH solutions.

SECTION 3: Nanofiltration, a pre-treatment step to enhance magnesium purity and recovery

Building on the insights gained in the previous section, an operational strategy for the MF-PFR was identified, in order to enhance the properties of $\text{Mg}(\text{OH})_2$ recovered from Mg-containing brines in terms of sedimentation rates, filterability, and particle size. However, to further improve the revenue of $\text{Mg}(\text{OH})_2$ produced within MLD schemes for seawater/brine treatment, two additional aspects had to be taken into full account: purity and recovery. These properties are significantly influenced by the characteristics of the MF-PFR feed solution. Therefore, Section 3 was devoted to investigating the potential of NF as a pre-treatment step to enhance both the purity and recovery of $\text{Mg}(\text{OH})_2$ obtained through the MF-PFR. This investigation involved the synthesis of novel NF membranes, experimental exploration of alternative commercial NF membranes, and a detailed techno-economic analysis, entirely supported by **Publication 4** [148], **Publication 5** [149] and **Publication 6** [150], respectively.

Literature review

In recent years, the pursuit for a sustainable and seemingly endless supply of raw minerals and metals has become a critical challenge [151]. With the global population expected to increase [152], the demand for raw materials is expected to double by 2060, resulting in a 70% surge in waste production by 2050 [86]. Relying solely on land-based mining is no longer a viable option. Land mining encounters significant obstacles: (i) the gradual depletion of high-grade mineral reserves [100], (ii) escalating water and energy requirements for extracting minerals from low-grade ores and (iii) the diminished purity of the final products recovered from hydrometallurgical facilities [153]. These issues contribute to amplified costs and environmental concerns [10]. In addition, certain raw materials have been classified as “critical” (CRMs) and/or “strategic” by the European Union (EU) [101], playing a crucial role in the socio-economic structure of Europe [91]. To tackle these

challenges, strategic initiatives (i.e., Green Deal action plan [103]) have been introduced. These initiatives aim to embrace a circular economy approach, recovering CRMs from sustainable unconventional sources, primarily from wastes. Moreover, to foster collaboration among various stakeholders in this context, key European networks have been established, such as the European Innovation Partnership (EIP) on Raw Materials and the EIT Raw Materials Platform of the European Institute of Innovation and Technology (EIT). Furthermore, there are over 26 different EU projects focused on data analysis and the management of raw materials flow [154]. Among the several initiatives, aimed at recovering CRMs from secondary sources, seawater mining has emerged as an appealing option [20]. This is due to the comprehensive presence of elements in the ocean [151], spanning a majority of the periodic table [21]. The abundance of certain elements ($\text{Na}^+ > \text{Mg}^{2+} > \text{Ca}^{2+}$, K^+ (for cations) and $\text{Cl}^- > \text{SO}_4^{2-} > \text{HCO}_3^- > \text{Br}^-$ (for anions) [155]), makes their extraction economically possible. For instance, the extraction of NaCl from seawater has been practiced since ancient times due to its abundance [156]. However, certain elements, named as “trace elements”, hold higher economic value but are present in such low concentrations in seawater (below 1 mg/L) that their retrieval is currently not economically feasible. Figure 35 illustrates the range of elements recoverable from seawater, providing their average concentrations (in mg/L) alongside their corresponding market values (in €/kg). It is worth mentioning that the economic feasibility threshold for seawater mining has exhibited slight discrepancies in various studies documented in the literature. For example, whilst Loganathan et al. [20] supported the feasibility of Indium recovery, Shahmansouri et al. [114] excluded such element from the viable extraction region. Alongside the major components, certain 'trace elements' such as Strontium (Sr), Boron (B), Lithium (Li), and Rubidium (Rb) present potential for extraction from seawater. In summary, to render mineral extraction from seawater viable, a first an important issue that has to be necessarily addressed is the concentration of such minerals, accompanied also by the issue of selective separation in order to potentially recover

high purity products in downstream technologies (i.e., downstream crystallization steps).

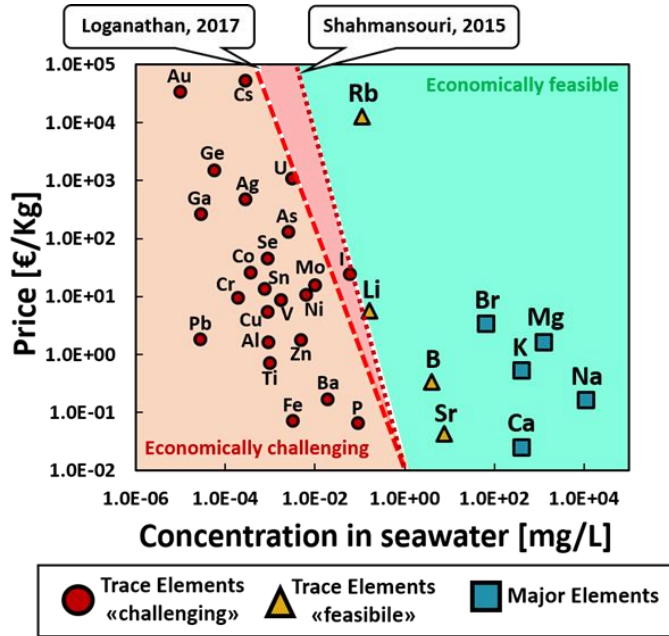


Figure 35: Economic feasibility of mineral recovery via seawater mining based on specific price [€/Kg] vs. concentration [mg/L] of elements present in seawater. Adapted from Sharkh et al. [151].

For this reason, numerous studies have redirected their focus towards valorising brine derived from seawater desalination (i.e. Seawater Reverse Osmosis brine (SWRO brine)). This is attributed to its concentration being nearly twice as high as that of seawater [4] and the advantage of pumping costs being covered by the water production stage. Bearing in mind just the EU, more than 7.3 million m³ of SWRO brine are produced every day, considering that 65% of the EU's desalination plants deal with seawater and assuming that all these plants are based on RO technology [157]. In other words, this means that around 2665 million m³ of SWRO brine are potentially available each year in the EU, demonstrating to be an appealing abundant source for resource recovery. Moreover, the valorisation of brine is considered more attracting due to the concurrent mitigation of (i) the high costs associated with brine

management [9] and (ii) the environmental impact resulting from brine discharge [125].

These appealing advantages have positioned brine valorisation as a promising alternative source for minerals recovery, aligning with the principles of circular economy [124]. In recent years, within this context, the scientific community has introduced several resource recovery schemes focusing on valorising seawater and brines. These schemes adopt either an MLD or ZLD approach, with the aim of maximizing mineral recovery whilst minimizing the volume of waste discharged into the environment [9]. ZLD and MLD approaches incorporate various processes, including membrane-based technologies, thermal-based methods, and crystallization processes, in a carefully orchestrated manner. However, a significant challenge arises when the employed technologies yield a relatively low quantity of recovered minerals, accompanied by low purity. These limitations can result in insufficient revenues, failing to offset the substantial capital and operating costs associated with MLD/ZLD schemes, rendering them economically unfeasible [148].

To address this issue, a selective pre-treatment step is deemed essential [57]. In recent literature, numerous resource recovery schemes in literature have integrated a pre-treatment step employing NF [158]. NF has gained prominence as a pivotal technology for brine valorisation within the scientific community [148]. This pressure-driven membrane process exhibits higher selectivity compared to RO [159]. NF membranes present a pore-size ranging from 0.5 nm to 2 nm [160], and through the combined effects of steric exclusion, Donnan exclusion and dielectric exclusion, they demonstrate high selectivity towards multivalent ions [49]. The process efficiently provides two separate streams from a single solution: (i) a permeate stream rich in monovalent ions (i.e., Na^+ , K^+ , Cl^-) and (ii) a retentate stream rich in multivalent ions (i.e., Mg^{2+} , Ca^{2+} , SO_4^{2-}) [160]. Attractive features of NF including low operating pressure, low energy consumption and high separation selectivity [161], have positioned it as a preferred pre-treatment step in most MLD/ZLD schemes. Numerous recent projects, focused on the development of innovative MLD/ZLD schemes for seawater/SWRO brine valorisation, have indeed integrated

NF as a crucial pre-treatment step. For example, the EU-funded project, Sea4Value [162], included NF as a pre-treatment step in a treatment chain. This process generated: (i) a multivalent ions-rich stream which underwent advanced membrane crystallization to recover magnesium hydroxide and water, and (ii) a stream rich in monovalent ions, from which water was extracted via an advanced MED unit. Downstream technologies employing selective membranes and adsorption modules facilitated the recovery of specific trace elements. Another EU-funded project, Water Mining [144], proposed to employ NF to pre-treat directly seawater in Lampedusa, Italy. Here, the NF retentate underwent (i) reactive crystallization for the recovery of magnesium and calcium hydroxides and (ii) EDBM for chemical production. Freshwater and NaCl were recovered from the NF permeate through MED and solar ponds, respectively. Besides EU funded projects, major corporation companies in the Middle East have invested recently in the development of a large pilot plant to valorise seawater using NF as a pre-treatment step. For example, Al-Amoudi et al. [163] report the development of a large-scale valorisation plant in Ummlujj, Saudi Arabia. This plant featured an NF unit (feed capacity of 16 m³/h) for the separation of monovalent and multivalent ions, producing two concentration steps: (i) the first comprising RO, HPRO and 2 stage OARO meanwhile the other step consisted of OARO fed by the NF retentate. Ultimately, freshwater was recovered alongside two concentrated streams: (i) a monovalent-rich stream with a salinity of 130 g/L and (ii) a multivalent-rich stream with a salinity of 83 g/L. Overall, such large projects demonstrate the importance of using NF in current resource recovery schemes. However, it is important the membrane performances of the NF plants treating seawater and SWRO brine.

Table 22 provides a comprehensive compilation of all the existing experimental studies on the performance of NF membranes in concentrating seawater or desalination brine within an MLD/ZLD context. However, a notable pattern in Table 22 is the focus on a limited set of NF membranes (i.e., NF90, NF270, and DL) in previous studies.

In summary, it is evident from the literature that all works based on NF in ZLD/MLD schemes have directly considered commercial polymeric membranes.

Table 22: List of experimental works in literature concerning nanofiltration application for seawater/SWRO brine treatment.

| Author | Ref. | NF membranes | Feed solution | | Rejection Performances [%] | | | | | | | | | | | Experimental conditions | |
|------------------|-------|-----------------|---------------|------------|----------------------------|----------------|------------------|------------------|-----------------|-----------------|-------------------------------|-------------------------------|---------------------------|-----------------|-----------------|-------------------------|---------------------------------------------|
| | | | Seawater | SWRO brine | Major Elements | | | | | | | | "Feasible" Trace Elements | | | | |
| | | | | | Na ⁺ | K ⁺ | Mg ²⁺ | Ca ²⁺ | Cl ⁻ | Br ⁻ | HCO ₃ ⁻ | SO ₄ ²⁻ | B | Li ⁺ | Rb ⁺ | | Sr ²⁺ |
| Hilal et al. | [164] | • NF90 | ✓ | - | 31.5 | 32.7 | 62.9 | 62.1 | 37.5 | - | - | 66.5 | - | - | - | - | P = 9 bar |
| | | • NF270 | ✓ | - | 9.7 | 12.8 | 52.7 | 35.3 | 12.7 | - | - | 86.5 | - | - | - | - | |
| Liu et al. | [165] | • DL | - | ✓ | 4.0 | 8.0 | 93.0 | 60.0 | 12.0 | - | 35.0 | 100.0 | - | - | - | - | P = 14 bar (was varied up to 32 bar) |
| Ali | [166] | • NF-2012-250 | - | ✓ | 45.7 | - | 98.4 | 90.7 | 54.1 | - | 45.2 | 51.4 | - | - | - | - | P = 7 bar (maximum pressure) |
| Bindels et al. | [167] | • NF270 | - | ✓ | 16.0 | - | 84.0 | 60.0 | 18.0 | - | - | 98.0 | - | - | - | - | P = 20 bar (was varied up to 35 bar) |
| | | • NE4040 | - | ✓ | 15.0 | - | 96.0 | 85.0 | 18.0 | - | - | 100.0 | - | - | - | - | |
| Song et al. | [168] | • ESNA3 | ✓ | - | - | - | 73.3 | 44.4 | - | - | - | 99.8 | - | - | - | - | P = 15 bar |
| Al-Amoudi et al. | [43] | • PRO-XS2 | ✓ | - | 18.0 | - | 93.5 | 71.4 | 27.4 | - | - | 99.4 | - | - | - | - | P = 19.3 bar (permeate recovery = 85.0%) |
| Turek et al. | [169] | • NF270 | ✓ | - | - | - | 65.7 | 50.0 | 13.0 | - | - | 84.0 | - | - | - | - | P = 14 bar |
| | | • NF200 | ✓ | - | - | - | 58.9 | 50.2 | 24.3 | - | - | 66.0 | - | - | - | - | |
| | | • SR2 KOCH | ✓ | - | - | - | 81.0 | 65.7 | 23.7 | - | - | 95.0 | - | - | - | - | |
| Su et al. | [170] | • NF90 | ✓ | - | - | - | 99.6 | 99.5 | - | - | - | 99.6 | - | - | - | - | P = 14 bar (was varied up to 35 bar) |
| | | • NF270 | ✓ | - | - | - | 87.5 | 72.0 | - | - | - | 99.0 | - | - | - | - | |
| | | • NF200 | ✓ | - | - | - | 88.0 | 56.0 | - | - | - | 99.0 | - | - | - | - | |
| | | • DL | ✓ | - | - | - | 69.0 | 53.0 | - | - | - | 97.0 | - | - | - | - | |
| Reig et al. | [171] | • NF270 | - | ✓ | 9.0 | 4.0 | 62.0 | 44.0 | 9.0 | - | - | 79.0 | - | - | - | 47.0 | P = 12 bar (was varied up to 20 bar) |
| Figueira et al. | [172] | • NF270 | - | ✓ | 9.60 | 4.85 | 75.4 | 53.4 | 15.4 | - | 44.4 | 98.6 | 3.84 | 5.46 | 10.6 | - | P = 14 bar (was varied up to 30 bar) |
| | | • Fortlife X-CN | - | ✓ | 14.0 | 19.7 | 91.2 | 80.2 | 24.3 | - | 39.0 | 97.4 | 8.90 | 6.02 | 22.7 | - | |
| | | • PRO-XS2 | - | ✓ | 12.4 | 6.70 | 89.1 | 65.4 | 17.7 | - | 45.3 | 98.4 | 0.00 | 1.06 | 6.64 | - | |

Furthermore, these experimental studies predominantly focused on reporting the rejection capacity of a limited number of major components found in seawater or SWRO brine, creating a substantial gap in understanding the recovery of valuable trace elements. Moreover, the majority of these studies have relied on the commonly used NF270 commercial membrane. Only a few investigations have explored alternative commercial membranes, focusing on ion rejections for various components found in seawater and brine under distinct operational conditions.

Commercial polymeric NF membranes, owing to their fabrication material, typically possess a neutral or negative surface charge when employed in seawater treatment or similar applications [173–175]. It is only in highly acidic environments, specifically at a pH below 4, that they exhibit a positive surface charge. It has been reported in literature that a negative surface charge is not ideal for certain applications requiring high multivalent cationic selectivity, such as salt recovery from textile effluents and heavy metal recovery from industrial wastewater [173]. This is also pertinent to the recovery of high-value minerals from seawater and brines.

As mentioned earlier, NF is frequently utilized as a pre-treatment step in ZLD/MLD systems, providing concentrated feed streams for its downstream technologies [44]. However, employing positively charged NF membranes could potentially yield an NF retentate stream rich in magnesium and calcium, offering several advantages. These include (i) achieving higher purity products when the retentate undergoes a downstream crystallization process and (ii) reducing the need for purification technologies, thus reducing the capital and operating costs of ZLD/MLD systems.

Over the past decade, various attempts have been made and proposed in literature to synthesize positively charged NF membranes. Table 23 provides an overview of selectivity and permeation performances of these novel membranes.

Table 23: Selectivities and water permeabilities of novel positively charged thin film NF membranes in literature.

| Ref. | Substrate/ Active layer | Permeability [L m ⁻² h ⁻¹ bar ⁻¹] | Feed Concentration | Operating Pressure [bar] | Rejection [%] | | | |
|-------|----------------------------|---------------------------------------------------------------------------|--------------------------|--------------------------------|-------------------|-------------------|------|---------------------------------|
| | | | | | MgCl ₂ | CaCl ₂ | NaCl | Na ₂ SO ₄ |
| [176] | PES/ PEI + TMC | 3.06 | 500 mg L ⁻¹ | 8 | 95 | - | 80 | 75 |
| [177] | PAN/ PEI + ECH | 1.67 | 2000 mg L ⁻¹ | 5 | 93 | - | 60 | - |
| [178] | PSF/ pDA | 13.90 | 0.01 mol L ⁻¹ | 6 | 65 | 70 | 25 | 30 |
| [179] | PAN/ catechol + PEI | 2.92 | 2000 mg L ⁻¹ | 5 | 85 | - | 48 | 55 |
| [180] | PSF/ DADMAC | 12.00 | 1000 mg L ⁻¹ | 5 | 90 | 92 | 50 | 15 |
| [181] | PES/ PEI + PIP | 5.20 | 2000 mg L ⁻¹ | 4 | 97 | 98 | 49 | 69 |
| [182] | PVC/ PIP + TMC | 8.70 | 1000 mg L ⁻¹ | 3.5 | 99 | 98 | - | 96 |
| [183] | PES/ PEI + TMC | 17.00 | 1000 mg L ⁻¹ | 5 | 95 | - | 40 | 55 |
| [184] | PSF/ DMC | 7.50 | 1000 mg L ⁻¹ | 5 | 92 | - | 62 | 22 |
| [185] | PAN/ HACC | 1.06 | 1000 mg L ⁻¹ | 5 | 95 | 95 | 28 | 60 |
| [186] | PEKC/ PAMAM + TMC | 10.00 | 1000 mg L ⁻¹ | 5 | 96 | - | 73 | 58 |
| [187] | PSF/ PDMAEMA | 1.00 | 1000 mg L ⁻¹ | 6 | 98 | - | 78 | 66 |
| [188] | PSF/ Chitosan + MOF | 3.50 | 1000 mg L ⁻¹ | 5 | 93 | 86 | 30 | 25 |

Acronyms of the materials employed for the novel NF membranes are reported in the Nomenclature section

It is important to highlight that none of the newly synthesized positively charged NF membranes found in the literature (listed in Table 23) have been (i) specifically designed and applied for mineral recovery from seawater/brine and (ii) characterized

by sufficiently high multi-cationic selectivity, often exhibiting significant membrane rejection for sodium chloride or sulphate-based salts.

All in all, in the broader context of NF being employed for high-value resource particularly magnesium recovery from seawater/desalination brines, several gaps still exist in the current literature. Firstly, the “novel synthesized positively charged” NF membranes proposed in literature, which could potentially enhance the overall performance of MLD/ZLD schemes have never been tested for seawater/brine valorisation. Additionally, these membranes lack sufficient high magnesium selectivity compared to other ions present in seawater. Secondly, a gap exists regarding commercial NF membranes. More specifically, in the context of seawater/brine valorisation, most experimental works in literature are confined to the study of a limited number of commercial NF membranes (i.e., NF270, NF90 and DL), providing little information on the global rejection performance of such membranes. Therefore, this gap is compounded by (i) the limited information on various other new commercially available NF membranes (developed to enhance multivalent/monovalent selectivity) and (ii) the absence of data on the rejection of trace elements in seawater and SWRO brines. Finally, a third significant gap in literature concerns the absence of studies devoted to thoroughly investigating NF technology operation in order to maximize the potential revenue from extracting magnesium from seawater and brines.

To address all these gaps, Section 3 of this PhD thesis aims to contribute to the literature by introducing (i) novel synthesized NF membranes with high magnesium selectivity, (ii) alternative highly selective commercial NF membranes for seawater/brine valorisation and (iii) results of a detailed techno-economic analysis devoted to increasing the revenue from magnesium recovery in seawater/brines. Specifically:

Chapter 4 (supported entirely by **Publication 4** [148]) introduces a novel positively-charged NF membrane, purposely synthesized to selectively extract magnesium

from seawater and waste brines in an MLD/ZLD context. The synthesized membrane was fully characterized, optimized and tested with single salt solutions. The performances of the optimized NF membrane were then compared with those of commercial NF membranes in the context of seawater/brine valorisation.

Chapter 5 (supported entirely by **Publication 5** [149]) examines the performance of five distinct commercial NF membranes (NF90, NFS, NFX, VNF1 and DK) in the recovery of both major and minor components, four of which have never been tested before for seawater/desalination brine valorisation. The membranes were tested in a closed-loop configuration to identify their optimal operating pressure, and their performances were compared in terms of permeability and multi-cationic selectivity. Experimental data were fitted with the Solution-Electro-Diffusion-Film (SEDF) mathematical model to determine the membrane ion permeances.

Chapter 6 (supported entirely by **Publication 6** [150]) focuses more precisely on the performances of 2 of the 5 previous membranes (NFX and VNF1). Such membranes were fully characterized and underwent experimental testing in an open loop configuration. Experimental data was fitted with the SEDF model to predict further membrane parameters, needed for a thorough techno-economic analysis.

4 “Metal-Organic-Framework-based nanofiltration membranes for selective multi-cationic recovery from seawater and brines”

In this chapter, a novel positively charged NF membrane was intentionally synthesized for the selective recovery of magnesium from seawater and waste brines within an MLD/ZLD context. The innovative membrane consisted of: (i) a highly permeable polysulfone ultrafiltration substrate and (ii) an active layer incorporating a positively charged metal-organic-framework (MOF) and a highly hydrophilic metal-oxide nanofiller within a chitosan matrix. One specific MOF, namely NH₂-MIL-101(Al), a member of the MIL-101 family known for its high specific surface area and microporosity was used in the current study [189]. NH₂-MIL-101(Al) was selected due to its high charged metal centre with cationic functional groups (amino groups), ensuring a consistently high positive surface charge across a broad pH range- an advantage not shared by other MOFs introduced in previous NF membrane fabrication [188,190–192]. Chitosan played a crucial role as a binder between the active layer and substrate. Its selection was motivated by its attributes as a low-cost, biodegradable and anti-microbial material [193]. Additionally, a nanofiller was incorporated to enhance the separation performance of the new membrane. Dense (non-porous) nanofillers, such as TiO₂, amorphous SiO₂, silver, and carbon quantum dots (CQDs), have been recently proposed in literature to improve the permeability-selectivity trade-off of polymeric NF and RO membranes [194–196] and provide antifouling properties [197,198]. However, ZnO was chosen for this study due to (i) its positive charge in aqueous solutions within a wide pH range, and (ii) hydrophilic properties [199,200]. These characteristics provide the potential to increase Mg²⁺ rejection without compromising the membrane permeability. Moreover, ZnO nanoparticles are cost-effective compared to other nanofillers and exhibit low toxicity, making them suitable as active components in food packaging [201,202] new NF membrane was optimized varying the loading of ZnO/NH₂-MIL-101(Al) within the active layer. Lab-scale filtration tests were conducted using both single salt solutions and synthetic seawater and brine. Results highlighted superior selectivity towards magnesium and calcium when compared to the commercial and lab-made NF membranes documented in literature.

4.1 Experimental

4.1.1 Materials

2-Aminoterephthalic acid (Sigma-Aldrich, purity = 99%), AlCl₃·6H₂O (Alfa Aesar, 98%), and dimethylformamide (DMF, VWR chemicals, HPLC grade, > 99.9%) were utilized in synthesizing the MOF nanocrystals. Acetone and methanol (HPLC grade, ≥ 99.9%), used for MOF washing, were provided by VWR Chemicals. NaOH pellets were sourced from VWR Chemicals. Chitosan (Aldrich, medium molecular weight),

ZnO nanopowder (Sigma Aldrich Merck, particle size < 100 nm), and acetic acid (Fisher Chemical, > 99.7%) were employed in fabricating the selective active layer of the NF membranes. NaCl (Chemsolute, 99%), Na₂SO₄ (Sigma Aldrich, > 99.0%), MgCl₂·6H₂O (PanReac AppliChem, pharma grade), and CaCl₂·2H₂O (VWR chemicals, pharma grade) were used to assess the salt rejection of the NF membranes introduced in this study. Deionized water (resistivity > 18 MΩ) was used consistently throughout MOF syntheses, membrane fabrication, and the preparation of salt solutions for all filtration tests. Additionally, two commercial NF membranes (models: NF90 and NF270) were procured from Dupont for filtration tests and comparative analysis.

4.1.2 MOF synthesis

NH₂-MIL-101(Al) synthesis was conducted using the solvothermal method [203]. In this procedure, 0.51 g of AlCl₃·6H₂O and 0.56 g of 2-aminoterephthalic acid were physically mixed in 30 mL of DMF and stirred for 30 minutes. The resulting solution was transferred to a Teflon-lined autoclave and subjected to 72 hours of heating at 130°C in a static oven (Memmert UF 30). After cooling to room temperature, the yellow powder obtained was vacuum-filtered and subjected to three washes with acetone. To eliminate residual organic species trapped within the pores, the remaining powder underwent an activation process, involving refluxing the MOF in boiling methanol overnight. Subsequently, the MOF was dried in a static oven for 16 hours at 200°C.

4.1.3 Membrane fabrication

A polysulfone (PSF) ultrafiltration membrane, featuring a molecular weight cut-off of 25,000 Da and obtained from Alfa Laval (model: DSS-GR60PP), served as the substrate for the innovative NF membranes. Prior to coating, the substrate underwent pre-treatment by immersing it in a 1M NaOH solution for 1 hour. This step aimed to (i) activate the substrate surface, facilitating bonding between the substrate and the active layer, and (ii) remove glycerine from the pores of the commercial UF

membrane. Subsequently, the pre-treated substrate underwent three rinses with deionized water.

Once the substrate pre-treatment concluded, the NF membranes were fabricated by solvent-casting the coating solution onto the substrate using a spiral bar-coater (procured from TQC) with a thickness of 50 μm . The dispersions for the coating of the membrane active layers were prepared as follows: chitosan was dissolved (20% wt) in a 2%wt aqueous acetic acid solution. ZnO nanopowder and the MOF were then gradually added to the chitosan solution under stirring conditions. Active layers with different compositions, as detailed in Table 24, were prepared to subsequently investigate the influence of ZnO and MOF loadings on the membranes' structure, selectivity, and permeability.

The active layer dispersions were stirred magnetically for 24 hours to ensure a homogeneous coating. Subsequently, they underwent a 30-minute treatment in an ultrasonic bath to eliminate any gas that may affect the coating procedure. Finally, the coated membranes were dried in a static oven at 80°C for 2 hours, completing the solvent evaporation process and consolidating the active layer.

Table 24: Composition of the membranes fabricated and tested in this study.

| Name | Weight composition (w/w) | | |
|--------|--------------------------|----------------------------------|--------------|
| | ZnO [%] | NH ₂ -MIL-101(Al) [%] | Chitosan [%] |
| CMZ-0 | 0 | 80 | 20 |
| CMZ-20 | 20 | 60 | 20 |
| CMZ-35 | 35 | 45 | 20 |
| CMZ-60 | 60 | 20 | 20 |
| CMZ-80 | 80 | 0 | 20 |

4.1.4 Membrane Characterization

X-ray diffraction (XRD) analyses were conducted to verify the crystallographic structure of both the MOF and ZnO using an Empyrean diffractometer (Malvern Panalytical) equipped with monochromator Cu K α radiation (1.5406 Å). The X'Pert HighScore Plus software (Malvern Panalytical) and associated references were employed for analysing the diffractograms of crystal phases (ZnO hexagonal and cubic, ZnS hexagonal, and MIL-53), with the exception of the MIL-101 phase peaks, which were determined by referencing relevant literature [203].

The size distribution and ζ -potential of nanopowder and coating dispersions were examined through dynamic light scattering (DLS) using a Zetasizer Nano ZS (Malvern Instruments). Particle size measurements were performed on MOF and ZnO dispersions at a concentration of 0.1 mg L⁻¹. For ζ -potential measurements, coating dispersions were diluted 1:250 in deionized water, and the pH was adjusted using NaOH or HCl. Zeta-potential was measured within the pH range of 3-12, and each sample at a specific pH value was analysed three times, with the final average value considered.

Attenuated Total Reflectance - Fourier-transform infrared (ATR-FTIR) spectroscopy analyses (Bruker Tensor II) were conducted to confirm the presence of characteristic moieties of Chitosan, ZnO, and the MOF (NH₂-MIL-101(Al)) in the active layer of the NF membrane. Each ATR-FTIR spectrum comprised 30 scans at a resolution of 4 cm⁻¹, covering a wavenumber range from 4000 to 350 cm⁻¹.

The morphologies of the MOF powder and coated membranes were analysed through Field Emission Scanning Electron Microscopy (FE-SEM) (Zeiss 1540XB). Gold was sprayed on the sample surface prior to the analysis, and images were taken at a magnification of 180,000. EDX spectroscopy accompanied the FE-SEM to identify the active layer by determining the concentration of relevant elements (C, S, O, Zn, Al).

To investigate the impact of ZnO on the surface hydrophilicity of the NF membrane, contact angle measurements were performed using a contact angle meter (Biolin Scientific - Attension Theta Lite). Membrane samples were air-dried before analysis, and the measurements involved a sessile drop of deionized water with a diameter of 5 mm. The contact angle camera presented the following parameters: Exposure = 1400, Gain = 1110, Gamma = 2793. Three different readings were taken per sample, and for each reading, 40 images were captured per second for 30 seconds. The average value of the measurements was considered for each membrane sample.

4.1.5 Filtration tests

The separation performance of the NF membranes was assessed based on salt rejection and permeability. Experimental tests were conducted at 5 bar and room temperature, utilizing a crossflow experimental setup depicted schematically in Figure 36.

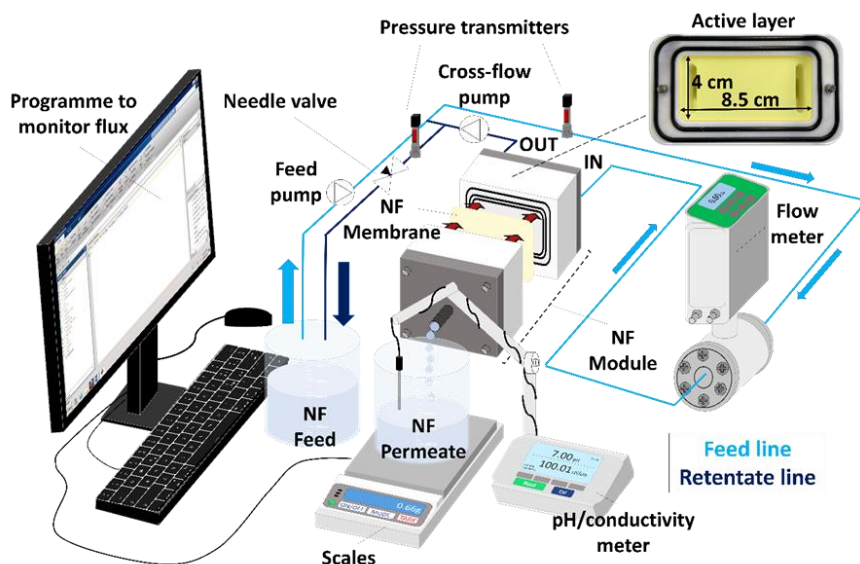


Figure 36: Conceptual scheme and main components of the flat sheet nanofiltration experimental set-up used in this study.

A 3 L solution was sent by a dosing pump (Wanner Hydracell dosing pump, model G03) to a flat sheet stainless steel NF module (Sterlitech). The flow rate of the feed solution entering the module was measured using a flow meter (Siemens, Sitrans F M Magflo MAG5000). The permeation active area of the NF module was 33.4 cm². In the tests, the NF retentate circulated through a crossflow rotary lobe pump (Hilge, Grundos, model Novalobe 10). A portion was recycled back to the NF module, while the remaining retentate was returned to the feed solution. The transmembrane pressure was monitored with two pressure transmitters (Danfoss, model MBS 4010) positioned on the feed pipeline and the retentate pipeline. The operating pressure was tuned using a needle valve on the retentate pipeline. The NF permeate, on the other hand, was collected in a beaker on an analytical scale (Kern, PCB). A simple algorithm was implemented in Matlab to record and compute the NF transmembrane permeability (Equation 25) on the basis of the permeate mass collected over a specific period, as monitored by the scale.

$$\Phi = \frac{V}{A * t * (\Delta P - \Delta \Pi)} = \frac{J_v}{(\Delta P - \Delta \Pi)} = \frac{c_{w0}^m D_w V_w}{\rho_w L * R * T} * 3600 * 10^{-5} \quad (25)$$

Where Φ is the permeability of the NF membrane [L m⁻² h⁻¹ bar⁻¹], V is the volume of NF permeate [L], A is the membrane active area [m²], t is the operation time [h], ΔP is the relative transmembrane pressure during the experiment [bar] and $\Delta \Pi$ is the difference of osmotic pressure between the feed solution and the permeate [bar]. J_v represents the transmembrane flux [L m⁻² h⁻¹]. It is worth mentioning that the same permeability, as reported by Geise et al. [204], can also be expressed in terms of the effective concentration-averaged water diffusion coefficient D_w [m² s], the mass concentration of water sorbed in the membrane at the upstream face c_{w0}^m [kg m⁻³], the molar volume of water V_w [m³ mol⁻¹], the density of water ρ_w [kg m⁻³], the membrane thickness L [m], the gas constant R [m³ Pa K⁻¹ mol⁻¹] and the absolute temperature T [K].

Before each filtration test, the membrane under investigation underwent pressurization at 5 bar with deionized water for 1 hour. This ensured a stabilized water flux during experimental tests and removed potential traces of glycerine in the substrate that could compromise the conductivity of the NF permeate.

The selectivity of each NF membrane was examined by testing four different single salt solutions at a concentration of 1000 mg L⁻¹: NaCl, Na₂SO₄, MgCl₂, and CaCl₂. The conductivity and pH of both the feed and permeate solutions were monitored using a pH/conductivity meter (Mettler Toledo, SevenCompactDuo). Salt rejection was evaluated using the formula:

$$R(\%) = \left(1 - \frac{C_p}{C_f}\right) * 100 \quad (26)$$

where $R(\%)$ is single salt rejection, C_f and C_p are the conductivity of the feed solution and permeate solution [mS cm⁻¹], respectively. It is important noting that this equation was exclusively employed for pure single salt solutions due to the linear relationship between concentration and conductivity. For ion rejection calculations with synthetic seawater and brine feed solutions, Equation 27 was expressed in terms of ion concentration rather than conductivity.

Additionally, it is noteworthy that the volume of permeate solution collected was fixed at 50 mL, which was negligible compared to the initial feed solution volume of 3 L. This substantial volume difference ensured that the retentate solution recycling strategy did not concentrate the feed solution during filtration tests. All experiments were conducted at least twice, and average values of salt rejection and permeability were reported in Paragraph 4.2.5. Following the filtration tests with single salt solutions, the most effective NF membrane was chosen and tested with synthetic solutions of seawater and RO desalination brine, with the major ion compositions provided in Table 25.

Table 25: Major ions concentration of synthetic seawater and RO desalination brine.

| Ion | Concentration [mg L ⁻¹] | |
|-------------------------------|-------------------------------------|------------------------|
| | Seawater | RO Desalination Brine* |
| Na ⁺ | 12500 | 22727 |
| Mg ²⁺ | 1450 | 2636 |
| Ca ²⁺ | 450 | 818 |
| Cl ⁻ | 22100 | 40182 |
| SO ₄ ²⁻ | 3410 | 6200 |

*A desalination plant with a typical permeate recovery of 45% was taken into consideration for the composition of the desalination brine.

Experimental tests were conducted at 30 bar (typical pressure of industrial scale NF plants) with synthetic solutions. Samples of feed and permeate were collected and analysed employing Ionic Chromatography. Ion selectivity of the novel NF membrane was determined via Equation 27:

$$IS_{\frac{ion1}{ion2}} = \left(1 - \frac{R_{ion2}}{R_{ion1}}\right) \quad (27)$$

Where IS is the ion selectivity between the rejections R of two ions ion_1 and ion_2 . When the rejections of two ions present the same value, IS is equal to 0 (no selectivity). Meanwhile, IS is equal to 1 when the two rejections assume values of 100% and 0% respectively. The IS of the newly synthesized NF membrane was compared to that of two widely used commercial NF membranes (NF90, NF270) tested at the same operating conditions (same feed solution and 30 bar).

4.2 Results and Discussion

4.2.1 Characterization of the membrane materials

4.2.1.1 MOF and ZnO nanoparticles

The structure and composition of the initial nanomaterials, specifically the MOF, were examined through XRD analysis. The diffractogram depicted in Figure 37a)

displays characteristic reflections of the MIL-101 phase, with prominent peaks at 2θ values of 8.6° , 9.3° , 15.1° , and 18.2° , consistent with previous findings [205]. The broad peaks align with approximately 15 nm large crystallites [206]. Additionally, peaks at 12.3° , 17.5° , and 25.1° suggest the presence of the MIL-53 phase as an impurity. Notably, no discernible peaks corresponding to the reagents used in the MOF synthesis were detected, indicating their complete conversion into MOF nanoparticles. In contrast, ZnO nanopowder, acquired rather than synthesized like the MOF, exhibited well-defined peaks in its diffractogram, indicative of a highly ordered crystalline structure (Figure 37b)). The analysis revealed that more than 97 wt% of this ZnO nanopowder consisted of the wurtzite (hexagonal phase), with minor impurities identified as cubic ZnO and cubic ZnS phases. For the deposition of thin film filtration layers necessary in thin film NF membranes, the dispersibility of nanoparticles in a solvent, typically water, is a crucial aspect. As illustrated in Figure 37c), the water dispersion of ZnO nanopowder exhibited a narrow size distribution, with an average hydrodynamic diameter below 90 nm, aligning with product specifications (i.e., particle size < 100 nm). Therefore, DLS analysis indicates that ZnO nanoparticles could be readily dispersed in water without the need for chemical additives, consistent with the high hydrophilicity and surface charge of this material [207,208]. Similarly, the MOF powder also formed a stable dispersion in water, but the particle size ranged between 300 and 450 nm (Figure 37c)), indicating aggregation of the MOF into colloids with sizes much larger than individual crystallites.

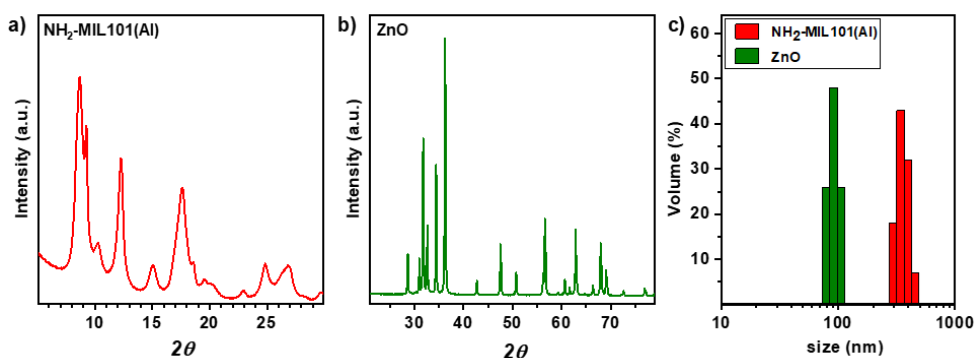


Figure 37: a) XRD analysis of NH₂-MIL-101(Al); b) XRD analysis of ZnO; c) Size distributions of NH₂-MIL-101(Al) and ZnO nanoparticles dispersed in demineralized water as measured by DLS analysis.

The homogeneity of the MOF powder was affirmed by the SEM micrograph in Figure 38a). The inset high magnification image revealed that the material comprised small crystallites aggregated into secondary particles, reaching dimensions of a few hundred nanometres. The morphology closely resembled that documented for NH₂-MIL-101(Al) in existing literature [209]. Furthermore, a specific surface area of 501 m² g⁻¹ was derived from the nitrogen adsorption/desorption isotherms at low temperature (77 K) in Figure 38b). This value aligned with previous literature reports [188], providing additional evidence of the successful synthesis of the MOF. Notably, the analysis indicated a highly microporous product, evident from the substantial nitrogen uptake at low relative pressures. This significant microporosity was a crucial attribute that influenced the selection of the MOF as the primary component for the separation layer in this study. It was indeed necessary to achieve a thin film NF membrane with a delicate balance between high ion selectivity and water permeability.

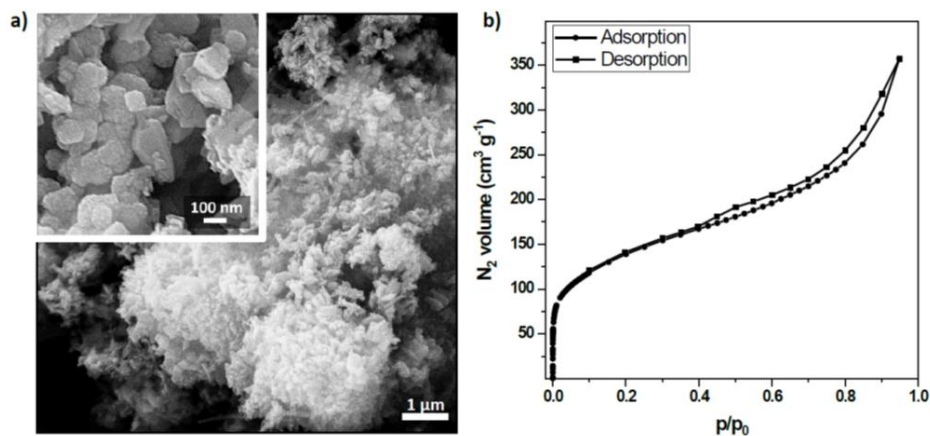


Figure 38: $\text{NH}_2\text{-MIL-101(Al)}$ powder: a) low-magnification and high-magnification (in the insert) SEM micrographs, and b) nitrogen adsorption/desorption isotherms (77 K).

4.2.1.2 CMZ nanoparticles

Figure 39 enables to compare the ATR-FTIR spectra among the individual membrane components (chitosan, MOF, and ZnO) and the CMZ-35 nanocomposite, utilized as the active layer in the membrane. The primary objective of this comparison was to assess whether the structural characteristics of the individual components were retained upon their integration into the active layer of the membrane.

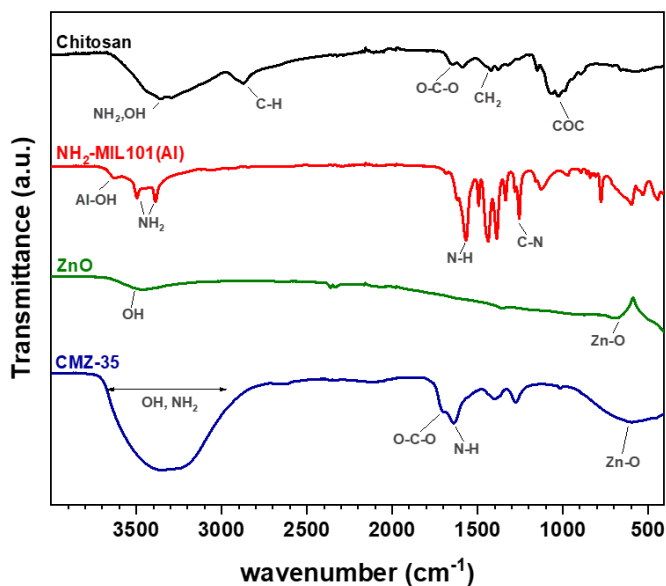


Figure 39: FTIR analysis of chitosan, NH₂-MIL 101(Al), ZnO, and CMZ-35 nanocomposite.

The ATR-FTIR spectrum of commercial chitosan displayed characteristic peaks, including stretching modes of -OH and -NH₂ groups within the polysaccharide structure (3000-3500 cm⁻¹), C-H stretching (2870 cm⁻¹), and distinct signals at 1724, 1447, and 1000 cm⁻¹, corresponding to O-C-OH, -CH₂, and -C-O-C- groups, respectively. The spectrum of NH₂-MIL-101(Al) aligned well with previous reports in the literature [205,210,211], thus confirming the successful synthesis of the MOF in this study. Notable peaks included one at 3640 cm⁻¹ for Al-OH groups, and two distinctive peaks in the 3385-3495 cm⁻¹ range associated with symmetrical and asymmetrical -NH₂ stretching. Peaks at 1565 and 1340 cm⁻¹ indicated the presence of N-H and C-N moieties, respectively. The ATR-FTIR spectrum of ZnO nanopowder revealed two prominent peaks: one at a high frequency (3500 cm⁻¹) attributed to the vibration bands of hydroxides and adsorbed water molecules, and another at a low frequency (600 cm⁻¹) indicative of the Zn-O scaffold [212]. Lastly, the ATR-FTIR spectrum of the CMZ-35 nanocomposite, employed in crafting the most efficient NF membrane in this study (as detailed in Paragraph 4.2.3), exhibited

four main signals: (i) a broad band within $3000\text{-}3600\text{ cm}^{-1}$ corresponding to hydroxyls and -NH_2 groups on chitosan and MOF, and physisorbed water molecules, (ii) an absorption band at 600 cm^{-1} associated with the presence of ZnO, (iii) a peak at 1639 cm^{-1} distinctive for the vibration of N-H groups, and (iv) a final peak at 1708 cm^{-1} for O-C-O groups. Notably, the positions of the latter two peaks, originating from chitosan and $\text{NH}_2\text{-MIL-101(Al)}$, respectively, exhibited slight shifts in the composite compared to those in the pristine materials. This suggests a robust interaction between the components of the membrane active layer.

4.2.2 Characterization of nanocomposite membranes

Figure 40 depicts SEM micrographs of the surfaces and cross-sections of the original PSF substrate and the CMZ-35 membranes after coating.

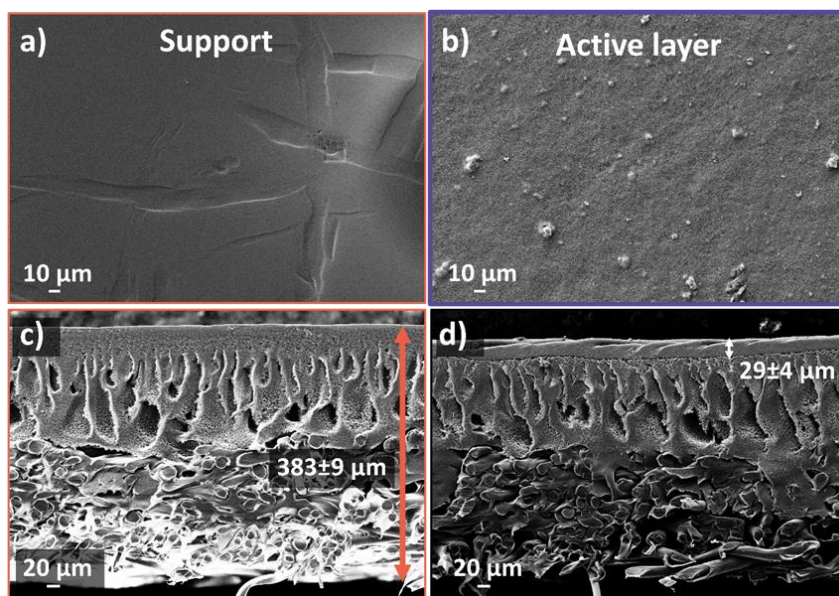


Figure 40: SEM images of the surfaces (a,b) and the cross-sections (c,d) of the membrane support and active layer (CMZ-35). The orange arrow indicates the support layer thickness; the white arrow indicates the active layer thickness.

The commercial PSF substrate exhibited a smooth surface in Figure 40a), with the exception of a few valleys likely resulting from the fabrication process. Upon closer inspection at the same level of magnification, the surface of the CMZ-35 membrane in Figure 40b) showed a polycrystalline and rough texture, evenly distributed with some exceptions attributed to the aggregation of nanoparticles during the active layer deposition. This observation indicated the successful deposition of the selective active layer onto the PSF substrate during the coating stage. The cross-section morphology of both the support and CMZ-35 membrane was analysed and compared. In Figure 40c), the PSF substrate displayed an asymmetrical structure with a thin and relatively dense skin at the top and a macroporous finger-like sublayer. The overall thickness of the substrate measured $383 \pm 9 \mu\text{m}$. Concerning the cross-section of CMZ-35 (Figure 40d)), a thin, dense active layer was visible on top of the PSF substrate, with an average thickness of $29 \pm 4 \mu\text{m}$. Such value was higher than that of current commercial NF membranes that can present an active layer thickness of up to 20 nm (i.e. for the NF270 membrane [213]). Nevertheless, this was not a main issue since the main objective of the CMZ membranes was to enhance the multi-valent ion selectivity in nanofiltration.

Aiming to verify that the identified top dense thin layer in Figure 40d) corresponds to the CMZ-35 active layer, Energy-Dispersive X-ray (EDX) spectroscopy was employed. EDX analyses were performed considering only the cross-section of the NF membrane. The concentrations of key elements (C, S, O, Al, and Zn) constituting both (i) the substrate polymer (PSF) and (ii) the selective active layer were determined. Figure 41 indicates that the characteristic elements of CMZ materials, namely Al and Zn, were detected at high concentrations in the top layer, thereby confirming its identity as the selective active layer.

The higher concentration of oxygen (O) in the active layer was attributed to the presence of ZnO, -OH groups, and C-O bonds of chitosan, as well as the O atoms in the $\text{NH}_2\text{-MIL101(Al)}$ framework. Conversely, sulphur (S) and carbon (C) were distinctly located in the region corresponding to the membrane support, consistent with their characteristic presence in the PSF polymer forming the substrate.

Additionally, the characteristic elements of MOF (Al) and ZnO (Zn) were uniformly distributed in the active layer, indicating effective dispersion of nanoparticles within the chitosan matrix. Notably, the concentration of these elements was negligible outside the micrograph area corresponding to the active layer, signifying minimal infiltration of the CMZ material into the membrane support.

As for the macroscopic homogeneity of the active layer, no EDX analyses were performed on the surface of the NF membrane. The main reason for this was that such analysis could not have provided sufficient information concerning the homogeneous distribution of the active layer concerning the whole membrane area employed for filtration tests.

Concerning the porosimetry of the active layer, this was assessed by N₂ absorption porosimetry performed on the unsupported composite membrane materials. With the addition of chitosan, the specific surface area decreased to 42 m² g⁻¹ for CMZ-0 and dropped to values below 5 m² g⁻¹ for all other membrane materials (CMZ-20, CMZ-35, CMZ-60, and CMZ-80). This reduction in accessible porosity is indicative of the complete embedding of nanoparticles within the continuous chitosan matrix.

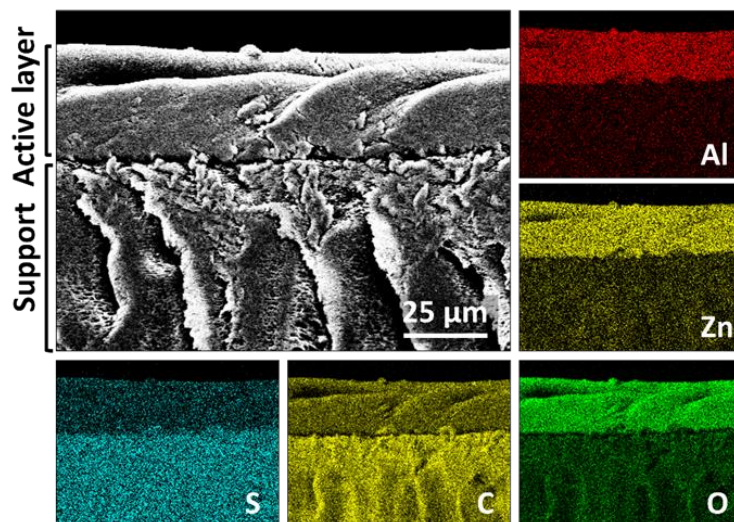


Figure 41: EDX analysis of the CMZ-35 membrane.

The hydrophilicity of NF membranes is a crucial property, as demonstrated in literature where hydrophilic membranes have been shown to resist fouling effectively [214]. Hydrophilic surfaces can establish strong hydrogen bonds or electrostatic attractions with water molecules, creating a water boundary layer that repels potential foulants. Given the primary objective of this study to synthesize a highly selective NF membrane for recovering magnesium and calcium from seawater and waste brines containing organic matter, the evaluation of membrane hydrophilicity is particularly important.

To assess the impact of ZnO loading on membrane hydrophilicity, water contact angle measurements were conducted for each membrane. In Figure 42a), the water contact angles were measured at a fixed time interval of 30 seconds after the water drop contacted the membrane surface. It is noteworthy that the water contact angle measurements remained relatively stable during the analysis time. As it can be seen in Figure 42a), the presence of an active layer (without ZnO) reduced the water contact angle of the PSF substrate from $48.9^{\circ} \pm 3$ (PSF) to $37.8^{\circ} \pm 2$ (CMZ-0), indicating increased hydrophilicity. This change can be attributed to the amino and hydroxyl groups on the membrane active layer and the higher surface roughness. Additionally, the gradual increase in ZnO within the active layer further reduced the water contact angle from $37.8^{\circ} \pm 2$ (CMZ-0) to $14.1^{\circ} \pm 1$ (CMZ-60). This reduction was primarily attributed to the high polarity and abundance of hydroxyl groups in the ZnO nanocrystals [215]. Therefore, it was inferred that ZnO played a significant role in enhancing surface hydrophilicity, potentially providing anti-fouling properties to the membrane. However, at higher ZnO loading, two phenomena were observed: (i) the effect of ZnO on increasing surface hydrophilicity became less dominant, consistent with previous reports [207,216]; (ii) high ZnO loading without the presence of MOF (CMZ-80) led to the formation of a very defective and unstable active layer, resulting in a membrane behaviour similar to that of an ultrafiltration membrane. This instability was also reflected in its selective performance (see Paragraph 4.2.3).

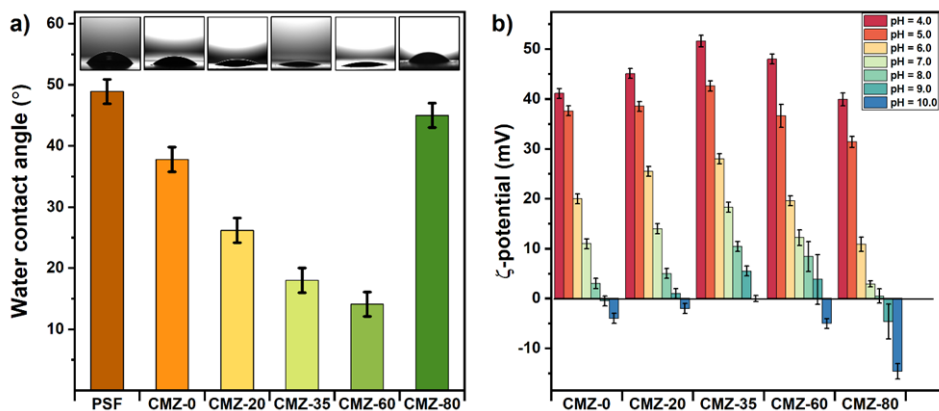


Figure 42: a) Water contact angle analysis of UF membrane (PSF) and NF membranes of this work; b) ζ potential of the membrane materials CMZ-0, CMZ-20, CMZ-35, CMZ-60, CMZ-80 as a function of the pH.

Additionally, ZnO is recognized not only for its hydrophilic properties but also for its highly positive electric charge in aqueous solutions due to the acid-base characteristics of the surface groups, resulting in an isoelectric point higher than pH 9.0 [215]. This property is crucial to tailor in the synthesized NF membrane to achieve high selectivity towards Mg^{2+} and Ca^{2+} ions. However, CMZ membranes are ternary systems comprising chitosan, NH_2 -functionalized MOF, and ZnO nanoparticles. Consequently, the surface charge of CMZ depends on the type and density of functionalities available on the nanocomposite surface. To investigate the effect of composition on the electric surface charge of CMZ membranes, ζ -potential was measured across a wide pH range (from 3.0 to 12.0).

As shown in Figure 42b), the NF membrane without ZnO (CMZ-0) exhibited a very high ζ -potential value of +43 mV at pH = 3.0 and only became negatively charged at pH values exceeding 9. The high positive surface charge of CMZ-0 can be attributed to the protonated amino groups in the MOF. However, with the increase in ZnO loading from 0 (CMZ-0) to 35% (CMZ-35), there was a noticeable augmentation in the electric surface charge of the membrane at any fixed pH value, indicating a robust interaction between CMZ components. Yet, when ZnO surpassed the MOF as the primary component, the rise in ZnO was accompanied by a decrease

in ζ -potential at a fixed pH value. This is because the MOF provides a high density of amino groups, contributing to a substantial surface charge and aiding in the dispersion of nanocomposite nanoparticles. As ZnO nanoparticles became the predominant component relative to the MOF, the CMZ nanocomposites exhibited an isoelectric point close to that expected for ZnO nanoparticles embedded in chitosan ($pK_a \approx 6.5$) [216,217]. It is noteworthy that the ζ -potential of the newly synthesized membranes consistently maintained a positive value within the pH range of 5 to 8, aligning with the relevant pH interval for the tests in this study and real-life applications. Specifically, the ζ -potential of CMZ-35 ranged from +44 mV at pH = 5.0 to +11 mV at pH = 8.0. Moreover, CMZ-35 displayed a neutral surface charge only in highly alkaline environments (pH = 10), unlike commercial NF membranes, which are typically neutral or negatively charged even at pH = 7 [173].

4.2.3 Filtration of single salt solutions

The filtration performance of four distinct NF membranes, each characterized by varying ZnO loadings, was examined at 5 bar using four different single salt solutions: NaCl (1000 mg L⁻¹), Na₂SO₄ (1000 mg L⁻¹), MgCl₂ (1000 mg L⁻¹), and CaCl₂ (1000 mg L⁻¹). The outcomes, including salt rejection and permeability, are presented in Figure 43, with a maximum standard deviation of 5% for salt rejection and 4% for permeability.

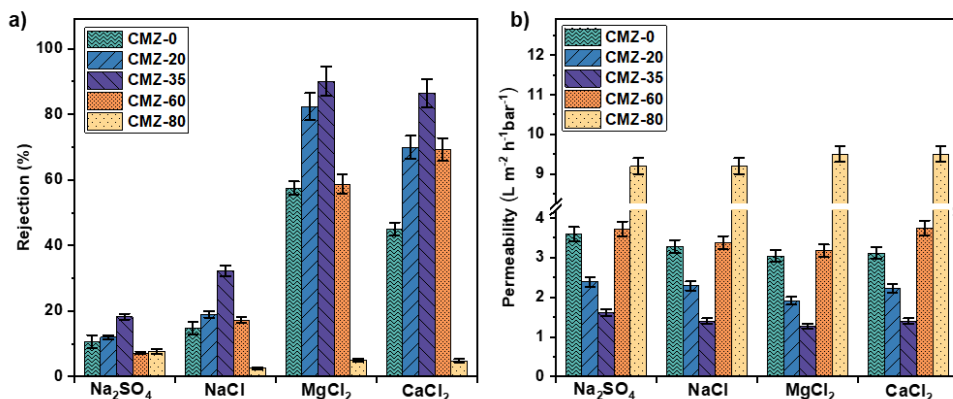


Figure 43: a) Salt rejections and b) permeabilities of the tested NF membranes for single salt solution feed at 1000 mg L⁻¹ and at 5 bar.

In Figure 43a), the salt rejection pattern of the investigated membranes (CMZ-0, 20, 35) was the same, following the order: $R_{MgCl_2} > R_{CaCl_2} > R_{NaCl} > R_{Na_2SO_4}$. This trend can be attributed to the interplay of two factors: (i) steric exclusion and (ii) Donnan exclusion.

(i) Regarding the steric effect, Mg²⁺ and Ca²⁺ have larger hydrated and Stokes radii compared to Na⁺, hindering their transport across the membrane more significantly.

(ii) As for the Donnan effect, the NF membranes of this study possess a positive surface charge, and since Mg²⁺ and Ca²⁺ exhibit higher charge density than Na⁺, multivalent cations experience greater rejection. Counterions, especially those with high charge density like SO₄²⁻, permeate more due to stronger electrostatic attraction, explaining therefore the lowest salt rejection for Na₂SO₄ across all membranes.

Additionally, Figure 43a) reveals that increasing ZnO loading enhances salt rejection for all salts, peaking with CMZ-35 ($R_{MgCl_2} = 90.1\%$, $R_{CaCl_2} = 86.49\%$, $R_{NaCl} = 32.29\%$, $R_{Na_2SO_4} = 18.28\%$). This improvement is attributed to two effects resulting from higher ZnO concentration: (i) an increase in membrane positive surface charge (as depicted in Figure 42b)) and (ii) nanopowder aggregation, densifying the active

layer and reducing membrane pore size (specific area decreased from 42 m²/g in CMZ-0 to 4 m²/g in CMZ-35).

However, from CMZ-35 to CMZ-80, a decline in salt rejection performance is observed, allegedly due to excessive ZnO concentrations. High concentrations lead to nanoaggregate formation [216], causing a decrease in ζ -potential (as discussed in Paragraph 4.2.2) and compromising the homogeneity and mechanical integrity of the active layer film. This, confirmed by SEM analysis (Figure 44), results in fractures in the thin film membrane active layer, ultimately reducing its rejection capabilities.

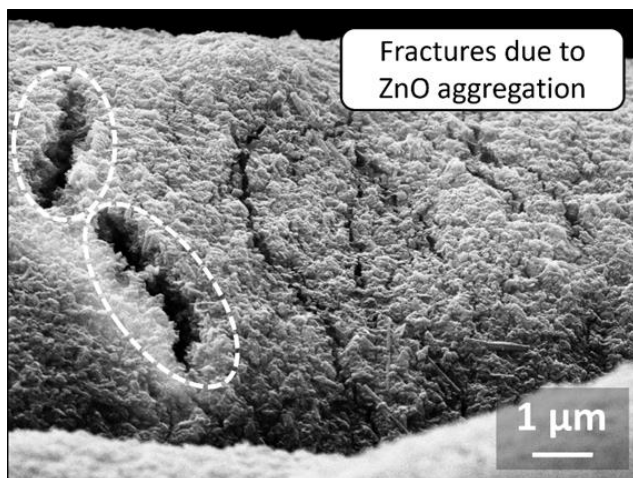


Figure 44: Post-mortem SEM image of the active layer of CMZ-60. Microfractures (circled) are present due to the aggregation of ZnO nanoparticles.

It is noteworthy that both the reduction in ζ -potential and the presence of fractures are likely contributors to the altered salt rejection sequence observed in CMZ-60 (i.e. $R_{CaCl_2} > R_{MgCl_2} > R_{NaCl} > R_{Na_2SO_4}$), where the electric expulsion effect would have less influence than in previous cases. Moreover, due to the high defect density in the active layer, as discussed in Paragraph 4.2.2, CMZ-80 exhibited a behaviour similar to an ultrafiltration membrane, demonstrating low rejection values for all salts.

In Figure 43b), the trend of membrane permeability for the four ZnO loadings is presented. It is to be noted that the reported permeability in Figure 43b) is different than the permeability with pure water. As a matter of fact, unlike the water

permeability, it takes into account several factors as described in Equation 25. Among these factors, some (i.e., c_{w0}^m and D_w) vary with the presence of the salt in a solution. By increasing the salt content in water, c_{w0}^m and D_w decrease, thus leading to an overall reduction of the permeability when compared to the water permeability. Furthermore, for NF membranes that can be considered as charged membranes, the interaction of ions in a solution can interact with the functional groups of the membrane polymer, thus reducing the water intake and the permeability.

While the salt rejection trend reached a maximum with CMZ-35, the permeability trend showed a minimum value corresponding to CMZ-35, averaging $1.5 \text{ L m}^2 \text{ h}^{-1} \text{ bar}^{-1}$ (within the typical range of permeability values for commercial NF membranes [217]). This result is surprising, considering that the active layer of this membrane has a thickness of $29 \pm 4 \text{ }\mu\text{m}$ (much more than the active layer thickness of commercial NF membranes that is in the order of nanometres [213]).

The best-performing membrane, CMZ-35, exhibited high selectivity towards multivalent cations such as Mg^{2+} and Ca^{2+} and high permeation of SO_4^{2-} . Subsequently, this selectivity was compared to that of commercial NF membranes and recently introduced positively charged NF membranes under operating conditions similar to those in this study. As shown in Figures 45a-d), CMZ-35 fell within the region of interest (high selectivity towards MgCl_2 and CaCl_2), unlike all other considered membranes. This positions CMZ-35 as the current top-performing NF membrane with the desired properties.

Conversely, some NF membranes, like the commercial NF90 [218] and others [177,181,182,186], exhibit high rejection for all salts. NF270, being a looser NF membrane than NF90 with a negative surface charge [219], shows high rejections towards sulphates due to its negative charge, placing it in the opposite region of interest for this study. Additionally, recently proposed NF membranes [178] and [189] display relatively low rejections for all salts.

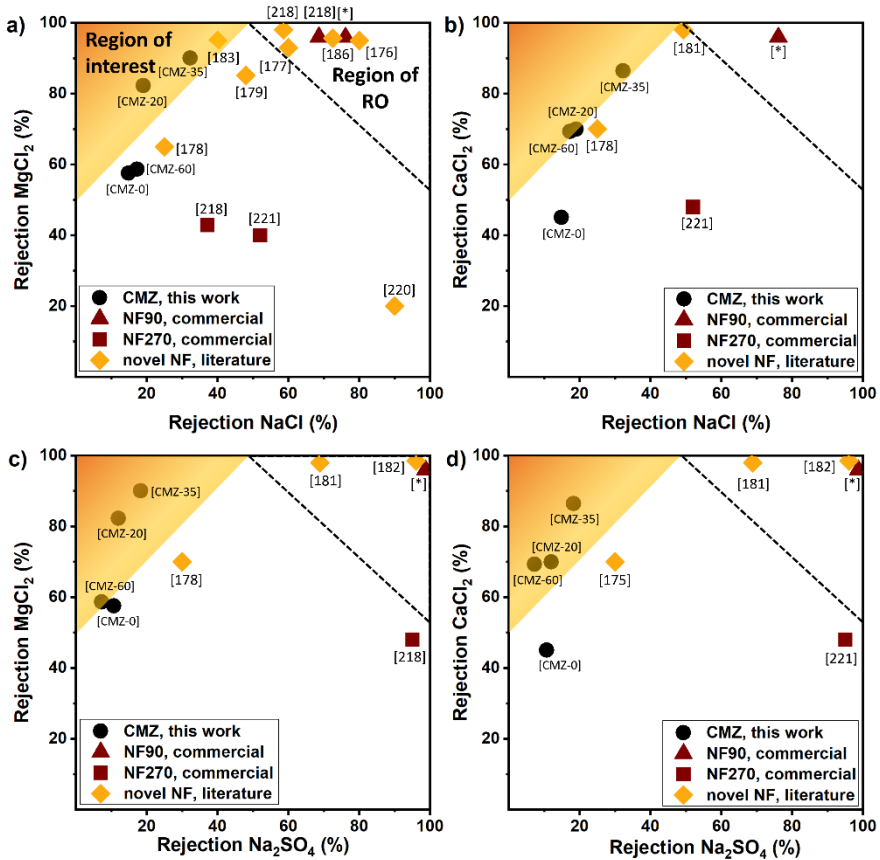


Figure 45: Rejections for CMZ membranes manufactured in this work, commercial NF membranes, and (novel) positively charged NF membranes in literature ([176–179, 181–183, 186, 218, 220, 221]) for the salt couples: (a) $\text{MgCl}_2/\text{NaCl}$, (b) $\text{CaCl}_2/\text{NaCl}$, (c) $\text{MgCl}_2/\text{Na}_2\text{SO}_4$, and (d) $\text{CaCl}_2/\text{Na}_2\text{SO}_4$ at operating pressures reported in Table 23. Region of interest: high rejection values towards MgCl_2 and CaCl_2 respect to NaCl and Na_2SO_4 ; Region of RO: typical rejection values for RO membranes.

*Tested in this work

4.2.4 Filtration of real seawater and desalination brine

The ionic selectivities (IS) of CMZ-35 were examined in practical applications, tested under conditions of 30 bar and a cross-flow velocity of 3.5 L/min using synthetic seawater and desalination brine solutions.

In Figure 46, the IS results of CMZ-35 were compared with those of two commercial NF membranes (NF90, NF270). Notably, in the case of seawater treatment, CMZ-

35 generally exhibited higher multivalent/monovalent IS when compared to the two commercial NF membranes. Exceptions, where CMZ-35 showed intermediate selectivity between NF90 and NF270, were observed in Mg^{2+}/Na^+ and Ca^{2+}/SO_4^{2-} . This behaviour is allegedly due to the novel NF membrane which keep a positive surface charge in slightly alkaline environments (i.e., seawater or brine), unlike NF90 and NF270.

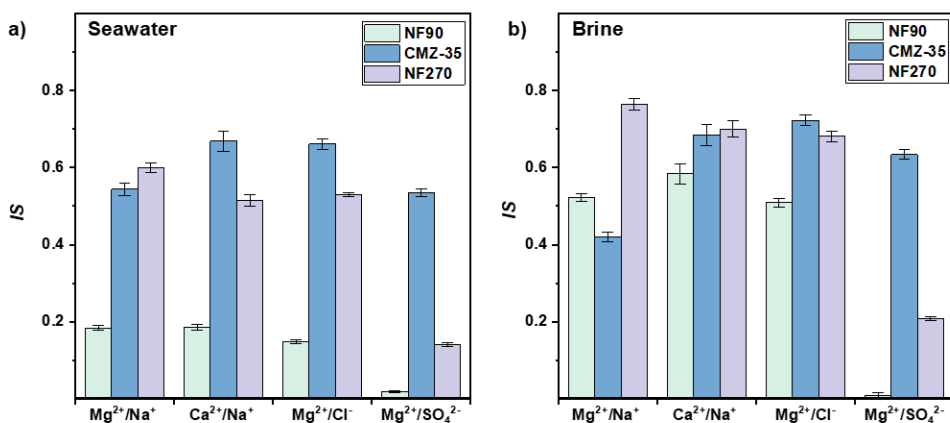


Figure 46: Ion Selectivities (IS , calculated according to Equation 3) of CMZ-35 and the commercial membranes NF90 and NF270 in the treatment of a) seawater and b) brine.

Concerning the desalination brine scenario, the elevated ionic concentration of the feed solution resulted in a greater reduction of monovalent ion rejection compared to multivalent rejections for all membranes. This led to an overall higher ionic selectivity for each membrane in brine treatment compared to seawater. In the brine scenario, CMZ-35 demonstrated higher ionic selectivity values than NF90 and NF270 in most cases. However, with the exceptions of Mg^{2+}/Na^+ and Ca^{2+}/SO_4^{2-} , CMZ-35 also showed lower selectivity values for Ca^{2+}/Na^+ than NF270. Nevertheless, in brine treatment, CMZ-35 remained competitive with commonly used commercial NF membranes at an industrial scale.

4.3 Conclusions

A new positively charged NF membrane was developed in order to improve the recovery of valuable multivalent cations in MLD/ZLD processes from seawater and desalination brine. This membrane aimed to specifically reject magnesium (a CRM) and calcium (a major component in seawater/brine with various industrial applications), in alkaline environments (i.e., seawater/desalination brine). The novel NF membrane comprised: (i) a microporous asymmetric UF-membrane-like substrate for mechanical strength and (ii) a selective active layer consisting of the MOF "NH₂-MIL-101(Al)" and ZnO embedded within a chitosan matrix. Characterization analyses, including SEM, FTIR, DLS, and BET, were performed on the nanoparticles within the active layer. Additionally, morphology, hydrophilicity, and electric surface charge of the nanocomposites were analysed. Results from the characterization analyses and initial filtration tests (at 5 bar using 1000 mg/L single salt solutions (NaCl, Na₂SO₄, MgCl₂, CaCl₂)) indicated:

(i) an increase in ZnO content within the active layer enhanced membrane hydrophilicity and zeta potential, leading to higher rejections of multivalent cations.

(ii) excessive ZnO concentrations resulted in pore blockage and microfractures in the active layer, reducing overall ionic rejections.

(iii) the NF membrane with the highest rejections of MgCl₂ (90.10%) and CaCl₂ (86.49%) was CMZ-35 (20%wt Chitosan, 35%wt ZnO, and 45%wt MOF).

The selectivity properties of CMZ-35 were then compared with those of common commercial NF membranes and novel positively charged NF membranes from literature at the same operating conditions. Results of the comparison demonstrated that CMZ-35 exhibited the highest selectivity towards MgCl₂ and CaCl₂. Furthermore, the performance of CMZ-35 was evaluated in real application scenarios, being tested with synthetic seawater and desalination brine at 30 bar. The ion selectivity values achieved were compared with those of two commercial

membranes (NF90, NF270) under the same operating conditions. CMZ-35 demonstrated higher Mg^{2+} and Ca^{2+} selectivity than NF90 for seawater treatment and generally higher values than NF270 in most cases. Similar successful results were obtained for desalination brine treatment.

CMZ-35, thanks to its cost-effective fabrication materials (0.4 €/cm² for CMZ-35 vs. 1.2 €/cm² for NF90/NF270 [222]) and a simple synthesis procedure that avoids hazardous organic solvents, emerges as a competitive alternative to commercial NF membranes. All in all, CMZ-35 could significantly enhance mineral recovery in ZLD/MLD systems for the valorisation of seawater and brine.

5 “New generation of commercial nanofiltration membranes for seawater/brine mining: Experimental evaluation and modelling of membrane selectivity for major and trace elements”

In the pursuit of selectively recovering minerals from seawater and Seawater Reverse Osmosis (SWRO) brines, in Chapter 5 five distinct commercial NF membranes (NF90, NFS, NFX, VNF1, and DK) were investigated. Notably, four of these membranes had not been previously studied in this specific field. The research concerned a comprehensive assessment of their efficacy in separating both major ions (Na^+ , Cl^- , Mg^{2+} , Ca^{2+} , K^+ , HCO_3^- , Br^-) and trace elements (B, Li^+ , Rb^+ , Sr^{2+}). The investigation was carried out by using a flat-sheet experimental setup in a closed-loop configuration in order to gather extensive experimental data concerning the impact of operating pressure on trans-membrane flux and rejections concerning two distinct solutions (seawater and SWRO brine). This dataset was subsequently employed to determine the membrane permeances to various species using the Solution-Electro-Diffusion Film (SEDF) model. The SEDF model was capable of describing ion transport in scenarios involving both seawater and brine treatment. In essence, the findings of this investigation were intended to provide a comprehensive understanding of the potential of NF technology in selectively separating both major and trace elements from seawater and brine. This was accomplished through the exploration of a diverse array of commercially available NF membranes, offering insights into their performance in this specific application.

5.1 Experimental

5.1.1 NF membranes and Synthetic solutions

For the comprehensive comparative analysis of this study, five commercial flat sheet NF membranes were used: (i) NF90 from Dow Filmtec (USA), (ii) NFS and (iii) NFX from Synder Filtration (USA), (iv) VNF1 from Vontron (China), and (v) DK from Veolia (France). Table 26 outlines the key properties of the NF membranes sourced from the respective manufacturers, accompanied by supplementary details previously documented in the literature (such as water contact angle, zeta potential, and pure water permeability). It is important to note that the information reported in Table 27 originates from diverse sources, obtained under varying operational conditions, making a direct comparison unfeasible. Furthermore, as far as the pure water permeability is taken into account, values found in literature were compared

with those experimentally obtained in this work. A good agreement was achieved (as observed in Table 26).

Table 26: Main properties of the 5 NF commercial membranes.

| NF membrane | Manufacturer | Type of polymer | Molecular Weight Cut-Off (MWCO) [Da] | MgSO ₄ rejection [%]* | NaCl rejection [%]* | Water contact angle [°] | Zeta potential [mV] | Pure water permeability [LMH/bar] | |
|-------------|-------------------|-----------------|--------------------------------------|----------------------------------|---------------------|-------------------------|--------------------------------------------------------|-----------------------------------|-----------|
| | | | | | | | | Literature | This work |
| NF90 | Dow Filmtec | PA TFC | 200-400 | 99.0 | 90.0 | 61.2+3 ^a | -26.5 ^b (pH = 7) | 8.67 ^f | 8.42 |
| NFS | Synder Filtration | PA TFC | 100-250 | 99.5 | 50.0-55.0 | 49.8 ^{d, e} | -23+1 ^c -33+1 ^e (pH = 7.6) | 6.30 ^c | 5.80 |
| NFX | Synder Filtration | PA TFC | 150-300 | 99.0 | 40.0 | 17.6+2.8 ^d | -25+2 ^e (pH = 7.6) | 4.21 ^f | 4.51 |
| VNF1 | Vontron | PA TFC | 260 | > 96.0 | 30.0-50.0 | 49.9+2 ^a | -11.9 ^a (pH = 7) | 4.75 ⁱ | 4.73 |
| DK | Veolia | PA TFC | 150-300 | 96.0 | - | 50.2 ^g | -40 ^h (pH = 7) | 6.50 ^j | 6.45 |

*Test conditions according to membrane supplier information: 2000mg/L inlet solution at 110 psi (760 kPa) operating pressure, isothermal process conditions at 25 °C, tests at 15% permeate recovery after 24 h of filtration. ^a [223], ^b [224], ^c [225], ^d [226], ^e [227], ^f [228], ^g [229], ^h [230], ⁱ [231], ^j [232].

The performance evaluations of the mentioned NF membranes were conducted in two precise scenarios: (i) seawater and (ii) SWRO brine treatment. To achieve this, synthetic solutions were utilized that replicated the composition of the Mediterranean Sea, considered as an average between the relatively lower concentrated seawater of the North/Baltic Sea and the comparatively higher concentrated one from the Middle East region [233]. As for the desalination brine, the investigation took into account the brine generated from SWRO desalination plants, currently the most widely employed technology for desalination [234]. Specifically, a SWRO plant with a water recovery rate of 45% was considered, reflecting the typical recovery rate of contemporary industrial-scale SWRO plants worldwide [113]. The compositions and pH of the two synthetic solutions are given in Table 27.

Synthetic solutions mimicking seawater and desalination brine were carefully prepared using deionized water, NaCl, MgSO₄·7H₂O, MgCl₂·6H₂O, KCl, NaBr,

H₃BO₃, LiCl (PanReac), CaCl₂·2H₂O (Chem-lab), NaHCO₃ (Scharlau), Rb₂CO₃ (Aldrich), Sr(NO₃)₂ (Acros Organics). All reagents utilized were of analytical grade. Furthermore, HNO₃ 69% (w/w) and HCl 37% (w/w) were procured from Panreac for sample preparation for ICP (Inductively Coupled Plasma) and to regulate the pH of the synthetic solutions, respectively.

Table 27: Composition and pH of synthetic seawater and SWRO desalination brine.

| Ref. | Major ions | Concentration [mg/L] | | Ref. | Minor ions | Concentration [mg/L] | |
|----------------|-------------------------------|----------------------|------------|------------------------------------------------------------------------------------------------------------------------------------------------------------------------------------------------------------------------------------------------------------------------------------------------------------|------------------|----------------------|------------|
| | | Seawater | SWRO brine | | | Seawater | SWRO brine |
| [235] | Na ⁺ | 12,500 | 22,727 | [236] | B | 4.2 | 7.6 |
| [235] | Cl ⁻ | 22,100 | 40,181 | [237] | Li ⁺ | 0.5* | 0.9 |
| [235] | K ⁺ | 450 | 818 | [237] | Rb ⁺ | 0.5* | 0.9 |
| [235] | Ca ²⁺ | 450 | 818 | [238] | Sr ²⁺ | 8.3 | 15.0 |
| [235] | Mg ²⁺ | 1,450 | 2,636 | * Due to the limit of quantification of the ICP instrumentation used in this study, the concentration of lithium and rubidium in seawater were fixed to 0.5 mg/L (e.g. slightly higher than the actual values in most oceans) to increase the accuracy in the rejection value estimation of both elements. | | | |
| [235] | SO ₄ ²⁻ | 3,410 | 6,200 | | | | |
| [235] | HCO ₃ ⁻ | 160 | 291 | | | | |
| [239] | CO ₃ ²⁻ | 79 | 143 | | | | |
| [240] | Br ⁻ | 65 | 118 | | | | |
| pH of solution | | 6.5 | 6.5 | To be noted that for the experimental tests the pH of both solutions was fixed to 6.5 via HCl dosing. | | | |

5.1.2 NF Experimental set-up and procedure

Figure 47 illustrates the flat-sheet experimental set-up which was employed in this study to assess the performance of the five commercial NF membranes.

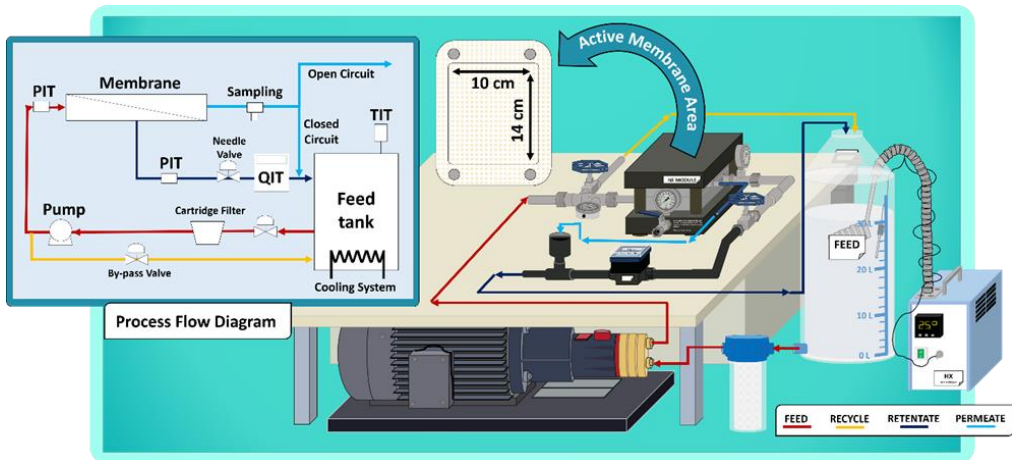


Figure 47: Process flow diagram of NF experimental set-up including main components.

Before commencing the experimental tests, a coupon of the NF membrane was extracted from a larger area supplied by the manufacturer and immersed in ultrapure water for 24 hours to ensure the elimination of any impurities. Subsequently, the membrane was inserted in a crossflow flat-sheet cell (GE SEPA™ CF II) with a membrane active area of 140 cm², placed between a spacer on the feed side (PP, 31 mil diamond (145 × 97 mm)) and a permeate carrier (PP, 145 × 97 mm).

The feed solution, whether seawater or SWRO brine, was contained in a 30 L tank maintained at a constant temperature of 25 ± 2 °C employing a DIGIT-COOL refrigerator (J.P.Selecta). To avoid potential membrane surface scaling, primarily associated with carbonates, the pH of the feed solution was corrected to 6.5 by adding HCl (35%w/w). A high-pressure diaphragm pump (Hydra-Cell, USA) conveyed the feed solution to the membrane cell, with a 10 μm cartridge filter installed before the pump to remove any potential corrosion solids that could compromise the integrity of the pump.

Two operating parameters (Cross-flow rate and operating pressure) were controlled by a bypass valve at the pump exit and a needle valve along the retentate line. The transmembrane pressure was monitored by two manometers placed at the entrance and exit of the cell, while a Bürkert FLOW flow meter on the retentate line tracked the cross-flow velocity (cfv). A closed-loop configuration was employed, recycling

both the retentate and permeate back to the feed solution to guarantee a constant composition of the feed solution throughout the entire experimental tests. Initially, the membrane underwent compaction for 2 hours at 32 bars and a crossflow velocity of 1 m/s (5 L/min) using deionized water. Following membrane pressurization, the same procedure was repeated with the actual solution to be tested. The impact of transmembrane pressure on membrane performance (i.e., permeate flux and rejections) was assessed. The pressure varied from 8 to 30 bar at a fixed crossflow velocity of 0.7 m/s (3.46 L/min). At 2 bar intervals during the experiments, 50 mL samples of permeate solutions were taken and analysed, in addition to taking feed samples before and after the test. Finally, at the end of each test, the NF membrane was cleaned twice with de-ionized water under the following conditions: (i) 10 bar and cfv of 1 m/s for 30 min, and (ii) 32 bars and cfv of 1 m/s for 2 h.

5.1.3 Analytical procedure

Based on the specific ion and its concentration, to determine the complete composition of each sample, it was necessary to use three distinct analytical instruments. Once diluted the samples, the sodium and chloride content were analysed using IC, employing (i) a Dionex IonPac™ AS11-HC column and a mobile phase consisting of a 25 mM KOH solution for anionic analyses and (ii) a Dionex IonPac CS16 column with a mobile phase of 30 mM metasilicic acid ($\text{CH}_3\text{SO}_3\text{H}$) for cationic analyses. Carbonate concentration was assessed through automatic titration using a Mettler Toledo T70–Rondolino system, employing a standardized 1 mM HCl solution as the titrant. For all other elements, inductively coupled plasma spectrometry (ICP) was employed, utilizing both 7800 inductively coupled plasma mass spectrometry (ICP-MS) and 5100 inductively coupled plasma optical emission spectrometry (ICP-OES) from Agilent Technologies to accurately achieve their concentrations. It is to be noted that before every ICP analysis, all samples were diluted in a 2% wt HNO_3 solution. Additionally, on-site measurements

of pH and conductivity of the samples were conducted using a CRI-SON GLP-22 pH-meter and a CRISON GLP-31 conductivity meter, respectively.

5.1.4 Membrane performance indicators

In order to evaluate the performance differences among the NF membranes, 4 indicators were taken into account. The first one was the permeate flux J_v [LMH] at a precise operating pressure was calculated via Equation 28:

$$J_v = \frac{V_p}{A_m * t} = k_w * (\Delta P - \Delta \Pi) = \frac{c_{w0}^m D_w V_w}{\rho_w L * R * T} * 3600 * 10^{-5} * (\Delta P - \Delta \Pi) \quad (28)$$

Furthermore, the membrane permeability [LMH/bar], the ion rejection [%] and selectivity factor [-] were also calculated for this study. However, since they were previously defined in Paragraph 4.1.5, refer to Equations 25, 26 and 27, respectively for their calculation. It is to be noted that for how the permeability was defined, it can also be calculated from the slope when plotting the membrane flux as a function of the operating pressure. Furthermore, as reported by Geise et al. [204], the flux can also be expressed in terms of the effective concentration-averaged water diffusion coefficient D_w [m² s], the mass concentration of water sorbed in the membrane at the upstream face c_{w0}^m [kg m⁻³], the molar volume of water V_w [m³ mol⁻¹], the density of water ρ_w [kg m⁻³], the membrane thickness L [m], the gas constant R [m³ Pa K⁻¹ mol⁻¹] and the absolute temperature T [K].

5.1.5 Ion transport descriptions by means of the SEDF model

Firstly, it is important to highlight that the mathematical model utilized in the techno-economic analysis in Chapter 1, namely the Donnan Steric Pore Model with Dielectric Exclusion (DSPM-DE), was not applied in the present study. This decision stemmed from the absence of specific details in the literature regarding the NF membranes under investigation, which are essential inputs for the DSPM-DE model. These details include parameters like pore radius, active layer membrane thickness,

dielectric constant within the pores, and charge density. As a matter of fact, whilst such properties were available in literature for the NF270 membrane (employed in Chapter 1), for the NF membranes analysed in this chapter, no data were to be found. Consequently, the SEDF model was chosen for this study. The SEDF model, an irreversible thermodynamics model, treats the membrane as a "black box" without necessitating an exhaustive characterization of membrane properties, in contrast to mechanistic models [241]. One of the main assumptions of the model is that no coupling between solute and solvent flows within the membrane is considered [242]. Many recent studies, in fact, have shown that such convective coupling in NF membranes is very weak, thus allowing to consider the NF membrane as a dense membrane [243]. It delineates the transport of species through an NF membrane, taking into account their movement towards the concentration polarization (CP) and active layers [244–246]. This model employs the concept of a virtual solution, defined as such when being in thermodynamic equilibrium with an infinitely small fluid volume inside the membrane. Utilizing virtual concentration simplifies the characterization of species transport, requiring determination of only the membrane permeance to species (P_i) as the sole parameter [247]. The membrane permeances to species are the products of local diffusion and partition coefficients, where the partition coefficients are the ratios between the concentrations in the real solutions and the virtual ones. Table 28 compiles the principal equations used to depict membrane performance. The model assumes a species flux governed by a solution-diffusion transport mechanism within the membrane, incorporating electromigration resulting from varying transport velocities of species across the active layer (refer to Equation 29). Such equation, as all the other equations, is solved for the element (or compound) that makes up the species in solution. The description of transport necessitates the use of the membrane permeances to species (P_i), influenced by species properties (e.g., diffusion inside the membrane), membrane properties (e.g., membrane thickness, surface charge), and the interplay between both the species and the membrane (e.g., partition coefficients). Nevertheless, it is worth mentioning that such membrane permeances across the membrane are assumed to be constant [243].

Furthermore, the CP phenomenon incorporates similar transport mechanisms while also considering convective flux (see Equation 30). In this scenario, an average mean thickness (δ , a fitting parameter) is considered, despite literature indicating potential inhomogeneity of CP within membrane modules and test cells, impacting membrane performance [248]. For simplicity, δ , considered as one of the fitting parameters, is assumed to have a constant average value [246]. It is to be noted that Equation 30 is a fundamental equation solved numerically (valid within the studied domains) and not a semi-empirical equation that would have depended on the geometry of the module. CP permeances to species are derived from diffusion coefficients in the bulk solution. Additionally, the transport of species across the system (CP-layer and membrane) adheres to flux conservation at the membrane surface (Equation 31), electro-neutrality (Equation 32), and zero-current flow (Equation 33). To accurately fit experimental data for carbonates, the model accounts for their equilibrium in aqueous solution ($\text{H}_2\text{CO}_3/\text{HCO}_3^-/\text{CO}_3^{2-}$). The transport of these species induces pH variations within the membrane, potentially influencing membrane charge through protonation/deprotonation of functional groups and, consequently, ion exclusion mechanisms. Therefore, the model also incorporates the transport of alkalinity (basicity) across the membrane, as previously discussed by Hall et al. [249] and Nir et al. [250], who have elucidated the transport of H^+ and OH^- across RO membranes.

*Table 28: Main equations to describe the transport of species across NF membranes *
[244–246]*

Transport of species across the membrane

$$j_i = -P_i \cdot \left(\frac{dc_i}{dx} + z_i \cdot c_i \cdot \frac{d\varphi}{dx} \right) \quad (29)$$

Transport of species across the CP layer

$$j_i = J_v \cdot c_{p_i} = -P_i^\delta \cdot \left(\frac{dc'_i}{dx'} + z_i \cdot c'_i \cdot \frac{d\varphi'}{dx'} \right) + J_v \cdot c'_i \quad (30)$$

where $P_i^\delta = \frac{D_i^\delta}{\delta}$

Flux conservation at the membrane boundary

$$-P_i^\delta \cdot \left(\frac{dc'_i}{dx'} + z_i \cdot c'_i \cdot \frac{d\varphi'}{dx'} \right) + J_v \cdot c'_i = -P_i \cdot \left(\frac{dc_i}{dx} + z_i \cdot c_i \cdot \frac{d\varphi}{dx} \right) \quad (31)$$

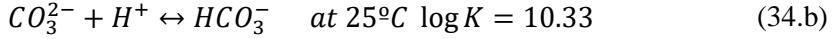
Electro-neutrality condition

$$\sum z_i \cdot c_i = 0 \quad (32)$$

Zero-current condition

$$\sum z_i \cdot j_i = 0 \quad (33)$$

Chemical equilibria for carbonate system



$$J_{C(IV)} = J_{H_2CO_3} + J_{HCO_3^-} + J_{CO_3^{2-}} \quad (34.c)$$

Net alkalinity (basicity flux)

$$J_{alk} = J_{HCO_3^-} + 2J_{CO_3^{2-}} + J_{OH^-} - J_{H^+} \quad (35)$$

* j_i is the flux of species i through the membrane, x is the dimensionless position in the membrane, P_i and P_i^δ are the membrane and CP-layer permeance species to species i , c_i is the concentration of species i , z_i is the valence charge of species i , and φ is the dimensionless virtual electrostatic potential in the membrane. Subscript ‘ refers to the CP layer.

For the description of the transport of species inside the CP-layer, the diffusion coefficients in the bulk solution were provided by Vanýsek [251] (see Table 29).

Table 29: Diffusion coefficients of the species in bulk solution ($D_i^\delta \cdot 10^{-12} \text{ m}^2/\text{s}$)[251].

| Na ⁺ | Cl ⁻ | K ⁺ | Ca ²⁺ | Mg ²⁺ | SO ₄ ²⁻ | Br ⁻ | H ₃ BO ₃ |
|-----------------|-----------------|------------------|--------------------------------|-------------------------------|-------------------------------|-----------------|--------------------------------|
| 1334 | 2032 | 1957 | 792 | 706 | 1065 | 2080 | 1281 |
| Li ⁺ | Rb ⁺ | Sr ²⁺ | H ₂ CO ₃ | HCO ₃ ⁻ | CO ₃ ²⁻ | H ⁺ | OH ⁻ |
| 1029 | 2072 | 791 | 2046 | 1185 | 923 | 9311 | 5273 |

The set of equations outlined in Table 28 was implemented and numerically solved using the Runge-Kutta method in Matlab, specifically with the ode23s function. As a result, and with the initial feed composition and permeate flux provided, the fitting parameters, comprising membrane permeances and CP-layer thickness, were adjusted to effectively align with the experimental data.

5.2 Results and Discussion

5.2.1 Effect of transmembrane pressure on permeate flux

An initial performance comparison of the NF membranes was carried out by examining the relationship between permeate flux and transmembrane pressure. Figures 48a) and 48b) illustrate the evaluation of permeate flux variation with

transmembrane pressure for the NF membranes when dealing with seawater and SWRO brine, respectively.

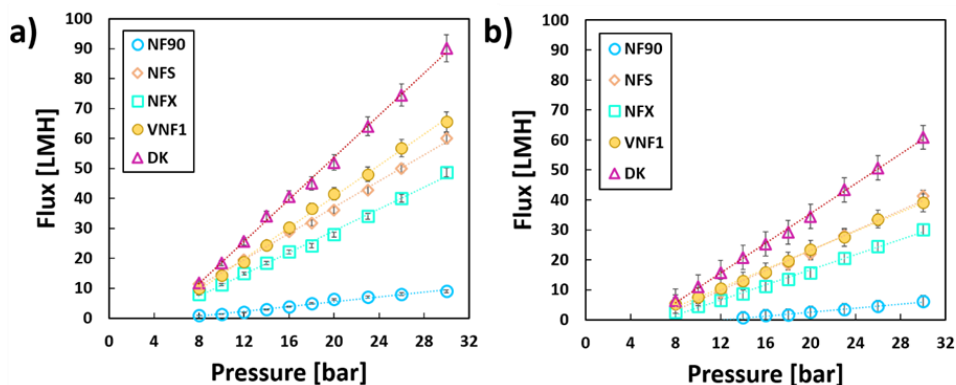


Figure 48: Experimental variation of permeate flux with transmembrane pressure for the 5 NF membranes treating seawater a) and SWRO brine b). Error bars are related to both the reproducibility and analytical procedure.

An increase in transmembrane pressure (8-30 bar) was found to result in a linear rise in flux for all experiments. According to the definition of permeability (refer to Equation 25), the slope of the flux variation allowed to compute the permeability of each NF membrane for the tested solution. Such permeability is not to be confused with the water permeability. As a matter of fact, the computed permeability considers specific factors (i.e., c_{w0}^m and D_w) whose values decrease with the increase of salt content in water, thus leading to a lower value of permeability than that of the water permeability of the membrane. It is worth mentioning that the values of the difference of osmotic pressure between the feed solution and permeate solution concerning the 5 commercial NF membranes when treating seawater and SWRO brine are given in Table 31 in Appendix C. Notably, DK exhibited the highest permeability among all NF membranes, with values of 3.5 LMH bar^{-1} and $2.48 \text{ LMH bar}^{-1}$ for seawater and SWRO brine, respectively. Despite DK and the other investigated membranes having active layers based on polyamide, it is likely that DK possesses a thinner active layer and a lower cross-linking degree, thereby enabling higher fluxes. In Figure 48a), a decreasing order of membrane permeability was observed as follows: DK ($3.5 \pm 0.05 \text{ LMH bar}^{-1}$) > VNF1 ($2.60 \pm 0.04 \text{ LMH}$

bar^{-1}) > NFS ($2.19 \pm 0.04 \text{ LMH bar}^{-1}$) > NFX ($1.81 \pm 0.04 \text{ LMH bar}^{-1}$) > NF90 ($0.40 \pm 0.02 \text{ LMH bar}^{-1}$). Concerning SWRO brine treatment, the permeability values were reduced. Hence, hydraulic permeability depended on intrinsic membrane properties, such as tortuosity and membrane thickness, as well as physico-chemical interactions, including solution viscosity, water diffusivity inside the polymer, the partial volume of water in the membrane, and the sorption coefficient of water by the membrane. The increase in concentration might have induced variations in these physico-chemical interactions, resulting in lower hydraulic permeability [58]. Notably, the order of permeability differed from that observed during seawater treatment. In Figure 48b), a distinct descending order was noted: DK ($2.48 \pm 0.05 \text{ LMH bar}^{-1}$) > NFS ($1.66 \pm 0.03 \text{ LMH bar}^{-1}$) > VNF1 ($1.58 \pm 0.04 \text{ LMH bar}^{-1}$) > NFX ($1.22 \pm 0.03 \text{ LMH bar}^{-1}$) > NF90 ($0.34 \pm 0.02 \text{ LMH bar}^{-1}$). Moreover, it was possible to observe that the performance of VNF1 was more susceptible to changes in feed salinity compared to NFS. Furthermore, NF90 consistently demonstrated significantly lower permeability when compared to all the other NF membranes, given its tight active layer structure, causing it to behave more like an RO membrane.

5.2.2 Effect of transmembrane pressure on rejections for seawater

In addition to hydraulic permeability, a crucial property to evaluate, characteristic of NF membranes, is the ability to selectively separate multivalent elements from monovalent ones. Figure 49 reported the experimentally achieved element rejections for the NF membranes, plotted against permeate flux, when (i) treating seawater with (ii) varied transmembrane pressure ranging from 8 to 30 bar. Specifically, Figures 49a) to 49e) depict the rejection of major elements present in seawater, while Figures 49f) to 49j) show the membrane rejection of "feasible" trace elements. It is noteworthy that the discrete points represent experimental data, complemented by the fitting of the SEDF model (described in Paragraph 5.1.5).

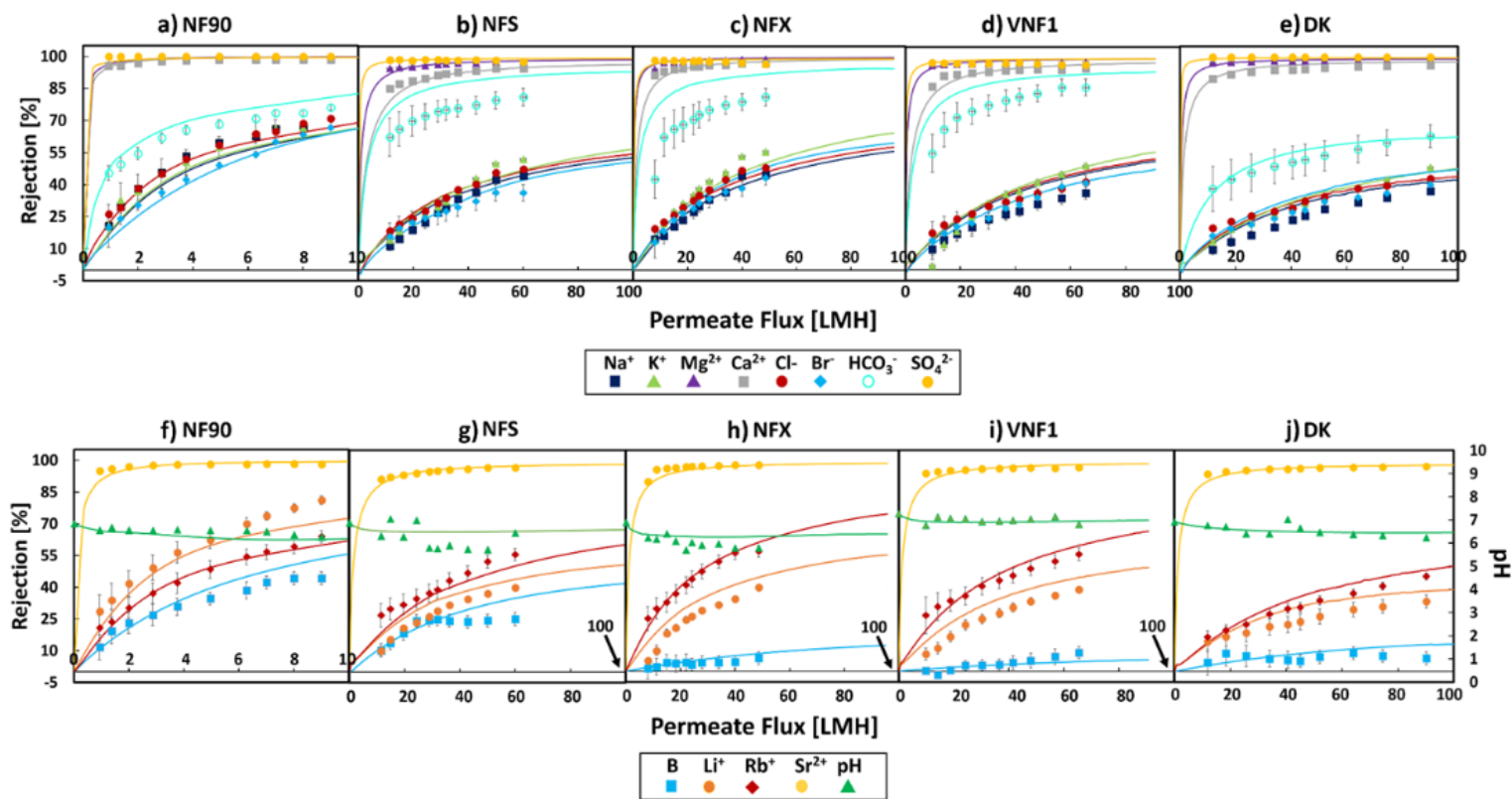


Figure 49: Experimental rejections as a function of permeate flux treating seawater for the 5 NF membranes: NF90 (a) major elements, f) trace elements), NFS (b) major elements, g) trace elements), NFX (c) major elements, h) trace elements), VNF1 (d) major elements, i) trace elements) and DK (e) major elements, j) trace elements). Points: experimental data. Lines: model fitting by the SEDF model.

Furthermore, due to the overlapping of magnesium and calcium rejections, a zoom of their trends for all NF membranes is provided in Figure 72 (Appendix C) to distinguish better the trends.

To begin, independently from the specific membrane or solute characteristics, it is essential to note that increasing transmembrane pressure led to an augmentation in the rejection of all solutes. This phenomenon was possible due to increasing permeate flux resulting from the elevated operating pressure. Specifically in the context of NF membranes, it is asserted that the flux of ions and solvent is not tightly coupled, or the coupling is minimal. In other words, the ion flux is primarily associated with diffusion and electro-migration [241,252,253]. This observation implies that a higher water flux, induced by increased operating pressure, caused solute dilution in the permeate, thereby enhancing membrane rejection for all solutes. However, as transmembrane pressure increased to relatively high operating levels, the impact on rejections gradually diminished, culminating in a rejection plateau for all NF membranes above 20 bar due to concentration polarization. It is worth mentioning that the concentration polarization factors of the investigated ions for all the 5 commercial NF membranes are reported in Figures 73 and 74 in Appendix C. Consequently, 20 bar was identified as the optimal operating pressure that maximizes membrane rejection, beyond which no significant improvements could be observed. Another noteworthy aspect applicable to all examined NF membranes was the identification of two distinct regions, independent of charge polarity: (i) high rejections for multivalent ions and (ii) low rejections for monovalent ions. The threshold distinguishing these regions varied depending on the NF membrane; for instance, NF90 exhibited this threshold at a rejection value of 70%, while the remaining four NF membranes (NFS, NFX, VNF1, and DK) had a lower threshold around 50%. This dual-region identification was attributed to the influence of both Donnan and dielectric exclusions on the transport of ionic species across the NF membrane.

Donnan exclusion, arising from the presence of fixed charges within the active layer, leads to the repulsion of ions with the same charge [175]. Commercial composite NF

membranes with an active layer made of polyamide typically present ionizable carboxylic and amine functional groups. Depending on the pH of operation, these groups may be ionized or not. In the present case, with the solution at neutral pH (refer to Table 26), it was expected the non-cross linked carboxylic groups of the amide structure would be ionized ($R-COO^-$) meanwhile the non-cross linked amine groups would be de-protonated ($R-NH_2$) [254]. In such case, therefore, the membrane would present a negative surface charge, allowing the transport of counter-ions (cations) while repelling co-ions (anions). On the other hand, dielectric exclusion derives from interactions between charged solutes and bound charges, induced by electrical polarization. It is associated with the electrostatic component of ion solvation energy, proportional to the square of the ion charge. In contrast to Donnan exclusion, dielectric exclusion operates independently of the sign of the ion charge, causing an extra rejection mechanism for each ion [241,255].

Discrepancies in the threshold between monovalent and multivalent solutes were likely linked to the free volume of the membrane active layer, resulting to be a more dominant factor for NF90 than for other membranes [254]. As the free volume of the polyamide membrane active layer narrows, dielectric exclusion becomes stronger, enhancing rejections [241,255]. It is possible to observe in Figure 49 that for NF90, major multivalent solutes exhibited rejections higher than 98% due to dielectric exclusion at operating pressures exceeding 20 bar (flux above 6.28 LMH) and a feed pH of 6.5. On the other hand, due to Donnan exclusion, the average rejection of SO_4^{2-} (100%) was higher than that of Mg^{2+} (98.4%) and Ca^{2+} (98.3%) due to the negatively charged membrane. Monovalent species showed average rejections within the range of 54-70%. More precisely, the positive monovalent ions, Na^+ and K^+ , exhibited rejections of 59.39% and 57.46%, respectively, whereas Cl^- , a negative monovalent ion, was rejected by 63.65%.

The distinction between monovalent and multivalent solute rejections confirmed the dielectric exclusion effect, while differences between positive and negative charged ions further confirmed the Donnan effect. In addition, despite its negative charge, Br^- exhibited the lowest rejection value (54% at 20 bar), likely due to the presence

of electric fields induced by the high SO_4^{2-} rejection, which accelerates the transport of anionic traces. Regarding HCO_3^- rejections, consistent with the dielectric exclusion effect, values lower than those of multivalent ions are reached (71% at 20 bar). However, unlike other ions, the presence of bicarbonates in seawater depended on the equilibrium with atmospheric $\text{CO}_2(\text{g})$ to which the feed solution was exposed. Concerning minor elements rejected by NF90 (see Figure 49f), at a pressure of 20 bar, B, Li^+ , Rb^+ , and Sr^{2+} were rejected by 49%, 70%, 54%, and 98%, respectively. This exemplifies how dielectric exclusion promotes higher rejections for multivalent ions. Taking into account the acid-base properties of B, the major B species at pH 6.5 was $\text{H}_3\text{BO}_3(\text{aq})$ ($\text{pK}_a(\text{H}_3\text{BO}_3/\text{H}_2\text{BO}_3^-) = 9.24$), a neutral species, that in theory was not expected to be affected by the polyamide active layer electric fields. Despite its small size, H_3BO_3 , with a Stokes diameter of 0.31 nm and a weak hydration shell, experiences rejections higher than 30% due to the active layer free volume of NF90. Overall, in the context of trace elements recovery from seawater, NF90 emerged as a viable option for selectively recovering Sr^{2+} . However, for major elements, NF90 proved effective for concentrating seawater but not for producing selective ion streams that are essential for MLD/ZLD schemes.

In the pressure range of 8-30 bar, meanwhile NF90 exhibited fluxes up to 9 LMH, the other NF membranes were considerably more permeable, with maximum fluxes at 30 bar ranging from 48 LMH (NFX) to 90 LMH (DK). The rejection patterns for NFS, NFX, VNF1, and DK can be explained in a manner similar to the NF90 membrane. Specifically, the four NF membranes exhibited higher selectivity between divalent and monovalent ions, with all major monovalent ions having rejections lower than 50%. All the four membranes showed SO_4^{2-} rejection higher than 97% at pressures higher than 20 bar: VNF1 (97.5%) < NFX (98%) < NFS (98.5%) < DK (>99.8%), a result of a combination of Donnan and dielectric exclusions. Similar observations could be made for Mg^{2+} at 20 bar, with NFS (97%) < VNF1 (97.5%) < DK (98.3%) < NFX (98.4%). Unlike magnesium, the latter membranes exhibited larger differences in Ca^{2+} rejection. While NFX and VNF1

kept presenting rejections higher than 95%, Ca^{2+} rejections dropped to 93% for NFS and 94% for VNF1.

A noteworthy distinction emerged, on the other hand, between NF90 and the other NF membranes under investigation regarding monovalent rejections, with all monovalent rejections falling below 40% at 20 bar. Among the monovalent ions, Cl^- and K^+ were particularly rejected, with the order of rejection being VNF1 (33%) < DK (34%) < NFS (38%) < NFX (37%) for Cl^- and DK (34%) < NFS (36%) < VNF1 (37%) < (42%) for K^+ . Slightly lower rejections were observed for Na^+ and Br^- at the same operating pressure, following the order VNF1 (28%) < DK (28.5%) < NFX (33%) < NFS (33.5%) for Na^+ and NFX (28%) < NFS (29.5%) < VNF1 (30.7%) < DK (32%) for Br^- .

Regarding the “feasible” trace elements, NFS, NFX, VNF1, and DK exhibited similar trends, displaying high selectivity towards Sr^{2+} (higher than 95%) and high permeability towards Rb^+ and Li^+ . As far as B is concerned, rejections were more or less equal to 0 due to its neutral behaviour at pH 6.5.

As for the fitting of the SEDF model with the experimental data, excellent results were achieved for most of the ions. Higher discrepancies were achieved for instance in the case of HCO_3^- . The main reasons for this are:

- (i) the equations of the SEDF model are subjected to electro-neutrality, so the fitting for one of the components is not so accurate (major ions);
- (ii) the alkalinity defines the pH of the solution, so the model fitted properly one of them (pH) and not the other (alkalinity). Most likely some of the species controlling the buffering capacity of the solution were not considered.

In summary, these four newly commercial NF membranes are well-suited for pre-treatment steps in MLD and ZLD schemes due to their exceptional selectivity, distinguishing them from NF90. However, it is essential to highlight that, due to the fact of presenting positive lithium rejections when dealing with seawater, it will avoid their total recovery, since part of them will be concentrated in the retentate stream, but in a lesser extent in comparison to multivalent elements.

5.2.3 Effect of transmembrane pressure on rejections for SWRO brine

The rejection performances of the NF membranes for various solutes were assessed in the context of SWRO brine treatment. In this case, the experimental variations of element rejections over permeate flux are illustrated in Figure 50. Specifically, Figures 50a)-e) focus on membrane rejections of components present in substantial amounts in the brine, while Figures 50f)-j) depict those of the "feasible" trace elements. Similar to the previous case (seawater treatment), the experimental data for this scenario were accompanied by the results achieved with the SEDF model.

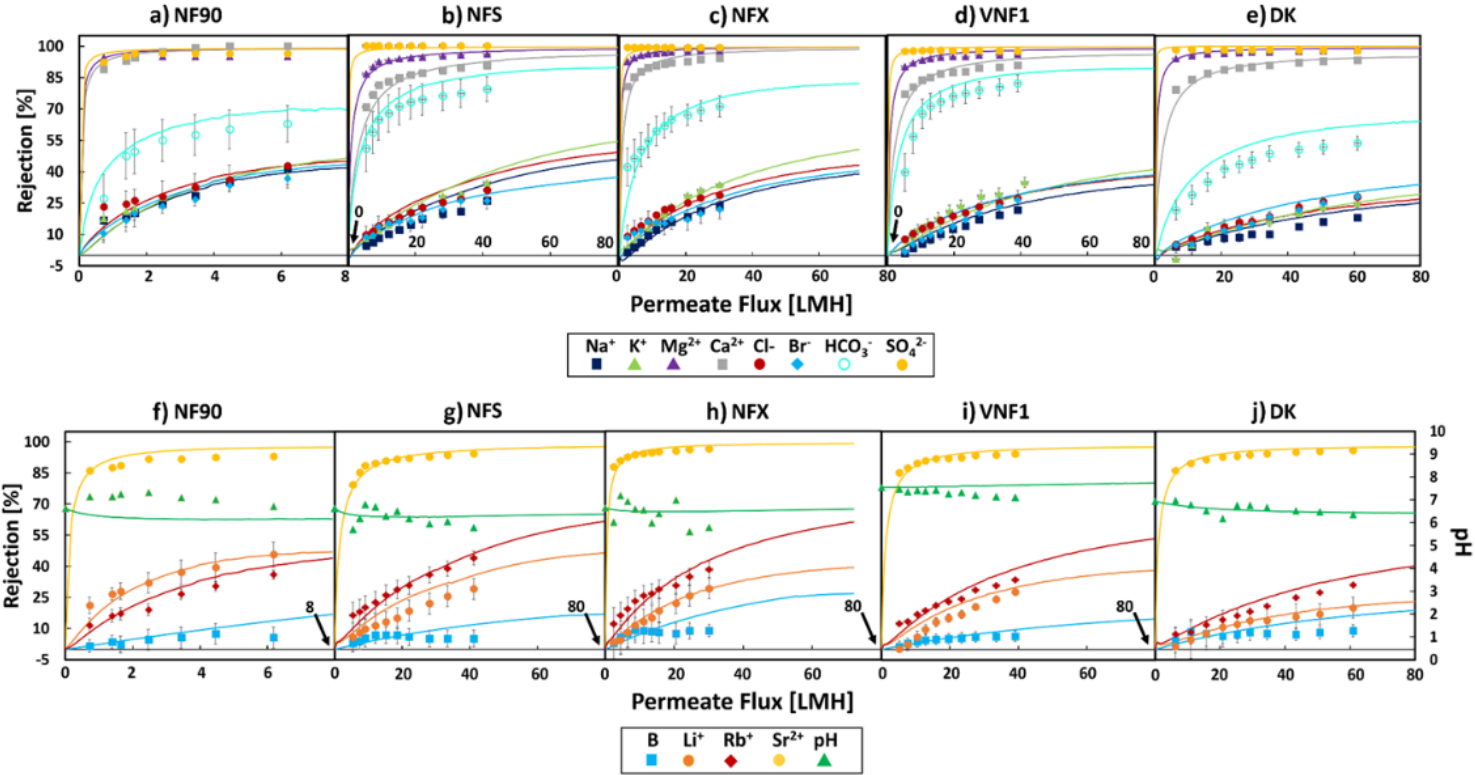


Figure 50: Experimental rejections as a function of permeate flux treating SWRO brine for the 5 NF membranes: NF90 (a) major elements, f) trace elements), NFS (b) major elements, g) trace elements), NFX (c) major elements, h) trace elements), VNF1 (d) major elements, i) trace elements) and DK (e) major elements, j) trace elements). Points: experimental data. Lines: model fitting by the SEDF model.

In this scenario, it was also possible to distinguish two primary groups: (i) characterized by the prevalence of multivalent elements (present in the brine in significant quantities) and (ii) associated the monovalent elements present in major quantity. This categorization exemplified the dominance of the dielectric exclusion effect over the Donnan exclusion effect, particularly evident when the five NF membranes were previously evaluated for seawater valorisation. Upon comparing the two scenarios, namely seawater and SWRO brine treatment, a noticeable reduction in all ion rejections was observed at the same operating pressure (i.e., 20 bar). This decrease was attributed to the increased feed concentration, causing charge screening and consequently diminishing the dielectric exclusion effect [241]. However, the decline in rejections was not uniform for all ions and varied among the NF membranes too. For instance, considering the rejection of SO_4^{2-} , NF90 and DK exhibited reduced rejections (from >99.9% to 97% and >99.9% to 98% for NF90 and DK, respectively), whereas NFS, NFX, and VNF1 maintained rejections above 97% at 20 bar. Concerning positive multivalent ions, a different behaviour among the membranes was also noted. NF90 experienced the most significant drop in Mg^{2+} rejection (from 98.5% to 95%), while NFS and VNF1 displayed similar patterns with Mg^{2+} rejections slightly above 94.6%. In contrast, NFX and DK demonstrated less susceptibility to variations in Mg^{2+} feed content, maintaining Mg^{2+} rejections higher than 97% when treating SWRO brine. As for Ca^{2+} , meanwhile NF90 was the only membrane to exhibit larger rejection drops for both SO_4^{2-} and Mg^{2+} , no important differences were witnessed for Ca^{2+} (i.e., 98% to 97%). Conversely, the other NF membranes showed more substantial rejection drops for Ca^{2+} , surpassing those for SO_4^{2-} and Mg^{2+} , with values reaching up to 87%. NFX and DK demonstrated to be slightly more resistant to variations in feed concentration, achieving Ca^{2+} rejections above 91%. Despite a few exceptions, a general trend could be observed for the drop in rejection of multivalent ions across the five NF membranes passing from seawater to brine: $\text{SO}_4^{2-} < \text{Mg}^{2+} < \text{Ca}^{2+}$. This reaffirmed the influence of dielectric exclusion on the rejection of multivalent elements, while emphasizing that the increase in concentration led to charge screening, thereby weakening the dielectric exclusion

effect. In contrast to the multivalent elements, the monovalent ones exhibited significantly more pronounced drops in rejection when transitioning from seawater to brine treatment. Notably, NF90 displayed substantial decreases in monovalent rejections compared to the other investigated NF membranes. While monovalent rejections decreased by over 50% for NF90, the remaining four NF membranes experienced drops below 50%. Nevertheless, a consistent trend in the single values of monovalent rejections was seen across all membranes for each monovalent element: $NF90 > NFS > NFX > VNF1 > DK$, with NF90 demonstrating the highest rejections for major monovalent elements and DK exhibiting the lowest. The larger rejection drops for major monovalent elements compared to major multivalent ones proved the impact of charge screening resulting from increased feed concentration. Notably, DK stood out as the only NF membrane with Na^+ rejection falling below 10% at 20 bar, suggesting potential higher selectivity than the other NF membranes, particularly in treating SWRO brine. Examining HCO_3^- rejections, NF90 experienced the most substantial drop (71% to 55%), while NFS and VNF1 maintained rejections above 75%. Considering the minor elements, also known as the “feasible trace elements” (see Figures 50f-j)), similar trends were noted as for the major elements. NF90 exhibited rejection drops exceeding 50%, unlike the other NF membranes which saw drops below 50%. While Sr^{2+} maintained high rejections above 92%, monovalent elements experienced larger drops. In addition, NF90 and NFS displayed substantial drops for B (38.5% to 4.5% and 24.3% to 6.0%, respectively), whereas NFX, VNF1, and DK demonstrated consistently low rejections when comparing seawater and SWRO brine scenarios. As for the fitting of the SEDF model, also in this case good results were achieved, and similar considerations can be made as the ones of the previous paragraph (seawater treatment).

5.2.4 Membrane permeances to species through the SEDF model

As noted in Figures 49 and 50, the SEDF model effectively fitted the trends and rejection values in relation to the permeate flux. Consequently, the SEDF model facilitated the determination of membrane permeances to species for each case study. The permeance values for both major and trace elements are presented in Figure 51. It is important to highlight that the model specifically considered the predominant species of the chemical element at the brine pH, as mentioned previously.

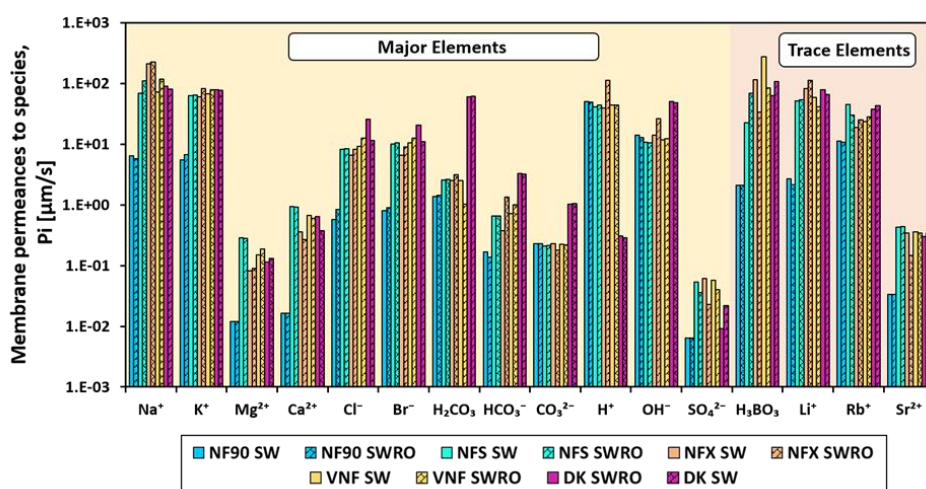


Figure 51: Membrane permeances to species [$\mu\text{m/s}$] for the 5 NF membranes tested with seawater and SWRO brine. Filled and dashed pattern represent seawater and SWRO brine, respectively.

The calculated membrane permeances to species demonstrated strong alignment with both Donnan and dielectric exclusion phenomena. Notably, the membranes in this study exhibited a negative surface charge at the operational pH, resulting in higher permeances towards cations than anions. For instance, across all cases, membrane permeances to single-charged cations (Na^+ , K^+ , Li^+ , Rb^+ , and H^+) surpassed those to single-charged anions (Cl^- , Br^- , HCO_3^- , and OH^-), often differing by an order of magnitude. In the case of treating seawater with the NFS membrane, the permeances followed the order: Na^+ ($69.1 \mu\text{m/s}$) > K^+ ($62.9 \mu\text{m/s}$) > Li^+ (51.6

$\mu\text{m/s}) > \text{Rb}^+ (44.6 \mu\text{m/s}) > \text{H}^+ (41.1 \mu\text{m/s}) \gg \text{OH}^- (10.7 \mu\text{m/s}) > \text{Br}^- (10.1 \mu\text{m/s}) > \text{Cl}^- (8.2 \mu\text{m/s}) > \text{HCO}_3^- (0.6 \mu\text{m/s})$.

Moreover, the influence of dielectric exclusion was evident, with membrane permeances to double-charged ions exhibiting values up to two orders of magnitude lower. Specifically, permeances to species like Ca^{2+} ($0.94 \mu\text{m/s}$), Sr^{2+} ($0.43 \mu\text{m/s}$), Mg^{2+} ($0.28 \mu\text{m/s}$), and SO_4^{2-} ($0.05 \mu\text{m/s}$) reflected this effect. Membrane permeances towards neutral species ($\text{H}_3\text{BO}_3(\text{aq})$ and $\text{H}_2\text{CO}_3(\text{aq})$) were not affected by membrane charge, but primarily governed by steric hindrance, allowing their free permeation. For instance, the NFS membrane permeance to $\text{H}_3\text{BO}_3(\text{aq})$ was $22.4 \mu\text{m/s}$ when treating seawater, with similar trends observed for all membranes in both scenarios. Comparing the different NF membranes, NF90 exhibited significantly lower permeances to species than the others, attributed to its structural similarity to RO membranes. Notably, a slight increase in permeances was observed when transitioning from seawater to SWRO brine for all NF membranes. This increment could be linked to the higher initial composition, enhancing ion transport across the membranes. This relationship between membrane permeances and ionic composition has been previously reported by Bason et al. [252] and Yaroshchuk et al. [256].

5.2.5 Selectivity of the NF membranes

The performance of NF membranes often grapples with a significant challenge: the trade-off between permeability and selectivity. Typically, achieving high selectivity entails a compromise with reduced permeability, and vice versa. To spot the most efficient NF membrane among those examined in this study, the selectivity of each membrane against the permeability was illustrated, focusing on the selectivity between the dominant multivalent elements (Mg^{2+} and Ca^{2+}) in relation to the prevalent monovalent elements (Na^+ and Cl^-). Figure 52 depicts these relationships. The reported permeability is not to be confused with the water permeability, presenting lower values than the one of the latter due to c_{w0}^m and D_w that decrease with the increase of salt content in water. The data is presented for a pressure of 20

bar, chosen as the optimal value. This decision was based on the enhanced selectivity observed for both monovalent and multivalent elements at this operational pressure. Beyond 20 bar, concentration polarization occurs, leading to reduced rejection rates for multivalent elements and thereby compromising selectivity. Notably, there is a significant difference in permeate flux between seawater and brine solutions, with the flux potentially doubling for seawater compared to brine.

In Figure 52a), NF90 deviates from the typical NF membrane behaviour and mirrors that of a RO membrane, displaying relatively low selectivity (<0.2) and low permeability (0.4 LMH bar^{-1}) during seawater treatment. This deviation from the typical NF membrane behaviour, which aims to generate two ion-selective streams rather than desalinate seawater/brine, suggests that NF90 may not be optimal for its intended role as a membrane used in a pre-treatment step in MLD/ZLD schemes focused on mineral recovery from seawater/brine. NFS and NFX exhibited comparable selectivity (around 0.5) but behaved differently in terms of permeability, with NFS having slightly higher permeability. Similarly, VNF1 and DK showed similar selectivities (>0.6), but DK boasted higher permeability, placing it in the region of ideal NF membranes.

This trend among the five NF membranes was maintained when treating SWRO brine, as depicted in Figure 52b). However, all selectivity values were higher than those in the seawater scenario. This disparity was attributed to the decrease in multivalent element rejections being less pronounced compared to the decrease in monovalent element rejections, owing to the increase in feed concentration. It is worth noting that for each NF membrane, the selected selectivity factors remained relatively consistent when treating seawater. However, when employing SWRO brine as the feed solution, the factors $\text{Mg}^{2+}/\text{Na}^+$ and $\text{Ca}^{2+}/\text{Na}^+$ for each membrane exceeded the factors $\text{Mg}^{2+}/\text{Cl}^-$ and $\text{Ca}^{2+}/\text{Cl}^-$. This discrepancy likely arose from the significant decrease in Na^+ rejection relative to Cl^- rejection, influenced by the Donnan exclusion effect.

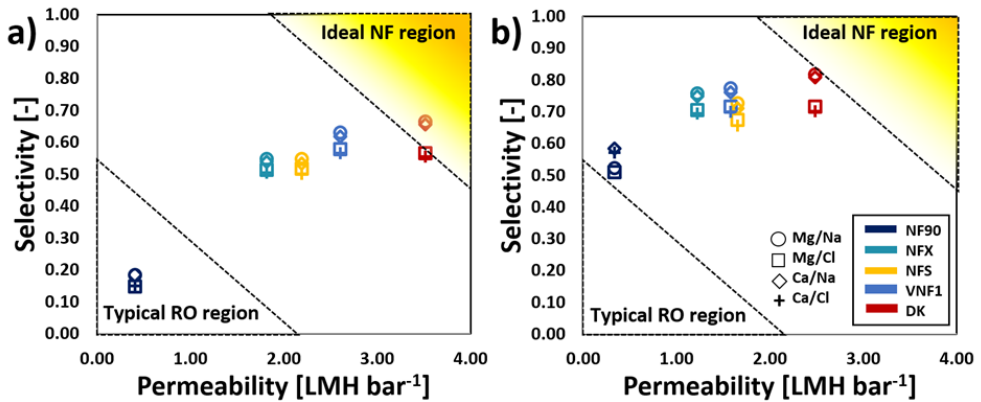


Figure 52: Selectivity vs. Permeability for the 5 NF membranes treating seawater a) and SWRO brine b) at 20 bar.

The outcomes illustrated in Figure 52 underscored DK's superior performance relative to the other evaluated NF membranes, showcasing an exceptional balance of enhanced selectivity and permeability. This discovery holds significant implications for the selection of the most suitable NF membrane in the context of MLD/ZLD schemes for seawater and brine treatment, as depicted in Figure 53. It is noteworthy mentioning that, in the new RO seawater desalination schemes, the integration of a NF stage before the RO stage is being postulated since the benefit of removing divalent scaling species at the RO stage promotes a decrease of the operation expenses. This integration offers several advantages: firstly, downstream RO operations can occur at lower pressures and experience reduced membrane scaling, thus extending the lifespan of RO membranes. While the upfront capital expenses increase due to the integration of the NF stage, the subsequent reduction in operational costs justifies this investment. The permeate stream feeds the RO stage and the rejected stream becomes a source for mineral recovery, specially Ca and Mg salts [163]. Alternatively, Scenario 2 (RO-NF) offers additional benefits. Firstly, compared to a standalone RO plant, incorporating a downstream NF stage reduces the volume of brine discharged into the environment and enhances overall desalination facility recovery rates. Typically, brine disposal costs constitute a

significant portion (ranging from 5% to 30%) of total desalination plant expenses [166]. By reducing brine discharge volume and capitalizing on revenue generated from recovered minerals, significant cost savings in brine disposal can be achieved, as demonstrated by Morgante et al. [44].

Secondly, compared to Scenario 1 (NF-RO), Scenario 2 enables higher multivalent/monovalent selectivity. This translates into the recovery of higher purity products, leading to increased revenue potential, and simplifies downstream purification steps in potential MLD/ZLD schemes, consequently reducing both capital and operational expenses associated with such schemes.

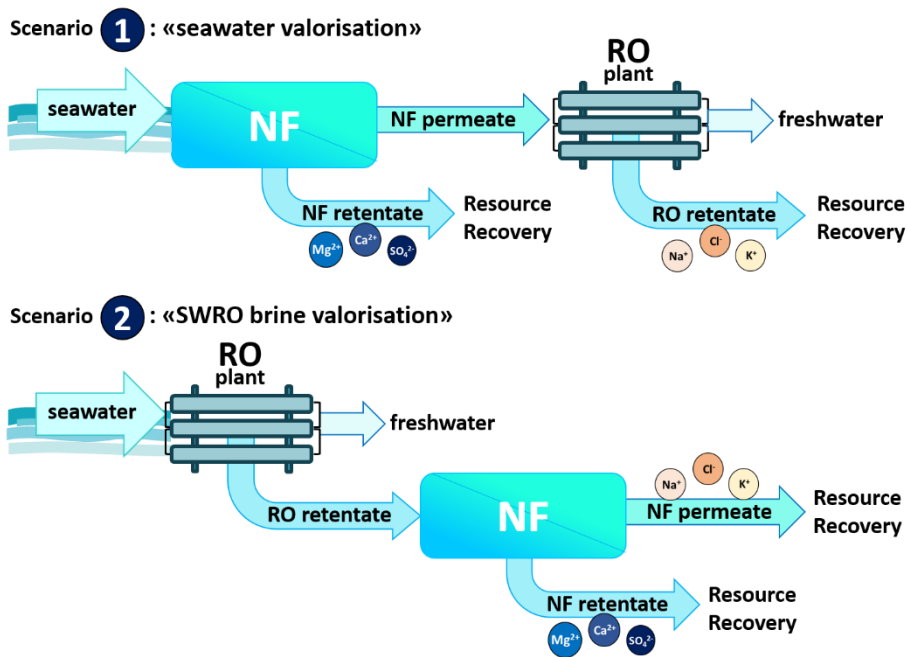


Figure 53: Integration of NF technology within seawater desalination schemes.

All in all, while this study primarily explored the valorisation of seawater and SWRO desalination brine through NF, its findings offer broader implications for evaluating NF treatment across diverse saline sources. For instance, the results provide insights into the potential application of the investigated NF membranes for recovering Li^+ from geothermal brines, where Li^+ concentrations surpass those found in seawater

[257]. Additionally, the research findings could guide the assessment of the suitability of these membranes for selectively separating Mg/Li from salt-lake brines, which often boast Li^+ concentrations exceeding 1 g/L [258]. Finally, this work extends its utility to investigate the feasibility of NF treatment for Mg^+ recovery from coal mining brines or, more broadly, resource recovery and desalination of brackish water [259,260].

5.3 Conclusions

The study of Chapter 5 focused on assessing the feasibility of NF as a selective pre-separation process for the potential downstream retrieval of minerals from seawater and SWRO brine. The performance of five NF membranes (NF90, NFS, NFX, VNF1 and DK) was comprehensively examined, with a focus on their effectiveness in rejecting both major and minor elements. The NF membranes exhibited notable potential in separating multivalent cations, such as Mg^{2+} , Ca^{2+} , and Sr^{2+} , from monovalent ions like Na^+ , K^+ , Cl^- , and Br^- .

The main results can be summarized as follows:

1. Validation of experimental data and model fitting: The study observed a strong agreement between the experimental ion rejection rates and the predictions produced by the SEDF model.
2. Optimal transmembrane pressure: The optimal operating pressure was 20 bar at which stable rejection levels with limited increases were observed.
3. Surface membrane charge analysis: All NF membranes displayed a negative surface membrane charge, as deduced from the computed membrane permeances and experimental rejection trends.
4. Multivalent cation rejection: Consistent with the Donnan and dielectric exclusion effects, the membranes exhibited high rejections for multivalent cations. For instance, Mg^{2+} , Ca^{2+} , and Sr^{2+} rejections exceeded 97.1%, 92.8%, and 96.5% in seawater, and 94.5%, 87.1%, and 91.7% in SWRO brine, respectively.

5. Comparison between seawater and SWRO brine treatment: Rejections of monovalent elements experienced more significant declines during the transition from seawater to SWRO brine treatment compared to multivalent ones, attributed to a screening effect.
6. Performance of the DK membrane: Among the membranes studied, the DK membrane demonstrated the highest permeability (3.5 LMH bar^{-1}) and selectivity factor (>0.6) for multivalent elements relative to monovalent ones, proving its superior efficacy for selective separation of minerals.

In conclusion, the research confirmed the suitability of the studied NF commercial membranes for selective pre-concentration of valuable minerals from seawater and SWRO brine. The DK membrane emerged as the most efficient candidate. This study significantly contributes to understanding NF potential in the circular valorisation of seawater and SWRO brine.

The next steps (reported in Chapter 6) involved characterizing and evaluating more in depth the performances of two of these high-performing membranes (NFX and VNF1) with a spiral-wound configuration and validating the SEDF mathematical model. It is to be noted that the main reason of selecting these two membranes lied in the fact that the DK membrane already presented a substantial amount of data concerning its characterization, therefore the focus was brought to NFX and VNF1.

6 “Evaluation of enhanced nanofiltration membranes for improving magnesium recovery schemes from seawater/brine: integrating experimental data with a techno-economic assessment”

This study delves deeper into the performance analysis of two out of the five highly selective commercial membranes tested in Chapter 5. More specifically, these were Synder NFX and Vontron VNF1. While the Synder NFX has found occasional applications in the food industry for phenolic compound recovery [226,261] and in wastewater treatment for micro-pollutant removal [262,263], Vontron VNF1 usage has been even scarcer, primarily in the shale gas industry [223] and radioactive solutions treatment [264]. Due to their limited utilization, comprehensive information about the materials and properties of these membranes in scientific literature is currently poor. To address this gap, the initial approach of this study involved a detailed physicochemical characterization of both membranes using advanced analytical techniques such as Scanning Electron Microscopy (SEM), Fourier Transform Infrared Spectroscopy (FTIR), Water Contact Angle (WCA) and streaming potential analysis. Then, both NFX and VNF1 were experimentally tested in an open-loop configuration (i.e. concentration mode), using synthetic seawater and SWRO brine. The results of these tests were utilized to validate a multi-scale mathematical model previously introduced in Chapter 5 [265]. Following this validation, a holistic approach integrating the technical model and an in-depth economic analysis was employed to conduct a thorough techno-economic evaluation. The focus of this evaluation was specifically on maximizing the revenue generated by magnesium recovery from seawater and desalination brine.

6.1 Materials and methods

6.1.1 Membranes and characterization procedure

The two NF membranes under investigation in this study were:

1. NFX 2540 (Synder Filtration, USA)
2. VNF1 2540 (Vontron, China)

The main properties provided by the manufactures of such membranes were already reported in Table 26 (Paragraph 5.1.1). In this study, NFX and VNF1 were firstly characterized to gain knowledge on their chemical structure, morphology, hydrophilicity and surface charge.

In order to perform a thorough comparative assessment of membrane chemical structures, Attenuated Total Reflection Fourier Transform Infrared Spectroscopy

(ATR-FTIR) was employed, utilizing the Jasco 4700 instrument from Japan. This advanced analytical technique enabled precise characterization of the membranes' functional groups, providing valuable insights into their molecular structures for comparative analysis. The FTIR Jasco 4700 has a spectrum range of 350-4400 cm^{-1} , and the Attenuated Total Reflection (ATR) crystal used in this study is constructed from diamond material.

Cross-sectional and surface imaging were carried out employing the Neon40 Crossbeam™ Field Emission Scanning Electron Microscopy (FESEM) system by Carl Zeiss, operating at an acceleration voltage of 5 kV. Before FESEM analysis, the membrane samples were precisely sectioned with a scalpel to maintain structural integrity and then coated with a 5 nm-thick carbon layer using an ion spotter coater, the LITH-SD900C (USA).

The assessment of surface hydrophilicity and wettability characteristics was conducted by determining water contact angles (WCAs) using the sessile drop method with a KRUSS DSA25S instrument (Germany). To guarantee precision, a water drop volume of 5 μL was used, and measurements were carried out at a controlled rate of 2.67 $\mu\text{l/s}$, maintaining a constant temperature of 20°C. Each WCA measurement was repeated four times, and an average value was considered. All samples were adequately dried in a vacuum at 25°C for 24 hours before the measurement.

For streaming potential analysis, measurements were carried out using the electrokinetic analyser SURPASS (Anton Paar). Two film specimens of the NF membrane (20x10 mm^2) were mounted face-to-face in the adjustable-gap cell (105 \pm 5 μm). Streaming potentials were measured at 25°C using 1 mmol/L KCl as the background electrolyte, adjusting the pH from 3 to 6 with HCl or NaOH.

6.1.2 Preparation of synthetic solutions

To evaluate in depth the efficiency of NFX and VNF1 for both seawater and SWRO brine valorisation, synthetic solutions were employed for this specific study. As in

the previous study reported in Chapter 5, synthetic seawater with a typical composition of the Mediterranean region was employed. Concerning the brine, a synthetic SWRO brine was prepared, taking into account a 45% water recovery of a SWRO desalination plant. The composition of the solutions was previously reported in Table 27 (in Paragraph 5.1.1). Synthetic seawater and desalination brine solutions were meticulously prepared using deionized water and high-grade analytical reagents. These were: NaCl, $\text{MgSO}_4 \cdot 7\text{H}_2\text{O}$, $\text{MgCl}_2 \cdot 6\text{H}_2\text{O}$, KCl, NaBr, H_3BO_3 , LiCl (PanReac), $\text{CaCl}_2 \cdot 2\text{H}_2\text{O}$ (Chem-lab), NaHCO_3 (Scharlau), Rb_2CO_3 (Aldrich), and $\text{Sr}(\text{NO}_3)_2$ (Acros Organics). Their analytical grade was necessary to ensure precision and accuracy in the experimental results. Additionally, HNO_3 69% (w/w) and HCl 37% (w/w), obtained from Panreac, were used for preparing samples for ICP analysis and adjusting the pH of the synthetic solutions, respectively.

6.1.3 Pilot set-up description

A spiral-wound pilot setup (see Figure 54) was employed to evaluate the performance of two commercial NF membranes in the context of seawater and brine valorisation.

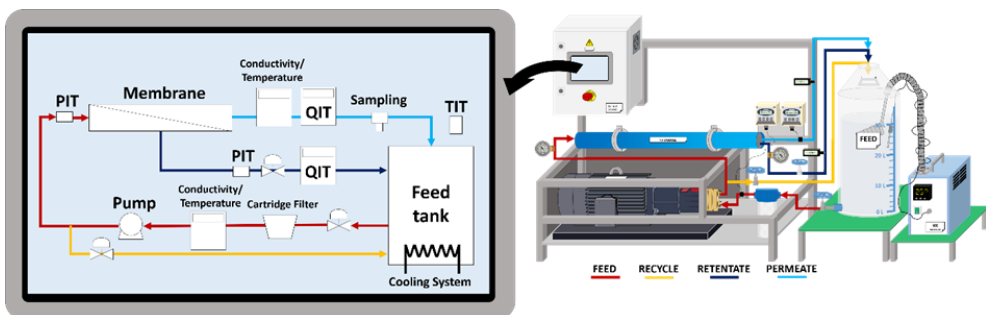


Figure 54: Process flow diagram and conceptual scheme of the experimental NF pilot unit.

As depicted in Figure 54, the pilot plant consisted of several essential components. Initially, 30 L of the feed solution (seawater or SWRO brine) was stored in a feed

tank, where it was rigorously maintained at a temperature of 25 ± 2 °C through the use of a refrigerator (DIGITCOOL, J.P.Selecta). A high-pressure diaphragm pump (Hydracell Wanner G10X, USA) was employed to propel the feed solution, which first passed through a cartridge filter (positioned before the pump inlet). This pre-filtering step aimed to eliminate corrosion solids that could potentially compromise the functionality of the pump.

Following this, a portion of the feed solution was redirected back to the feed tank, while the remaining portion was directed to a pressure vessel (Phoenix 2540) housing a spiral-wound NF membrane with an active area of 1.4 m². The retentate and permeate streams could then be circulated back to the feed tank based on the adopted configuration and test type. Regulation of the transmembrane pressure (TMP) and cross-flow rate was achieved through a bypass and needle valve positioned on the feed and retentate streams, respectively. Additionally, pressure gauges at the feed and retentate streams facilitated the continuous monitoring of the TMP.

Furthermore, sensors, connected to a Programmable Logic Controller (PLC), played a crucial role in monitoring:

1. The flow rates (measured by an SMC flow meter) of the permeate and retentate streams.
2. The conductivity and temperature (measured by Greisinger electronic devices) of both the feed and permeate streams.

6.1.4 Experimental testing

The experimental campaign conducted in this study consisted of four main tests, each assessing the performance of the NF membranes with seawater and SWRO brine. The primary objective was to conduct each test at various permeate recovery values while maintaining a fixed optimal operating pressure. The results of these tests were crucial for validating a technical model, providing essential insights into the economic aspects of each NF membrane for seawater/brine valorisation.

Before each test, the NF membrane underwent pressurization with distilled water at 22 bar to eliminate traces of glycerine, initially present in the membrane to maintain the pore structure. Subsequently, two essential steps were performed:

1. Adjusting the pH of the feed solution to 6.5 through the addition of HCl and inserting anti-scalants to prevent potential scaling within the NF module.
2. Fixing the feed solution temperature at 25°C using a refrigerator.

Following these preparations, the NF membrane was pressurized with 30 L of the original feed solution for two hours at 22 bar, maintaining a cross-flow rate of 3.46 L/min. The pressurization step was conducted in a "Closed-Loop" configuration, where both retentate and permeate solutions were recycled back to the feed tank, ensuring the constant composition of the feed solution. After pressurization, the pressure was adjusted to 20 bar, the optimal operating pressure identified in Chapter 5 and this pressure was maintained for all the subsequent experimental tests.

To evaluate the performances of NFX and VNF1 at different permeate recoveries, tests were conducted in an "Open Loop" configuration. In this setup, the permeate solution was collected in a separate tank meanwhile the retentate solution continued to be recirculated back to the feed solution, simulating multiple NF modules in series. Permeate recovery was assessed within a range from 0 to 80%. During the entire test, 50 mL samples of both the feed solution and permeate solution were taken at permeate recovery steps of 10%, with continuous monitoring of conductivity, pH, and temperature. At the conclusion of each test, the membrane was subjected to cleaning with de-ionized water twice, following these conditions: (i) 10 bar and cross-flow velocity of 1 m/s for 30 min, and (ii) 32 bar and cross-flow velocity of 1 m/s for 2 hours.

6.1.5 Analytical procedure and data analysis of samples

For the analysis of aqueous samples (feed, retentate, and permeate) taken during the tests, the concentration of Cl^- and SO_4^{2-} was determined using IC with a DIONEX AQUION system. Specifically, a DIONEX-ADRS 600 column and 25 mM KOH as

the mobile phase were employed for this analysis. The concentration of HCO_3^- was determined through automatic titration using a Mettler Toledo T70 - Rondolino instrument, with a standardized 1 mM HCl solution as the titrant.

The concentration of other elements in solution was achieved using spectrometry, specifically the 7800 inductively coupled plasma mass spectrometry (ICP-MS) and 5100 inductively coupled plasma optical emission spectrometry (ICP-OES) instruments from Agilent Technologies. Conductivity and pH of the samples were directly measured during the tests using a pH-meter (CRISON GLP-22) and a conductivity meter (CRISON GLP-31).

To assess the performance of NFX and VNF1 in this specific study, four indicators were determined. Two of them are the ion Rejection and the permeate flux which were described previously: More precisely, they were calculated according to Equation 26 (Paragraph 4.1.5) and Equation 28 (Paragraph 5.1.4), respectively. Since tests were conducted employing an “Open Loop” configuration, the feed solution concentration increased during the experiments, thus the concentration factor CF [-] of element i was calculated (see Equation 36):

$$CF_i = \frac{C_{r,i}}{C_{f,i,0}} \quad (36)$$

Where $C_{r,i}$ is the concentration of element i in the retentate solution at a certain fixed permeate recovery [mg/L] and $C_{f,i,0}$ is the feed concentration of that element at the beginning of the experiment. Finally, the permeate recovery $p.r$ [%] was determined according to Equation 37:

$$p.r = \frac{V_p}{V_f} * 100 \quad (37)$$

Where V_p and V_f are the volume [L] of the permeate solution.

6.2 Modelling

6.2.1 NF multi-scale technical model

To conduct a technical analysis of NF that treats seawater or SWRO brine the SEDF model was employed. The model was previously described in Chapter 5 (more precisely, refer to Paragraph 5.1.5). However, in this study, the membrane permeances to species, that were achieved in the previous study (Paragraph 5.2.4), were used to describe the flux of the species across the membrane, accounting for ion diffusivity inside the membrane, partition coefficients, and membrane properties, among others. Therefore, the SEDF model, based on the previously computed permeances to species, was used to predict the membrane behaviour (but also validate the SEDF model used for the flat-sheet configuration) and carry out the techno-economic assessment.

6.2.2 MRC technical model

To recover $\text{Mg}(\text{OH})_2(\text{s})$ from the NF treated seawater/SWRO brine, a downstream reactive crystallizer was considered. Simple mass balance equations (see Equations 39a-c) of Table 30 were utilized to determine the final quantity of $\text{Mg}(\text{OH})_2(\text{s})$ produced. The MRC is a plug flow reactor in which magnesium is recovered from the feed solution (i.e., NF retentate) in the form of solid $\text{Mg}(\text{OH})_2(\text{s})$ through direct mixing with an alkaline reactant: an aqueous solution of NaOH. For the precipitation of $\text{Mg}(\text{OH})_2(\text{s})$ (which occurs at a reaction pH 10.4 [100]), one magnesium ion of the brine must react with two hydroxyl ions from the alkaline solution. It is noteworthy that at pH < 10.4 all bicarbonates precipitate as calcium carbonates, potentially compromising the purity of recovered $\text{Mg}(\text{OH})_2(\text{s})$. The mass flow rate Q_{NaOH} [kg/h] of the required alkaline solution was calculated according to Equation 38a). More precisely, the calculation of Q_{NaOH} took into account two contributions: (i) the molar flow rate of magnesium $Q_{\text{feed}, \text{Mg}^{2+}}$ [mol/h] multiplied by the effective conversion rate of magnesium $\%_{\text{Mg}^{2+}}$ and (ii) the quantity of NaOH employed in precipitating the bicarbonates present in the brine. Here, Q_{feed} is the volumetric feed

flow rate [m³/h] and C_{feed,HCO_3^-} is the molar concentration [mol/m³] of the bicarbonates in the brine. The conversion factor was assumed to be equal to 100% operating at pH > 10.4 (since at this precise pH, a maximum conversion of 98% was previously observed in literature [60]). Additionally, the flow rate Q_{NaOH} depends on the operating molar concentration of NaOH C_{NaOH} (assumed to be 1 mol/L in this study). Simple mass balances (Equations 38b and 38c) were further used to compute the total outlet volumetric flow rate Q_{out} and the mass flow rate of Mg(OH)₂(s) produced $M_{Mg(OH)_2}$ where $MW_{Mg(OH)_2}$ is the molecular weight of Mg(OH)₂(s) [g/mol].

Table 30: Main mass balance equations of the MRC unit.

| MRC Mass Balance Equations | |
|------------------------------------------------------------------------------------------------------|--------|
| $Q_{NaOH} = \frac{2Q_{feed,Mg^{2+}} \cdot \%_{Mg^{2+}} + Q_{feed} \cdot C_{feed,HCO_3^-}}{C_{NaOH}}$ | (38.a) |
| $Q_{out} = Q_{NaOH} + Q_{feed}$ | (38.b) |
| $M_{Mg(OH)_2} = Q_{feed,Mg^{2+}} \cdot \%_{Mg^{2+}} \cdot MW_{Mg(OH)_2}$ | (38.c) |

6.2.3 NF Economic model description

It is worth noting that the primary focus of this study is to assess the economics of NF (and not the MRC) utilizing the NFX or VNF1 membrane for seawater/SWRO brine valorisation. For this purpose, the Verberne cost model was employed [266]: the same model employed in the techno-economic analysis of Chapter 1. For the sake of brevity, all equations are reported in Appendix B. Nevertheless, it is noteworthy that the economic analysis of this specific study was conducted for a potential industrial plant with a feed capacity of 100 m³/h, consisting of 8040 NF modules (37.4 m² each), and operating for 8000 hours per year. Furthermore, the values of all the parameters (i.e., discount factor, depreciation period) are the same as those adopted for the analysis in Chapter 1. The only updated values concerned the chemical engineering price index $CEPCI$ (= 803.2 referred to year 2023 [267]).

In addition, since the analysis concerned NFX and VNF1 membranes and not NF270, it was also important to update the specific prices of the NF modules: 1047 €/NFX module and 646 €/VNF1 module (costs provided by membrane suppliers).

6.2.4 Technical and Economic performance indicators

As mentioned earlier, the primary objective of this study is to determine the operating conditions of NF that maximize the revenue from selling magnesium. The literature indicates that magnesium is commonly recovered from seawater/brine in the form of $Mg(OH)_2(s)$. However, for any resource, the purity of $Mg(OH)_2$ is a crucial factor that influences its market value. In the case of $Mg(OH)_2(s)$, the main compound that can potentially compromise its purity is calcium carbonate ($CaCO_3(s)$). Therefore, two key performance indicators were assessed: (i) the Mg/HCO_3^- selectivity of the NF membrane (see Equation 39) and (ii) the resulting purity of $Mg(OH)_2(s)$ precipitated via a possible downstream crystallizer (see Equation 40):

$$S_{Mg^{2+}/HCO_3^-} = \left(1 - \frac{R_{HCO_3^-}}{R_{Mg^{2+}}}\right) \quad (39)$$

$$Purity_{Mg(OH)_2} = \left(\frac{Q_{Mg(OH)_2}}{Q_{Mg(OH)_2} + Q_{CaCO_3}}\right) \quad (40)$$

Where $R_{HCO_3^-}$ and $R_{Mg^{2+}}$ are the membrane rejections of HCO_3^- and Mg^{2+} , respectively and Q is the mass flow rate [kg/h]. Moreover, to evaluate the economics of the NF and the potential revenue related to $Mg(OH)_2(s)$ recovery, the sum of normalized capEX and opEX along with the annual revenue of $Mg(OH)_2(s)$ were calculated according to Equations 41 and 42, respectively:

$$Ncosts = NcapEX_{NF} + NopEX_{NF} \quad (41)$$

$$Rev_{Mg(OH)_2} = Q_{Mg(OH)_2} \left[\frac{ton}{yr} \right] \cdot Price_{Mg(OH)_2} \quad (42)$$

Where $Rev_{Mg(OH)_2}$ is the revenue [€/yr], $Q_{Mg(OH)_2}[\frac{ton}{yr}]$ is the annual mass flow rate [ton/yr] and $Price_{Mg(OH)_2}$ is the specific price of $Mg(OH)_2(s)$ (i.e., 1500 €/ton [268]).

6.3 Results and Discussion

6.3.1 NFX and VNF1: membrane characterization

FTIR analysis was performed to examine the chemical composition of the two commercial NF membranes, namely VNF1 and NFX. Both membranes displayed identical spectral patterns in the substrate layer, as depicted in Figure 55a). The achieved substrate spectra indicated a polyester-based material, specifically polyethylene terephthalate (PET), supported by the presence of carbonyl stretching (1711 cm^{-1}), carbon monoxide stretching ($1341, 1410\text{ cm}^{-1}$), deformation of terephthalate residues (1242 cm^{-1}), a methylene group (1094 cm^{-1}), and an aromatic ring ($846, 871, 970\text{ cm}^{-1}$) [269].

In Figure 55b), the spectra of the active layer, including the intermediate layer, provided evidence that both membranes comprised two major components: polysulfone and polyamide. It was possible to identify the polysulfone layer via various characteristic vibrations, such as aromatic in-plane ring bend stretching ($1586, 1505, 1488\text{ cm}^{-1}$), C-H symmetric deformation of $C(CH_3)_2$ ($1365\text{-}1385\text{ cm}^{-1}$), asymmetric SO_2 stretching vibration ($1294\text{-}1323\text{ cm}^{-1}$), C-O-C asymmetric stretching vibration in the aryl-O-aryl group (1241 cm^{-1}), symmetric SO_2 stretching vibration ($1151\text{-}1170\text{ cm}^{-1}$), and in-phase out-of-plane hydrogen deformation of a para-substituted phenyl group (833 cm^{-1}) [270]. Additionally, the presence of polyamide derivatives in the active layer was identified due to characteristic spectral features, precisely the amide I band at 1646 cm^{-1} and the amide II band at 1542 cm^{-1} , associated with the in-plane bending of N-H and the stretching vibration of N-C within the $-CO-NH-$ group, providing compelling evidence of polyamide components within the membrane [271]. Moreover, the FTIR spectra of VNF1 and

NFX membranes revealed the presence of specific functional groups, including hydroxyl (OH), amino (NH), and carbonyl (CO). Furthermore, both the support and active layers exhibited the presence of aromatic and heteroaromatic structural elements within their polymeric chains, as indicated by prominent bands in the spectral regions of $3800\text{-}3000\text{ cm}^{-1}$ and $1600\text{-}1300\text{ cm}^{-1}$ [271]. It is worth noting, however, that the peaks in the range of $3800\text{-}300\text{ cm}^{-1}$ could also be associated with the presence of water molecules inside the membrane.

Whereas VNF1 and NFX membranes shared similarities in terms of substrate and active layer, a notable distinction aroused in the active surface spectra. VNF1 presented two further peaks at 1042 cm^{-1} and 921 cm^{-1} compared to NFX, corresponding to sulfonate and C-N bonds. The existence of these hydrophilic functional groups likely contributed to a higher permeability for VNF1. Therefore, the differences in the composition of the active layer, particularly the additional modifications in VNF1, may provide an explanation for the variations in permeability and selectivity observed between VNF1 and NFX.

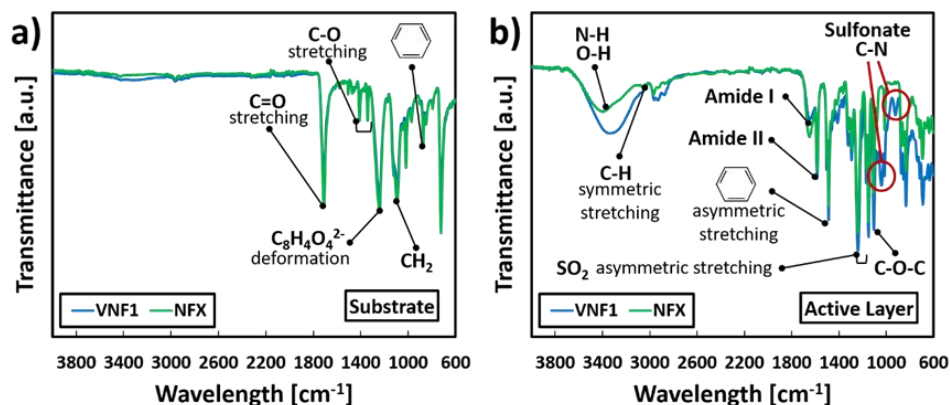


Figure 55: a) FTIR analysis of substrate of NF membranes (VNF1 and NFX); b) FTIR analysis of active layer of NF membranes (VNF1 and NFX).

Additionally, SEM analyses were performed to assess the morphology of the two NF membranes, and the results are presented in Figure 56. The front section images of the substrate for both membranes (Figures 56a) and d)) visually confirmed the

microfiber structure within the PET polymer matrix, consistent with earlier observations from the FTIR spectra. Regarding the substrates, cross-sectional imaging (see Figures 56c) and f)) further emphasized the dense and asymmetric porous structure of the substrate. This structure is indicative of the free volume phenomena inherent in polymer materials, coupled with the presence of an extremely thin, non-porous active layer.

Frontal images of the active surfaces of VNF1 and NFX are illustrated in Figures 56b) and 56e), respectively. In Figure 56e), NFX displayed numerous round structures randomly distributed on the surface, a feature not observed on the VNF1 surface. Such differences in surface morphology could influence the contact angle, a key parameter in surface wettability. In general, contact angles below 90° indicate favourable water interaction, signifying that the surface is highly wettable, and there is strong liquid-solid surface adhesion. Lower contact angle measurements typically suggest greater water affinity and improved hydrophilicity behaviour.

In the specific case of the contact angle analysis for the two NF membranes, both displayed notably low values, demonstrating high hydrophilicity. VNF1 showed a slightly higher statistical contact angle of 36° compared to NFX at 30° . This difference could be associated with an increased filtration surface area, potentially contributing to the higher permeability observed in VNF1 compared to NFX.

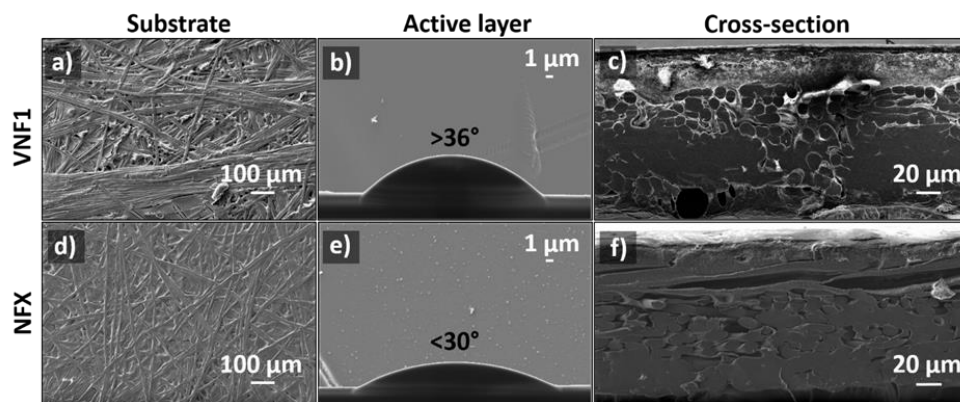


Figure 56: Front section of substrate (VNF1 (a) and NFX (d)); Front section of active layer and water contact angle (VNF1 (b) and NFX (e)); Cross-section (VNF1 (c) and NFX (f)).

Lastly, streaming potential results are depicted in Figure 57. Both NFX and VNF1 exhibited their isoelectric points (IEP) at similar pH values (3.48 and 3.52, respectively). Considering the polyamide chemistry of both membranes, at pH values below the IEP, the carboxylic and amine groups were protonated (R-COOH and R-NH_3^+), imparting a positive charge to the membrane. In contrast, at pH values above the IEP, both carboxylic and amine groups were de-protonated (R-COO^- and R-NH_2), resulting in a negatively charged membrane surface.

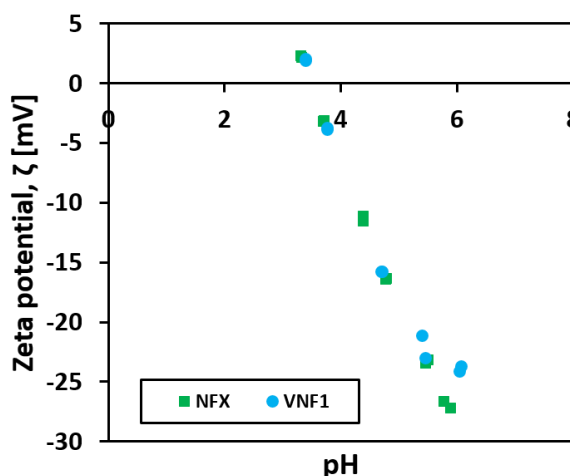


Figure 57: Zeta potential trends with pH of NFX and VNF1.

6.3.2 Mass transfer model validation

After the initial characterization of the two NF membranes, which yielded crucial insights into their potential performance, both membranes were subjected to rigorous experimental testing. Operating at an optimal pressure of 20 bar, the performance of each membrane was assessed across various permeate recovery rates, ranging from 0% to 80%, in two specific scenarios: (i) seawater treatment and (ii) SWRO brine treatment. The findings of all examined scenarios (i.e., NFX with seawater, NFX with SWRO brine, VNF1 with seawater, VNF1 with SWRO brine) are reported in the subsequent sections.

These findings were complemented by results obtained from the application of the SEDF mass transfer model, which was employed to effectively assess and interpret the data. Exploiting the results achieved via the SEDF model, a comprehensive techno-economic evaluation of the two membranes was performed, with a precise focus on their performance in seawater and brine treatment processes. The main scope of this assessment was to identify the optimal operational parameters that would maximize revenue generated from the recovery of $\text{Mg}(\text{OH})_2(\text{s})$ via the NF process.

6.3.2.1 NFX treating seawater

Figure 58 presents the experimental rejection values attained for both major and minor components present in seawater (a and b, respectively) and their corresponding concentration factors (c and d, respectively) as the permeate recovery increases from 0% to 80%, treating seawater with the NFX membrane. Furthermore, the experimental data points were presented along with the simulation predictions of the SEDF model (represented by lines).

At a consistent operating pressure of 20 bar, the NFX membrane demonstrated significantly higher rejections for multivalent ions (>91%) compared to monovalent ions (<41%). Notably, SO_4^{2-} exhibited greater rejection than Mg^{2+} and Ca^{2+} . Specifically, at a permeate recovery of 10%, the rejections for multivalent ions were as follows: SO_4^{2-} (99.8%) > Mg^{2+} (99.2%) > Ca^{2+} (97.3%). In contrast, major monovalent ions displayed much lower rejection values, following this decreasing order at 10% permeate recovery: Cl^- (38%) > Br^- (35%) > K^+ (32%) > Na^+ (28%).

These results can be attributed to electrostatic effects between the membrane and solution. As outlined in Paragraph 6.3.1, the NFX membrane featured amine and carboxylic functional groups, which could ionize based on the solution pH. At the solution pH (of 6.5), carboxylic groups were ionized (R-COO^-) while amine groups were de-protonated (R-NH_2), resulting in a negatively charged surface that repelled anions and facilitated the transport of cations in line with Donnan exclusion [175].

However, the preferential rejection of multivalent ions cannot be solely explained by Donnan exclusion.

The dielectric exclusion theory posits that the variance in dielectric constants between seawater and the polymeric matrix of the membrane causes ions in the feed solution to lose their hydration shell. This loss is proportional to the square of the absolute charge of the ions [241,255]. Consequently, single-charged ions were less repelled than their double-charged counterparts, offering an explanation for the observed selective rejection of multivalent ions.

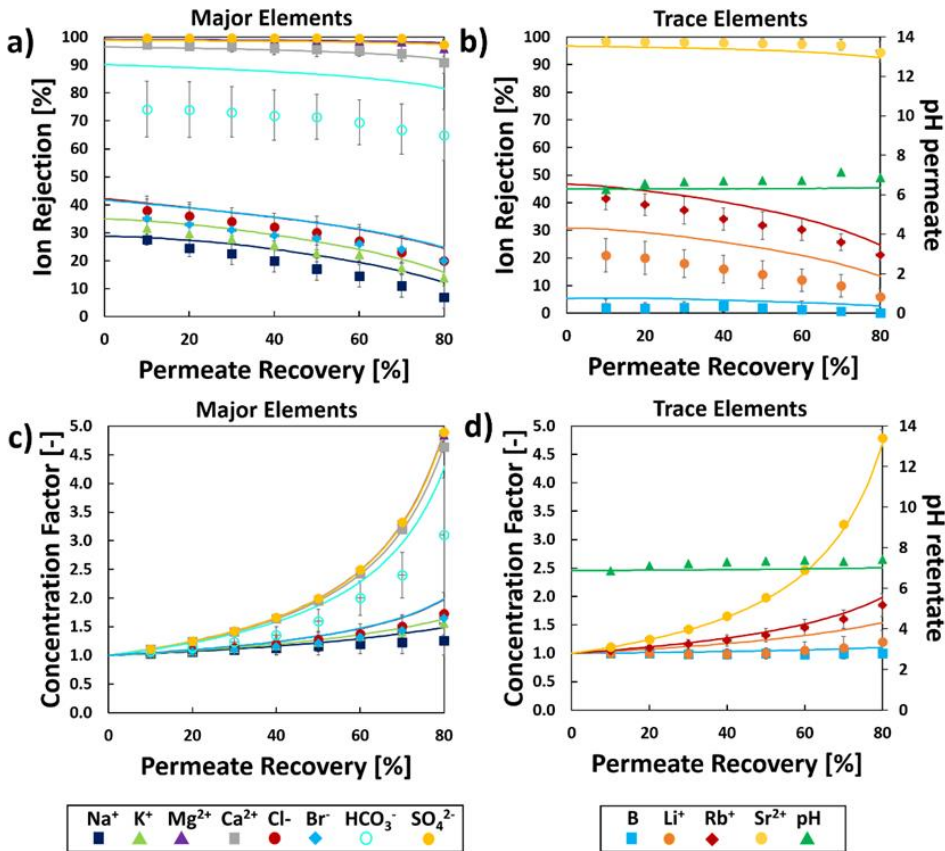


Figure 58: Performance of NFX treating seawater: a) Major Ion rejections vs. Permeate recovery; b) Minor Ion rejections vs. Permeate recovery; c) Concentration factor of Major ions vs. Permeate Recovery; d) Concentration factor of Minor ions vs. Permeate Recovery.

With the increasing permeate recovery, a declining trend in ion rejections was observed (refer to Figure 58a)). A moderate decrease was witnessed for multivalent ions from 10% to 80% permeate recovery, with SO_4^{2-} declining from 99.8% to 97.3%, Mg^{2+} from 99.2% to 96.0%, and Ca^{2+} from 97.3% to 91.0%. In contrast, a more significant decline was observed for monovalent ions: Cl^- from 38% to 20%, Br^- from 35% to 20%, K^+ from 32% to 14%, and Na^+ from 28% to 7.0%. This declining behaviour of ion rejections with increasing permeate recovery stemmed from the increased concentration at the retentate stream as permeate recovery increased. This concentration increase at the feed side could lead to (i) higher concentrations at the membrane surface, resulting in a greater diffusive flux across the membrane, and (ii) a lower permeate flux, leading to lower dilution of the permeate side. The disparity in the slope between multivalent and monovalent ion rejections was consistently explained by the impact of dielectric exclusion.

Regarding the minor elements in seawater, Figure 58b) reports the rejections of B, Li^+ , Rb^+ , and Sr^{2+} for the case of permeate recoveries ranging 10%-80%. Notably, Sr^{2+} exhibited high rejections with a smooth, gradual decline from 98.6% (10% p.r) to 94.6% (80% p.r), mirroring the trend observed for major elements. Declining slopes were also observed for the remaining trace elements: B (2% to 0.1%), Li^+ (21% to 6%), and Rb^+ (21% to 11%). It is important to highlight the presence of B as a neutral species ($\text{H}_3\text{BO}_3(\text{aq})$), unaffected by membrane electric fields, allowing to permeate freely across the membrane, with rejections decreasing from 2% to 0.07%.

Figures 58c) and 58d) illustrate the corresponding concentration factors for major and minor components, respectively. It is worth mentioning that multivalent ions (SO_4^{2-} , Mg^{2+} , Ca^{2+} , and Sr^{2+}) exhibited concentration factors exceeding 4.9 times at an 80% permeate recovery. Conversely, for monovalent ions, both in major and minor quantities in seawater, a maximum concentration factor lower than 2 was reached. This behaviour highlighted the potential of NFX to (i) concentrate specific high-value minerals such as Mg^{2+} and (ii) selectively remove monovalent species.

Regarding model validation, the SEDF model reliably predicted the experimental trends. However, notable differences were witnessed for bicarbonate ions, where the model tended to predict rejections higher than those observed experimentally (up to 20%). Such higher discrepancies were related to the reasons discussed in Paragraph 5.2.2. However, another reason lied in the fact that the membrane permeances are a function of concentration, therefore it was expected to have higher discrepancies as the solution got concentrated. Additionally, slight variations were noted for Li^+ and Rb^+ , with the model predicting rejections up to 10% and 5% higher in both cases. Minor differences were seen for B and major monovalent elements. It is important to highlight that the set of membrane permeances was achieved employing a flat-sheet configuration. Despite these small discrepancies, the model effectively captured the experimental trend. These differences may be attributed to (i) the lower cross-flow velocity in the spiral-wound modules and (ii) fluid distribution, which could lead to an uneven distribution of concentration polarization and, consequently, lower experimental rejections [248].

It is worth noting that the NFX membrane exhibited significantly higher rejections for divalent elements compared to common commercial NF membranes when treating seawater, such as NF270 and DL. For instance, at the same operating conditions, average Mg^{2+} rejections were reported to be <80% and 68% for NF270 and DL, respectively, as previously documented by Su et al. [170].

6.3.2.2 NFX treating desalination brine

In addition to seawater treatment, the rejection efficacy of the NFX membrane was evaluated using SWRO brine as the feed solution. Figure 59 presents the experimental rejection values attained for major and minor components (a and b, respectively) and their corresponding concentration factors (c and d, respectively) with increasing permeate recovery from 10% to 80% during the treatment of SWRO brine using NFX. Similar to the previous scenario, the data generated from the SEDF model are plotted as continuous lines.

Comparing Figures 58a) and 59a), it is possible to observe that there were no important differences in the NFX rejections for major multivalent ions when treating seawater and SWRO brine across the range of permeate recoveries (0% to 80%). For direct comparison of the two scenarios (NFX seawater and NFX SWRO brine) consult Figure 75 in Appendix C. Specifically, from 10% to 80% permeate recovery, the rejections for major multivalent ions when treating SWRO brine experienced declines as follows: SO_4^{2-} (99.3% to 97.9%), Mg^{2+} (99.1% to 97.0%), and Ca^{2+} (96.6% to 89.9%). This decline mirrored the pattern observed in the previous scenario, indicating that the NFX membrane could effectively recover Mg^{2+} even when treating a more concentrated feed solution, showcasing successful outcomes. For major monovalent elements, their rejections at a fixed permeate recovery were lower than those observed in the seawater treatment scenario. This can be attributed to the higher salt content of the feed solution, leading to increased diffusive ion transport, resulting in more salt permeation and lower rejections. This effect did not impact multivalent ions due to the strong electrostatic effects (Donnan and dielectric exclusions). However, similar drops in major monovalent ion rejections were observed when comparing Figures 58a) and 59a), with increases in permeate recovery from 10% to 80%: Cl^- (27% to 12%), Na^+ (17% to 2%), K^+ (30% to 17%), and Br^- (25% to 12%). The same considerations made for the previous scenario regarding the main reasons behind the membrane behaviour with respect to multivalent and monovalent ions can be applied for this scenario too.

Furthermore, Figure 59c) illustrates the corresponding concentration factor of the major components. Compared to the previous scenario, comparable concentration factors were achieved for multivalent ions (SO_4^{2-} , Mg^{2+} , Ca^{2+}) and monovalent ions (Cl^- , Na^+ , K^+ , Br^-), achieving factors up to 4.9 and 1.6, respectively. As for the trace elements (see Figure 59b)), high rejections with a smooth decrease with the increase of permeate recovery were attained for Sr^{2+} : from 98.3% (10% p.r) to 95.0% (80% p.r). However, the rest declined more significantly compared to Sr^{2+} : B (11% to 6%), Li^+ (18% to 6%), and Rb^+ (37% to 19%). The same trend observed for the

concentration factors of the major components was achieved for the trace elements too (see Figure 59d)).

In summary, the results from the NFX membrane testing indicated that the treatment of SWRO brine could be more advantageous than treating seawater. This conclusion stems from two key observations: firstly, there was no reduction in Mg^{2+} rejections at a fixed permeate recovery rate, despite the higher Mg^{2+} feed content; and secondly, a decrease in the rejection of monovalent ions was noted. These factors suggest a potential for higher selectivity and recovery of Mg^{2+} when valorising SWRO brine.

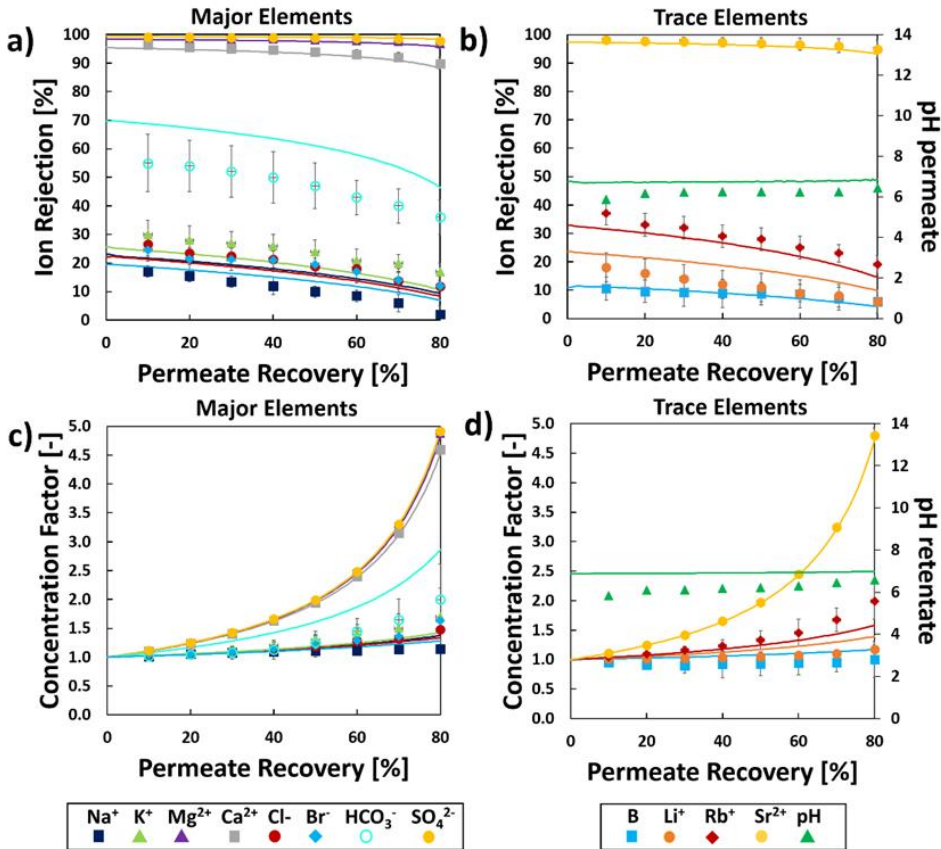


Figure 59: Performance of NFX treating SWRO brine: a) Major Ion rejections vs. Permeate recovery; b) Minor Ion rejections vs. Permeate recovery; c) Concentration factor of Major ions vs. Permeate Recovery; d) Concentration factor of Minor ions vs. Permeate Recovery.

Furthermore, the model tended to predict higher rejections of bicarbonate ions than what was experimentally observed. While the model captured the trends for multivalent elements with a good agreement, it predicted rejections for monovalent elements being lower than those experimentally observed. Additionally, the model anticipated a decline in rejections as the percentage of permeate recovery increased. Moreover, when comparing the performance of the NFX membrane to other common and modified commercial NF membranes under similar operating conditions, the NFX membrane demonstrated enhanced bivalent/monovalent selectivity. Specifically, in contrast to NF270, Fortilife, and PRO-XS2, which exhibited lower Mg^{2+} rejections (60%, 75%, and 83%, respectively), the NFX membrane showcased superior performance. Similarly, the rejection values for Na^+ were similar, if not higher, in the case of the NF270, Fortilife and PRO-XS2 (21%, 15% and 27%, respectively) [272].

6.3.2.3 VNF1 treating seawater

Similar to the evaluation conducted for NFX, the performance of VNF1 was assessed in treating seawater. Figure 60 illustrates the experimental rejection values for both major and minor components (a and b, respectively) and their corresponding concentration factors (c and d, respectively). These values were observed during the gradual increase in permeate recovery from 10% to 80% when utilizing VNF1 for seawater treatment. The continuous lines in Figure 60 represent the data derived from the SEDF model.

The principles governing transport phenomena across the NFX membrane, as discussed in Paragraph 6.3.2.1, are applicable to the VNF1 membrane. Although both membranes present ionogenic carboxylic and amine groups, conferring a negative surface charge at the working pH, notable differences emerged when comparing NFX and VNF1.

Firstly, a comparison between Figures 58a) and 60a) can be done. For direct comparison of the two scenarios (NFX seawater and VNF1 seawater) consult Figure

76 in Appendix C. The comparison reveals that, unlike the NFX membrane, the VNF1 membrane displayed significantly lower rejection drops when increasing permeate recovery from 10% to 80%. This characteristic indicated a more robust performance during operation. Specifically, rejections remained consistently high for SO_4^{2-} (99.8% to 99.7%) and Mg^{2+} (99.6% to 99.0%), with a gradual drop observed for Ca^{2+} (96.1% to 93.9%). Another distinction was the higher major monovalent rejections of VNF1 at a fixed permeate recovery rate, suggesting a lower selectivity than NFX between multivalent and monovalent ions abundant in seawater. The rejection drops were slightly bigger for Cl^- (39% to 20%), Na^+ (30% to 6%), K^+ (36% to 11%), and Br^- (39% to 24%).

The greater rejection drops between NFX and VNF1 during seawater treatment translated into higher concentration factors (see Figure 60c). At a permeate recovery rate of 80%, the major multivalent ions could achieve an average concentration factor of 5, while the major monovalent ions could be concentrated by a factor of 2.

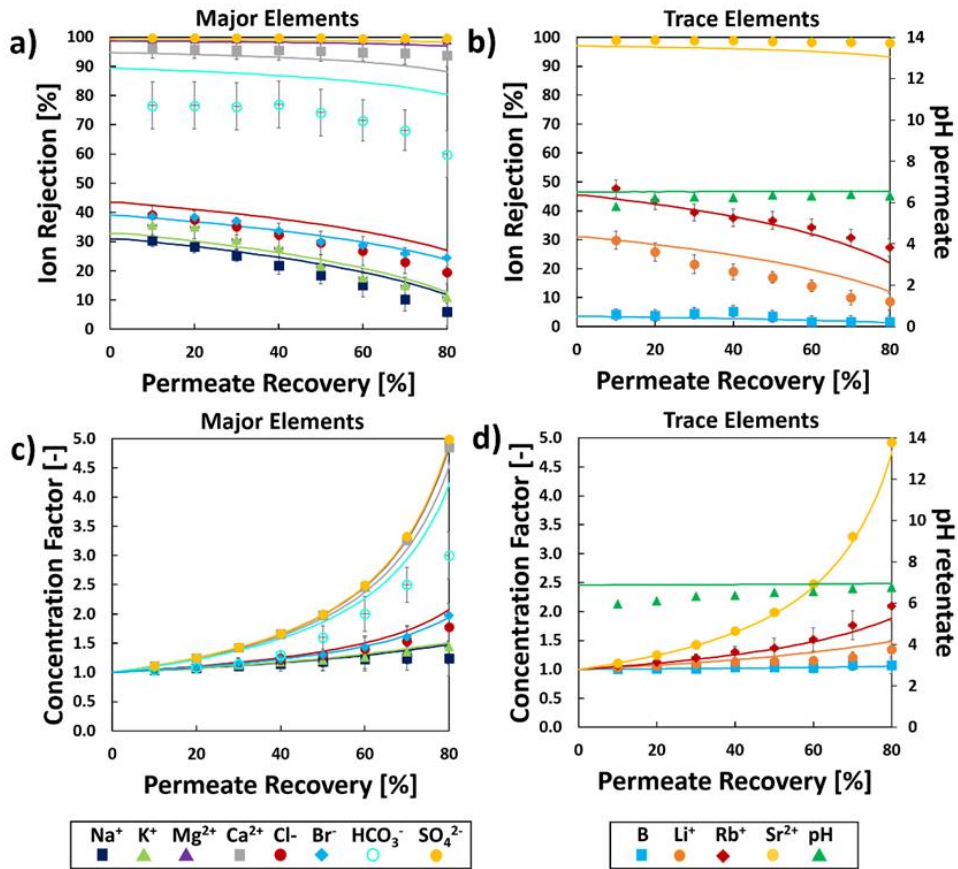


Figure 60: Performance of VNF1 treating seawater: a) Major Ion rejections vs. Permeate recovery; b) Minor Ion rejections vs. Permeate recovery; c) Concentration factor of Major ions vs. Permeate Recovery; d) Concentration factor of Minor ions vs. Permeate Recovery.

Concerning the trace elements, VNF1 consistently demonstrated significant rejections of Sr²⁺ across the entire range of permeate recoveries, ranging from 99.2% to 98.1%. Similar to major monovalent ions, the other trace elements exhibited higher rejections and comparable rejection drops/concentration factors when comparing VNF1 performance to that of NFX (refer to Figures 60b) and 60d)). The experimental results from seawater treatment using VNF1 led to two key conclusions: (i) VNF1 exhibited slightly higher concentration factors and lower rejection drops for multivalent ions compared to NFX, and (ii) higher rejections and rejection drops for monovalent ions were observed with VNF1 than with NFX. This

suggests that VNF1 has a lower multi/monovalent selectivity than NFX, potentially impacting the purity of $\text{Mg}(\text{OH})_2(\text{s})$ recoverable from a downstream crystallizer.

In terms of the SEDF model predictive capabilities, deviations between the model and experimental data were notably lower than in previous cases. The model predicted higher bicarbonate rejections, reaching up to 10%, and successfully anticipated the observed decay of rejections. However, it is noteworthy that the experimental data did not confirm the predicted decay for Ca^{2+} and Sr^{2+} , as indicated by the model.

Furthermore, despite VNF1's higher permeability and lower selectivity compared to NFX, VNF1 still demonstrated superior bivalent rejections when compared to common NF membranes like NF270 and DL [170].

6.3.2.4 VNF1 treating desalination brine

The last scenario experimentally examined pertained to the performance of VNF1 in treating SWRO brine. In Figure 61, the achieved experimental rejection values for major and minor components (denoted as a and b, respectively) and their corresponding concentration factors (represented by c and d, respectively) are illustrated. These values were observed during the increment of permeate recovery from 10% to 80% while treating SWRO brine with VNF1. Similar to the previous cases, discrete points on the graph represent the experimental data, while the lines depict the model derivation.

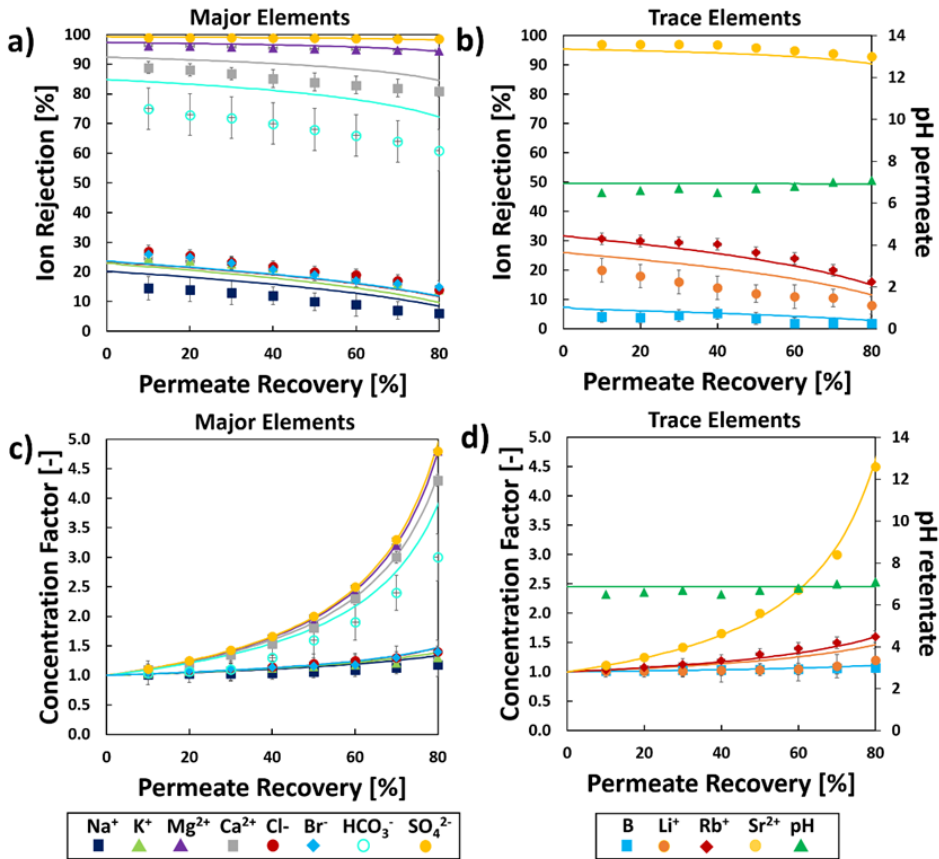


Figure 61: Performance of VNF1 treating SWRO brine: a) Major Ion rejections vs. Permeate recovery; b) Minor Ion rejections vs. Permeate recovery; c) Concentration factor of Major ions vs. Permeate Recovery; d) Concentration factor of Minor ions vs. Permeate Recovery.

For SO_4^{2-} and Mg^{2+} , two observations stand out: (i) rejections were lower compared to seawater treatment, likely due to an increased screening effect on charge resulting from elevated feed concentrations, and (ii) rejection drops were more moderate compared to NFX when treating SWRO brine. A direct comparison between the scenarios VNF1 seawater and VNF1 SWRO brine can be observed in Figure 77 in Appendix C whilst a direct comparison between the scenarios NFX SWRO brine and VNF1 SWRO brine can be observed in Figure 78 in Appendix C. Specifically, passing from seawater to brine, VNF1 rejections decreased from 99.1% and 96.3%

to 98.6% and 94.6% for SO_4^{2-} and Mg^{2+} , respectively. This suggested that VNF1 is more sensitive to variations in feed concentration than NFX.

In all four scenarios, the lowest Ca^{2+} rejections were witnessed with VNF1 treating SWRO brine. From a permeate recovery rate of 10% to 80%, Ca^{2+} rejections decreased from 88.9% to 81.0%. In contrast to major multivalent components, the monovalent ions exhibited similar rejections and rejection drops compared to the NFX SWRO treatment scenario: Cl^- (27% to 14%), Na^+ (15% to 6%), K^+ (25% to 14%), and Br^- (26% to 15%). Regarding the corresponding concentration factors (refer to Figure 61c), the lowest values were recorded: a maximum concentration factor of 4.8 for SO_4^{2-} and Mg^{2+} at 80% permeate recovery, and an average value of 1.4 for the monovalent ions at the same permeate recovery rate.

The reduction in rejection rates for trace elements found in SWRO brine was as follows: Sr^{2+} (97% to 93%), B (4% to 2%), Li^+ (20% to 8%), and Rb^+ (31% to 16%). Additionally, Figure 61d) illustrates the corresponding concentration factors of these trace elements, reaching up to 4.5 for Sr^{2+} and a maximum value of 1.6 for the monovalent ions at 80% permeate recovery. In evaluating the last case scenario (VNF1 with SWRO brine), it is noteworthy that the lowest rejections were observed for multivalent ions compared to the three preceding scenarios. Despite the "low recovery rate" of Mg, the higher Mg^{2+} feed content, and increased selectivity in seawater treatment via VNF1, this scenario could potentially be more economically attractive than the previous one.

Regarding the SEDF model, it accurately predicted the experimental trends. Significant disparities were observed for carbonates, with the model predicting rejections 10% higher than those observed experimentally. For calcium, the model anticipated rejections 5% higher than the experimental observations. In the case of lithium, predicted rejections were 10% higher than the actual experimental results. Moreover, the model appropriately captured the decrease in rejections as permeate recovery increased.

In addition, similar to the NFX SWRO brine scenario, the VNF1 membrane outperformed other commercial and enhanced NF membranes in terms of bivalent/monovalent selectivity (i.e., NF270, Fortilife, and PRO-XS2 [272]).

6.3.3 Techno-economic assessment

In the techno-economic assessment, four distinct scenarios were examined, each featuring the utilization of a specific NF membrane and addressing a particular feed solution:

- i) NFX treating seawater;
- ii) NFX treating SWRO brine;
- iii) VNF1 treating seawater;
- iv) VNF1 treating SWRO brine.

The techno-economic analysis involved evaluating the four indicators (as mentioned in Paragraph 6.2.4) across an extensive operating pressure range (8 – 30 bar) and permeate recovery levels ranging from 10% to 80%.

6.3.3.1 NFX treating seawater

The outcomes of the techno-economic assessment for a potential industrial plant (with a feed capacity of 100 m³/h) utilizing NFX 8040 modules to treat seawater are illustrated in Figures 62a-d). Specifically, the figures depict the impact of key operating variables (pressure and permeate recovery) on Mg²⁺/HCO₃⁻ selectivity, the purity of recovered Mg(OH)₂(s), NF treatment cost, and revenue associated with the recuperated Mg(OH)₂.

Figure 62a) depicts the variation in Mg²⁺/HCO₃⁻ selectivity of the NFX membrane when exposed to seawater. Notably, the membrane selectivity gradually increases with a simultaneous rise in permeate recovery and a reduction in operating pressure. Specifically, increasing the operating pressure enhances membrane rejections for both Mg²⁺ and HCO₃⁻. However, the selectivity decreases due to an increase in

HCO_3^- rejection while Mg^{2+} rejections remain consistently high at elevated pressures.

Concerning the impact of permeate recovery, an increase results in a decrease in single-ion rejections due to heightened feed solution concentration. Consequently, the combined effects of operating pressure and permeate recovery cause selectivity to surge from 0.07 (30 bar at 10% recovery) to a more than tripled value, reaching 0.33 (8 bar at 80% recovery). Given that the purity of potentially recovered $\text{Mg}(\text{OH})_2(\text{s})$ from a downstream crystallizer depends on membrane selectivity, a similar trend was observed for purity (refer to Figure 62b)). However, unlike selectivity, the increase in $\text{Mg}(\text{OH})_2(\text{s})$ purity was more limited, ranging from 94.6% (30 bar at 10% recovery) to 95.9% (8 bar at 80% recovery).

This limitation was attributed to the higher concentration of Mg^{2+} in seawater compared to HCO_3^- , resulting in minimal variations in the mass recovered for the two ions due to rejection changes. Moreover, a purity range exceeding 95% was identified, as this value represents the minimum purity required for commercial applications [273] (e.g., low-grade flame retardants for subway seats or car materials [268] with a specific price of 1500€/ton). It is important to note that the SEDF model predicted higher carbonate rejections than those observed experimentally, potentially expanding the range where the 95% purity threshold could be achieved.

In terms of economic considerations, Figure 62c) illustrates the total sum of normalized capital expenditure (capEX) and operational expenditure (opEX) in relation to both operating variables, taking into account the seawater feed capacity of the plant. The lowest costs (0.77 €/m³) are attained when the NF plant operates at the minimum operating pressures and permeate recoveries (8 bar and 10% recovery). However, the overall trend of total normalized costs does not exhibit a linear relationship with both operating conditions. The highest costs are incurred at both low and high operating pressures with 80% permeate recovery (0.98€/m³ and 1.02€/m³, respectively). This outcome results from a combination of factors.

Notably, NopEX increases with recovery and operating pressure due to larger electricity and chemical requirements. Regarding NcapEX, civil, mechanical, and

membrane investments rise with increasing recovery and decreasing operating pressure, given their direct dependence on the number of NF modules constituting the plant. In contrast, electro-technical investments increase exclusively with the rise in operating pressure. In addition, since N_{capEX} surpass N_{opEX} , the trend of total costs is predominantly influenced by normalized capital costs (see Figure 79 in Appendix C).

Finally, Figure 62d) underscores that the maximum revenue for $Mg(OH)_2(s)$ (3.716 M€/yr) can be reached under intermediate operating conditions (16 bar and 50% recovery). This can be explained by the combined effects of purity and recovery. Larger Magnesium recoveries are attained at lower permeate recoveries (larger retentate flow rates), while purity depends on higher pressures and greater permeate recoveries, as mentioned earlier.

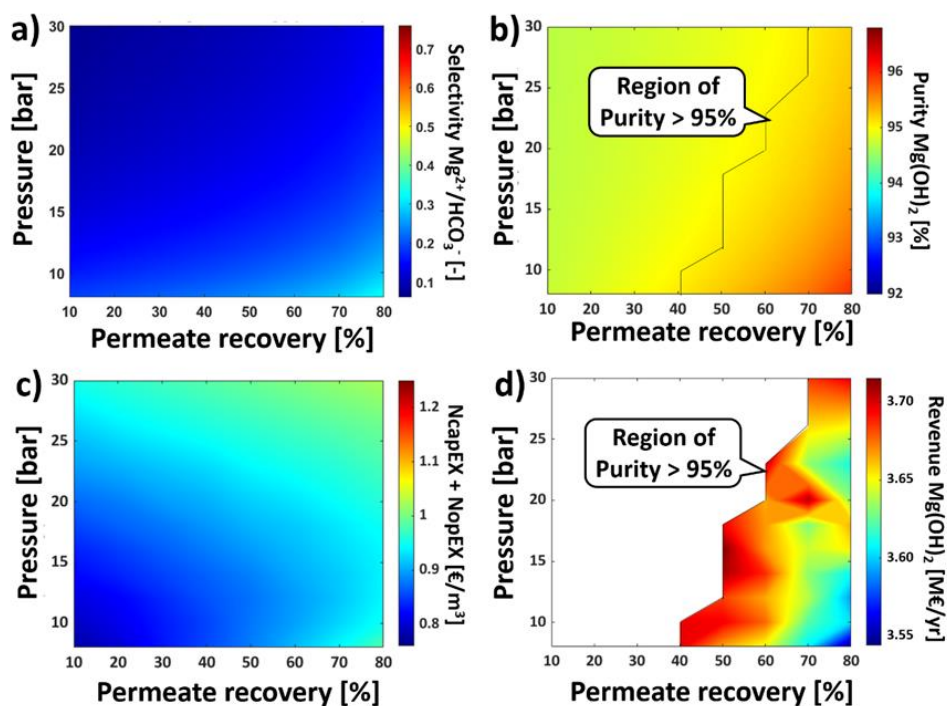


Figure 62: a) Mg^{2+}/HCO_3^- selectivity [-], b) $Mg(OH)_2$ purity [%], c) $N_{capEX} + N_{opEX}$ [€/m³] and d) $Mg(OH)_2$ revenue [M€/yr] at pressure (8-30 bar) vs. permeate recovery (10-80%) when treating seawater with NFX membrane.

6.3.3.2 NFX treating SWRO brine

Figures 63a)-63d) present the techno-economic assessment results of the NFX membrane when processing SWRO brine. Similar considerations to those discussed in the seawater treatment scenario can be applied here. However, compared to the previous scenario, notable differences in the resulting values emerge in this case.

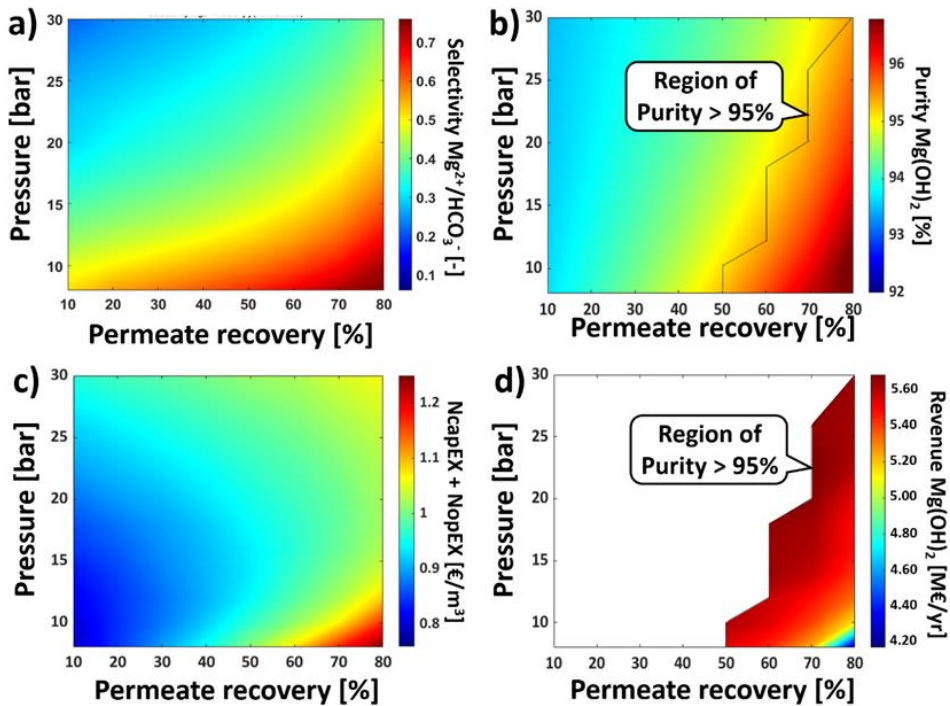


Figure 63: a) Mg^{2+}/HCO_3^- selectivity [-], b) $Mg(OH)_2$ purity [%], c) $N_{capEX} + N_{opEX}$ [$€/m^3$] and d) $Mg(OH)_2$ revenue [$M€/yr$] at pressure (8-30 bar) vs. permeate recovery (10-80%) when treating SWRO brine with NFX membrane.

Firstly, dealing with a more concentrated feed solution than seawater resulted in reduced ion rejections. While the decrease in Mg^{2+} rejection was limited, HCO_3^- rejection saw a more significant reduction, leading to higher selectivity values than in the previous scenario. As illustrated in Figure 63a), selectivity could reach as high

as 0.76 (at 8 bar and 80% permeate recovery), more than double the value achieved when treating seawater. However, this elevated selectivity did not uniformly translate into proportionally higher $\text{Mg}(\text{OH})_2(\text{s})$ purity across the wide range of operating pressures and permeate recoveries.

For low permeate recoveries, a higher bicarbonate content resulted in lower purity values compared to the seawater treatment scenario. As the pressure increased and 50% water recovery was attained, Mg rejection became sufficiently high, unlike that of bicarbonates, leading to purities surpassing those achieved when treating seawater. Purity values as high as 97% were realized at 8 bar and 80% permeate recovery.

The overall trend of total normalized costs showed no significant difference between seawater and brine treatment. Undoubtedly, both capital and operating costs experienced an increase when transitioning from seawater to brine treatment. However, the rise in NcapEX exceeded that of NopEX, primarily influenced by the growing number of required NF modules due to the lower permeate flux (see Figure 80 in Appendix C). This behaviour resulted in the attainment of the highest normalized costs (1.25 €/m^3 for SWRO brine $> 1.02 \text{ €/m}^3$ for SW) only at 8 bar and 80% recovery (refer to Figure 63c)), in contrast to the previous scenario where the highest values could be achieved at both low and high operating pressures (see Figure 63c)).

Furthermore, Figure 63d) highlighted increased revenues when treating brine, primarily attributable to the higher mass recovery of magnesium. The peak revenue (5.683 M€/yr) was observed at 23 bars and 70% permeate recovery.

6.3.3.3 VNF1 treating seawater

Similar to the NFX membrane, the performance of the VNF1 membrane was evaluated and is specifically presented in Figures 64a)-d). As previously noted, VNF1 exhibited higher permeability than NFX, resulting in a generally lower selectivity between multivalent and monovalent ions, as depicted in Figure 64a).

However, the selectivity of VNF1 was to such an extent lower that achieving a purity of $\text{Mg}(\text{OH})_2(\text{s})$ of 95% was not possible across the entire range of operating conditions considered in this study. Consequently, no revenue was generated. While the recovered $\text{Mg}(\text{OH})_2(\text{s})$ might have found application in wastewater neutralization, the specific market price for such an application would likely be too low ($< 500 \text{ €}/\text{ton}$) to warrant consideration in the analysis.

Moreover, the total normalized costs were lower when using VNF1 compared to NFX (refer to Figure 64c)). This reduction was primarily attributed to: (i) the lower number of NF modules required due to higher membrane permeability and (ii) the lower cost of the VNF1 module in comparison to the NFX module.

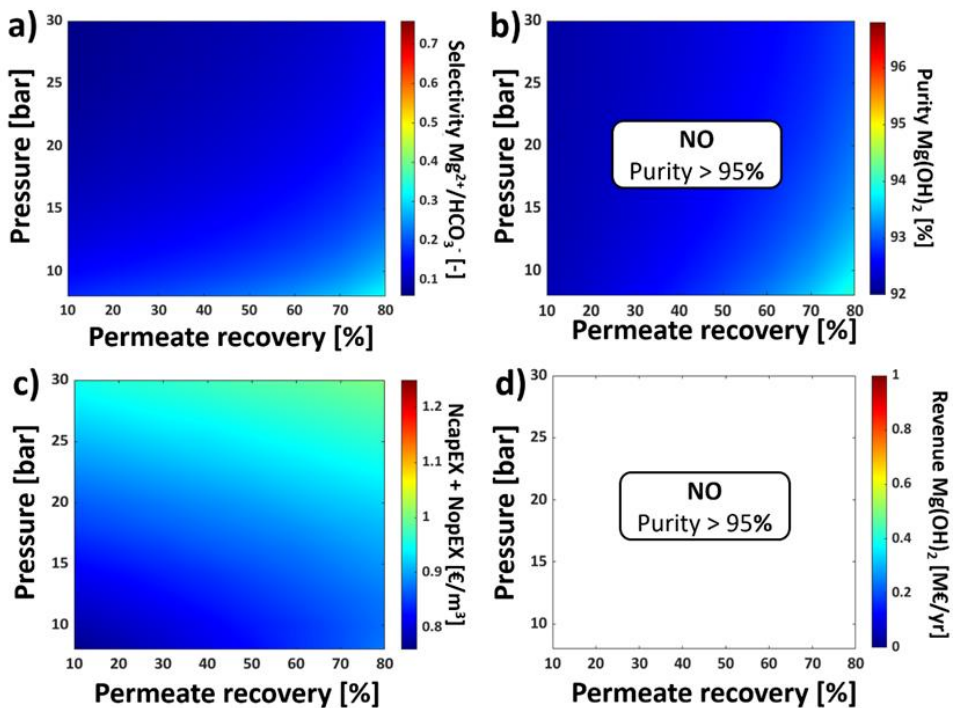


Figure 64: a) $\text{Mg}^{2+}/\text{HCO}_3^-$ selectivity [-], b) $\text{Mg}(\text{OH})_2$ purity [%], c) $N_{\text{capEX}} + N_{\text{opEX}} [€/\text{m}^3]$ and d) $\text{Mg}(\text{OH})_2$ revenue [M€/yr] at pressure (8-30 bar) vs. permeate recovery (10-80%) when treating seawater with VNF1 membrane.

6.3.3.4 VNF1 treating desalination brine

The analysis of VNF1 treating SWRO brine, as illustrated in Figures 65a-d), revealed that VNF1 faced challenges in achieving high-purity $\text{Mg}(\text{OH})_2(\text{s})$ also when treating desalination brine. Purity exceeding 95% was only attainable when operating at 80% water recovery and a maximum operating pressure of 10 bar, as depicted in Figure 65b). This condition implied that potential revenue (4.293 M€/yr) could be realized solely under these specific operating conditions.

Additionally, the total normalized costs of VNF1 treating SWRO brine were slightly lower compared to NFX with brine, for the same reasons outlined in Paragraph 6.3.3.3. Specifically, at 10 bar and 80% permeate recovery (the only operating conditions where revenue was achieved), the costs were 1.03 €/m³ (VNF1) as opposed to 1.25 €/m³ (NFX).

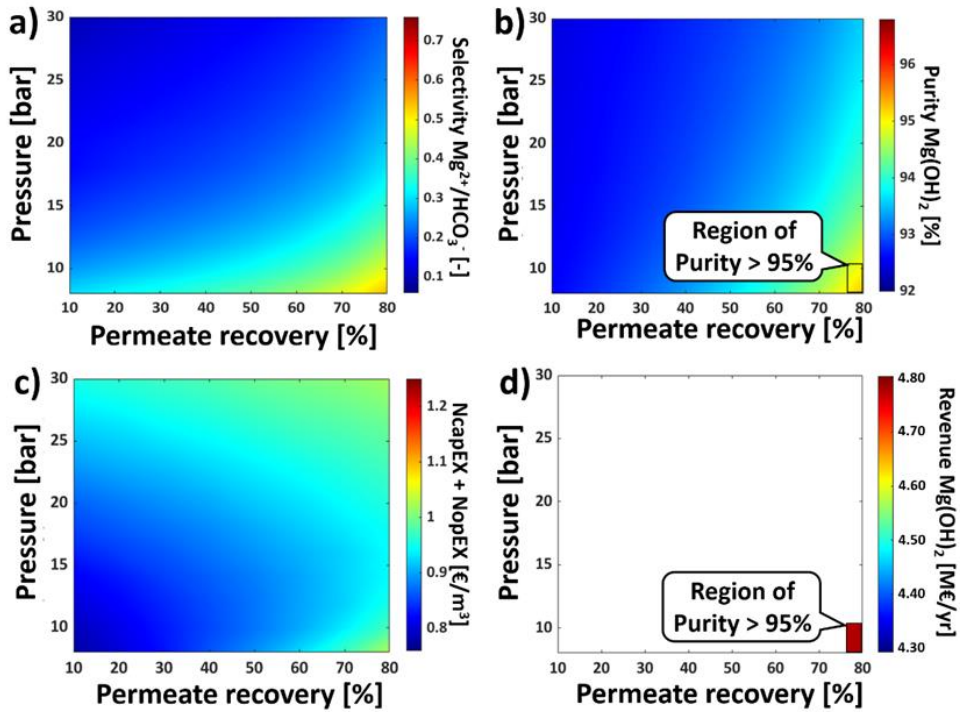


Figure 65: a) Mg^{2+}/HCO_3^- selectivity [-], b) $Mg(OH)_2$ purity [%], c) $N_{capEX} + N_{opEX}$ [€/m^3] and d) $Mg(OH)_2$ revenue [M€/yr] at pressure (8-30 bar) vs. permeate recovery (10-80%) when treating SWRO brine with VNF1 membrane.

6.3.4 Global techno-economic overview of the 4 scenarios

Following the analysis of the preceding four case scenarios, Figure 66 illustrates a comparative examination of the techno-economic performances of NFX and VNF1 in the valorisation of seawater and brine, with revenue maximization as the focal point in each scenario. Two primary conclusions can be drawn:

- (i) In both seawater and brine valorisation, NFX consistently outperforms VNF1 in terms of $Mg(OH)_2(s)$ purity. The superior selectivity of the NFX membrane enables the recovery of a final product with higher purity. Despite the higher permeability and lower module cost of VNF1, an industrial-scale NF plant incorporating NFX membranes can exhibit comparable capital and operating

costs to one equipped with VNF1 membranes yet achieving revenues nearly double in magnitude.

- (ii) When considering a specific membrane, marginal differences in normalized costs between seawater and brine valorisation are observed. However, the potential for significantly increased revenues arises from the higher concentration of Mg^{2+} in SWRO brine, rendering brine valorisation economically more appealing than seawater valorisation.

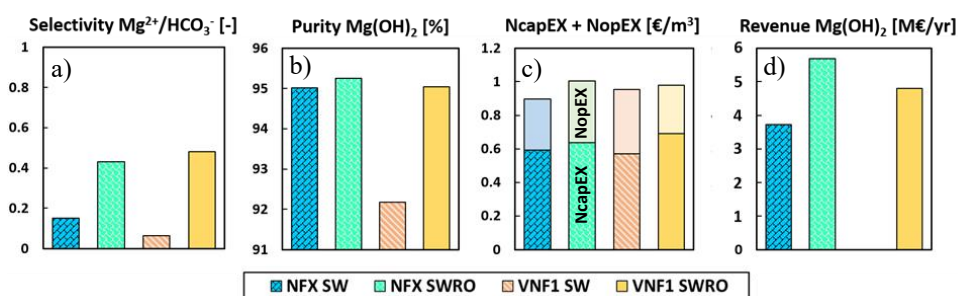


Figure 66: The four different scenarios: (i) NFX SW, (ii) NFX SWRO, (iii) VNF1 SW and (iv) VNF1 SWRO are compared in terms of a) selectivity, b) $Mg(OH)_2$ purity, c) normalized annualized total costs and d) $Mg(OH)_2$ revenue in the case of maximizing the $Mg(OH)_2$ revenue for each scenario.

All in all, it could be possible to determine the gross annual income (Annual revenue - total annual costs) for all four scenarios in order to identify the most profitable case scenario. The gross income follows the increasing order: VNF1 SW (-0.84M€/yr) < NFX SW (2.82M€/yr) < VNF1 SWRO brine (3.98M€/yr) < NFX SWRO brine (4.89M€/yr), thus confirming that SWRO brine treatment via NFX membranes represents the best-case scenario.

6.4 Conclusions

Within the framework of seawater and SWRO brine valorisation, this research explores the viability of two selective commercial NF membranes, NFX and VNF1,

previously unused in seawater/brine treatment, to maximize $\text{Mg}(\text{OH})_2$ revenue in potential MLD/ZLD schemes. Following the characterization of NF membranes, providing valuable insights into their materials and potential performance properties, NFX and VNF1 underwent experimental testing with seawater and SWRO brine at 20 bar under varying permeate recovery rates (10% to 80%). The key experimental findings include:

- (i) The NFX membrane displayed notable capacity for high Mg^{2+} rejection and relatively lower monovalent ion rejections when processing SWRO brine, suggesting enhanced selectivity and recovery compared to seawater treatment.
- (ii) Conversely, the VNF1 membrane achieved the highest Mg^{2+} concentration factor when treating seawater, accompanied by elevated concentration factors and the highest rejections of monovalent ions, indicating reduced selectivity.
- (iii) VNF1 exhibited greater susceptibility to feed concentration variation compared to NFX, resulting in lower Mg^{2+} rejections when treating SWRO brine at higher permeate recovery rates.

The experimental data was meticulously cross validated with simulation results from the SEDF mathematical model, showing remarkable consistency with errors below 10%. Subsequently, the simulation model facilitated a comprehensive techno-economic assessment, yielding the following key findings:

- (i) Unlike the case of NFX, a purity of Mg equal or higher than 95% was not achievable when treating seawater with VNF1 membranes, thus leading to no revenue.
- (ii) Due to its superior selectivity, NFX demonstrated the capacity to produce $\text{Mg}(\text{OH})_2(\text{s})$ with the highest purities (97%) at an operational pressure of 10 bar and a permeate recovery rate of 80%.
- (iii) The most economically favourable scenario involved applying NFX in conjunction with SWRO brine, resulting in the highest potential revenues from $\text{Mg}(\text{OH})_2(\text{s})$ production, estimated at 5.683 M€/yr. This was achieved at an operating pressure of 23 bar and a permeate recovery rate of 70%.

In summary, this study underscores the significant promise of NF membranes, particularly NFX, in optimizing $\text{Mg}(\text{OH})_2$ production within the intricate landscape of seawater and brine treatment, highlighting substantial potential for revenue generation in this domain.

SECTION 4: Economic perspectives of a final MLD process for SWRO brine valorisation

Building upon the positive outcomes previously achieved within the PhD project, a final MLD scheme to valorise SWRO brine was proposed and underwent a rigorous economic analysis in order to evaluate its feasibility. This proposed scheme comprised 5 distinct technologies: (i) NF, (ii) MRC, (iii) EDBM, (iv) MED and (v) NTC. As depicted in Figure 67, the final MLD scheme (Figure 67b) differed from the initial scheme presented in Chapter 1 (Figure 67a)).

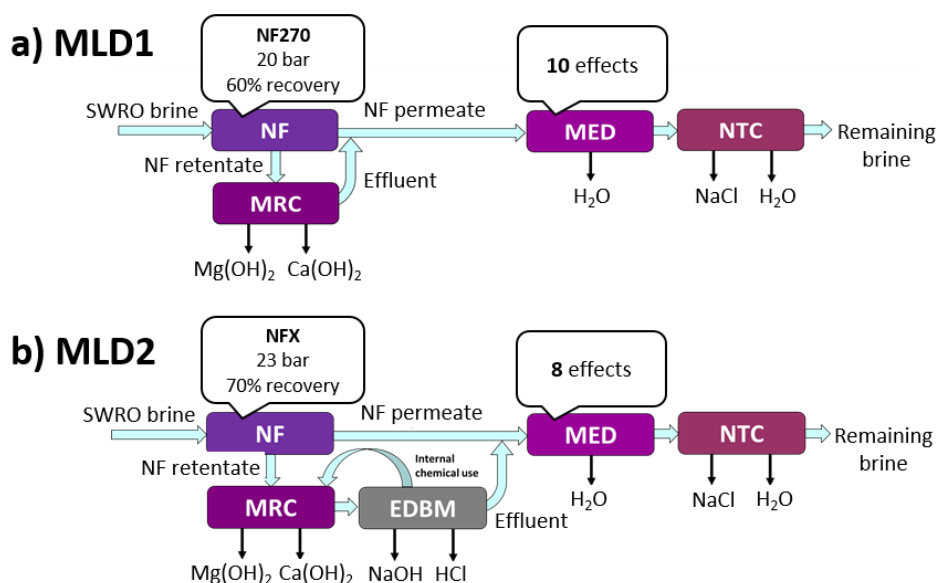


Figure 67: a) Conceptual scheme of MLD scheme for SWRO brine valorisation proposed in Chapter 1; b) Conceptual scheme of newly proposed MLD scheme in this Chapter (7).

The main objective of the novel proposed scheme was to (i) improve the bottleneck technology (MRC) by reducing its high operating costs and (ii) increase the revenue of Mg(OH)₂ recovered from SWRO brine by increasing both purity and recovery. For these reasons, firstly, the performances of the NF unit were improved. The NF plant of the final proposed MLD scheme incorporated a commercial NF membrane,

NFX, with high selectivity towards magnesium as assessed during the PhD thesis. Additionally, the plant operated under specific conditions identified in the techno-economic analysis of Chapter 6 to maximize $\text{Mg}(\text{OH})_2$ revenue—specifically, the NF plant operated at 23 bar with a permeate recovery of 70%. It is to be noted that despite the higher magnesium selectivity of the novel synthesized NF membrane CMZ-35 when compared to current commercial NF membranes, CMZ-35 was not taken into account for the final proposed MLD scheme. The main reason was that specific economic data of the CMZ-35 membrane, essential for the analysis, are still not available (e.g., the specific cost of a spiral wound module composed of CMZ-35 membranes). However, if CMZ-35 was to be considered in such analysis, higher purity $\text{Mg}(\text{OH})_2$ would have been achieved (compared to NF270 and NFX), thus leading to a higher overall revenue. Furthermore, (i) a reduction of the maintenance of the NF plant with CMZ-35 membranes due to the fabrication materials of CMZ-35 and (ii) simplified downstream crystallization steps would be achieved, leading to overall lower operating costs of the treatment chain when compared to all the previous MLD scenarios analysed within the present PhD thesis. Nevertheless, the NFX membrane was considered for the present analysis due to its promising performances and available economic data among the tested commercial NF membranes.

The MRC, on the other hand, emulated the behaviour of the MF-PFR introduced by Vassallo et al. [61] and further examined in Chapter 3 of this PhD thesis.

Another important difference between the two MLD schemes was the addition of an EDBM unit, integrated between the MRC and MED. The rationale behind this modification stemmed from the findings in Chapter 1, which underscored that a major operating cost was attributed to the use of chemicals (NaOH and HCl) in the MRC for reaction and cleaning purposes. Consequently, an EDBM unit was introduced to potentially reduce or entirely eliminate the external demand for such chemicals by producing them in-situ.

Regarding the techno-economic performance of the EDBM unit, both the technical and economic models previously reported by Culcasi et al. [87] were employed.

Notably, the EDBM plant operated in an open-loop configuration, featuring 20 EDBM stacks arranged in parallel to process the entire effluent from the Membrane Reactor Crystallization (MRC). Each stack comprised 100 triplets, with an installed membrane area of 169 m². The salt line of the EDBM plant received the neutralized MRC effluent, while the acid and base lines were supplied with deionized water. The quantity of the required water for the EDBM plant was more or less half of the quantity of freshwater produced by the RO plant (that produces the initial SWRO brine). The design of the EDBM plant aimed to produce 1M of NaOH and 1M of HCl, achieved through operation at an electric current of 394 A and an electric potential of 306 V. It operated for 8000 hours per year, with a project lifetime of 10 years and a discount rate of 6%.

Regarding the Multi-Effect Distillation (MED) unit in the new MLD scheme, it operated under the same conditions considered in the techno-economic analysis of Chapter 1. The sole modification made pertained to the number of effects, with the optimal number identified in Chapter 1 (8 effects) being adopted here.

Finally, the last technology concerned the NTC. For the production of NaCl, an NTC was always employed. No alternative technologies for NaCl recovery such as evaporation ponds (as in the case of the MLD chain of Chapter 2) were taken into consideration for one main reason:

- (i) Evaporation ponds are characterized by a large-footprint, which could be a critical factor if the potential industrial-scale MLD chain was to be implemented on a small remote island (i.e., Pantelleria, Lampedusa);

It is also to be noted that the NTC operated under the same conditions outlined in Chapter 1.

The results of the economic analysis for the newly proposed MLD scheme, treating 95 m³/h of SWRO brine, were compared with those of the initial MLD chain presented in Chapter 1.

Firstly, however, it was interesting to provide insights on the electrical and thermal energy consumption of both MLD processes (the scheme presented in Chapter 1 and the newly proposed scheme), shown in Figure 68. It is to be noted that, throughout

the subsequent figures, the MLD chain from Chapter 1 is denoted as MLD Chain N°1 (MLD 1), while the recently proposed MLD process is referred to as MLD Chain N°2 (MLD 2).

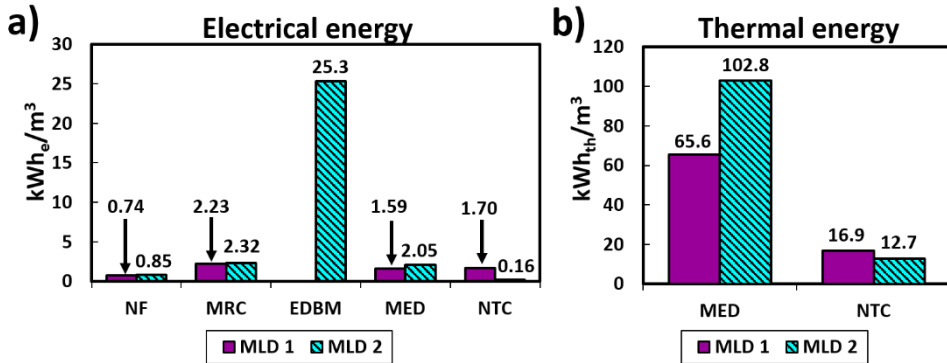


Figure 68: a) Electrical energy consumption of MLD 1 and MLD 2 processes; b) Thermal energy consumption of MLD 1 and MLD 2 processes.

For the thermal energy, as expected, the MED consumed more energy than the NTC. However, the MED consumed more in MLD 2 than in MLD 1. This was associated with the quantity of freshwater that was produced. Accordingly, the opposite trend was observed for the NTC. As for the electrical energy, the most important observation is how the total energy consumption for MLD 2 was much higher than that of MLD 1. This was due to the presence of EDBM that consumed a much larger quantity of electricity than all the other technologies present in the MLD processes.

In Figure 69, a comparative analysis of the total capital expenditures (capEX) and total operating expenditures (opEX) for the two MLD processes per technology is shown.

Notably, the NF technology in MLD 2 exhibited higher capital and operating costs compared to MLD 1. This discrepancy was attributed to the use of NFX membranes in MLD 2, which are more expensive than the NF270 membranes employed in MLD 1. Additionally, the NFX membrane presents higher rejections and lower fluxes than

NF270 and the plant in MLD 2 operated at a higher permeate recovery (70% instead of 60%) and a higher operating pressure (23 bar instead of 20 bar). For this reason, presenting lower fluxes but needing to reach higher recoveries, the NF plant of NFX membranes required more modules than the NF plant of NF270 membranes. These factors collectively contributed to the higher capital and operating expenditures.

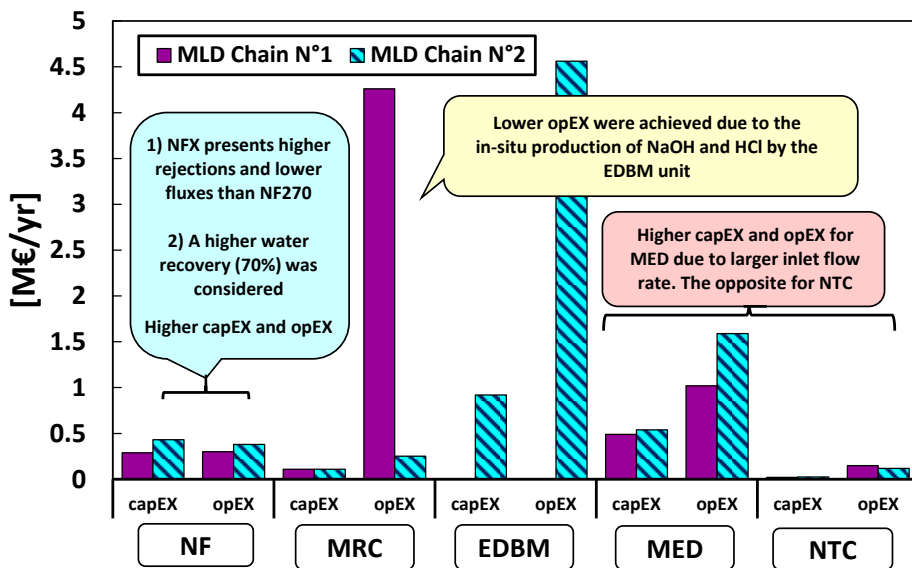


Figure 69: capEX and opEX for both MLD processes (i.e., this chapter and chapter 1) per technology.

As for the MRC, marginal differences in capital costs were observed. Although the crystallizer itself was slightly smaller due to lower feed flow rates, the larger quantity of magnesium required a larger drum filter, resulting in similar total capEX for the MRC in both MLD processes. Conversely, a substantial difference emerged in terms of opEX. In MLD 2, the MRC opEX witnessed a significant reduction since the downstream EDBM unit supplied all required chemicals, including the alkaline reactant (NaOH) and HCl for cleaning. The residual MRC opEX were predominantly associated with the energy consumption of the crystallizer and drum filter, which

were inherently lower than those of the NF since the MRC is not a pressure-driven process.

As far as the EDBM was concerned, a direct comparison with MLD 1 was not feasible due to its exclusive presence in MLD 2. However, noteworthy observations included high EDBM capEX, attributed to the use of expensive ion exchange and bipolar membranes and the large membrane area required for chemical production. Furthermore, EDBM opEX were the highest among all technologies in the MLD process due to substantial external electrical energy requirements for chemical production from the MRC effluent.

The MED unit presented capEX and opEX in MLD 2 higher than in MLD 1. Reasons for this were attributed to the higher inlet flow rate resulting from the additional water input to the EDBM unit. However, due to the higher efficiency of the MED in MLD 2 compared to MLD 1, the inlet of the final NTC was more or less the same in both MLD processes, leading to similar capEX and opEX in both scenarios.

Figure 70 reports the revenue achieved for each recovered resource in both scenarios: MLD 1 and MLD 2.

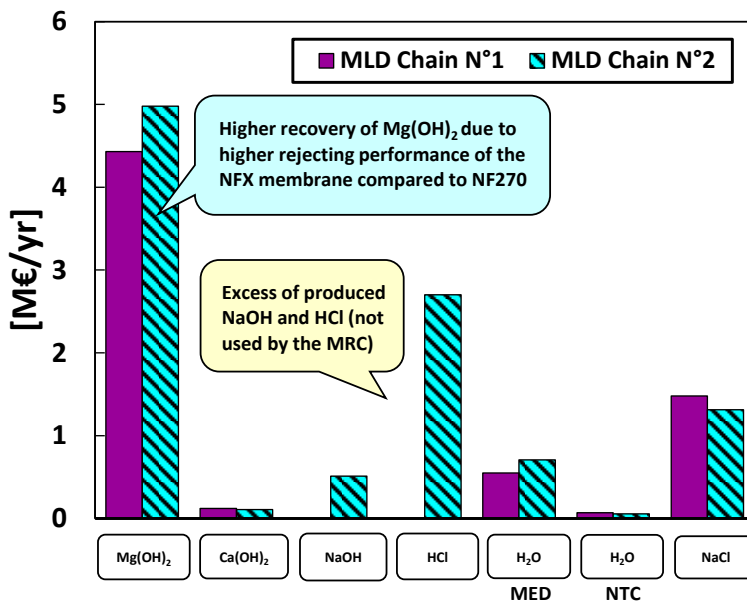


Figure 70: Revenue associated to each resource recovered from the MLD schemes.

As expected, the primary source of revenue across both MLD processes was the sale of $\text{Mg}(\text{OH})_2$, owing to both its significant quantity in the initial brine and a higher selling price compared to other recovered resources. Notably, the $\text{Mg}(\text{OH})_2$ revenue was higher in MLD 2 than in MLD 1, attributed to the superior rejection performance of the NFX membrane in MLD 2, resulting in a higher recovery of Mg.

In terms of $\text{Ca}(\text{OH})_2$ recovery, MLD 2 exhibited a slightly lower yield compared to MLD 1. This small difference arose from the higher rejection of multivalent ions in MLD 2, which was accompanied by an increased rejection of bicarbonates. Consequently, this led to a greater formation of CaCO_3 and a lesser quantity of $\text{Ca}(\text{OH})_2$.

Figure 70 provides insights into the revenue generated by NaOH and HCl production. It is important to note that this revenue is associated solely with the excess quantity of chemicals not utilized in the MRC. The surplus of HCl was notably larger, as it is predominantly used for cleaning purposes. Water recovery occurred in both the MED and NTC units. Generally, the MED produced a larger quantity of water. Additionally, the revenue from the MED was higher in MLD 2 compared to MLD 1, reflecting its enhanced efficiency.

Conversely, the NTC in MLD 2 generated lower revenue than its counterpart in MLD 1. This discrepancy can be attributed to the lower sodium concentration in the feed solution of both the MED and, consequently, the NTC in MLD 2.

In Figure 71, it is possible to observe the remaining total annual costs of each MLD process and the levelized costs for each recovered resource.

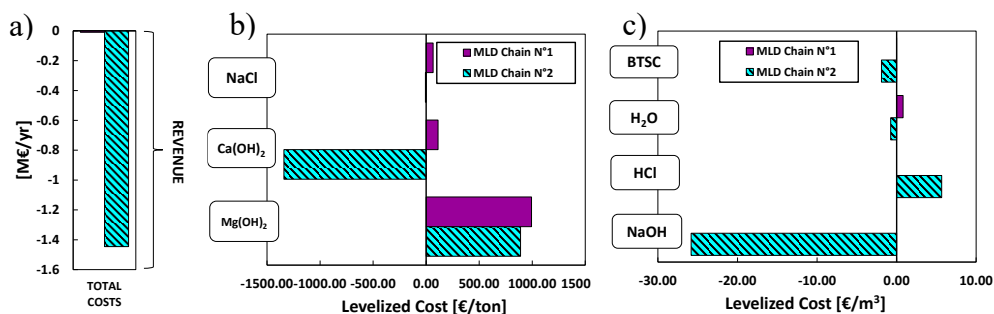


Figure 71: a) Total annual costs (*capEX+opEX-revenue*) of the MLD processes; b) Levelized costs of recovered solid products; c) Levelized costs of recovered water and chemicals and BTSC.

Firstly, it is possible to note how both of them present negative costs. This is translated into remaining annual revenue. This surplus, driven by the substantial revenue associated with $\text{Mg}(\text{OH})_2$ and the excess chemicals, significantly exceeded the total annual capital expenditures (*capEX*) and operating expenditures (*opEX*). Consequently, the levelized costs of all resources were lower than current market prices, with some even displaying negative values. Also, the BTSC presented a negative value. Therefore, taking into account that (i) MLD 1 is better than conventional brine disposal methods (as demonstrated in Chapter 1) and (ii) MLD 2 presents lower levelized costs and BSTC than MLD 1, it is possible to state that the newly proposed MLD process represents a better alternative for valuable resource recovery to MLD 2 or an even better alternative brine treatment method to conventional brine disposal methods. All in all, it is worth noting that these results were possible only thanks to the presence of the EDBM technology that allowed to significantly improve the global economic feasibility of MLD processes for SWRO brine valorisation.

SUMMARY & FINAL REMARKS

In light of critical issues such as water scarcity and land-mining depletion, the main objective of the present PhD thesis is the exploration of seawater and desalination brine as unconventional sources for recovering valuable minerals and freshwater. By doing so, the aim was to (i) improve the techno-economic efficiency of their production and (ii) mitigate the environmental impact of such recovery. To such end, the thesis focused on the valorisation of seawater and desalination brines through the development and/or integration of innovative and emerging technologies, adopting a Minimum Liquid Discharge (MLD) approach. The thesis is structured into four main sections:

Section 1 evaluated the potential of two proposed MLD schemes for seawater and desalination brine valorisation. The first proposed MLD chain focused on valorising directly desalination brine generated in Pantelleria island. It comprised four main technologies: Nanofiltration (NF), Magnesium Reactive Crystallizer (MRC), Multi-Effect Distillation (MED) and NaCl Thermal Crystallizer (NTC). The MLD chain could recover $\text{Mg}(\text{OH})_2$, $\text{Ca}(\text{OH})_2$, freshwater and NaCl. Via the coupling of technical and economic models, implemented in Python and integrated in an advanced simulation platform, namely RCE, the first MLD scheme underwent a thorough techno-economic assessment for a potential industrial scale implementation (feed capacity = $95 \text{ m}^3/\text{h}$, 50% of the brine generated by the SWRO plant in Pantelleria, Italy). Technical analysis results indicated the production of food-grade NaCl was feasible only if the NF membranes presented a specific set of ion rejections, thus underscoring the significant influence of NF performances on the overall performances of the MLD process. Economic analysis revealed opEXs five times higher than capEXs, primarily due to the cost of chemicals in the MRC. However, overall revenue surpassed the sum of capEXs and opEXs due to the sale of $\text{Mg}(\text{OH})_2$. The economic feasibility of the novel MLD system, as an alternative salt production method, was evaluated using the Levelized Cost Index, with all values lower or equal to current market prices. The Brine Treatment Specific Cost

(BTSC = -0.02 €/m^3) of the MLD process, as a brine treatment method, was also lower than conventional disposal methods. Final outcomes highlighted that significant fluctuations in NaOH and Mg(OH)_2 costs could jeopardize the economic feasibility, making the magnesium recovery step the bottleneck of the treatment chain. Within Section 1, a second MLD chain was introduced as an evolution of the first MLD scheme. Such scheme prioritized the utilization of seawater, featuring two notable advancements: the incorporation of Electrodialysis with Bipolar Membranes (EDBM) as an additional technology and the replacement of the NTC with Evaporation Ponds. The presence of EDBM allowed to produce in-situ the chemicals required for Mg precipitation (NaOH) and cleaning (HCl). Unlike the first MLD chain, the second chain was implemented at the pilot scale within the framework of the EU-funded project Water Mining. The chain, installed in Lampedusa island (Italy), represented the first MLD demonstration plant of such large scale worldwide, capable of recovering valuable salts in their final solid state. For such MLD process, the main scope was to actually assess the technical feasibility of the process via an extensive experimental campaign. Results demonstrated the chain capability to recover three valuable resources (Mg(OH)_2 with a purity of 90-98%, Ca(OH)_2 , and NaCl with a purity exceeding 99%), along with high-quality freshwater (achieving a recovery rate of up to 85% and freshwater conductivity below $30 \text{ }\mu\text{S/cm}$). The two chemicals employed as reactants and for cleaning/neutralizing purposes within the treatment chain, namely 1M NaOH and 0.65M HCl solutions, were also successfully reclaimed. Moreover, the stability of each unit during daily operations was meticulously assessed and achieved, showcasing not only the technical feasibility of the proposed demo plant but also affirming the viability of MLD as a sustainable alternative for minerals recovery. Lastly, a circularity assessment underscored the treatment chain capability to operate under a fully circular mode, with zero external chemical input and remarkably high recovery rates for water and chemicals generated within the process.

In light of improving the “bottleneck technology” of both proposed MLD schemes, Section 2 was focused on the operational strategy optimization of the Magnesium Reactive Crystallizer at the pilot scale, also known as MF-PFR (Multiple Feed-Plug Flow Reactor). Three different operational assets were considered, differing in the approach of to whether inject the brine into the alkaline reactant (NaOH) or vice-versa or to whether adopt a product recycling strategy within the MF-PFR. It was important to evaluate which asset could better enhance the properties of the final product $\text{Mg}(\text{OH})_2$ (such as sedimentation rate, filterability, particle size distribution), improving therefore its potential resulting revenue. The different reactor operational assets were investigated addressing the influence of (i) initial Mg^{2+} concentrations (Mg^{2+} 0.24 M to 1.0 M) mimicking a wide range of different brines, (ii) different reactants flow rates; and (iii) adopting a product recycling strategy (seeded crystallization). Higher initial Mg^{2+} concentration of the feed brine produced larger and stronger agglomerates of $\text{Mg}(\text{OH})_2$ particles than those produced by a lower initial concentration (0.24 M). More specifically, after an ultrasound post-treatment and use of a dispersant agent, micro-sized $\text{Mg}(\text{OH})_2$ agglomerates/aggregates were measured in the case of 1.0 M Mg^{2+} solutions, while nano-sized and micro-sized particles were detected for the 0.24 M case. As for the reactants flow rates, regardless the operational configuration, no influences were observed on the sedimentation trends, filtration times and granulometry of the final product. However, when operating at pH 12 (over-stoichiometric NaOH amounts) lower sedimentation rates and cake permeability coefficient values were obtained. Finally, the adoption of a product recycling strategy resulted to be significant, overcoming filterability and sedimentation issues of large-scale $\text{Mg}(\text{OH})_2$ suspensions production. As a matter of fact, compared to suspensions produced without product recycling, $\text{Mg}(\text{OH})_2$ suspensions sedimented up to 4 times faster and cake permeability coefficients increased reaching values up to one order of magnitude higher. However, two further important factors that could highly influence the revenue of $\text{Mg}(\text{OH})_2$ recovered from seawater/desalination brine are its purity and recovery that highly depend on the performances of the MF-PFR pre-treatment step (in this specific case NF).

Section 3 was dedicated to the comprehensive evaluation of NF as a discerning pre-treatment and separation stage. In this context, the performance of both newly developed NF membranes, engineered to enhance magnesium selectivity, and existing commercial NF membranes were assessed. Firstly, a novel positively charged NF membrane was purposely fabricated to increase magnesium membrane selectivity. Carefully chosen components endowed the NF membrane with a highly positive surface charge in alkaline environments, thereby selectively rejecting magnesium. The membrane composition included a microporous asymmetric UF-membrane-like substrate for mechanical strength and a selective active layer incorporating MOF "NH₂-MIL-101(Al)" and ZnO within a chitosan matrix. Characterization of the active layer nanoparticles involved SEM, FTIR, DLS, and BET analyses; nanocomposite morphology, hydrophilicity, and electric surface charge were also examined. The impact of varying MOF and ZnO loadings within the active layer on the NF membrane selective and permeation performance was thoroughly investigated. Initial filtration tests, conducted at 5 bar with 1000 mg/L single salt solutions (NaCl, Na₂SO₄, MgCl₂, CaCl₂), showed that an increase in ZnO content within the active layer enhanced membrane hydrophilicity and zeta potential, leading to elevated rejections of multivalent cations. However, excessive ZnO concentrations resulted in pore blockage and microfractures in the active layer, diminishing overall ionic rejections. The CMZ-35 variant of the novel NF membrane, with a composition of 20%wt Chitosan, 35%wt ZnO, and 45%wt MOF, exhibited the highest rejections for MgCl₂ (90.10%) and CaCl₂ (86.49%). Lastly, the selectivity properties of the synthesized NF membrane were compared to those of common commercial NF membranes (NF90, NF270) and other positively charged NF membranes documented in literature, all under the same operating conditions. CMZ-35 exhibited the highest selectivity towards MgCl₂ and CaCl₂ among all the membranes. Similar successful achievements were also reached in synthetic seawater and desalination brine at 30 bar. Therefore, due to its low-cost fabrication materials, simple fabrication procedure and appealing performances, the novel synthesized membrane presents an intriguing competitive alternative to commercial

NF membranes, that could considerably enhance mineral recovery in ZLD/MLD systems for seawater and brine valorisation. As mentioned previously, Section 3 also focused on evaluating the performances of existing commercial NF membranes for seawater and SWRO brine valorisation in a wide range of operating pressures (8 – 30 bar), adopting a closed-loop configuration. In this comprehensive investigation, the performance of five NF membranes (NF90, NFS, NFX, VNF1, DK) was meticulously assessed, emphasizing their effectiveness in rejecting both major and minor components. Notably, these membranes exhibited substantial potential in separating multivalent cations such as Mg^{2+} , Ca^{2+} , and Sr^{2+} from Na^+ , K^+ , Cl^- , and Br^- . Experimental data on ion rejection rates were fittingly correlated with model predictions, specifically using the SEDF model, resulting in good agreement. Optimal operating pressure was identified at 20 bar, beyond which limited improvements were observed. In accordance with Donnan and dielectric exclusion effects, the commercial NF membranes demonstrated high rejections for multivalent cations, surpassing 97.1%, 92.8%, and 96.5% for Mg^{2+} , Ca^{2+} , and Sr^{2+} in seawater and 94.5%, 87.1%, and 91.7% in SWRO brine, respectively. Among the membranes investigated, the DK membrane exhibited the highest permeability (3.5 LMH bar⁻¹) and selectivity factor (>0.6) for multivalent elements relative to monovalent ones, establishing its superior efficacy for the selective pre-separation of minerals from seawater and SWRO brine, followed by VNF1 and NFX. Given the existing literature on DK for similar applications, attention was directed towards a more in-depth exploration of the performances of VNF1 and NFX membranes. Specific focus of such exploration was given to magnesium recovery from seawater/SWRO brines (being magnesium the most economically important component in seawater). Following membrane characterization, NFX and VNF1 were experimentally tested at 20 bar under varying permeate recovery rates (10% to 80%). Key findings revealed the NFX notable characteristic of high Mg^{2+} rejection and relatively reduced monovalent ion rejections in processing SWRO brine, outperforming seawater treatment. VNF1 achieved the highest concentration factor of Mg^{2+} with seawater but exhibited elevated concentration factors and the highest rejections of

monovalent ions, indicating diminished selectivity. VNF1 also showed higher susceptibility to feed concentration fluctuations compared to NFX, resulting in lower Mg^{2+} rejections at higher permeate recovery rates in SWRO brine. Moreover, experimental data was cross-validated with simulation results from the SEDF mathematical model, demonstrating remarkable consistency with errors maintained below 10%. Subsequently, a techno-economic assessment focused on the potential recovery and revenue of $Mg(OH)_2$ by coupling NF with a downstream crystallizer. Due to its superior selectivity, NFX facilitated the production of $Mg(OH)_2$ with the highest purities (97%) at an operational pressure of 10 bar and a permeate recovery rate of 80%. The most economically favourable scenario involved the application of NFX with SWRO brine, resulting in the highest potential revenues from $Mg(OH)_2$ production, estimated at 5.68 M€/yr. Overall, the results from Section 3 underscore the crucial role of NF as a pre-separation step in MLD schemes to enhance the quality of recovered magnesium and, consequently, the revenue generated by MLD processes when treating seawater or SWRO brine. Furthermore, the study demonstrated how separation performances can be significantly enhanced through the synthesis of novel positively charged NF membranes.

Section 4 finally incorporated all successful results achieved in the previous sections in the proposal of a final novel MLD scheme for SWRO brine valorisation. The novel scheme comprised: (i) NF unit with NFX membranes, (ii) MF-PFR, (iii) EDBM, (iv) optimized MED and (v) NTC. The scheme underwent a techno-economic analysis, and results were compared to those of Chapter 1. The final outcomes of such comparison indicated (i) a much larger revenue and (ii) overall lower product Levelized costs and BTSC with the novel MLD scheme, due to the in-situ production of chemicals via EDBM. In conclusion, the attractive economic viability of the ultimate scheme serves as a testament to the potential of seawater/SWRO brine valorisation schemes employing an MLD approach for freshwater and mineral recovery. This not only substitutes conventional methods but, more significantly, addresses critical challenges such as water scarcity, depletion of land-mining

resources, and the environmental impact associated with desalination brine discharge.

Future perspectives

Drawing from the significant achievements outlined in this PhD thesis, it is evident that mineral recovery through MLD schemes from unconventional sources such as seawater and desalination brine holds substantial promise. The economic feasibility of such schemes, however, hinges crucially on the judicious selection of technologies and the targeted minerals for recovery. Magnesium, uniquely characterized by both a high market price and relatively elevated concentration in seawater, emerges as a particularly promising candidate. The pivotal role of NF as a pre-separation process in MLD schemes, coupled with the superior performance of CMZ-35 over several commercial NF membranes, underscores the importance of optimizing and further exploring the potential of CMZ-35. To maximize the revenue from $\text{Mg}(\text{OH})_2$ in MLD schemes, ongoing efforts should focus on refining and comprehensively understanding the capabilities of CMZ-35. As CMZ-35 advances towards potential commercialization, it becomes imperative to evaluate aspects such as its long-term stability and anti-fouling properties. These considerations will be instrumental in shaping the future viability and success of CMZ-35 in the framework of mineral recovery. Additionally, it would also be of significant importance to conduct in the future a Life Cycle Assessment of the final proposed MLD treatment chain, thus evaluating not only the economic feasibility but also the sustainability of seawater/brine mining via MLD schemes.

NOMENCLATURE

Acronyms

| | |
|---------------------------|---------------------------------------------------------|
| AEM | Anionic Exchange Membrane |
| ATR-FTIR | Attenuated Total Reflectance-Fourier Transform Infrared |
| BC | Brine Concentrator |
| BCr | Brine Crystallizer |
| BEC | Brine Excellence Centre |
| BPM | BiPolar Membrane |
| BTSC | Brine Treatment Specific Cost [€/m ³] |
| capEX | Capital Expenditure [€/year] |
| Ca(OH)₂ | Calcium hydroxide |
| CCI | Circular Chemical Inflow |
| CEM | Cationic Exchange Membrane |
| CEPCI | Chemical Engineering Plant Cost Index |
| cfv | Cross Flow Velocity |
| CMZ | Chitosan Metal organic framework Zinc oxide |
| CP | Concentration Polarization |
| Cr | Crystallizer |
| CRM | Critical Raw Material |
| DADMAC | Diallyl Dimethyl Ammonium Chloride |
| DLR | German Aerospace Center |
| DLS | Dynamic Light Scattering |
| DPNF | Double Pass NanoFiltration |
| EC | Electric Conductivity |
| ECH | Epichlorohydrin |
| ED | ElectroDialysis |
| EDBM | ElectroDialysis with Bipolar Membranes |
| EDR | Electrodialysis Reversal |
| EDX | Energy-dispersive X-ray |

| | |
|------------------------------|----------------------------------------------------------|
| EIP | European Innovation Partnership |
| EIT | European Institute of Innovation and Technology |
| EPs | Evaporation Ponds |
| ESS | Energy Self-Sufficiency |
| EU | European Union |
| Ev | Evaporator |
| FE-SEM | Field Emission Scanning Electron Microscopy |
| FO | Forward Osmosis |
| FTIR | Fourier Transform Infrared Spectroscopy |
| HACC | 2-hydroxypropyltrimethyl Ammonium Chloride Chitosan |
| HCl | Hydrochloric acid |
| HDH | Humidification DeHumidification |
| HDPE | High-Density PolyEthylene |
| HPLC | High Performance Liquid Chromatography |
| HPRO | High Pressure Reverse Osmosis |
| ICP-MS | Inductively Coupled Plasma-Mass Spectrometry |
| ICP-OES | Inductively Coupled Plasma-Optical Emission Spectroscopy |
| IEX | Ion Exchange |
| LCOC_{a(OH)2} | Levelized Cost of Calcium Hydroxide [€/ton] |
| LCOM_{g(OH)2} | Levelized Cost of Magnesium Hydroxide [€/ton] |
| LCOS_{alt} | Levelized Cost of Salt (NaCl) [€/ton] |
| LCOW_{ater} | Levelized Cost of Water [€/m ³] |
| MCr | Membrane Crystallizer |
| MD | Membrane Distillation |
| ME | Membrane Electrolysis |
| MED | Multi-Effect Distillation |
| MF-PFR | Multiple Feed – Plug Flow Reactor |
| Mg²⁺ | Magnesium ion |
| MgCl₂ | Magnesium chloride |
| MgCO₃ | Magnesium carbonate |
| Mg(OH)₂ | Magnesium hydroxide |

| | |
|-------------------------|--------------------------------------------|
| MLD | Minimum Liquid Discharge |
| MMF | Multi-Media Filter |
| MO | Metal Oxide |
| MOF | Metal Organic Framework |
| MRC | Magnesium Reactive Crystallizer |
| MSF | Multi-Stage Flash |
| Na⁺ | Sodium ion |
| NaOH | Sodium Hydroxide |
| NcapEX | Normalized Capital Expenditure |
| NF | Nanofiltration |
| NH₄OH | Ammonium Hydroxide |
| NopEX | Normalized Operating Expenditure |
| NTC | NaCl Thermal Crystallizer |
| OARO | Osmotic Assisted Reverse Osmosis |
| opEX | Operating Expenditure [€/year] |
| PAI | Polyamide-imide |
| PAMAM | Poly(amidoamine) |
| PAN | Polyacrylonitrile |
| PDA | Polydopamine |
| PDMAEMA | Poly (N,N-dimethylaminoethyl methacrylate) |
| PEI | Polyethylenimine |
| PEKC | Poly(ether ether ketone) |
| PES | Polyethersulfone |
| PET | PolyEthylene Terephthalate |
| PIP | Piperazine |
| PIT | Pressure Indicator Transmitter |
| PLC | Programmable Logic Control |
| p.r | Permeate Recovery |
| PSF | Polysulfone |
| PVC | PolyVinyl Chloride |
| QIT | Flow Rate Indicator Transmitter |

| | |
|--------------|-------------------------------------|
| RCE | Remote Component Environment |
| RE | Resource Efficiency |
| REV | Revenue [€/year] |
| RED | Reverse Electrodialysis |
| RO | Reverse Osmosis |
| SCWD | Super Critical Water Desalination |
| SED | Selective Electrodialysis |
| SEDF | Solution Electro-Diffusion Film |
| SW | Seawater |
| SWCC | Saline Water Conversion Corporation |
| SWRO | Seawater Reverse Osmosis |
| TBT | Top Brine Temperature [°C] |
| TDS | Total Dissolved Salts [g/L] |
| TIT | Temperature Indicator Transmitter |
| TMC | Trimesoyl Chloride |
| TMP | Transmembrane Pressure |
| TVC | Thermal Vapour Compression |
| TWP | Total Water Production |
| UF | Ultrafiltration |
| V-PSD | Volume Particle Size Distribution |
| WAIV | Wind Aided Intensified eVaporation |
| WCA | Water Contact Angle |
| XRD | X-Ray Diffraction |
| ZLD | Zero Liquid Discharge |

APPENDIX A

Nanofiltration NF technical model

The NF technical model is a multi-scale model which comprises: (i) a low-scale model that describes the transport mechanisms within the NF membrane, (ii) a middle-scale model for a single NF unit and (iii) a high-scale model of a whole NF plant.

- **Small-scale model (NF membrane)**

The Donnan Steric Pore Model with Dielectric Exclusion (DSPM-DE) is employed to describe the transport mechanisms that occur within the NF membrane. Such model exploits the extended Nernst-Planck equation across the membrane. Within the equation, three different ionic transport mechanisms are considered: (i) convection, (ii) diffusion and (iii) electro-migration (see Table A1). The width of the membrane is discretized in a specific number of elements (50 based on sensitivity analyses). The ‘j’ index refers to the discretised element, while the ‘i’ index refers to a specific ion.

The main equations of the technical model are listed in Table A1, where $C_{i,j}^m$, $C_{i,j}^{bm}$, C_i^b and C_i^p are the concentration of the i species in the j^{th} element in the membrane, at the bulk-membrane interface, in the bulk solution and in the permeate stream, respectively. J_i and J_v represent the total flux of the species i and the water convective transmembrane flux, respectively. ψ is the electric potential across the membrane, ζ the electric potential gradient at the bulk-membrane interface, outside the electric double layer, and $\Delta\psi_{D,bm}$ and $\Delta\psi_{D,pm}$ represent the Donnan potential difference at the bulk-membrane interface and at the permeate-membrane interface, respectively. $K_{i,c}$ and $k_{i,d}$ represent the hindered convective and diffusive mass transfer coefficients of the ions within the pore, depending on λ_i , i.e. the ratio between the solute radius (r_i) and the pore radius (r_{pore}). $D_{i,p}$ is the diffusivity of the species i within the pore, corrected taking into account the diffusivity in the bulk via $k_{i,d}$.

Ion partitioning at the two membrane interfaces, the steric effect and the dielectric exclusion are given by solving the system of equations listed in Table A1. Furthermore, the electro-neutrality on the bulk, on the permeate side and inside the membrane (which presents a fixed charge density X_d) are conditions that must be contemporarily satisfied. Mass transfer resistance on the bulk side is considered to compute the ions concentration on the bulk-membrane interface. It is then possible to calculate the solute flux from the bulk to the membrane. As for the mass transfer coefficients, the mass transfer coefficient in the bulk, $k^{bulk}_{c,i}$ depends on the flow regime whereas $k^{bulk}_{c,i}$ is obtained multiplying the mass transfer coefficient $k^{bulk}_{c,i}$ by a factor depending on the permeation flux through the membrane. The Hagen-Poiseuille relation is employed to calculate the solvent transmembrane flux J_v . Such flux depends on the geometric parameters of the membrane and on the net driving pressure, ΔP (given by the pressure gradient between bulk and permeate channel minus the osmotic pressure $\Delta \Pi$) where η_{mix} is the mixing efficiency of the spacer, h_f is the height of the feed channel, L_{mix} is the mixing length of the spacer, Pe and Sc are the Peclet and the Schmidt adimensional numbers respectively. The system of equations is implemented in Python and solved in an iterative manner.

Table A1. Equations of the implemented DSPM-DE model.

| | |
|----------|---------------------------------------------------------------------------------------------------------------------------------------------------------------------------------------------------------------------------------------|
| (1)[274] | $j_i = J_v C_{i,p} = -D_{i,p} \frac{C_{i,j+1}^m - C_{i,j}^m}{\delta y_j} - \frac{1}{2} z_i (C_{i,j+1}^m + C_{i,j}^m) D_{i,p} \frac{F}{RT} \frac{\psi_{j+1} - \psi_j}{\delta y_j} + \frac{1}{2} k_{i,c} (C_{i,j+1}^m + C_{i,j}^m) J_v$ |
| (2)[275] | $k_{i,d} = \frac{1 + \sqrt[9]{8} \lambda_i \ln(\lambda_i) - 1.56034 \lambda_i + 0.528155 \lambda_i^2 + 1.91521 \lambda_i^3 - 2.81903 \lambda_i^4 + 0.270788 \lambda_i^5 + 1.10115 \lambda_i^6 - 0.435933 \lambda_i^7}{\phi_i}$ |
| (3)[275] | $k_{i,c} = \frac{1 + 3.867 \lambda_i - 1.907 \lambda_i^2 - 0.834 \lambda_i^3}{1 + 1.867 \lambda_i - 0.741 \lambda_i^2}$ |
| (4)[275] | $D_{i,p} = k_{i,d} D_{i,\infty}$ |
| (5)[276] | $\frac{\gamma_{i,1}^m C_{i,1}^m}{\gamma_{i,j}^{bm} C_{i,j}^{bm}} = \phi_i \phi_{B_i} \exp\left(-\frac{z_i F}{RT} \Delta \psi_{D,bm}\right)$ |
| (6)[276] | $\frac{\gamma_{i,N}^m C_{i,N}^m}{\gamma_{i,1}^p C_{i,1}^p} = \phi_i \phi_{B_i} \exp\left(-\frac{z_i F}{RT} \Delta \psi_{D,pm}\right)$ |
| (7)[277] | $\log \gamma_i = -A z_i^2 \left(\frac{\sqrt{I}}{1 + \sqrt{I}} - 0.3 I \right)$ |
| (8)[277] | $A = \frac{e_0^3 N_A^{1/2}}{\ln(10) 4\pi \sqrt{2} (\epsilon k_B T)^{3/2}}$ |
| (9)[278] | $\phi_{B_i} = \exp\left(-\frac{\Delta W_i}{k_B T}\right)$ |

| | |
|-----------|----------------------------------------------------------------------------------------------------------------------------------------------------------------------------------------------|
| (10)[278] | $\Delta W_i = \frac{z_i^2 e_0^2}{8\pi\epsilon_0 r_i} \left(\frac{1}{\epsilon_{pore}} - \frac{1}{\epsilon_{bulk}} \right)$ |
| (11)[278] | $\phi_i = (1 - \lambda_i)^2$ |
| (12)[279] | $\sum_i z_i C^{bm}_i = 0$ |
| (13)[279] | $\sum_i z_i C^p_i = 0$ |
| (14)[279] | $\sum_i z_i C^m_{i,j} + X_d = 0$ |
| (15)[279] | $j_i = -k'_{c,i}{}^{bulk} (C^{bm}_i - C^b_i) + J_v C^{bm}_i - z_i C^{bm}_i D_{i,\infty} \frac{F}{RT} \xi$ |
| (16)[280] | $k'_{c,i}{}^{bulk} = k_{c,i}{}^{bulk} \Xi = k_{c,i}{}^{bulk} \left[\frac{J_v}{k_{c,i}{}^{bulk}} + \left(1 + 0.26 \left(\frac{J_v}{k_{c,i}{}^{bulk}} \right)^{1.4} \right)^{-1.7} \right]$ |
| (17)[280] | $k_{c,i}{}^{bulk} = 0.753 \left(\frac{\eta_{mix}}{2 - \eta_{mix}} \right)^{1/2} \left(\frac{D_{i,\infty}}{h_f} \right) S C^{-1/6} \left(\frac{Pe_i h_f}{L_{mix}} \right)^{1/2}$ |
| (18)[81] | $J_v = \frac{\Delta P r_{pore}^2}{8 \eta \delta_m}$ |
| (19)[81] | $\Delta \Pi = RT \sum_i (C^{bm}_i - C^p_i)$ |

• **Medium-scale model (NF element)**

The medium-scale model refers to an NF element in which the low-scale model is integrated. The NF element length is discretised in a series of units. For each discrete unit, average values of the concentration, flow rates and pressure are firstly guessed to calculate the osmotic pressure and the bulk mass transfer coefficient. Then, the small-scale model allows to compute the ions rejection and the water flux. Finally, the outlet concentrations and flow rates of each discrete unit are computed by means of mass balances (Table A2) [70].

| |
|------------------------------------------------------------------------------------------------------|
| $M_{p_x} = M_{p_{x-1}} + J_{v_x} \frac{A_{membr,elem}}{n_{discr,L}}$ |
| $M_{ret_x} = M_{b_x} - J_{v_x} \frac{A_{membr,elem}}{n_{discr,L}}$ |
| $C^p_{i_x} = \frac{C^p_{i_{x-1}} M_{p_{x-1}} + j_{i_x} \frac{A_{membr,elem}}{n_{discr,L}}}{M_{p_x}}$ |
| $C^{ret}_{i_x} = \frac{C^b_{i_x} M_{b_x} - j_{i_x} \frac{A_{membr,elem}}{n_{discr,L}}}{M_{ret_x}}$ |
| $M_{b_x} = M_{ret_{x-1}}$ |
| $C^b_{i_x} = C^{ret}_{i_{x-1}}$ |
| $P_x = P_{x-1} - \Delta P_{losses} = P_{x-1} - \frac{f l}{2 D_H} \rho_f u_f^2$ |

$$f = \frac{6.23}{Re^{0.3}}$$

Table A2: Equations to model a nanofiltration element.

M_p and C^p_i are the mass flow rate and the concentrations in the permeate channel, M_{ret} and C^{ret}_i are the flow rate and the concentrations in the retentate channel, which are the same as those entering the next interval (M_b and C^b_i), and $A_{membr,elem}$ and $n_{discr,L}$ are the total membrane area of a NF element and the number of discretization intervals along the main feed flow direction. As for the equation to calculate the pressure losses, f is the friction factor, l is the length of the discretization interval and D_H is the hydraulic diameter relevant to the feed channel.

- **Large-scale model (NF plant)**

The main aim of the large-scale model is to calculate the total number of vessels necessary to reach a specific value of recovery. Firstly, an initial number of vessels in parallel is given by dividing the required permeate flow rate and a guessed average solvent transmembrane flux. Then, the feed flow rate for each vessel is calculated. Subsequently, the average solvent flux in the vessel is recalculated in relation to the net driving pressure along the elements, and the total recovery rate is computed. Once this value has been calculated, the number of pressure vessels in parallel can be updated considering a linear relationship between the number of vessels and the recovery. From this point, another iteration begins. Once the value of the total recovery is higher or equal to the required one, the loop is brought to an end.

Magnesium Reactive Crystallizer MRC technical model

The Magnesium Reactive Crystallizer MRC technical model is based on simple mass balance equations which are listed in Table B1. The MRC consists of two precipitation steps. In the first step, magnesium is recovered from the brine in the form of magnesium hydroxide $Mg(OH)_2$ by employing an alkaline reactant: a

sodium hydroxide solution NaOH. In order to promote $Mg(OH)_2$ precipitation, one magnesium ion of the brine has to react with two hydroxyl ions of the alkaline solution. The mass flow rate $Q_{NaOH_{1^\circ step}}$ of the required alkaline solution is calculated taking into account (i) such proportion with the molar flow rate of magnesium $Q_{feed, Mg^{2+}_{1^\circ step}}$ multiplied by the effective conversion rate of magnesium $\%_{Mg^{2+}_{1^\circ step}}$ and (ii) the quantity of NaOH which is used in precipitating the bicarbonates present in the brine where $Q_{feed_{1^\circ step}}$ is the volumetric feed flow rate and $C_{feed, HCO_3^-_{1^\circ step}}$ is the molar concentration of the bicarbonates in the brine. The latter phenomenon unfortunately is inevitable and has to be considered. The flow rate $Q_{NaOH_{1^\circ step}}$ depends on the operating molar concentration of NaOH $C_{NaOH_{1^\circ step}}$. Simple mass balance are further employed to calculate the total outlet volumetric flow rate of the 1° precipitation step $Q_{out_{1^\circ step}}$, the mass flow rate of $Mg(OH)_2$ produced $M_{Mg(OH)_{2_{1^\circ step}}}$ where $MW_{Mg(OH)_2}$ is the molecular weight of $Mg(OH)_2$ and the magma density of $Mg(OH)_2$ $M_{Mg(OH)_{2_{1^\circ step}}}$. Finally, the outlet ionic molar concentrations are computed where the index i is the generic ion present in the brine (K^+ , SO_4^{2-} , Cl^-) All bicarbonates are precipitated in the 1° step in the form of calcium carbonates. Such precipitation influences the final concentration of calcium in the outlet stream. The outlet of the 1° step becomes the inlet of the 2° step and mass balance equations are employed to estimate the mass flow rate of calcium hydroxide $Ca(OH)_2$ produced $M_{Ca(OH)_{2_{2^\circ step}}}$ where $\%_{Ca^{2+}_{2^\circ step}}$ is the effective conversion rate of calcium in the second step. As for the NaOH employed in the 2° step, its volumetric flow rate $Q_{NaOH_{2^\circ step}}$ takes into account three contributes: (i) the stoichiometric quantity $Q_{NaOH, stoic_{2^\circ step}}$ to precipitate calcium, (ii) the quantity employed to complete magnesium precipitation $Q_{NaOH, Mg_{2^\circ step}}$ and (iii) the quantity needed to reach pH =13 and complete calcium precipitation $Q_{NaOH, added_{2^\circ step}}$. Within the equation to calculate $Q_{NaOH, added_{2^\circ step}}$ it is worth mentioning that $C_{Ca(OH)_{2_{sol}}}$ is the $Ca(OH)_2$ solubility and $C_{NaOH_{pH=13}}$ is the molar concentration of

NaOH at pH 13. Finally, the volumetric flow rate of acid HCl $Q_{HCl_{TOT}}$ is computed (necessary to neutralize the final effluent exiting the MRC $Q_{effluent}$).

Table B1. Mass balance equations of the Magnesium Reactive Crystallizer plant.

| 1° precipitation step | 2° precipitation step |
|-------------------------------------------------------------------------------------------------------------------------------------------------------------------------------------------------------------------------------|--------------------------------------------------------------------------------------------------------------------------------------------------------------------------------------|
| $Q_{NaOH_{1^{st}step}} = \frac{2Q_{feed,Mg^{2+}_{1^{st}step}} \cdot \%Mg^{2+}_{1^{st}step} + Q_{feed_{1^{st}step}} \cdot C_{feed,HCO_3^{-}_{1^{st}step}}}{C_{NaOH_{1^{st}step}}}$ | $Q_{feed,Ca^{2+}_{2^{st}step}} = Q_{out_{1^{st}step}} \cdot C_{out,Ca^{2+}_{1^{st}step}}$ |
| $Q_{out_{1^{st}step}} = Q_{NaOH_{1^{st}step}} + Q_{feed_{1^{st}step}}$ | $Q_{NaOH,stoic_{2^{st}step}} = \frac{2Q_{feed,Ca^{2+}_{2^{st}step}} \cdot \%Ca^{2+}_{2^{st}step}}{C_{NaOH_{2^{st}step}}}$ |
| $M_{Mg(OH)_{21^{st}step}} = Q_{feed,Mg^{2+}_{1^{st}step}} \cdot \%Mg^{2+}_{1^{st}step} \cdot MW_{Mg(OH)_2}$ | $Q_{NaOH,Mg_{2^{st}step}} = \frac{2Q_{out_{1^{st}step}} \cdot C_{out,Mg^{2+}_{1^{st}step}}}{C_{NaOH_{2^{st}step}}}$ |
| $Magma\ density_{Mg(OH)_{21^{st}step}} = \frac{M_{Mg(OH)_{21^{st}step}}}{Q_{out_{1^{st}step}}}$ | $Q_{NaOH,added_{2^{st}step}} = \frac{(C_{Ca(OH)_{2sol}} - C_{NaOH_{pH=13}}) \cdot (Q_{out_{1^{st}step}} + Q_{NaOH,stoic_{2^{st}step}})}{(C_{NaOH_{pH=13}} - C_{NaOH_{2^{st}step}})}$ |
| $C_{out,Mg^{2+}_{1^{st}step}} = \frac{Q_{feed_{1^{st}step}} \cdot C_{feed,Mg^{2+}_{1^{st}step}} (1 - \%Mg^{2+}_{1^{st}step})}{Q_{NaOH_{1^{st}step}} + Q_{feed_{1^{st}step}}}$ | $Q_{NaOH_{2^{st}step}} = Q_{NaOH,stoic_{2^{st}step}} + Q_{NaOH,Mg_{2^{st}step}} + Q_{NaOH,added_{2^{st}step}}$ |
| $C_{out,Na^+_{1^{st}step}} = \frac{Q_{feed_{1^{st}step}} \cdot C_{feed,Na^+_{1^{st}step}} + Q_{NaOH_{1^{st}step}} \cdot C_{NaOH_{1^{st}step}}}{Q_{out_{1^{st}step}}}$ | $Q_{out_{2^{st}step}} = Q_{NaOH_{2^{st}step}} + Q_{out_{1^{st}step}}$ |
| $C_{out,i^{th}_{1^{st}step}} = \frac{Q_{feed_{1^{st}step}} \cdot C_{feed,i^{th}_{1^{st}step}}}{Q_{out_{1^{st}step}}}$ | $M_{Ca(OH)_{22^{st}step}} = Q_{feed,Ca^{2+}_{2^{st}step}} \cdot \%Ca^{2+}_{2^{st}step} \cdot MW_{Ca(OH)_2}$ |
| $C_{out,Ca^{2+}_{1^{st}step}} = \frac{Q_{feed_{1^{st}step}} \cdot C_{feed,Ca^{2+}_{1^{st}step}} - Q_{feed_{1^{st}step}} \cdot C_{feed,HCO_3^{-}_{1^{st}step}}}{Q_{out_{1^{st}step}}}$ $C_{out,HCO_3^{-}_{1^{st}step}} = 0$ | $Magma\ density_{Ca(OH)_{22^{st}step}} = \frac{M_{Ca(OH)_{22^{st}step}}}{Q_{out_{2^{st}step}}}$ |
| $M_{CaCO_3_{1^{st}step}} = Q_{feed_{1^{st}step}} \cdot C_{feed,HCO_3^{-}_{1^{st}step}} \cdot MW_{CaCO_3}$ | $C_{out,Na^+_{2^{st}step}} = \frac{Q_{out_{1^{st}step}} \cdot C_{out,Na^+_{1^{st}step}} + Q_{NaOH_{2^{st}step}} \cdot C_{NaOH_{2^{st}step}}}{Q_{out_{2^{st}step}}}$ |
| | $C_{out,Mg^{2+}_{2^{st}step}} = C_{out,HCO_3^{-}_{2^{st}step}} = 0$ |
| | $C_{out,i^{th}_{2^{st}step}} = \frac{Q_{out_{1^{st}step}} \cdot C_{out,i^{th}_{1^{st}step}}}{Q_{out_{2^{st}step}}}$ |
| | $C_{out,Ca^{2+}_{2^{st}step}} = \frac{Q_{out_{1^{st}step}} \cdot C_{out,Ca^{2+}_{1^{st}step}} (1 - \%Ca^{2+}_{2^{st}step})}{Q_{out_{2^{st}step}}}$ |
| | $Q_{HCl_{TOT}} = Q_{NaOH,added_{2^{st}step}} \cdot C_{NaOH_{2^{st}step}}$ |
| | $Q_{effluent} = Q_{out_{2^{st}step}} + \frac{Q_{HCl_{TOT}}}{C_{HCl}}$ |

Multi-Effect Distillation MED technical model

The technical model for the MED refers to a Forward Feed configuration in which both feed water and vapour flow in the same direction. The MED unit comprises three different classes of effects for which different mass and energy equations are

applied ((i) the first effect, (ii) the intermediate effects and (iii) the last effect with the end condenser). All equations are reported in Table C1. It is to be noted that some variables within the equations are accompanied by “[I]”, “[i]” or “[N]”. This means that they refer to the first effect, the generic intermediate effect or the last effect, respectively. Furthermore, λ is the latent heat of water, h_{vap} is the enthalpy of the steam, h_{liq} is the enthalpy of the liquid water, h_{sw} is the enthalpy of the NaCl salt-water solution and $c_{p,sw}$ is the NaCl salt-water solution specific heat. The water properties are function of temperature, while the NaCl-water solution properties are functions of temperature and composition.

Table C1. Main mass and energy balance equations of the forward-feed MED model [67].

| |
|----------------------------------------------------------------------------------------------------------------------------------------------------------------------------------------------------------------------------------|
| $M_{feed} = M_{dist} + M_{brine}$ |
| $M_{feed} X_{feed} = M_{brine} X_{brine}$ |
| $T_{vsat} = T - BPE(T, X_{brine})$ |
| $T'_{vsat} = T_{vsat} - \Delta T_{demister}$ |
| $T'_c = T'_{vsat} - \Delta T_{lines}$ |
| $T_c = T'_c - \Delta T_{grav} - \Delta T_{acc}$ |
| $M_s \lambda(T_s) + M_{feed} h_{sw}(T_{preh}[1], X_{feed})$ $= M_b[1] h_{sw}(T[1], X_b[1])$ $+ (1 - \alpha_{cond}[1]) M_{vap}[1] h_{vap}(T'_{vsat}[1])$ $+ \alpha_{cond}[1] M_{vap}[1] h_{liq}(T'_{vsat}[1])$ |
| $M_b[i-1] = M_d[i] + M_{fbrine}[i] + M_b[i]$ |
| $M_{feed} X_{feed} = M_b[i] X_b[i]$ |
| $M_{vap}[i] = M_d[i] + M_{fbrine}[i] + M_{fb}[i]$ |
| $M_c[i-1] + \alpha_{cond}[i] M_{vap}[i]$ $+ (1 - \alpha_{cond}[i-1]) M_{vap}[i-1] = M_{fb}[i] + M_c[i]$ |
| $M_c[i-1] h_{liq}(T'_{vsat}[i-1])$ $+ \alpha_{cond}[i] M_{vap}[i] h_{liq}(T'_{vsat}[i]) +$ $(1 - \alpha_{cond}[i-1]) M_{vap}[i-1] h_{liq}(T_c[i-1])$ $= M_{fb}[i] h_{vap}(T'_{vsat}[i]) + M_c[i] h_{liq}(T'_{vsat}[i])$ |
| $M_{fbrine}[i] \lambda(T_{brine,f}[i])$ $= M_{brine}[i-1] c_{p,sw}(T_{mean}, X_b[i-1])$ $(T[i-1] - T_{brine,f}[i])$ |
| $M_{feed} c_{p,sw}(T_{mean}, X_f) (T_{preh}[i] - T_{preh}[i+1]) = \alpha_{cond}[i] M_{vap}[i] \lambda(T'_{vsat}[i])$ $(1 - \alpha_{cond}[i-1]) M_{vap}[i-1] \lambda(T_c[i-1])$ |
| $+ M_{fbrine}[i] (h_{sw}(T[i-1], X_b[i-1]) - h_{vap}(T'_{vsat}[i]))$ $+ M_b[i] (h_{sw}(T[i-1], X_b[i-1]) - h_{sw}(T[i], X_b[i]))$ $= M_d[i] (h_{vap}(T'_{vsat}[i]) - h_{sw}(T[i-1], X_b[i-1]))$ |
| $(1 - \alpha_{cond}[N-1]) M_{vap}[N-1] \lambda(T_c[N-1])$ $+ M_{fb}[N] h_{vap}(T'_{vsat}[N])$ $+ M_b[N-1] h_{sw}(T[N-1], X_b[N-1])$ $= M_b[N] h_{sw}(T[N], X_b[N])$ |

| |
|--------------------------------------------------------------------------------------------------------|
| $+M_{vap}[N] h_{vap}(T'_{vsat}[N])$ |
| $M_{cw} c_{P_{sw}}(\overline{T_{cw}}, X_{feed})(T_{cw,out} - T_{cw,in}) = M_{vap}[N] \lambda(T'_c[N])$ |

As can be observed in Table C1, firstly, global mass and salinity balances are employed to calculate the brine flow rate (M_{brine}), the distillate flow rate (M_{dist}) and the brine salinity (X_{brine}), assuming that the distillate is pure water. From this point onwards, the mass flow rate, temperature and pressure are computed for each effect. As for the temperature profiles, six main quantities must be taken into account and computed: (i) temperature of the brine generated in the effect (T), (ii) temperature reached by the feed in the preheater of the effect (T_{preh}), (iii) temperature of the saturated vapor generated in the effect (T_{vsat}), (iiii) temperature of the vapour after crossing the demister (T'_{vsat}), (v) temperature of the vapour after crossing the connecting lines (T'_c) and (vi) condensation temperature of the vapour in the following effect (T_c). All six quantities are connected by means of the boiling point elevation (BPE) and the pressure drops, leading to temperature drops ($\Delta T_{demister}$, ΔT_{lines} , ΔT_{grav} , ΔT_{acc}), in the case of saturated vapour. The Pitzer model is employed to estimate the BPE .

Among the three classes of effects, the first one is the only one which receives heat from an external source (M_s at temperature equal to T_s) and where the feed stream (M_{feed} at a concentration equal to X_{feed}) has been through all the preheaters. The feed of the first effect is sprayed onto a tube bundle whereas M_s circulates within the tubes. The vapour (M_{vap}) is generated by the partial evaporation of the feed stream (M_d). The vapour then crosses the demister and the first preheater, where it partially condenses. The part that does not condense is fed to next effect where it acts as the heating source. The remaining brine that exits the first effect (M_b at a concentration equal to X_b) is also fed to the next effect where it is sprayed on the external surface of the tube bundle. As already mentioned, the modelling of the intermediate effects is slightly different. It comprises two energy balances on the preheater and on the heat exchanger required to calculate the condensed fraction on the preheater tube surface (α_{cond}) and M_d , respectively. Furthermore, other two vapour contributions have to be taken into account: the vapour produced by the inlet brine flash. As for

the modelling of the last effect, the latter does not have any preheater and all the vapour is sent directly to the end condenser, where it condenses completely. This can be mathematically translated into different energy balances on the effect and on the last flashing box, since the total M_{vap} in the last effect condenses in the end condenser and then collected in the flash box. The brine M_b that exits the last effect is the generated in the last effect is the final brine of the entire MED plant. The condensate of the flash box M_c , on the other hand, is the final distillate of the plant. These outlets however have to respect the global mass balance equations. As far as the end condenser is concerned its feed is used to condensate the vapour. The required total cooling water flow rate (M_{cw}) is computed by means of the heat balance and the surplus ($M_{cw} - M_{feed}$) is cooled down and reused.

Table C2 reports the equations to calculate the areas of the heat exchangers, the areas of the preheaters and the areas of the end condenser where $DTML_{preh}$ and $DTML_{cond}$ are the temperature logarithmic mean in the preheater and in the condenser and U_{cond} and U_{evap} are the heat transfer coefficients for the condenser and the evaporator, respectively. For further details on the MED technical model, consult [67].

Table C2. Equations to calculate exchange areas of the heat exchangers, preheaters and end condenser of the MED plant.

| |
|------------------------------------------------------------------------------------------------------------------------------------------------|
| $A_{hx} [0] = \frac{M_{feed} c_{p,sw} (T_{mean}, X_f) (T[1] - T_{preh}[1]) + M_d[1] \lambda(T_{vsat}[1])}{U_{evap} (T[1]) (T_{steam} - T[1])}$ |
| $A_{hx} [i] = \frac{(1 - \alpha_{cond}[i - 1]) M_{vap}[i - 1] \lambda(T_c[i - 1])}{U_{evap} (T[i]) (T_c[i - 1] - T[i])}$ |
| $A_{preh} [i] = \frac{\alpha_{cond}[i] M_{vap}[i] \lambda(T'_{vsat}[i])}{U_{cond} (T'_{vsat}[i]) DTML_{preh}}$ |
| $A_{cond} = \frac{M_{cw} c_{p,sw} (\overline{T_{cw}}, X_{feed}) (T_{cw,out} - T_{cw,in})}{U_{cond} (T'_c[N]) DTML_{cond}}$ |

NaCl Thermal Crystallizer NTC technical model

The technical model of the NaCl Thermal Crystallizer is based on simple mass and energy balance equations where M is the generic mass flow rate and Q is the generic volumetric flow rate (see Table D1). However, the model was developed in such a

way that it depends on the previous MED plant and takes into account the desired final recovery of NaCl salt $\%_{recovery}$ achieved globally from the coupling of MED-NTC. It is therefore possible to calculate the mass flow rate of salt $M_{out,salt_{NTC}}$ and of brine $M_{out,brine_{NTC}}$ both exiting the crystallizer. As can be observed in Table D1, logical conditions are then taken into account depending on the NF membrane rejection correction factor α . It is worth mentioning that the rejection performances of an NF membrane can be corrected by a factor α that can vary between 0 and 1. Varying α means achieving a different outlet NF composition and subsequently different compounds that could precipitate in the NF downstream technologies. By means of PHREEQC software it is possible to associate to each value of α , a specific set of compounds that can precipitate. Therefore, according to the value of α , a specific set of equations is used related to the specific compound that precipitates. Finally, the molar concentration of the generic ion i in the brine $C_{out,i^{th},brine_{NTC}}$ is calculated along with the mass distillate flow rate $M_{out,dist_{NTC}}$. As for the energy balance equations, the sensible heat $H_{sens_{NTC}}$ and latent heat $H_{evap_{NTC}}$ are computed where T_{NTC} is the operating temperature of the crystallizer and T_{IN} is the temperature of the inlet stream of the crystallizer.

Table D1. Mass and Energy balance equations of the NaCl Thermal Crystallizer plant.

| | |
|---------------------------------------------------------------------------------------------------------------------------------|-----------------------------------------------------------------------------|
| $Q_{feed,Na^+_{MED}} = M_{feed,MED} \cdot C_{feed,Na^+_{MED}}$ | |
| $Q_{out,Na^+,salt_{NTC}} = \%_{recovery} \cdot Q_{feed,Na^+_{MED}}$ | |
| $M_{out,salt_{NTC}} = Q_{out,Na^+,salt_{NTC}} \cdot MW_{NaCl}$ | |
| $Q_{out,Na^+,brine_{NTC}} = \frac{M_{feed,NTC} \cdot C_{feed,Na^+_{NTC}} - Q_{out,Na^+,salt_{NTC}} \cdot MW_{Na^+}}{MW_{Na^+}}$ | |
| $M_{out,brine_{NTC}} = \frac{M_{feed,NTC} \cdot MW_{NaCl} - Q_{out,Na^+,salt_{NTC}}}{C_{NaCl_{sat}}}$ | |
| if $\alpha = 0.1$ or 0.7 | if $\alpha \neq 0.1$ or 0.7 |
| $C_{out,SO_4^{2-},brine_{NTC}} = \frac{M_{feed,NTC} \cdot C_{feed,SO_4^{2-}_{NTC}}}{M_{out,brine_{NTC}} \cdot MW_{SO_4^{2-}}}$ | if $C_{feed,Ca^{2+}_{NTC}} > C_{feed,SO_4^{2-}_{NTC}}$ |

| | |
|-----------------------------------------------------------------------------------------------------------------------------------|-------------------------------------------------------------------------------------------------------------------------------------------------------------------------------------------------------------|
| | $C_{out, Ca^{2+}, brine_{NTC}} = C_{Na_2Ca(SO_4)_2, sat}$ |
| $C_{out, Na_2SO_4, prec. NTC} = C_{out, SO_4^{2-}, brine_{NTC}} - C_{Na_2SO_4, sat}$ | $C_{out, Na_2Ca(SO_4)_2, prec. NTC} = \frac{M_{feed, NTC} \cdot C_{feed, Ca^{2+}, NTC} - C_{Na_2Ca(SO_4)_2, sat} \cdot M_{out, brine_{NTC}}}{M_{out, brine_{NTC}}}$ |
| $C_{out, Na^+, brine_{NTC}} = C_{NaCl, sat}$ if Na_2SO_4 precipitates | if $C_{feed, Ca^{2+}, NTC} < C_{feed, SO_4^{2-}, NTC}$ $C_{out, Ca^{2+}, brine_{NTC}} = 0$ |
| $C_{out, Na^+, brine_{NTC}} = 2C_{out, Na_2SO_4, prec. NTC}$ if Na_2SO_4 does not precipitate | $C_{out, Na_2Ca(SO_4)_2, prec. NTC} = \frac{M_{feed, NTC} \cdot C_{feed, Ca^{2+}, NTC}}{M_{out, brine_{NTC}}}$ |
| $Q_{out, Na_2SO_4, prec. NTC} =$ $M_{feed, NTC} \cdot C_{feed, SO_4^{2-}, NTC} - M_{out, brine_{NTC}} \cdot C_{Na_2SO_4, sat}$ | $C_{out, Na^+, brine_{NTC}} = C_{NaCl, sat} - 2C_{out, Na_2Ca(SO_4)_2, prec. NTC}$ |
| | $\frac{C_{out, SO_4^{2-}, brine_{NTC}}}{M_{out, brine_{NTC}}} = \frac{M_{feed, NTC} \cdot C_{feed, SO_4^{2-}, NTC} - 2C_{out, Na_2Ca(SO_4)_2, prec. NTC} \cdot M_{out, brine_{NTC}}}{M_{out, brine_{NTC}}}$ |
| $C_{out, i^{th}, brine_{NTC}} = \frac{M_{feed, NTC} \cdot C_{feed, i^{th}, NTC}}{M_{out, brine_{NTC}}}$ | |
| $C_{out, Cl^-, brine_{NTC}} = \frac{M_{feed, NTC} \cdot C_{feed, Cl^-, NTC} - Q_{out, Na^+, salt_{NTC}}}{M_{out, brine_{NTC}}}$ | |
| $M_{out, dist_{NTC}} = M_{feed, NTC} - Q_{out, Na^+, salt_{NTC}} \cdot MW_{NaCl} - M_{out, brine_{NTC}}$ | |
| $H_{sens_{NTC}} = M_{feed, NTC} \cdot Cp_{NaCl sol_{sat}} \cdot (T_{NTC} - T_{IN})$ | |
| $H_{evap_{NTC}} = M_{out, dist_{NTC}} \cdot Cp_{NaCl sol_{sat}} \cdot (T_{NTC} - T_{IN}) \lambda_{dist}$ | |
| $H_{TOT_{NTC}} = H_{sens_{NTC}} + H_{evap_{NTC}}$ | |

APPENDIX B

Nanofiltration NF economic model

The equations for the calculation of the capital and operating costs are reported in Table E1.

Table E1: Equations for the calculation of capEX and opEX of the NF unit.

| capEX equations for NF * | opEX equations for NF |
|----------------------------------------------------------------------------------------------------------------------------------------------------|----------------------------------------------------------------------------------------------------------------------|
| $C_{civil,NF} = \frac{(1034.4V_{feed,NF} + 1487x_{vessel})CEPCI_{current}^{***} (1+i)^{ncivil}i}{CEPCI_{ref}^{**} (1+i)^{ncivil} - 1}$ | $C_{elec,NF} = \frac{Cost_{elec} \cdot V_{feed,NF} \cdot N_{oper,hours}}{\%_{eff}} (cons_{memb,syst} + P_{feed,NF})$ |
| $C_{mech,NF} = \frac{(4329.6V_{feed,NF}^{0.85} + 1089.6x_{vessel})CEPCI_{current} (1+i)^{nmech}i}{CEPCI_{ref} (1+i)^{nmech} - 1}$ | $C_{chem,NF} = Cost_{chem,NF} \cdot V_{permeate} \cdot N_{oper,hours}$ |
| $C_{electro,NF} = \frac{(1.68 \cdot 10^6 + 64.8P_{feed,NF} \cdot V_{feed,NF})CEPCI_{current} (1+i)^{nelectro}i}{CEPCI_{ref} (1+i)^{nelectro} - 1}$ | $C_{main,NF} = 2\%capEX_{NF}$ |
| $C_{memb,NF} = \frac{1200x_{vessel} \cdot CEPCI_{current} (1+i)^{nmemb}i}{CEPCI_{ref} (1+i)^{nmemb} - 1}$ | $C_{quality,NF} = 2\%capEX_{NF}$ |
| | $C_{install,NF} = 2\%capEX_{NF}$ |
| $capEX_{NF} = C_{civil,NF} + C_{mech,NF} + C_{electro,NF} + C_{memb,NF}$ | $opEX_{NF} = C_{elec,NF} + C_{chem,NF} + C_{main,NF} + C_{quality,NF} + C_{install,NF}$ |

* The Verbene Cost Model equations were employed

**CEPCI_{ref} is referred to 2001 (394.3)

***CEPCI_{current} is referred to 2021 (754.0)

Among the capital costs, $C_{civil,NF}$ [€/y] represents the cost for buildings housing the plant, $C_{mech,NF}$ [€/y] is the cost for pumps, filters and piping, $C_{electro,NF}$ [€/y] is the costs for the energy supply systems, $C_{memb,NF}$ [€/y] is the investment for the membrane modules, $V_{feed,NF}$ [m³/h] is the feed flow rate, n_{vessel} is the number of NF vessels, $P_{feed,NF}$ [Pa] is the feed pressure and $CEPCI$ is the chemical engineering price index. All capEX contributions are depreciated considering a specific depreciation period (n_{civil} for $C_{civil,NF}$, $n_{mech} = n_{electro}$ for $C_{mech,NF}$ and $C_{electro,NF}$, n_{memb} for the membrane) with a discount rate i . Among the operating costs, $C_{elec,NF}$ [€/y] is the cost of electrical energy consumption, $C_{chem,NF}$ [€/y] is the chemical

consumption, $C_{main,NF}$ [€/y] is the cost of maintenance, $C_{quality,NF}$ [€/y] is the cost for quality control and $C_{install,NF}$ [€/y] is the cost of daily operation. $Cost_{elec}$ [€/kWh] is the specific cost of electricity, $\%_{eff}$ is the pump efficiency (80%), $N_{oper,hours}$ [h/y] is the annual number of operating hours, $cons_{memb,sys}$ is the specific energy consumption for a membrane system (40 Wh/m³ of feed). $Cost_{chem,NF}$ (0.023 €/m³ of permeate) is the specific cost of chemicals employed and $V_{permeate}$ [m³/h] is the NF permeate flow rate.

Magnesium Reactive Crystallizer MRC economic model

Equations to compute the capital costs of the MRC unit are reported in Table F1 where C_p^0 [€] is the purchase cost in standard conditions for the crystallizer and the filter, Vol_{cryst} [m³] is the volume of crystallizer, A_{filter} [m²] is the area of the filter, F_{BM} is the bare module factor (equal to 1.6 and 1.65 for the crystallizer and the filter, respectively), C_{BM} [€] is the bare module cost, $\alpha_{cont} = 15\%$ and $\alpha_{fee} = 5\%$ are the two correction factors to account for contingency and fee, respectively. C_{TM} [€] is the total module cost which is depreciated (straight line depreciation) within a period (n_{MRC}) with a discount rate i . Among the operating costs of the MRC, $C_{elec,MRC}$ [€/y] is the cost of energy consumption for pumping and the drum filter, $Power_{MRC,TOT}$ [kW] is the total consumed power, $C_{NaOH,MRC}$ [€/y] is the cost of reaction chemicals, $Cost_{NaOH}$ [€/ton] is the specific cost of NaOH, $Q_{NaOH,TOT}$ [ton/h] is the mass flow rate of NaOH, (iii) $C_{HCl,MRC}$ [€/y] is the cost of chemicals for the neutralization step, $Cost_{HCl}$ [€/ton] is the specific cost of HCl and $Q_{HCl,TOT}$ [ton/h] is the mass flow rate of HCl.

Table F1: Equations for the calculation of capEX and opEX of the MRC unit.

| capEX equations for MRC * | opEX equations for MRC |
|----------------------------------------------------------------------------------------------------------------------------------------------------------------------------------------------------------------------------------------------------------------------------------------------------------------------------------------------------------------------------------------------------------------------------------------------------------------------------------------------|---------------------------------------------------------------------------------------------------------------------------------------------------------------------------------------------------------------------------------|
| $C_{p,Cryst}^0 = 10^{(4.509+0.173\text{Log}_{10}(Vol_{cryst})+0.134*(\text{Log}_{10}(Vol_{cryst}))^2)}$ $C_{p,filter}^0 = 10^{(4.812+0.286\text{Log}_{10}(A_{filter})+0.042*(\text{Log}_{10}(A_{filter}))^2)}$ $C_{BM,Cryst} = \frac{C_{p,Cryst}^0 \cdot CEPCI_{current}^{***}}{CEPCI_{ref}^{**}} (F_{BM,Cryst})$ $C_{BM,filter} = \frac{C_{p,filter}^0 \cdot CEPCI_{current}}{CEPCI_{ref}} (F_{BM,filter})$ $C_{TM,MRC} = (C_{BM,Cryst} + C_{BM,filter})(1 + \alpha_{cont} + \alpha_{fee})$ | $C_{elec,MRC} = \frac{Cost_{elec} \cdot Power_{TOT,MRC} \cdot N_{oper,hours}}{\%_{eff}}$ $C_{NaOH,MRC} = Cost_{NaOH} \cdot Q_{NaOH,TOT} \cdot N_{oper,hours}$ $C_{HCl,MRC} = Cost_{HCl} \cdot Q_{HCl,TOT} \cdot N_{oper,hours}$ |
| $capEX_{MRC} = C_{TM,MRC} \frac{(1+i)^{n_{MRC}i}}{(1+i)^{n_{MRC}} - 1}$ | $opEX_{MRC} = C_{elec,MRC} + C_{NaOH,MRC} + C_{HCl,MRC}$ |

* The Bare Module Cost Technique equations were employed [281]

** CEPCI_{ref} is referred to 2001 (394.3)

*** CEPCI_{current} is referred to 2021 (754.0)

Multi-Effect Distillation MED economic model

Equations to compute the capital costs of the MED unit are reported in Table G1 where N_{evap} is the number of evaporators, N_{preh} is the number of preheaters, $N_{flashbox}$ is the number of flashboxes and N_{cond} is the number of condensers. F_{BM} is the global correction factor, $\alpha_{cont} = 15\%$ and $\alpha_{fee} = 5\%$ are the two correction factors to account contingency and fee, C_{BM} [€] is the bare module cost, C_{TM} [€] is the total module cost depreciated within a period (n_{MED}) with a discount rate i . As for the operating costs, $C_{elec,MED}$ [€/y] is the electric energy consumption, $Cons_{elec,MED}$ [kWh/m³ of distillate] is the specific energy consumption of the MED unit, $V_{dist,MED}$ [m³/h] is the volumetric flow rate of the produced distillate, $C_{thermal,MED}$ [€/y] is the thermal energy consumption, $Cost_{heat}$ [€/kWh] is the specific cost of heat of the MED, $Cons_{heat,MED}$ [kW] is the required thermal energy, $C_{chem,MED}$ is the chemical consumption required for cleaning, anti-scaling and anti-foaming, Q_i is the quantity consumed of the i^{th} chemical [ton/h] and $Cost_i$ is the specific cost of the i^{th} chemical [€/ton].

Table G1: Equations for the calculation of capEX and opEX of the MED unit.

| capEX equations for MED * | opEX equations for MED |
|--------------------------------------------------------------------------------------------------------------|---------------------------------------------------------------------------------------------------------------------------------------------------------------------------------------------------------------------------------------------------------------------------------------------------------------------------|
| $C_{p,evap}^0 = 10^{(4.325-0.303\text{Log}_{10}(A_{evap})+0.163(\text{Log}_{10}(A_{evap}))^2)}$ | $C_{elec,MED} = Cost_{elec} \cdot Cons_{elec,MED} \cdot V_{dist,MED} \cdot N_{oper,hours}$ |
| $C_{p,preh}^0 = 10^{(4.325-0.303\text{Log}_{10}(A_{preh})+0.163(\text{Log}_{10}(A_{preh}))^2)}$ | $C_{thermal,MED} = Cost_{heat} \cdot Cons_{heat,MED} \cdot N_{oper,hours}$ |
| $C_{p,flash}^0 = 10^{(3.557+0.378\text{Log}_{10}(A_{flash})+0.091(\text{Log}_{10}(A_{flash}))^2)}$ | $C_{chem,MED}$ |
| $C_{p,cond}^0 = 10^{(4.325-0.303\text{Log}_{10}(A_{cond})+0.163(\text{Log}_{10}(A_{cond}))^2)}$ | $= (Cost_{pre-Chlorine} \cdot Q_{pre-Chlorine} + Cost_{antiscalant} \cdot Q_{antiscalant} + Cost_{antifoaming} \cdot Q_{antifoaming} + Cost_{Ca(OH)_2} \cdot Q_{Ca(OH)_2} + Cost_{polyelectrolyte} \cdot Q_{polyelectrolyte} + Cost_{CO_2} \cdot Q_{CO_2} + Cost_{post-Chlorine} \cdot Q_{post-Chlorine}) N_{oper,hours}$ |
| $C_{BM,evap} = N_{evap} \frac{C_{p,evap}^0 \cdot CEPCI_{current}^{***}}{CEPCI_{ref}^{**}} (F_{BM,evap})$ | |
| $C_{BM,preh} = N_{preh} \frac{C_{p,preh}^0 \cdot CEPCI_{current}^{***}}{CEPCI_{ref}^{**}} (F_{BM,preh})$ | |
| $C_{BM,flash} = N_{flash} \frac{C_{p,flash}^0 \cdot CEPCI_{current}^{***}}{CEPCI_{ref}^{**}} (F_{BM,flash})$ | |
| $C_{BM,cond} = N_{cond} \frac{C_{p,cond}^0 \cdot CEPCI_{current}^{***}}{CEPCI_{ref}^{**}} (F_{BM,cond})$ | |
| $C_{TM,MRC} = (C_{BM,evap} + C_{BM,preh} + C_{BM,flash} + C_{BM,cond})(1 + \alpha_{cont} + \alpha_{fee})$ | |
| $capEX_{MED} = C_{TM,MED} \frac{(1+i)^{n_{MED}} i}{(1+i)^{n_{MED}} - 1}$ | $opEX_{MED} = C_{elec,MED} + C_{thermal,MED} + C_{chem,MED}$ |

* The Bare Module Cost Technique equations were employed

**CEPCI_{ref} is referred to 2001 (394.3)

***CEPCI_{current} is referred to 2021 (754.0)

NaCl Thermal Crystallizer NTC economic model

Equations to compute the capital costs of the NTC unit are reported in Table H1 where Vol_{cryst} [m³] is the volume of NTC, $F_{BM,NTC}$ is the global correction factor equal to 1.6 and contingency and fee ($\alpha_{cont} = 15\%$ and $\alpha_{fee} = 5\%$) and $C_{TM,NTC}$ [€] is the total module cost depreciated within a period (n_{NTC}) with a discount rate i . Among the operating costs of the NTC unit, $C_{elec,NTC}$ [€/y] is the cost of electric energy consumption for pumping, $Cons_{elec,NTC}$ [kWh/m³ of distillate] is the specific energy consumption of the crystallizer, $V_{dist,NTC}$ [m³/h] is the volumetric flow rate of the produced distillate, $C_{thermal,NTC}$ [€/y] is the cost of thermal energy required for the precipitation of NaCl crystals, $Cost_{heat}$ [€/kWh] is the specific cost of heat

of the NTC, $Cons_{heat,NTC}$ [kW] is the required thermal energy, $C_{brine disposal}$ [€/y] is the disposal cost of the final brine, $Cost_{brine disp}$ [€/m³ of brine] is the specific cost of brine disposal and $V_{brine,NTC}$ [m³/h] is the volumetric flow rate of the final brine.

Table H1: Equations for the calculation of capEX and opEX of the NTC unit.

| capEX equations for NTC * | opEX equations for NTC |
|-----------------------------------------------------------------------------------------------------------------------------------------------------------------------------------------------------------------------------------------------------------------------------------------|----------------------------------------------------------------------------------------------------------------------------------------------------------------------------------------------------------------------------------------------------------------------------------|
| $C_{p,NTC}^0 = 10^{(4.509+0.173 \cdot \text{Log}_{10}(\text{Vol}_{NTC})+0.134 \cdot (\text{Log}_{10}(\text{Vol}_{NTC}))^2)}$ $C_{BM,NTC} = \frac{C_{p,NTC}^0 \cdot CEPCI_{current}^{***}}{CEPCI_{ref}^{**}} (F_{BM,NTC})$ $C_{TM,NTC} = (C_{BM,NTC})(1 + \alpha_{cont} + \alpha_{fee})$ | $C_{elec,NTC} = Cost_{elec} \cdot Cons_{elect,NTC}$ $\quad \cdot V_{dist,NTC} \cdot N_{oper,hours}$ $C_{thermal,NTC} = Cost_{heat} \cdot Cons_{heat,NTC}$ $\quad \cdot N_{oper,hours}$ $C_{brine disposal} = Cost_{brine disp} \cdot V_{brine,NTC}$ $\quad \cdot N_{oper,hours}$ |
| $capEX_{NTC} = C_{TM,NTC} \frac{(1+i)^{n_{NTC}} i}{(1+i)^{n_{NTC}} - 1}$ | $opEX_{NTC} = C_{elec,NTC} + C_{thermal,NTC}$ $\quad + C_{brine disposal}$ |

* The Bare Module Cost Technique equations were employed

**CEPCI_{ref} is referred to 2001 (394.3)

***CEPCI_{current} is referred to 2021 (754.0)

APPENDIX C

Table 31: Difference of osmotic pressure values between the feed and permeate solution for all the investigated commercial NF membranes when treating seawater and SWRO brine.

| NF membrane | Osmotic pressure gradient $\Delta\Pi$ [bar] | |
|--------------------|---------------------------------------------------------------|------------------------------|
| | Scenario (Seawater) | Scenario (SWRO brine) |
| NF90 | 6.16 | 12.42 |
| NFS | 3.08 | 5.33 |
| NFX | 3.94 | 6.78 |
| VNF1 | 4.39 | 5.33 |
| DK | 4.72 | 5.71 |

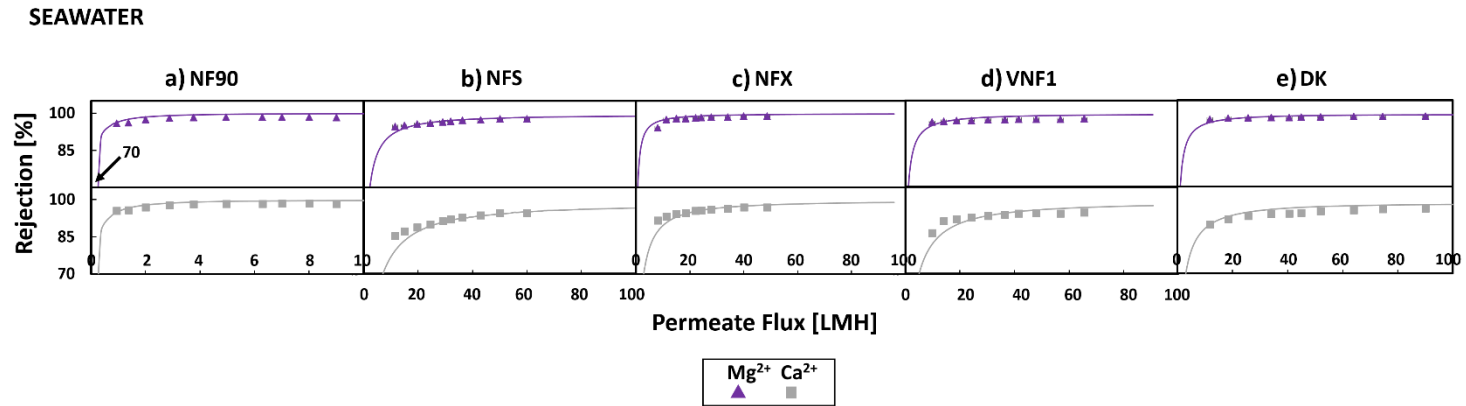


Figure 72: Zoom of experimental rejections of Mg^{2+} and Ca^{2+} as a function of permeate flux treating seawater for the 5 NF membranes: NF90 (a), NFS (b), NFX (c), VNF1 (d), DK (e). Points: experimental data. Lines: model fitting by the SEDF model.

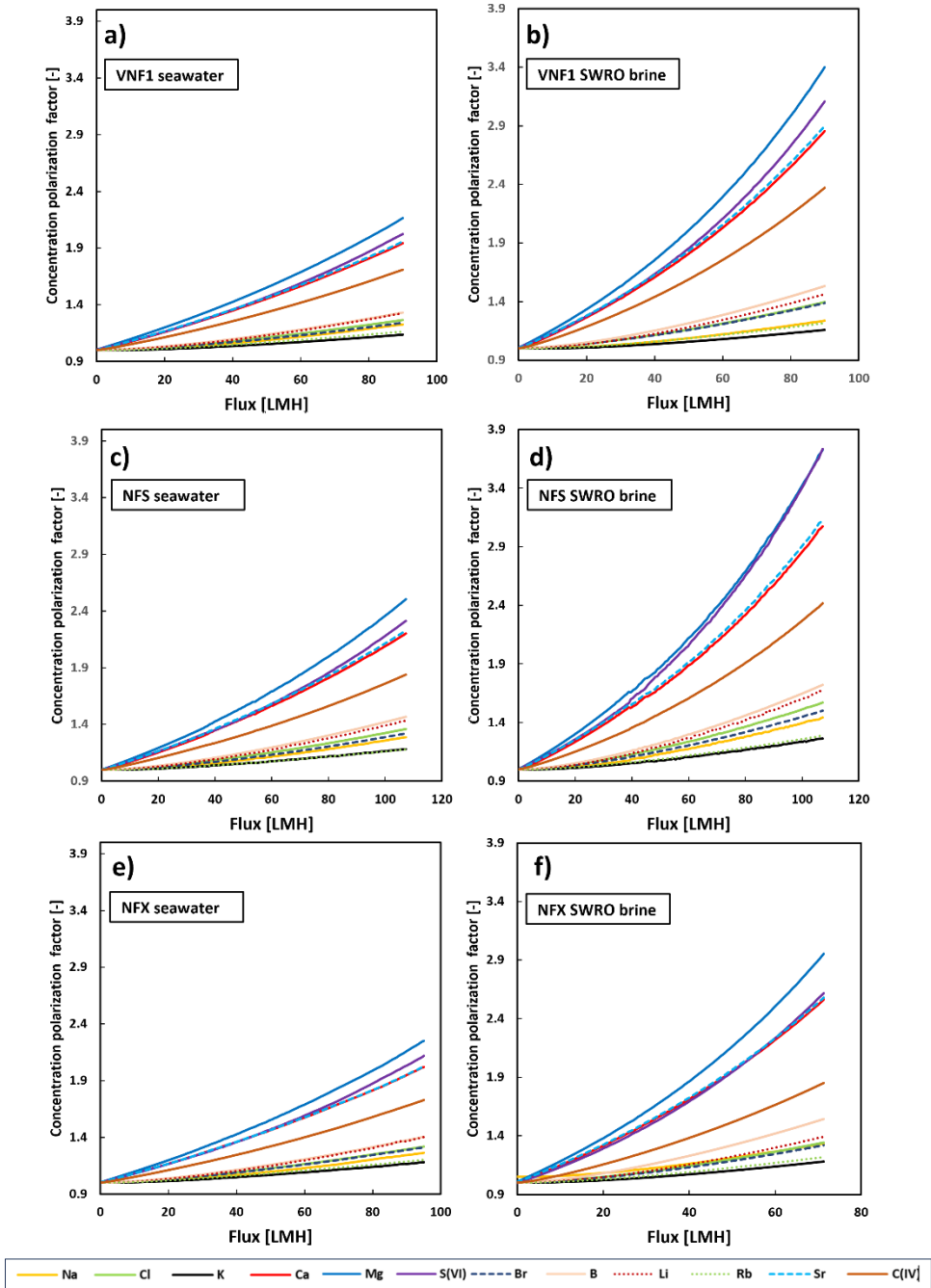


Figure 73: Concentration polarization factor of ions vs. flux for a) VNF1 treating seawater, b) VNF1 treating SWRO brine, c) NFS treating seawater, d) NFS treating SWRO brine, e) NFX treating seawater and f) NFX treating SWRO brine.

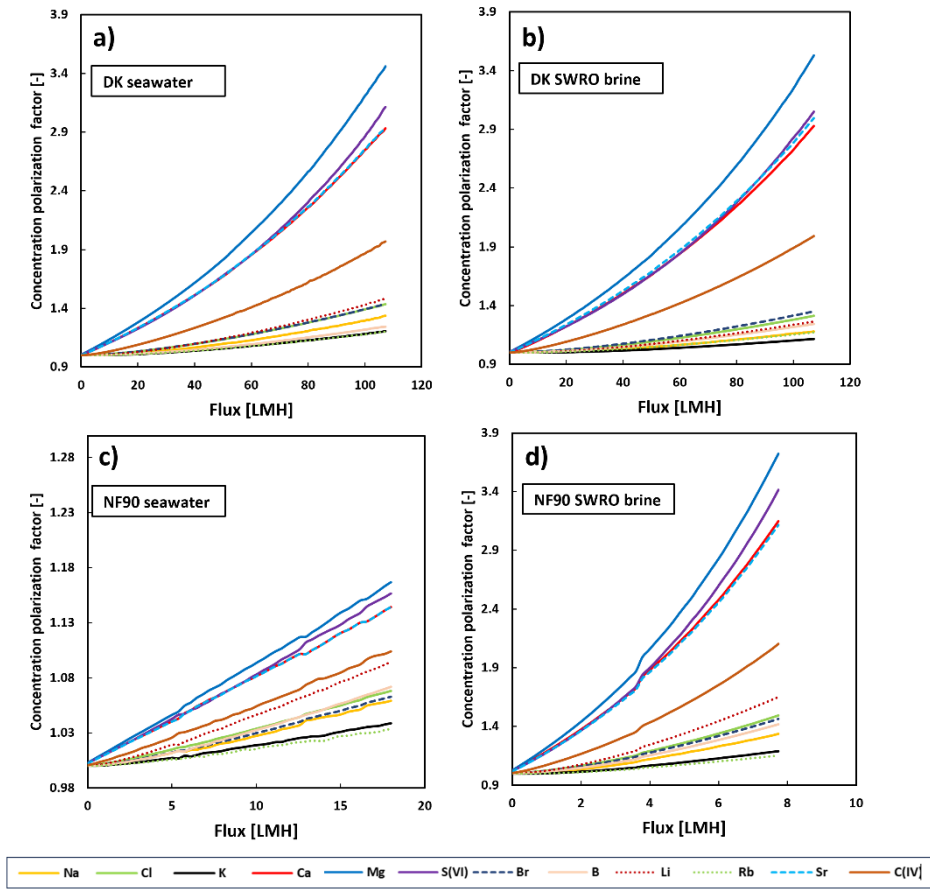


Figure 74: Concentration polarization factor of ions vs. flux for a) DK treating seawater, b) DK treating SWRO brine, c) NF90 treating seawater and d) NF90 treating SWRO brine.

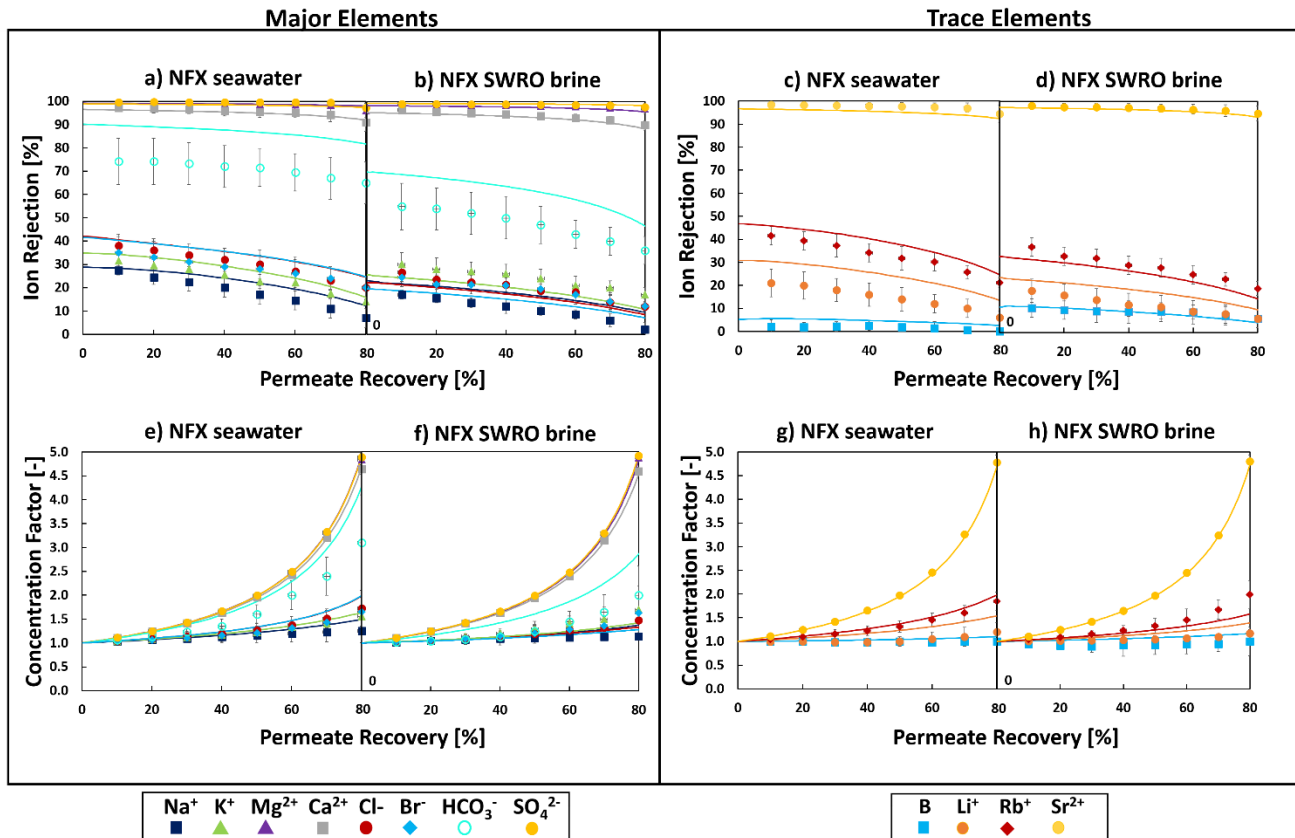


Figure 75: NFX seawater vs. NFX SWRO brine: Ion rejection of major elements (a) vs. b)), ion rejection of trace elements (c) vs. d)), concentration factor of major elements (e) vs. f)) and concentration factor of trace elements (g) vs. h)).

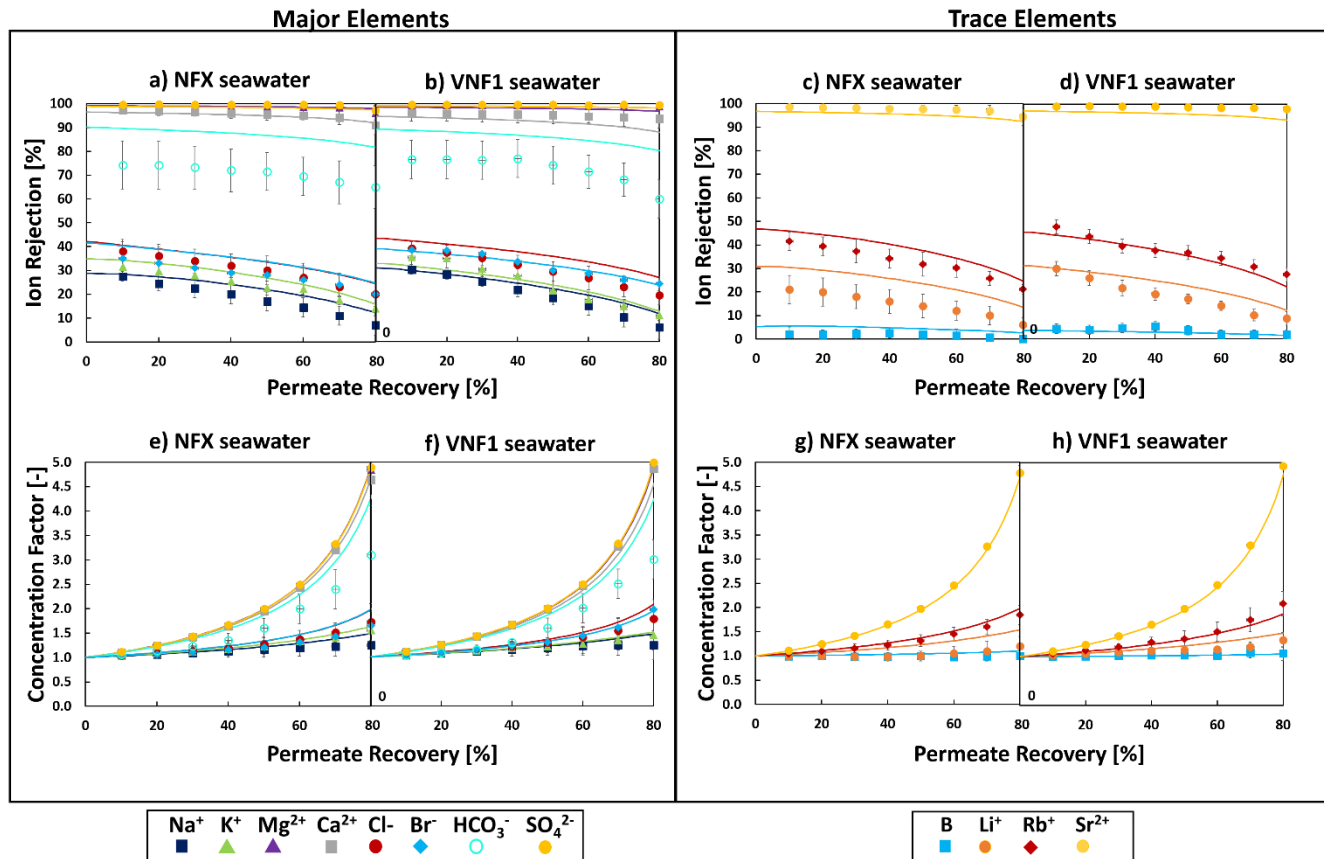


Figure 76: NFX seawater vs. VNF1 seawater: Ion rejection of major elements (a) vs. b)), ion rejection of trace elements (c) vs. d)), concentration factor of major elements (e) vs. f)) and concentration factor of trace elements (g) vs. h)).

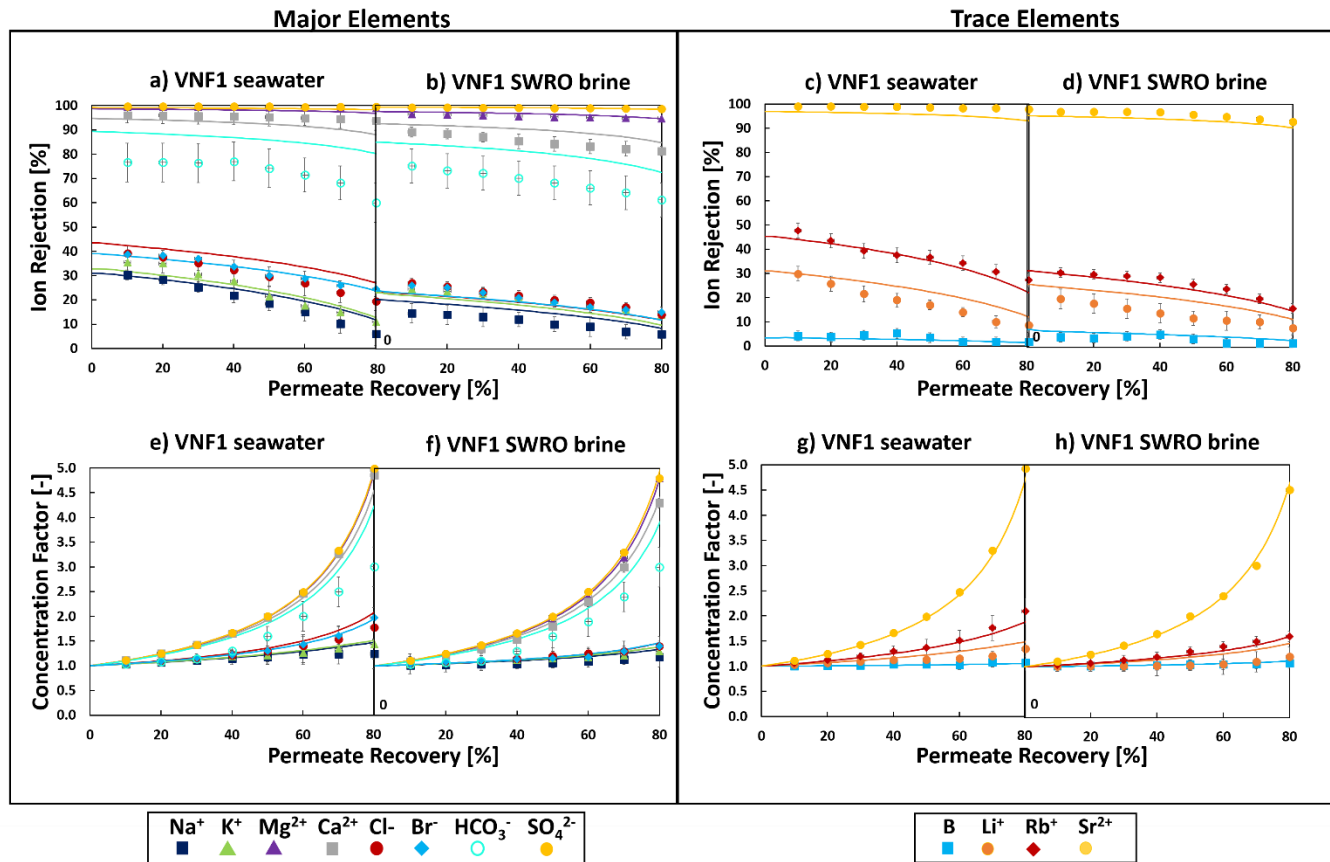


Figure 77: VNF1 seawater vs. VNF1 SWRO brine: Ion rejection of major elements (a) vs. b)), ion rejection of trace elements (c) vs. d)), concentration factor of major elements (e) vs. f)) and concentration factor of trace elements (g) vs. h)).

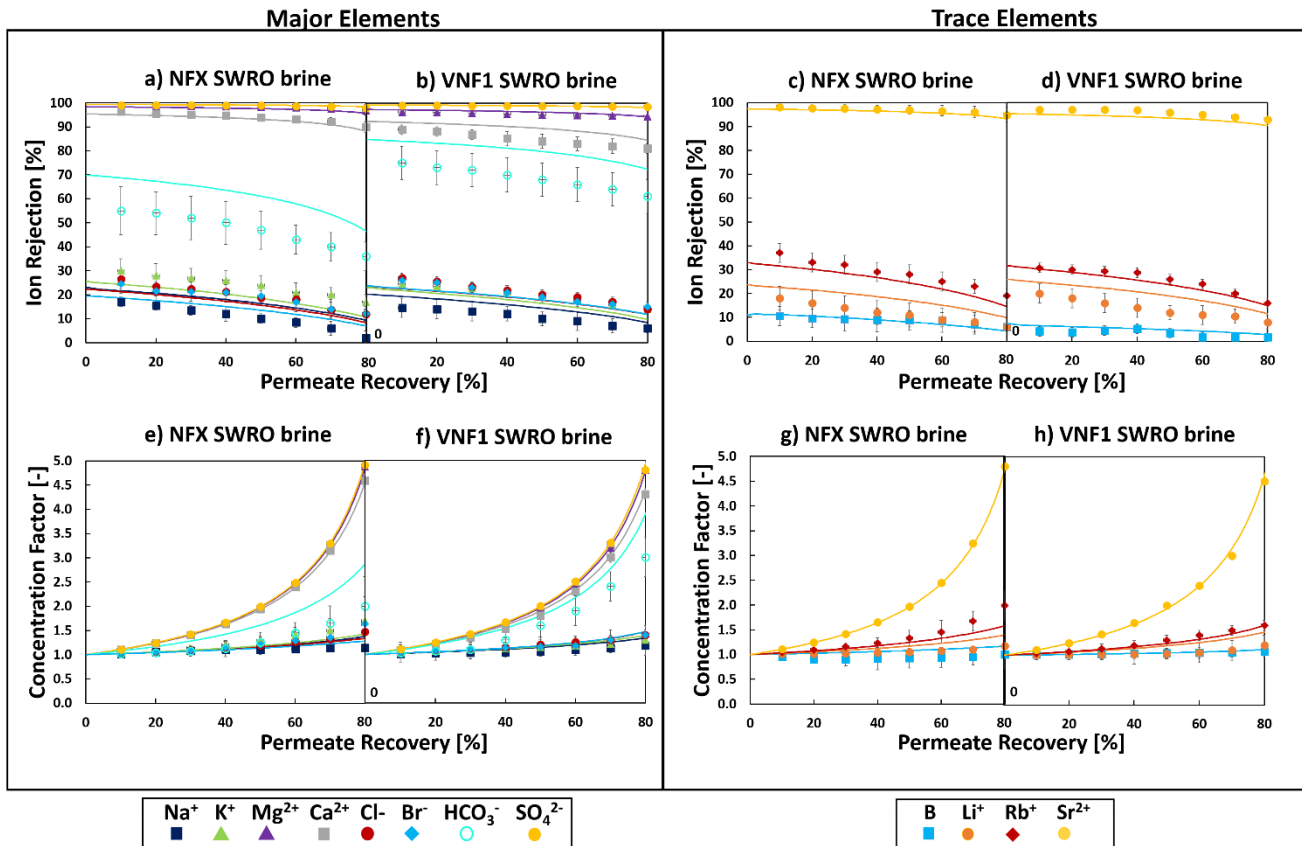


Figure 78: NFX SWRO brine vs. VNF1 SWRO brine: Ion rejection of major elements (a) vs. b)), ion rejection of trace elements (c) vs. d)), concentration factor of major elements (e) vs. f)) and concentration factor of trace elements (g) vs. h)).

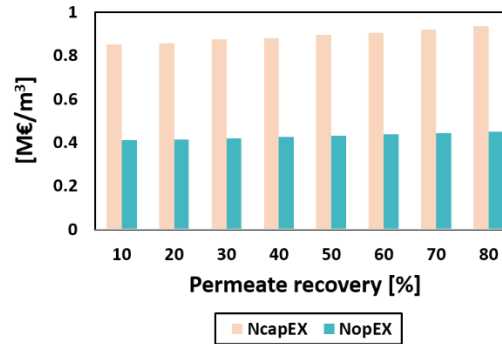


Figure 79: Increase of NcapEX and NopEX with permeate recovery for NFX treating seawater at 20 bar.

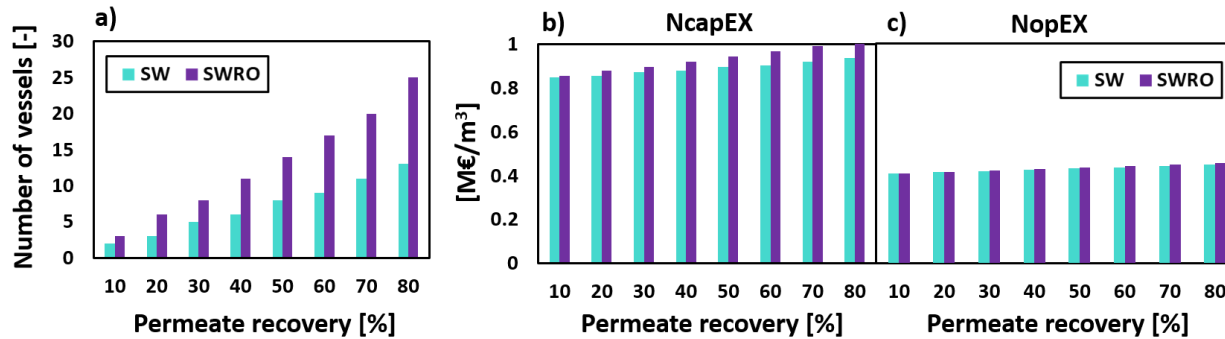


Figure 80: a) increase of number of NF vessels with permeate recovery for NFX treating seawater and NFX treating SWRO brine. b) increase of NcapEX and c) increase of NopEX with permeate recovery for NFX treating seawater and NFX treating SWRO brine.

REFERENCES

- [1] A.Y. Hoekstra, Water scarcity challenges to business, *Nat. Clim. Chang.* 4 (2014) 318–320. <https://doi.org/10.1038/nclimate2214>.
- [2] A. Panagopoulos, A comparative study on minimum and actual energy consumption for the treatment of desalination brine, *Energy* 212 (2020) 118733. <https://doi.org/10.1016/j.energy.2020.118733>.
- [3] M.N. Soliman, F.Z. Guen, S.A. Ahmed, H. Saleem, M.J. Khalil, S.J. Zaidi, Energy consumption and environmental impact assessment of desalination plants and brine disposal strategies, *Process Saf. Environ. Prot.* 147 (2021) 589–608. <https://doi.org/10.1016/j.psep.2020.12.038>.
- [4] E. Jones, M. Qadir, M.T.H. van Vliet, V. Smakhtin, S. mu Kang, The state of desalination and brine production: A global outlook, *Sci. Total Environ.* 657 (2019) 1343–1356. <https://doi.org/10.1016/j.scitotenv.2018.12.076>.
- [5] D. Xevgenos, K. Moustakas, D. Malamis, M. Loizidou, An overview on desalination & sustainability: renewable energy-driven desalination and brine management, *Desalin. Water Treat.* 57 (2016) 2304–2314. <https://doi.org/10.1080/19443994.2014.984927>.
- [6] T. Peters, D. Pintó, Seawater intake and pre-treatment/brine discharge - environmental issues, *Desalination* 221 (2008) 576–584. <https://doi.org/10.1016/j.desal.2007.04.066>.
- [7] F. Macedonio, E. Curcio, E. Drioli, Integrated membrane systems for seawater desalination: energetic and exergetic analysis, economic evaluation, experimental study, *Desalination* 203 (2007) 260–276. <https://doi.org/10.1016/j.desal.2006.02.021>.
- [8] M. Bornhoft, P. Takach, Consideration for implementaing a zero liquid discharge program, *Water Technol.* (2018) 1–18. <https://www.watertechonline.com/wastewater/article/15550690/considerations-for-implementing-a-zero-liquid-discharge-program>.
- [9] A. Panagopoulos, K.J. Haralambous, M. Loizidou, Desalination brine disposal methods and treatment technologies - A review, *Sci. Total Environ.* 693 (2019) 133545. <https://doi.org/10.1016/j.scitotenv.2019.07.351>.
- [10] M.O. Mavukkandy, C.M. Chabib, I. Mustafa, A. Al Ghaferi, F. AlMarzooqi, Brine management in desalination industry: From waste to resources generation, *Desalination* 472 (2019) 114187. <https://doi.org/10.1016/j.desal.2019.114187>.
- [11] S. van Wyk, A.G.J. van der Ham, S.R.A. Kersten, Potential of supercritical water desalination (SCWD) as zero liquid discharge (ZLD) technology, *Desalination* 495 (2020) 114593. <https://doi.org/10.1016/j.desal.2020.114593>.
- [12] J.M. Arnal, M. Sancho, I. Iborra, J.M. Gozálviz, A. Santafé, J. Lora, Concentration of brines from RO desalination plants by natural evaporation, *Desalination* 182 (2005) 435–439. <https://doi.org/10.1016/j.desal.2005.02.036>.
- [13] K.L. Petersen, A. Paytan, E. Rahav, O. Levy, J. Silverman, O. Barzel, D. Potts, E. Bar-Zeev, Impact of brine and antiscalants on reef-building corals in the Gulf of Aqaba – Potential effects from desalination plants, *Water Res.* 144 (2018) 183–191. <https://doi.org/10.1016/j.watres.2018.07.009>.
- [14] U.S. Department of the Interior Bureau of Reclamation, Brine-Concentrate Treatment and Disposal Options Report - Part 1, 2009. <http://s3-us-west-2.amazonaws.com/ucldc-nuxeo-ref-media/69c012ec-cae3-4b58-a56a-3a712960a918>.

- [15] J.H. Tsai, F. Macedonio, E. Drioli, L. Giorno, C.Y. Chou, F.C. Hu, C.L. Li, C.J. Chuang, K.L. Tung, Membrane-based zero liquid discharge: Myth or reality?, *J. Taiwan Inst. Chem. Eng.* 80 (2017) 192–202. <https://doi.org/10.1016/j.jtice.2017.06.050>.
- [16] I. Ersever, V. Ravindran, M. Pirbazari, Biological denitrification of reverse osmosis brine concentrates: I. Batch reactor and chemostat studies, *J. Environ. Eng. Sci.* 6 (2007) 503–518. <https://doi.org/10.1139/S07-021>.
- [17] A. Subramani, J.G. Jacangelo, Treatment technologies for reverse osmosis concentrate volume minimization: A review, *Sep. Purif. Technol.* 122 (2014) 472–489. <https://doi.org/10.1016/j.seppur.2013.12.004>.
- [18] M. Ahmed, W.H. Shayya, D. Hoey, J. Al-Handaly, Brine disposal from reverse osmosis desalination plants in Oman and the United Arab Emirates, *Desalination* 133 (2001) 135–147. [https://doi.org/10.1016/S0011-9164\(01\)80004-7](https://doi.org/10.1016/S0011-9164(01)80004-7).
- [19] R. Kaplan, D. Mamrosh, H.H. Salih, S.A. Dastgheib, Assessment of desalination technologies for treatment of a highly saline brine from a potential CO₂ storage site, *Desalination* 404 (2017) 87–101. <https://doi.org/10.1016/j.desal.2016.11.018>.
- [20] P. Loganathan, G. Naidu, S. Vigneswaran, Mining valuable minerals from seawater: A critical review, *Environ. Sci. Water Res. Technol.* 3 (2017) 37–53. <https://doi.org/10.1039/c6ew00268d>.
- [21] C.A. Quist-Jensen, F. Macedonio, E. Drioli, Membrane crystallization for salts recovery from brine—an experimental and theoretical analysis, *Desalin. Water Treat.* 57 (2016) 7593–7603. <https://doi.org/10.1080/19443994.2015.1030110>.
- [22] S. Yang, F. Zhang, H. Ding, P. He, H. Zhou, Lithium Metal Extraction from Seawater, *Joule* 2 (2018) 1648–1651. <https://doi.org/10.1016/j.joule.2018.07.006>.
- [23] B.A. Sharkh, A.A. Al-Amoudi, M. Farooque, C.M. Fellows, S. Ihm, S. Lee, S. Li, N. Voutchkov, Seawater desalination concentrate—a new frontier for sustainable mining of valuable minerals, *Npj Clean Water* 5 (2022) 1–16. <https://doi.org/10.1038/s41545-022-00153-6>.
- [24] Z. Wang, A. Deshmukh, Y. Du, M. Elimelech, Minimal and zero liquid discharge with reverse osmosis using low-salt-rejection membranes, *Water Res.* 170 (2020) 115317. <https://doi.org/10.1016/j.watres.2019.115317>.
- [25] A. Panagopoulos, Beneficiation of saline effluents from seawater desalination plants: Fostering the zero liquid discharge (ZLD) approach - A techno-economic evaluation, *J. Environ. Chem. Eng.* 9 (2021). <https://doi.org/10.1016/j.jece.2021.105338>.
- [26] A. Panagopoulos, Energetic, economic and environmental assessment of zero liquid discharge (ZLD) brackish water and seawater desalination systems, *Energy Convers. Manag. Comp. Techno-Economic Environ. Anal. Minimal Liq. Disch. Zero Liq. Disch. Desalin. Syst. Seawa* 235 (2021). <https://doi.org/10.1016/j.enconman.2021.113957>.
- [27] A. Panagopoulos, V. Giannika, Comparative techno-economic and environmental analysis of minimal liquid discharge (MLD) and zero liquid discharge (ZLD) desalination systems for seawater brine treatment and valorization, *Sustain. Energy Technol. Assessments* 53 (2022). <https://doi.org/10.1016/j.seta.2022.102477>.
- [28] A. Panagopoulos, Techno-economic assessment and feasibility study of a zero liquid discharge (ZLD) desalination hybrid system in the Eastern Mediterranean, *Chem. Eng. Process. - Process Intensif.* 178 (2022). <https://doi.org/10.1016/j.cep.2022.109029>.
- [29] A. Panagopoulos, Techno-economic assessment of zero liquid discharge (ZLD) systems for sustainable treatment, minimization and valorization of seawater brine, *J. Environ. Manage.* 306 (2022). <https://doi.org/10.1016/j.jenvman.2022.114488>.

- [30] E. El-Zanati, K.M. El-Khatib, Integrated membrane -based desalination system, *Desalination* 205 (2007) 15–25. <https://doi.org/10.1016/j.desal.2006.03.548>.
- [31] F. Tahir, S.G. Al-Ghamdi, Integrated MED and HDH desalination systems for an energy-efficient zero liquid discharge (ZLD) system, *Energy Reports* 8 (2022) 29–34. <https://doi.org/10.1016/j.egy.2022.01.028>.
- [32] K. Poirier, N. Al Mhanna, K. Patchigolla, Techno-Economic Analysis of Brine Treatment by Multi-Crystallization Separation Process for Zero Liquid Discharge, *Separations* 9 (2022). <https://doi.org/10.3390/separations9100295>.
- [33] G. Al Bazed, R.S. Ettouney, S.R. Tewfik, M.H. Sorour, M.A. El-Rifai, Salt recovery from brine generated by large-scale seawater desalination plants, *Desalin. Water Treat.* 52 (2014) 4689–4697. <https://doi.org/10.1080/19443994.2013.810381>.
- [34] D. von Eiff, P.W. Wong, Y. Gao, S. Jeong, A.K. An, Technical and economic analysis of an advanced multi-stage flash crystallizer for the treatment of concentrated brine, *Desalination* 503 (2021) 114925. <https://doi.org/10.1016/j.desal.2020.114925>.
- [35] Q. Chen, M. Burhan, M.W. Shahzad, D. Ybyraiymkul, F.H. Akhtar, Y. Li, K.C. Ng, A zero liquid discharge system integrating multi-effect distillation and evaporative crystallization for desalination brine treatment, *Desalination* 502 (2021) 114928. <https://doi.org/10.1016/j.desal.2020.114928>.
- [36] S. van Wyk, S.O. Odu, A.G.J. van der Ham, S.R.A. Kersten, Design and results of a first generation pilot plant for supercritical water desalination (SCWD), *Desalination* 439 (2018) 80–92. <https://doi.org/10.1016/j.desal.2018.03.028>.
- [37] R.A. Tufa, E. Curcio, E. Brauns, W. van Baak, E. Fontananova, G. Di Profio, Membrane Distillation and Reverse Electrodialysis for Near-Zero Liquid Discharge and low energy seawater desalination, *J. Memb. Sci.* 496 (2015) 325–333. <https://doi.org/10.1016/j.memsci.2015.09.008>.
- [38] W. Zhang, M. Miao, J. Pan, A. Sotto, J. Shen, C. Gao, B. Van Der Bruggen, Process Economic Evaluation of Resource Valorization of Seawater Concentrate by Membrane Technology, *ACS Sustain. Chem. Eng.* 5 (2017) 5820–5830. <https://doi.org/10.1021/acssuschemeng.7b00555>.
- [39] X. Ji, E. Curcio, S. Al Obaidani, G. Di Profio, E. Fontananova, E. Drioli, Membrane distillation-crystallization of seawater reverse osmosis brines, *Sep. Purif. Technol.* 71 (2010) 76–82. <https://doi.org/10.1016/j.seppur.2009.11.004>.
- [40] M. Kieselbach, T. Hogen, S.U. Geißen, T. Track, D. Becker, H.J. Rapp, J. Koschikowski, J. Went, H. Horn, F. Saravia, A. Bauer, R. Schwantes, D. Pfeifle, N. Heyn, M. Weissroth, B. Fitzke, Brines from industrial water recycling: New ways to resource recovery, *J. Water Reuse Desalin.* 10 (2020) 443–461. <https://doi.org/10.2166/wrd.2020.033>.
- [41] D. Xevgenos, P. Michailidis, K. Dimopoulos, M. Krokida, M. Loizidou, Design of an innovative vacuum evaporator system for brine concentration assisted by software tool simulation, *Desalin. Water Treat.* 53 (2015) 3407–3417. <https://doi.org/10.1080/19443994.2014.948660>.
- [42] D. Xevgenos, A. Vidalis, K. Moustakas, D. Malamis, M. Loizidou, Sustainable management of brine effluent from desalination plants: the SOL-BRINE system, *Desalin. Water Treat.* 53 (2015) 3151–3160. <https://doi.org/10.1080/19443994.2014.933621>.
- [43] A.S. Al-Amoudi, S. Ihm, A.M. Farooque, E.S.B. Al-Waznani, N. Voutchkov, Dual brine concentration for the beneficial use of two concentrate streams from desalination plant - Concept proposal and pilot plant demonstration, *Desalination* 564 (2023). <https://doi.org/10.1016/j.desal.2023.116789>.

- [44] C. Morgante, F. Vassallo, D. Xevgenos, A. Cipollina, M. Micari, A. Tamburini, G. Micale, Valorisation of SWRO brines in a remote island through a circular approach: Techno-economic analysis and perspectives, *Desalination* 542 (2022). <https://doi.org/10.1016/j.desal.2022.116005>.
- [45] C. Morgante, F. Vassallo, C. Cassaro, G. Virruso, D. Diamantidou, N. Van Linden, A. Trezzi, C. Xenogianni, R. Ktori, M. Rodriguez, G. Scelfo, S. Randazzo, A. Tamburini, A. Cipollina, G. Micale, D. Xevgenos, Pioneering minimum liquid discharge desalination : A pilot study in Lampedusa Island, *Desalination* 581 (2024) 117562. <https://doi.org/10.1016/j.desal.2024.117562>.
- [46] Deutsches Zentrum für Luft- und Raumfahrt, RCE, (2021) 1–6. <https://rcenvironment.de/>.
- [47] F. Macedonio, C.A. Quist-Jensen, O. Al-Harbi, H. Alromaih, S.A. Al-Jlil, F. Al Shabouna, E. Drioli, Thermodynamic modeling of brine and its use in membrane crystallizer, *Desalination* 323 (2013) 83–92. <https://doi.org/10.1016/j.desal.2013.02.009>.
- [48] INTERVENTO DI RICERCA E RIDUZIONE DELLE PERDITE NEL SISTEMA DI ADDUZIONE E DISTRIBUZIONE IDRICA NELL'ISOLA DI PANTELLERIA, (n.d.). <http://www.comunepantelleria.it/gare/68550928DE/R.1> Relazione illustrativa Consistenza della rete idrica.pdf.
- [49] Y. Roy, D.M. Warsinger, J.H. Lienhard, Effect of temperature on ion transport in nanofiltration membranes: Diffusion, convection and electromigration, *Desalination* 420 (2017) 241–257. <https://doi.org/10.1016/j.desal.2017.07.020>.
- [50] S. Jamaly, N.N. Darwish, I. Ahmed, S.W. Hasan, A short review on reverse osmosis pretreatment technologies, *Desalination* 354 (2014) 30–38. <https://doi.org/10.1016/j.desal.2014.09.017>.
- [51] A.E. Abdullatef, M. Farooque, G. Al-Otaibi, M. Kither, S. Al Khamis, Optimum nanofiltration membrane arrangements in seawater pretreatment - part-I, *Desalin. Water Treat.* 28 (2011) 270–286. <https://doi.org/10.5004/dwt.2011.1243>.
- [52] U.S. DEPARTMENT OF THE INTERIOR Bureau of Reclamation, Two-Pass Nanofiltration Seawater Desalination Prototype Testing and Evaluation, 2013. <https://www.usbr.gov/research/dwpr/reportpdfs/report158.pdf>.
- [53] J. Luo, Y. Wan, Effects of pH and salt on nanofiltration-a critical review, *J. Memb. Sci.* 438 (2013) 18–28. <https://doi.org/10.1016/j.memsci.2013.03.029>.
- [54] B.A. Abdelkader, M.A. Antar, Z. Khan, Nanofiltration as a Pretreatment Step in Seawater Desalination: A Review, *Arab. J. Sci. Eng.* 43 (2018) 4413–4432. <https://doi.org/10.1007/s13369-018-3096-3>.
- [55] D. Zhou, L. Zhu, Y. Fu, M. Zhu, L. Xue, Development of lower cost seawater desalination processes using nanofiltration technologies - A review, *Desalination* 376 (2015) 109–116. <https://doi.org/10.1016/j.desal.2015.08.020>.
- [56] A.M. Hassan, M.A.K. Al-Sofi, A.S. Al-Amoudi, A.T.M. Jamaluddin, A.M. Farooque, A. Rowaili, A.G.I. Dalvi, N.M. Kither, G.M. Mustafa, I.A.R. Al-Tisan, New approach to membrane and thermal seawater desalination processes using nanofiltration membranes (Part 1), *Water Supply* 17 (1999) 145–161.
- [57] G.U. Semblante, J.Z. Lee, L.Y. Lee, S.L. Ong, H.Y. Ng, Brine pre-treatment technologies for zero liquid discharge systems, *Desalination* 441 (2018) 96–111. <https://doi.org/10.1016/j.desal.2018.04.006>.
- [58] M. Turek, W. Gnot, Precipitation of Magnesium Hydroxide from Brine, *Ind. Eng. Chem. Res.* 34 (1995) 244–250. <https://doi.org/10.1021/ie00040a025>.
- [59] M.H. Gong, M. Johns, E. Fridjonsson, P. Heckley, Magnesium Recovery from Desalination Brine, in: 2018: pp. 49–54. <http://ceed.wa.edu.au/wp->

- content/uploads/2018/09/9.Gong_.WaterCorp.MagnesiumRecovery.pdf.
- [60] F. Vassallo, D. La Corte, A. Cipollina, A. Tamburini, G. Micale, High purity recovery of magnesium and calcium hydroxides from waste brines, *Chem. Eng. Trans.* 86 (2021) 931–936. <https://doi.org/10.3303/CET2186156>.
- [61] F. Vassallo, D. La Corte, N. Cancilla, A. Tamburini, M. Bevacqua, A. Cipollina, G. Micale, A pilot-plant for the selective recovery of magnesium and calcium from waste brines, *Desalination* 517 (2021) 115231. <https://doi.org/10.1016/j.desal.2021.115231>.
- [62] B. Rahimi, H.T. Chua, Introduction to Desalination, Low Grade Heat Driven Multi-Effect Distill. *Desalin.* (2017) 1–17. <https://doi.org/10.1016/b978-0-12-805124-5.00001-2>.
- [63] A. Ophir, F. Lokiec, Advanced MED process for most economical sea water desalination, *Desalination* 182 (2005) 187–198. <https://doi.org/10.1016/j.desal.2005.02.026>.
- [64] F.E. Ahmed, R. Hashaikheh, N. Hilal, Hybrid technologies: The future of energy efficient desalination – A review, *Desalination* 495 (2020). <https://doi.org/10.1016/j.desal.2020.114659>.
- [65] J.A. Fleck, The Influence of Pressure on Boiling Water Reactor Dynamic Behavior at Atmospheric Pressure, *Nucl. Sci. Eng.* 9 (1961) 271–280. <https://doi.org/10.13182/nse61-a15609>.
- [66] A. Panagopoulos, Process simulation and techno-economic assessment of a zero liquid discharge/multi-effect desalination/thermal vapor compression (ZLD/MED/TVC) system, *Int. J. Energy Res.* 44 (2020) 473–495. <https://doi.org/10.1002/er.4948>.
- [67] M. Micari, M. Moser, A. Cipollina, B. Fuchs, B. Ortega-Delgado, A. Tamburini, G. Micale, Techno-economic assessment of multi-effect distillation process for the treatment and recycling of ion exchange resin spent brines, *Desalination* 456 (2019) 38–52. <https://doi.org/10.1016/j.desal.2019.01.011>.
- [68] M.C. Georgiou, A.M. Bonanos, J.G. Georgiadis, Evaluation of a Multiple-Effect Distillation Unit under Partial Load Operating Conditions, *Conf. Pap. Energy* 2013 (2013) 1–9. <https://doi.org/10.1155/2013/482743>.
- [69] L.M. Vane, Water recovery from brines and salt-saturated solutions □ operability and thermodynamic efficiency considerations for desalination technologies, *Chem. Technol. Biotechnol.* (2017). <https://doi.org/doi:10.1002/jetb.5225>.
- [70] M. Micari, A. Cipollina, A. Tamburini, M. Moser, V. Bertsch, G. Micale, Combined membrane and thermal desalination processes for the treatment of ion exchange resins spent brine, *Appl. Energy* 254 (2019) 113699. <https://doi.org/10.1016/j.apenergy.2019.113699>.
- [71] M. Micari, M. Moser, A. Cipollina, A. Tamburini, G. Micale, V. Bertsch, Towards the implementation of circular economy in the water softening industry: A technical, economic and environmental analysis, *J. Clean. Prod.* 255 (2020) 120291. <https://doi.org/10.1016/j.jclepro.2020.120291>.
- [72] Eurostat, Customs code: 281610, Database: EU trade since 1988 by HS2-4-6 and CN8 (DS-045409), (2022). <http://epp.eurostat.ec.europa.eu/newxtweb/submitformatselect.do>.
- [73] Intratec, Calcium Hydroxide Prices: Current & Historical Data in Several Countries, (2021). https://www.intratec.us/chemical-markets/calcium-hydroxide-price?gclid=CjwKCAjw9aiIBhA1EiwAJ_GTSvik9uLcm9I4adTTbpANBGbMg15duTgKCRQIuZv5m4m4YmA0vUZWWWhoCXvsQAvD_BwE.
- [74] Intratec, Caustic Soda Prices: Current & Historical Data in Several Countries, 2021.

- https://www.intratec.us/chemical-markets/caustic-soda-price?gclid=CjwKCAjw9aiBhA1EiwAJ_GTSknGy4TOBaoTVLsviDB3Lfi00vgmUKuFagRDjYIafRrDlarrUHCxABoCCMMQAvD_BwE.
- [75] A. Culcasi, R. Gueccia, S. Randazzo, A. Cipollina, G. Micale, Design of a novel membrane-integrated waste acid recovery process from pickling solution, *J. Clean. Prod.* 236 (2019) 117623. <https://doi.org/10.1016/j.jclepro.2019.117623>.
- [76] A. Panagopoulos, Techno-economic evaluation of a solar multi-effect distillation/thermal vapor compression hybrid system for brine treatment and salt recovery, *Chem. Eng. Process. - Process Intensif.* 152 (2020) 107934. <https://doi.org/10.1016/j.cep.2020.107934>.
- [77] A. Pérez-González, R. Ibáñez, P. Gómez, A.M. Urriaga, I. Ortiz, J.A. Irabien, Nanofiltration separation of polyvalent and monovalent anions in desalination brines, *J. Memb. Sci.* 473 (2015) 16–27. <https://doi.org/10.1016/j.memsci.2014.08.045>.
- [78] K. Mitko, E. Laskowska, M. Turek, P. Dydo, K. Piotrowski, Scaling risk assessment in nanofiltration of mine waters, *Membranes (Basel)*. 10 (2020) 1–18. <https://doi.org/10.3390/membranes10100288>.
- [79] M.E.A. Ali, Nanofiltration process for enhanced treatment of RO brine discharge, *Membranes (Basel)*. 11 (2021). <https://doi.org/10.3390/membranes11030212>.
- [80] Codex Alimentarius Commission, CODEX STANDARD FOR FOOD GRADE SALT, 2006. [http://www.justice.gov.md/file/Centrul de armonizare a legislatiei/Baza de date/Materiale 2011/Legislatie/CODEX STAN 150-1985 1 CODEX STANDARD FOR FOOD GRADE SALT CX STAN.pdf](http://www.justice.gov.md/file/Centrul%20de%20armonizare%20a%20legislatiei/Baza%20de%20date/Materiale%202011/Legislatie/CODEX%20STAN%20150-1985%201%20CODEX%20STANDARD%20FOR%20FOOD%20GRADE%20SALT%20CX%20STAN.pdf).
- [81] M. Micari, D. Diamantidou, B. Heijman, M. Moser, A. Haidari, H. Spanjers, V. Bertsch, Experimental and theoretical characterization of commercial nanofiltration membranes for the treatment of ion exchange spent regenerant, *J. Memb. Sci.* 606 (2020) 118117. <https://doi.org/10.1016/j.memsci.2020.118117>.
- [82] Waternet, How much does a cubic metre of water cost?, (2021). <https://www.waternet.nl/en/veelgestelde-vragen/tap-water/what-does-a-cubic-metre-of-tap-water-cost/>.
- [83] ICIS, European economy will be a key driver for HCl in 2020 negotiations, (2021). <https://www.icis.com/explore/resources/news/2019/11/13/10443560/european-economy-will-be-a-key-driver-for-hcl-in-2020-negotiations>.
- [84] Eurostat, Electricity price statistics, *Eur. Comm.* (2020). https://ec.europa.eu/eurostat/statistics-explained/index.php/Electricity_price_statistics.
- [85] M. Bevacqua, F. Vassallo, A. Cipollina, G. Micale, A. Tamburini, M. Papapetrou, F. Vicari, Reattore e processo di precipitazione di un prodotto solido, *Application IT 102021000012473*, 202, n.d.
- [86] T. León, S. Abdullah Shah, J. López, A. Culcasi, L. Jofre, A. Cipollina, J.L. Cortina, A. Tamburini, G. Micale, Electrodialysis with Bipolar Membranes for the Generation of NaOH and HCl Solutions from Brines: An Inter-Laboratory Evaluation of Thin and Ultrathin Non-Woven Cloth-Based Ion-Exchange Membranes, *Membranes (Basel)*. 12 (2022). <https://doi.org/10.3390/membranes12121204>.
- [87] A. Culcasi, L. Gurreri, A. Cipollina, A. Tamburini, G. Micale, A comprehensive multi-scale model for bipolar membrane electrodialysis (BMED), *Chem. Eng. J.* 437 (2022). <https://doi.org/10.1016/j.cej.2022.135317>.
- [88] C. Cassaro, G. VIRRUSO, A. Culcasi, A. Cipollina, A. Tamburini, G. Micale, Electrodialysis with Bipolar Membranes for the Sustainable Production of Chemicals from Seawater Brines at Pilot Plant Scale, *ACS Sustain. Chem. Eng.* 11 (2023) 2989–3000. <https://doi.org/10.1021/acssuschemeng.2c06636>.

- [89] M. Al-Shammiri, M. Safar, Multi-effect distillation plants: State of the art, *Desalination* 126 (1999) 45–59. [https://doi.org/10.1016/S0011-9164\(99\)00154-X](https://doi.org/10.1016/S0011-9164(99)00154-X).
- [90] D.G. Akridge, Methods for calculating brine evaporation rates during salt production, *J. Archaeol. Sci.* 35 (2008) 1453–1462. <https://doi.org/10.1016/j.jas.2007.10.013>.
- [91] F. Vicari, S. Randazzo, J. López, M. Fernández de Labastida, V. Vallès, G. Micale, A. Tamburini, G. D'Alì Staiti, J.L. Cortina, A. Cipollina, Mining minerals and critical raw materials from bittern: Understanding metal ions fate in saltwork ponds, *Sci. Total Environ.* 847 (2022). <https://doi.org/10.1016/j.scitotenv.2022.157544>.
- [92] ENEA, Radiazione solare globale , diretta e diffusa al suolo Nota sul procedimento di calcolo 1 e modalità di cessione dei dati, (2008) 3–5.
- [93] C.E. Nika, V. Vasilaki, A. Expósito, E. Katsou, Water Cycle and Circular Economy: Developing a Circularity Assessment Framework for Complex Water Systems, *Water Res.* 187 (2020). <https://doi.org/10.1016/j.watres.2020.116423>.
- [94] K. Park, G.E.O. Kremer, Text mining-based categorization and user perspective analysis of environmental sustainability indicators for manufacturing and service systems, *Ecol. Indic.* 72 (2017) 803–820. <https://doi.org/10.1016/j.ecolind.2016.08.027>.
- [95] C.E. Nika, V. Vasilaki, D. Renfrew, M. Danishvar, A. Echchelh, E. Katsou, Assessing circularity of multi-sectoral systems under the Water-Energy-Food-Ecosystems (WEFE) nexus, *Water Res.* 221 (2022). <https://doi.org/10.1016/j.watres.2022.118842>.
- [96] D. Zhao, J. Xue, S. Li, H. Sun, Q. dong Zhang, Theoretical analyses of thermal and economical aspects of multi-effect distillation desalination dealing with high-salinity wastewater, *Desalination* 273 (2011) 292–298. <https://doi.org/10.1016/j.desal.2011.01.048>.
- [97] S. Aly, J. Jawad, H. Manzoor, S. Simson, J. Lawler, A.N. Mabrouk, Pilot testing of a novel integrated Multi Effect Distillation - Absorber compressor (MED-AB) technology for high performance seawater desalination, *Desalination* 521 (2022). <https://doi.org/10.1016/j.desal.2021.115388>.
- [98] V. Mavrov, H. Chmiel, B. Heitele, F. Rögener, Desalination of surface water to industrial water with lower impact on the environment. Part 3: Water desalination under alkaline conditions, *Desalination* 123 (1999) 33–43. [https://doi.org/10.1016/S0011-9164\(99\)00057-0](https://doi.org/10.1016/S0011-9164(99)00057-0).
- [99] M. Reig, S. Casas, C. Valderrama, O. Gibert, J.L. Cortina, Integration of monopolar and bipolar electrodialysis for valorization of seawater reverse osmosis desalination brines: Production of strong acid and base, *Desalination* 398 (2016) 87–97. <https://doi.org/10.1016/j.desal.2016.07.024>.
- [100] C. Morgante, F. Vassallo, G. Battaglia, A. Cipollina, F. Vicari, A. Tamburini, G. Micale, Influence of Operational Strategies for the Recovery of Magnesium Hydroxide from Brines at a Pilot Scale, *Ind. Eng. Chem. Res.* (2022). <https://doi.org/10.1021/acs.iecr.2c02935>.
- [101] European Commission, Study on the review of the list of Critical Raw Materials - Final Report, 2020. <https://doi.org/10.2873/11619>.
- [102] M. Grohol, C. Veeh, DG GROW, European Commission, Study on the Critical Raw Materials for the EU 2023, n.d. <https://doi.org/10.2873/725585>.
- [103] European Commission, Circular Economy Action Plan, (2021). https://ec.europa.eu/environment/strategy/circular-economy-action-plan_en.
- [104] Q. Yuan, Z. Lu, P. Zhang, X. Luo, X. Ren, T.D. Golden, Study of the synthesis and crystallization kinetics of magnesium hydroxide, *Mater. Chem. Phys.* 162 (2015) 734–742. <https://doi.org/10.1016/j.matchemphys.2015.06.048>.

- [105] S. Yousefi, B. Ghasemi, Ultrasound-assisted synthesis of porous Mg(OH)₂ nanostructures using hypersaline brine, *Micro Nano Lett.* 14 (2019) 1019–1023. <https://doi.org/10.1049/mnl.2019.0047>.
- [106] G. Balducci, L. Bravo Diaz, D.H. Gregory, Recent progress in the synthesis of nanostructured magnesium hydroxide, *CrystEngComm* 19 (2017) 6067–6084. <https://doi.org/10.1039/c7ce01570d>.
- [107] A. Pilarska, M. Wysokowski, E. Markiewicz, T. Jesionowski, Synthesis of magnesium hydroxide and its calcinates by a precipitation method with the use of magnesium sulfate and poly(ethylene glycols), *Powder Technol.* 235 (2013) 148–157. <https://doi.org/10.1016/j.powtec.2012.10.008>.
- [108] C.Y. Tai, C. Te Tai, M.H. Chang, H.S. Liu, Synthesis of magnesium hydroxide and oxide nanoparticles using a spinning disk reactor, *Ind. Eng. Chem. Res.* 46 (2007) 5536–5541. <https://doi.org/10.1021/ie060869b>.
- [109] S. Wada, J. Iijima, H. Takiyama, Crystallization operation method for recovering Mg resources from the sea water desalination process, *J. Chem. Eng. Japan* 48 (2015) 94–98. <https://doi.org/10.1252/jcej.14we157>.
- [110] Y. Gao, H. Wang, Y.L. Su, Q. Shen, D. Wang, Influence of magnesium source on the crystallization behaviors of magnesium hydroxide, *J. Cryst. Growth* 310 (2008) 3771–3778. <https://doi.org/10.1016/j.jcrysgro.2008.05.032>.
- [111] P. Fellner, J. Híveš, V. Khandl, M. Králik, J. Jurišová, T. Liptaj, L. Pach, Preparation of magnesium hydroxide from nitrate aqueous solution, *Chem. Pap.* 65 (2011) 454–459. <https://doi.org/10.2478/s11696-011-0038-x>.
- [112] C.A. Quist-Jensen, F. Macedonio, E. Drioli, Integrated membrane desalination systems with membrane crystallization units for resource recovery: A new approach for mining from the sea, *Crystals* 6 (2016). <https://doi.org/10.3390/cryst6040036>.
- [113] A. Kumar, G. Naidu, H. Fukuda, F. Du, S. Vigneswaran, E. Drioli, J.H. Lienhard, Metals Recovery from Seawater Desalination Brines: Technologies, Opportunities, and Challenges, *ACS Sustain. Chem. Eng.* 9 (2021) 7704–7712. <https://doi.org/10.1021/acssuschemeng.1c00785>.
- [114] A. Shahmansouri, J. Min, L. Jin, C. Bellona, Feasibility of extracting valuable minerals from desalination concentrate: A comprehensive literature review, *J. Clean. Prod.* 100 (2015) 4–16. <https://doi.org/10.1016/j.jclepro.2015.03.031>.
- [115] C. Balarew, Solubilities in seawater-type systems: Some technical and environmental friendly applications, *Pure Appl. Chem.* 65 (1993) 213–218. <https://doi.org/10.1351/pac199365020213>.
- [116] X. Song, K. Tong, S. Sun, Z. Sun, J. Yu, Preparation and crystallization kinetics of micron-sized Mg(OH)₂ in a mixed suspension mixed product removal crystallizer, *Front. Chem. Sci. Eng.* 7 (2013) 130–138. <https://doi.org/10.1007/s11705-013-1332-7>.
- [117] X. Song, S. Sun, D. Zhang, J. Wang, J. Yu, Synthesis and characterization of magnesium hydroxide by batch reaction crystallization, *Front. Chem. Sci. Eng.* 5 (2011) 416–421. <https://doi.org/10.1007/s11705-011-1125-9>.
- [118] A. Alamdari, M.R. Rahimpour, N. Esfandiari, E. Nourafkan, Kinetics of magnesium hydroxide precipitation from sea bittern, *Chem. Eng. Process. Process Intensif.* 47 (2008) 215–221. <https://doi.org/10.1016/j.cep.2007.02.012>.
- [119] A.F. Mohammad, M.H. El-Naas, A.H. Al-Marzouqi, M.I. Suleiman, M. Al Musharfy, Optimization of magnesium recovery from reject brine for reuse in desalination post-treatment, *J. Water Process Eng.* 31 (2019) 100810. <https://doi.org/10.1016/j.jwpe.2019.100810>.
- [120] S. Casas, C. Aladjem, E. Larrotcha, O. Gibert, C. Valderrama, J.L. Cortina,

- Valorisation of Ca and Mg by-products from mining and seawater desalination brines for water treatment applications, *J. Chem. Technol. Biotechnol.* 89 (2014) 872–883. <https://doi.org/10.1002/jctb.4326>.
- [121] D.H. Kim, A review of desalting process techniques and economic analysis of the recovery of salts from retentates, *Desalination* 270 (2011) 1–8. <https://doi.org/10.1016/j.desal.2010.12.041>.
- [122] F. Mohammedsmacili, M.K. Badr, M. Abbaszadegan, P. Fox, Byproduct Recovery from Reclaimed Water Reverse Osmosis Concentrate Using Lime and Soda-Ash Treatment, *Water Environ. Res.* 82 (2010) 342–350. <https://doi.org/10.2175/106143009x12487095236919>.
- [123] A. Neilly, V. Jegatheesan, L. Shu, Evaluating the potential for zero discharge from reverse osmosis desalination using integrated processes - A review, *Desalin. Water Treat.* 11 (2009) 58–65. <https://doi.org/10.5004/dwt.2009.843>.
- [124] T. Jeppesen, L. Shu, G. Keir, V. Jegatheesan, Metal recovery from reverse osmosis concentrate, *J. Clean. Prod.* 17 (2009) 703–707. <https://doi.org/10.1016/j.jclepro.2008.11.013>.
- [125] S. Lattemann, T. Höpner, Environmental impact and impact assessment of seawater desalination, *Desalination* 220 (2008) 1–15. <https://doi.org/10.1016/j.desal.2007.03.009>.
- [126] S.G.J. Heijman, H. Guo, S. Li, J.C. van Dijk, L.P. Wessels, Zero liquid discharge: Heading for 99% recovery in nanofiltration and reverse osmosis, *Desalination* 236 (2009) 357–362. <https://doi.org/10.1016/j.desal.2007.10.087>.
- [127] C. Chungcheng, G.H. Nancollas, The crystallization of magnesium hydroxide, a constant composition study, *Desalination* 42 (1982) 209–219. [https://doi.org/10.1016/S0011-9164\(00\)88753-6](https://doi.org/10.1016/S0011-9164(00)88753-6).
- [128] L. Sung-Tsuen, G.H. Nancollas, The crystallization of magnesium hydroxide, *Desalination* 12 (1973) 75–84. [https://doi.org/10.1016/S0011-9164\(00\)80176-9](https://doi.org/10.1016/S0011-9164(00)80176-9).
- [129] C. Henrist, J.P. Mathieu, C. Vogels, A. Rulmont, R. Cloots, Morphological study of magnesium hydroxide nanoparticles precipitated in dilute aqueous solution, *J. Cryst. Growth* 249 (2003) 321–330. [https://doi.org/10.1016/S0022-0248\(02\)02068-7](https://doi.org/10.1016/S0022-0248(02)02068-7).
- [130] G. Kordas, Sol-gel preparation of MgO fibers, *J. Mater. Chem.* 10 (2000) 1157–1160. <https://doi.org/10.1039/b001015o>.
- [131] E. Nduagu, T. Björklöf, J. Fagerlund, J. Wärn, H. Geerlings, R. Zevenhoven, Production of magnesium hydroxide from magnesium silicate for the purpose of CO₂ mineralisation - Part 1: Application to Finnish serpentinite, *Miner. Eng.* 30 (2012) 75–86. <https://doi.org/10.1016/j.mineng.2011.12.004>.
- [132] H. Tsuge, K. Okada, T. Yano, N. Fukushi, H. Akita, Reactive Crystallization of Magnesium Hydroxide, *ACS Symp. Ser.* 667 (1997) 254–266. <https://doi.org/10.1021/bk-1997-0667.ch021>.
- [133] M.A. Shand, *The chemistry and technology of magnesia*, Wiley-Interscience, 2006.
- [134] D. La Corte, F. Vassallo, A. Cipollina, M. Turek, A. Tamburini, G. Micale, A novel ionic exchange membrane crystallizer to recover magnesium hydroxide from seawater and industrial brines, *Membranes (Basel)*. 10 (2020) 1–14. <https://doi.org/10.3390/membranes10110303>.
- [135] F. Vassallo, C. Morgante, G. Battaglia, D. La Corte, M. Micari, A. Cipollina, A. Tamburini, G. Micale, A simulation tool for ion exchange membrane crystallization of magnesium hydroxide from waste brine, *Chem. Eng. Res. Des.* 173 (2021) 193–205. <https://doi.org/10.1016/j.cherd.2021.07.008>.
- [136] D.F. Kondakov, V.P. Danilov, Manufacturing of magnesium hydroxide from natural magnesium chloride sources, *Theor. Found. Chem. Eng.* 41 (2007) 572–576.

- <https://doi.org/10.1134/S0040579507050193>.
- [137] M. Turek, W. Gnot, Precipitation of Magnesium Hydroxide from Brine, *Ind. Eng. Chem. Res.* 34 (1995) 244–250. <https://doi.org/https://doi.org/10.1021/ie00040a025>.
- [138] S.W. Lee, J.H. Lim, Recovery of Magnesium Oxide and Magnesium Hydroxide from the Waste Bittren, *Adv. Mater. Res.* 26–28 (2007) 1019–1022. <https://doi.org/10.4028/www.scientific.net/amr.26-28.1019>.
- [139] X. Li, G.B. Ma, Y.Y. Liu, Synthesis and characterization of magnesium hydroxide using a bubbling setup, *Ind. Eng. Chem. Res.* 48 (2009) 763–768. <https://doi.org/10.1021/ie801306f>.
- [140] A. Jarosinski, P. Radomski, L. Lelek, J. Kulczycka, New production route of magnesium hydroxide and related environmental impact, *Sustain.* 12 (2020) 1–14. <https://doi.org/10.3390/su12218822>.
- [141] A. Cipollina, M. Bevacqua, P. Dolcimascolo, A. Tamburini, A. Brucato, H. Glade, L. Buether, G. Micale, Reactive crystallisation process for magnesium recovery from concentrated brines, *Desalin. Water Treat.* 55 (2015) 2377–2388. <https://doi.org/10.1080/19443994.2014.947771>.
- [142] M. Bevacqua, F. Vassallo, A. Cipollina, G. Micale, A. Tamburini, M. Papapetrou, F. Vicari, Reattore e processo di precipitazione di un prodotto solido, *IT* 102021000012473, 2021.
- [143] V.S. Shirure, A.S. Pore, V.G. Pangarkar, Intensification of precipitation using narrow channel reactors: Magnesium hydroxide precipitation, *Ind. Eng. Chem. Res.* 44 (2005) 5500–5507. <https://doi.org/10.1021/ie049248d>.
- [144] WATER MINING, (n.d.). <https://watermining.eu/>.
- [145] SEArcularMINE, (n.d.). <https://searcularmine.eu/>.
- [146] I.G. Wenten, D. Ariono, M. Purwasasmita, Khoirudin, Integrated processes for desalination and salt production: A mini-review, *AIP Conf. Proc.* 1818 (2017). <https://doi.org/10.1063/1.4976929>.
- [147] G. Battaglia, S. Romano, A. Raponi, D. Marchisio, M. Ciofalo, A. Tamburini, A. Cipollina, G. Micale, Analysis of particles size distributions in Mg(OH)₂ precipitation from highly concentrated MgCl₂ solutions, *Powder Technol.* 398 (2022) 117106. <https://doi.org/10.1016/j.powtec.2021.117106>.
- [148] C. Morgante, X. Ma, X. Chen, D. Wang, V. Boffa, V. Stathopoulos, J. Lopez, J.L. Cortina, A. Cipollina, A. Tamburini, G. Micale, Metal-Organic-Framework-based nanofiltration membranes for selective multi-cationic recovery from seawater and brines, *J. Memb. Sci.* 685 (2023). <https://doi.org/10.1016/j.memsci.2023.121941>.
- [149] C. Morgante, J. Lopez, J.L. Cortina, A. Tamburini, New generation of commercial nanofiltration membranes for seawater/brine mining: Experimental evaluation and modelling of membrane selectivity for major and trace elements, *Sep. Purif. Technol.* 340 (2024). <https://doi.org/10.1016/j.seppur.2024.126758>.
- [150] C. Morgante, T. Moghadamfar, J. Lopez, J.L. Cortina, A. Tamburini, Evaluation of enhanced nanofiltration membranes for improving magnesium recovery schemes from seawater / brine : Integrating experimental performing data with a techno-economic assessment, *J. Environ. Manage.* 360 (2024) 121192. <https://doi.org/10.1016/j.jenvman.2024.121192>.
- [151] B.A. Sharkh, A.A. Al-Amoudi, M. Farooque, C.M. Fellows, S. Ihm, S. Lee, S. Li, N. Voutchkov, Seawater desalination concentrate—a new frontier for sustainable mining of valuable minerals, *Npj Clean Water* 5 (2022) 1–16. <https://doi.org/10.1038/s41545-022-00153-6>.
- [152] European Commission, Report of the ad hoc working group on defining critical raw materials, 2015. [https://doi.org/Ref.Ares\(2015\)1819558-29/04/2015](https://doi.org/Ref.Ares(2015)1819558-29/04/2015).

- [153] I. Bellemans, E. De Wilde, N. Moelans, K. Verbeken, Metal losses in pyrometallurgical operations - A review, *Adv. Colloid Interface Sci.* 255 (2018) 47–63. <https://doi.org/10.1016/j.cis.2017.08.001>.
- [154] M. Smol, J. Kulczycka, Towards innovations development in the European raw material sector by evolution of the knowledge triangle, *Resour. Policy* 62 (2019) 453–462. <https://doi.org/10.1016/j.resourpol.2019.04.006>.
- [155] F.J. Millero, R. Feistel, D.G. Wright, T.J. McDougall, The composition of Standard Seawater and the definition of the Reference-Composition Salinity Scale, *Deep. Res. Part I Oceanogr. Res. Pap.* 55 (2008) 50–72. <https://doi.org/10.1016/j.dsr.2007.10.001>.
- [156] U. Bardi, Extracting minerals from seawater: An energy analysis, *Sustainability* 2 (2010) 980–992. <https://doi.org/10.3390/su2040980>.
- [157] European Commission, EU Blue Economy Observatory, (2023). https://blue-economy-observatory.ec.europa.eu/eu-blue-economy-sectors/desalination_en?prefLang=hu.
- [158] A. Shahmansouri, C. Bellona, Nanofiltration technology in water treatment and reuse: Applications and costs, *Water Sci. Technol.* 71 (2015) 309–319. <https://doi.org/10.2166/wst.2015.015>.
- [159] N. Hilal, H. Al-Zoubi, N.A. Darwish, A.W. Mohammad, M. Abu Arabi, A comprehensive review of nanofiltration membranes: Treatment, pretreatment, modelling, and atomic force microscopy, *Desalination* 170 (2004) 281–308. <https://doi.org/10.1016/j.desal.2004.01.007>.
- [160] H. Zhang, Q. He, J. Luo, Y. Wan, S.B. Darling, Sharpening Nanofiltration: Strategies for Enhanced Membrane Selectivity, *ACS Appl. Mater. Interfaces* 12 (2020) 39948–39966. <https://doi.org/10.1021/acsami.0c11136>.
- [161] K. Gu, S. Wang, Y. Li, X. Zhao, Y. Zhou, C. Gao, A facile preparation of positively charged composite nanofiltration membrane with high selectivity and permeability, *J. Memb. Sci.* 581 (2019) 214–223. <https://doi.org/10.1016/j.memsci.2019.03.057>.
- [162] Sea4Value Project, (n.d.) 1–7. <https://sea4value.eu/> (accessed January 10, 2023).
- [163] A.S. Al-Amoudi, S. Ihm, A.M. Farooque, E.S.B. Al-Waznani, N. Voutchkov, Dual brine concentration for the beneficial use of two concentrate streams from desalination plant - Concept proposal and pilot plant demonstration, *Desalination* 564 (2023) 116789. <https://doi.org/10.1016/j.desal.2023.116789>.
- [164] N. Hilal, H. Al-Zoubi, N.A. Darwish, A.W. Mohammad, Performance of nanofiltration membranes in the treatment of synthetic and real seawater, *Sep. Sci. Technol.* 42 (2007) 493–515. <https://doi.org/10.1080/01496390601120789>.
- [165] J. Liu, J. Yuan, Z. Ji, B. Wang, Y. Hao, X. Guo, Concentrating brine from seawater desalination process by nanofiltration-electrodialysis integrated membrane technology, *Desalination* 390 (2016) 53–61. <https://doi.org/10.1016/j.desal.2016.03.012>.
- [166] M.E.A. Ali, Nanofiltration Process for Enhanced Treatment of RO Brine Discharge, *Membranes (Basel)*. 11 (2021) 212. <https://doi.org/10.3390/membranes11030212>.
- [167] M. Bindels, J. Carvalho, C.B. Gonzalez, N. Brand, B. Nelemans, Techno-economic assessment of seawater reverse osmosis (SWRO) brine treatment with air gap membrane distillation (AGMD), *Desalination* 489 (2020) 114532. <https://doi.org/10.1016/j.desal.2020.114532>.
- [168] Y. Song, J. Xu, Y. Xu, X. Gao, C. Gao, Performance of UF-NF integrated membrane process for seawater softening, *Desalination* 276 (2011) 109–116. <https://doi.org/10.1016/j.desal.2011.03.064>.
- [169] M. Turek, M. Chor, Nanofiltration process for seawater desalination – salt production

- integrated system system, *Desalin. Water Treat.* (2012) 37–41. <https://doi.org/https://doi.org/10.5004/dwt.2009.713>.
- [170] B. Su, M. Dou, X. Gao, Y. Shang, C. Gao, Study on seawater nanofiltration softening technology for offshore oilfield water and polymer flooding, *Desalination* 297 (2012) 30–37. <https://doi.org/10.1016/j.desal.2012.04.014>.
- [171] M. Reig, S. Casas, O. Gibert, C. Valderrama, J.L. Cortina, Integration of nanofiltration and bipolar electrodialysis for valorization of seawater desalination brines: Production of drinking and waste water treatment chemicals, *Desalination* 382 (2016) 13–20. <https://doi.org/10.1016/j.desal.2015.12.013>.
- [172] M. Figueira, D. Rodríguez-Jiménez, J. López, M. Reig, J. Luis Cortina, C. Valderrama, Evaluation of the nanofiltration of brines from seawater desalination plants as pre-treatment in a multimineral brine extraction process, *Sep. Purif. Technol.* 322 (2023). <https://doi.org/10.1016/j.seppur.2023.124232>.
- [173] S. Cheng, D.L. Oatley, P.M. Williams, C.J. Wright, Characterisation and application of a novel positively charged nanofiltration membrane for the treatment of textile industry wastewaters, *Water Res.* 46 (2012) 33–42. <https://doi.org/10.1016/j.watres.2011.10.011>.
- [174] C. Bellona, J.E. Drewes, The role of membrane surface charge and solute physico-chemical properties in the rejection of organic acids by NF membranes, *J. Memb. Sci.* 249 (2005) 227–234. <https://doi.org/10.1016/j.memsci.2004.09.041>.
- [175] A.E. Yaroshchuk, Non-steric mechanism of nanofiltration: Superposition of donnan and dielectric exclusion, *Sep. Purif. Technol.* 22–23 (2001) 143–158. [https://doi.org/10.1016/S1383-5866\(00\)00159-3](https://doi.org/10.1016/S1383-5866(00)00159-3).
- [176] D. Wu, Y. Huang, S. Yu, D. Lawless, X. Feng, Thin film composite nanofiltration membranes assembled layer-by-layer via interfacial polymerization from polyethylenimine and trimesoyl chloride, *J. Memb. Sci.* 472 (2014) 141–153. <https://doi.org/10.1016/j.memsci.2014.08.055>.
- [177] C. Feng, J. Xu, M. Li, Y. Tang, C. Gao, Studies on a novel nanofiltration membrane prepared by cross-linking of polyethyleneimine on polyacrylonitrile substrate, *J. Memb. Sci.* 451 (2014) 103–110. <https://doi.org/10.1016/j.memsci.2013.10.003>.
- [178] X.L. Li, L.P. Zhu, J.H. Jiang, Z. Yi, B.K. Zhu, Y.Y. Xu, Hydrophilic nanofiltration membranes with self-polymerized and strongly-adhered polydopamine as separating layer, *Chinese J. Polym. Sci. (English Ed.)* 30 (2012) 152–163. <https://doi.org/10.1007/s10118-012-1107-5>.
- [179] Y.C. Xu, Z.X. Wang, X.Q. Cheng, Y.C. Xiao, L. Shao, Positively charged nanofiltration membranes via economically mussel-substance-simulated co-deposition for textile wastewater treatment, *Chem. Eng. J.* 303 (2016) 555–564. <https://doi.org/10.1016/j.cej.2016.06.024>.
- [180] F. Liu, B.R. Ma, D. Zhou, L.J. Zhu, Y.Y. Fu, L.X. Xue, Positively charged loose nanofiltration membrane grafted by diallyl dimethyl ammonium chloride (DADMAC) via UV for salt and dye removal, *React. Funct. Polym.* 86 (2015) 191–198. <https://doi.org/10.1016/j.reactfunctpolym.2014.09.003>.
- [181] H.Z. Zhang, Z.L. Xu, H. Ding, Y.J. Tang, Positively charged capillary nanofiltration membrane with high rejection for Mg^{2+} and Ca^{2+} and good separation for Mg^{2+} and Li^{+} , *Desalination* 420 (2017) 158–166. <https://doi.org/10.1016/j.desal.2017.07.011>.
- [182] C. Wu, S. Liu, Z. Wang, J. Zhang, X. Wang, X. Lu, Y. Jia, W.S. Hung, K.R. Lee, Nanofiltration membranes with dually charged composite layer exhibiting super-high multivalent-salt rejection, *J. Memb. Sci.* 517 (2016) 64–72. <https://doi.org/10.1016/j.memsci.2016.05.033>.

- [183] W. Fang, L. Shi, R. Wang, Interfacially polymerized composite nanofiltration hollow fiber membranes for low-pressure water softening, *J. Memb. Sci.* 430 (2013) 129–139. <https://doi.org/http://dx.doi.org/10.1016/j.memsci.2012.12.011>.
- [184] H. Deng, Y. Xu, Q. Chen, X. Wei, B. Zhu, High flux positively charged nanofiltration membranes prepared by UV-initiated graft polymerization of methacryloethyl trimethyl ammonium chloride (DMC) onto polysulfone membranes, *J. Memb. Sci.* 366 (2011) 363–372. <https://doi.org/10.1016/j.memsci.2010.10.029>.
- [185] R. Huang, G. Chen, M. Sun, Y. Hu, C. Gao, Studies on nanofiltration membrane formed by diisocyanate cross-linking of quaternized chitosan on poly(acrylonitrile) (PAN) support, *J. Memb. Sci.* 286 (2006) 237–244. <https://doi.org/10.1016/j.memsci.2006.09.045>.
- [186] L. Lianchao, W. Baoguo, T. Huimin, C. Tianlu, X. Jiping, A novel nanofiltration membrane prepared with PAMAM and TMC by in situ interfacial polymerization on PEK-C ultrafiltration membrane, *J. Memb. Sci.* 269 (2006) 84–93. <https://doi.org/10.1016/j.memsci.2005.06.021>.
- [187] R. Du, J. Zhao, Properties of poly (N,N-dimethylaminoethyl methacrylate)/polysulfone positively charged composite nanofiltration membrane, *J. Memb. Sci.* 239 (2004) 183–188. <https://doi.org/10.1016/j.memsci.2004.03.029>.
- [188] X.H. Ma, Z. Yang, Z.K. Yao, Z.L. Xu, C.Y. Tang, A facile preparation of novel positively charged MOF/chitosan nanofiltration membranes, *J. Memb. Sci.* 525 (2017) 269–276. <https://doi.org/10.1016/j.memsci.2016.11.015>.
- [189] J. Ma, Y. Ying, X. Guo, H. Huang, D. Liu, C. Zhong, Fabrication of mixed-matrix membrane containing metal-organic framework composite with task-specific ionic liquid for efficient CO₂ separation, *J. Mater. Chem. A* 4 (2016) 7281–7288. <https://doi.org/10.1039/c6ta02611g>.
- [190] L. Zhu, H. Yu, H. Zhang, J. Shen, L. Xue, C. Gao, B. Van Der Bruggen, Mixed matrix membranes containing MIL-53(Al) for potential application in organic solvent nanofiltration, *RSC Adv.* 5 (2015) 73068–73076. <https://doi.org/10.1039/c5ra10259f>.
- [191] S. Mohammad Nejad, S.F. Seyedpour, S. Aghapour Aktij, M. Dadashi Firouzjaei, M. Elliott, A. Tiraferri, M. Sadrzadeh, A. Rahimpour, Loose nanofiltration membranes functionalized with in situ-synthesized metal organic framework for water treatment, *Mater. Today Chem.* 24 (2022). <https://doi.org/10.1016/j.mtchem.2022.100909>.
- [192] H. Liu, M. Zhang, H. Zhao, Y. Jiang, G. Liu, J. Gao, Enhanced dispersibility of metal-organic frameworks (mofs) in the organic phase: Via surface modification for tfn nanofiltration membrane preparation, *RSC Adv.* 10 (2020) 4045–4057. <https://doi.org/10.1039/c9ra09672h>.
- [193] R.-H. Huang, G.-H. Chen, M.-K. Sun, C.-J. Gao, Hexamethylene diisocyanate crosslinking 2-Hydroxypropyltrimethyl ammonium chloride chitosan/poly(acrylonitrile) composite, *J. Appl. Toxicol.* 13 (1993) 435–439. <https://doi.org/10.1002/jat.2550130611>.
- [194] D.L. Zhao, S. Japip, Y. Zhang, M. Weber, C. Maletzko, T.-S. Chung, Emerging thin-film nanocomposite (TFN) membranes for reverse osmosis: A review, *Water Res.* (2020). <https://doi.org/https://doi.org/10.1016/j.watres.2020.115557>.
- [195] Z. Yang, H. Guo, Z.K. Yao, Y. Mei, C.Y. Tang, Hydrophilic Silver Nanoparticles Induce Selective Nanochannels in Thin Film Nanocomposite Polyamide Membranes, *Environ. Sci. Technol.* 53 (2019) 5301–5308. <https://doi.org/10.1021/acs.est.9b00473>.
- [196] W.J. Lau, S. Gray, T. Matsuura, D. Emadzadeh, J.P. Chen, A.F. Ismail, A Review on Polyamide Thin Film Nanocomposite (TFN) Membranes: History, Applications,

- Challenges and Approaches, (2015). <https://doi.org/10.1016/j.watres.2015.04.037>.This.
- [197] B. Khorshidi, I. Biswas, T. Ghosh, T. Thundat, M. Sadrzadeh, Robust fabrication of thin film polyamide-TiO₂ nanocomposite membranes with enhanced thermal stability and anti-biofouling propensity, *Sci. Rep.* 8 (2018). <https://doi.org/10.1038/s41598-017-18724-w>.
- [198] M. Ben-Sasson, X. Lu, E. Bar-Zeev, K.R. Zodrow, S. Nejadi, G. Qi, E.P. Giannelis, M. Elimelech, In situ formation of silver nanoparticles on thin-film composite reverse osmosis membranes for biofouling mitigation, *Water Res.* 62 (2014) 260–270. <https://doi.org/10.1016/j.watres.2014.05.049>.
- [199] L. Shen, Z. Huang, Y. Liu, R. Li, Y. Xu, G. Jakaj, H. Lin, Polymeric Membranes Incorporated With ZnO Nanoparticles for Membrane Fouling Mitigation: A Brief Review, *Front. Chem.* 8 (2020). <https://doi.org/10.3389/fchem.2020.00224>.
- [200] M. Sheikh, M. Pazirofteh, M. Dehghani, M. Asghari, M. Rezakazemi, C. Valderrama, J.L. Cortina, Application of ZnO nanostructures in ceramic and polymeric membranes for water and wastewater technologies: A review, *Chem. Eng. J.* 391 (2020). <https://doi.org/10.1016/j.cej.2019.123475>.
- [201] P. Kanmani, J.W. Rhim, Properties and characterization of bionanocomposite films prepared with various biopolymers and ZnO nanoparticles, *Carbohydr. Polym.* 106 (2014) 190–199. <https://doi.org/10.1016/j.carbpol.2014.02.007>.
- [202] M. Zare, K. Namratha, S. Ilyas, A. Sultana, A. Hezam, L. Sunil, M.A. Surmeneva, R.A. Surmenev, M.B. Nayan, S. Ramakrishna, S. Mathur, K. Byrappa, Emerging Trends for ZnO Nanoparticles and Their Applications in Food Packaging, *ACS Food Sci. Technol.* (2022). <https://doi.org/10.1021/acscfoodscitech.2c00043>.
- [203] P. Serra-Crespo, E. V. Ramos-Fernandez, J. Gascon, F. Kapteijn, Synthesis and characterization of an amino functionalized MIL-101(Al): Separation and catalytic properties, *Chem. Mater.* 23 (2011) 2565–2572. <https://doi.org/10.1021/cm103644b>.
- [204] G.M. Geise, D.R. Paul, B.D. Freeman, Progress in Polymer Science Fundamental water and salt transport properties of polymeric materials, *Prog. Polym. Sci.* 39 (2014) 1–42. <https://doi.org/10.1016/j.progpolymsci.2013.07.001>.
- [205] T. Wittmann, R. Siegel, N. Reimer, W. Milius, N. Stock, J. Senker, Enhancing the water stability of Al-MIL-101-NH₂ via postsynthetic modification, *Chem. - A Eur. J.* 21 (2015) 314–323. <https://doi.org/10.1002/chem.201404654>.
- [206] B.E. Warren, X-Ray Diffraction, Addison-Wesley Publishing Co., 1969.
- [207] S. Balta, A. Sotto, P. Luis, L. Benea, B. Van der Bruggen, J. Kim, A new outlook on membrane enhancement with nanoparticles: The alternative of ZnO, *J. Memb. Sci.* 389 (2012) 155–161. <https://doi.org/10.1016/j.memsci.2011.10.025>.
- [208] M. Purushothaman, V. Arvind, K. Saikia, V.K. Vaidyanathan, Fabrication of highly permeable and anti-fouling performance of Poly(ether ether sulfone) nanofiltration membranes modified with zinc oxide nanoparticles, *Chemosphere* 286 (2022). <https://doi.org/10.1016/j.chemosphere.2021.131616>.
- [209] B. Seoane, C. Téllez, J. Coronas, C. Staudt, NH₂-MIL-53(Al) and NH₂-MIL-101(Al) in sulfur-containing copolyimide mixed matrix membranes for gas separation, *Sep. Purif. Technol.* 111 (2013) 72–81. <https://doi.org/10.1016/j.seppur.2013.03.034>.
- [210] M. Hartmann, M. Fischer, Amino-functionalized basic catalysts with MIL-101 structure, *Microporous Mesoporous Mater.* 164 (2012) 38–43. <http://dx.doi.org/10.1016/j.micromeso.2012.06.044>.
- [211] R. Chang, J. Ma, J. Wang, Y. Liu, X. Guo, H. Qu, Efficient adsorption of dyes using polyethyleneimine-modified NH₂-MIL-101(Al) and its sustainable application as a

- flame retardant for an epoxy resin, *ACS Omega* 5 (2020) 32286–32294. <https://doi.org/10.1021/acsomega.0c04118>.
- [212] S.O.B. Oppong, W.W. Anku, F. Opoku, S.K. Shukla, P.P. Govender, Photodegradation of eosin yellow dye in water under simulated solar light irradiation using La-doped ZnO nanostructure decorated on graphene oxide as an advanced photocatalyst, *ChemistrySelect* 3 (2018) 1180–1188. <https://doi.org/10.1002/slct.201702470>.
- [213] A.I. Schaefer, Removal of adsorbing estrogenic micropollutants by nanofiltration membranes : Part B — Modeldevelopment Estrogenic micropollutant removal by nanofiltration membranes . Part B - modelling !, (2018). <https://doi.org/10.1016/j.memsci.2012.11.079>.
- [214] E. Virga, K. Žvab, W.M. de Vos, Fouling of nanofiltration membranes based on polyelectrolyte multilayers: The effect of a zwitterionic final layer, *J. Memb. Sci.* 620 (2021). <https://doi.org/10.1016/j.memsci.2020.118793>.
- [215] C. Ursino, R. Castro-Muñoz, E. Drioli, L. Gzara, M.H. Albeirutty, A. Figoli, Progress of nanocomposite membranes for water treatment, *Membranes (Basel)*. 8 (2018) 1–40. <https://doi.org/10.3390/membranes8020018>.
- [216] T. Kusworo, R.E. Nugraheni, N. Aryanti, The Effect of Membrane Modification Using TiO₂, ZnO, and GO Nanoparticles: Challenges and Future Direction in Wastewater Treatment, *IOP Conf. Ser. Mater. Sci. Eng.* 1053 (2021) 012135. <https://doi.org/10.1088/1757-899x/1053/1/012135>.
- [217] B. Thabo, B.J. Okoli, S.J. Modise, S. Nelana, Rejection capacity of nanofiltration membranes for nickel, copper, silver and palladium at various oxidation states, *Membranes (Basel)*. 11 (2021). <https://doi.org/10.3390/membranes11090653>.
- [218] C. Liu, L. Shi, R. Wang, Crosslinked layer-by-layer polyelectrolyte nanofiltration hollow fiber membrane for low-pressure water softening with the presence of SO₄²⁻ in feed water, *J. Memb. Sci.* 486 (2015) 169–176. <https://doi.org/10.1016/j.memsci.2015.03.050>.
- [219] A. Imbrogno, A. Tiraferri, S. Abbenante, S. Weyand, R. Schwaiger, T. Luxbacher, A.I. Schäfer, Organic fouling control through magnetic ion exchange-nanofiltration (MIEX-NF) in water treatment, *J. Memb. Sci.* 549 (2018) 474–485. <https://doi.org/10.1016/j.memsci.2017.12.041>.
- [220] C. Boo, Y. Wang, I. Zucker, Y. Choo, C.O. Osuji, M. Elimelech, High Performance Nanofiltration Membrane for Effective Removal of Perfluoroalkyl Substances at High Water Recovery, *Environ. Sci. Technol.* 52 (2018) 7279–7288. <https://doi.org/10.1021/acs.est.8b01040>.
- [221] Z. He, K. Wang, Y. Liu, T. Zhang, X. Wang, Fabrication of Loose Nanofiltration Membranes with High Rejection Selectivity between Natural Organic Matter and Salts for Drinking Water Treatment, *Membranes (Basel)*. 12 (2022). <https://doi.org/10.3390/membranes12090887>.
- [222] Sterlitech, (n.d.). <https://doi.org/10.1007/s13369-018-3096-3>.
- [223] H. Chang, B. Liu, B. Yang, X. Yang, C. Guo, Q. He, S. Liang, S. Chen, P. Yang, An integrated coagulation-ultrafiltration-nanofiltration process for internal reuse of shale gas flowback and produced water, *Sep. Purif. Technol.* 211 (2019) 310–321. <https://doi.org/10.1016/j.seppur.2018.09.081>.
- [224] C.Y. Tang, Y.N. Kwon, J.O. Leckie, Fouling of reverse osmosis and nanofiltration membranes by humic acid-Effects of solution composition and hydrodynamic conditions, *J. Memb. Sci.* 290 (2007) 86–94. <https://doi.org/10.1016/j.memsci.2006.12.017>.
- [225] A. Premachandra, C. Michaud-Lavoie, B. Chester, M. McClure, I. Sarkar, K. Lutes,

- S. Rollings-Scattergood, D.R. Latulippe, Development of a crossflow nanofiltration process for polishing of wastewater by-product from biogas production processes, *J. Water Process Eng.* 50 (2022). <https://doi.org/10.1016/j.jwpe.2022.103197>.
- [226] C.M. Sánchez-Arévalo, T. Croes, B. Van der Bruggen, M.C. Vincent-Vela, S. Álvarez-Blanco, Feasibility of several commercial membranes to recover valuable phenolic compounds from extracts of wet olive pomace through organic-solvent nanofiltration, *Sep. Purif. Technol.* 305 (2023). <https://doi.org/10.1016/j.seppur.2022.122396>.
- [227] S. Jafarinejad, H. Park, H. Mayton, S.L. Walker, S.C. Jiang, Concentrating ammonium in wastewater by forward osmosis using a surface modified nanofiltration membrane, *Environ. Sci. Water Res. Technol.* 5 (2019) 246–255. <https://doi.org/10.1039/c8ew00690c>.
- [228] R. Żyła, M. Foszpańczyk, I. Kamińska, M. Kudzin, J. Balcerzak, S. Ledakowicz, Impact of Polymer Membrane Properties on the Removal of Pharmaceuticals, *Membranes (Basel)*. 12 (2022). <https://doi.org/10.3390/membranes12020150>.
- [229] J. López, O. Gibert, J.L. Cortina, The role of nanofiltration modelling tools in the design of sustainable valorisation of metal-influenced acidic mine waters: The Aznalcóllar open-pit case, *Chem. Eng. J.* 451 (2023). <https://doi.org/10.1016/j.cej.2022.138947>.
- [230] L. Gao, H. Wang, Y. Zhang, M. Wang, Nanofiltration membrane characterization and application: Extracting lithium in lepidolite leaching solution, *Membranes (Basel)*. 10 (2020) 1–18. <https://doi.org/10.3390/membranes10080178>.
- [231] R. Xu, M. Zhou, H. Wang, X. Wang, X. Wen, Influences of temperature on the retention of PPCPs by nanofiltration membranes: Experiments and modeling assessment, *J. Memb. Sci.* 599 (2020). <https://doi.org/10.1016/j.memsci.2020.117817>.
- [232] L. Liu, Y. Liu, X. Chen, S. Feng, Y. Wan, H. Lu, J. Luo, A nanofiltration membrane with outstanding antifouling ability: Exploring the structure-property-performance relationship, *J. Memb. Sci.* 668 (2023). <https://doi.org/10.1016/j.memsci.2022.121205>.
- [233] M.W. Shahzad, M. Burhan, K.C. Ng, Pushing desalination recovery to the maximum limit: Membrane and thermal processes integration, *Desalination* 416 (2017) 54–64. <https://doi.org/10.1016/j.desal.2017.04.024>.
- [234] J.J. Feria-Díaz, F. Correa-Mahecha, M.C. López-Méndez, J.P. Rodríguez-Miranda, J. Barrera-Rojas, Recent desalination technologies by hybridization and integration with reverse osmosis: A review, *Water (Switzerland)* 13 (2021). <https://doi.org/10.3390/w13101369>.
- [235] Y.S. Oren, P.M. Biesheuvel, Theory of Ion and Water Transport in Reverse-Osmosis Membranes, *Phys. Rev. Appl.* 9 (2018) 1–15. <https://doi.org/10.1103/PhysRevApplied.9.024034>.
- [236] H. Demey, T. Vincent, M. Ruiz, M. Noguerras, A.M. Sastre, E. Guibal, Boron recovery from seawater with a new low-cost adsorbent material, *Chem. Eng. J.* 254 (2014) 463–471. <https://doi.org/10.1016/j.cej.2014.05.057>.
- [237] N.P. Morozov, Lithium and rubidium concentrations in waters of the Mediterranean Sea, (n.d.). <https://doi.org/10.1594/PANGAEA.753398>.
- [238] M. Bernat, T. Church, C.J. Allegre, Barium and strontium concentrations in pacific and mediterranean sea water profiles by direct isotope dilution mass spectrometry, *Earth Planet. Sci. Lett.* 16 (2016) 1–23. [https://doi.org/https://doi.org/10.1016/0012-821X\(72\)90238-5](https://doi.org/https://doi.org/10.1016/0012-821X(72)90238-5).
- [239] D.A. Wolf-Gladrow, R.E. Zeebe, C. Klaas, A. Körtzinger, A.G. Dickson, Total

- alkalinity: The explicit conservative expression and its application to biogeochemical processes, *Mar. Chem.* 106 (2007) 287–300. <https://doi.org/10.1016/j.marchem.2007.01.006>.
- [240] Composition of seawater Major ion composition of seawater (mg / L), (n.d.). <https://www.lenntech.com/composition-seawater.htm>.
- [241] A. Yaroshchuk, M.L. Bruening, E. Zholkovskiy, Modelling nanofiltration of electrolyte solutions, *Adv. Colloid Interface Sci.* 268 (2019) 39–63. <https://doi.org/https://doi.org/10.1016/j.cis.2019.03.004>.
- [242] J. López, M. Reig, A. Yaroshchuk, E. Licon, O. Gibert, Experimental and theoretical study of nanofiltration of weak electrolytes: $\text{SO}_4^{2-}/\text{HSO}_4^-/\text{H}^+$ system, *J. Memb. Sci.* 550 (2018) 389–398. <https://doi.org/10.1016/j.memsci.2018.01.002>.
- [243] J. López, M. Reig, O. Gibert, E. Torres, C. Ayora, J.L. Cortina, Application of nanofiltration for acidic waters containing rare earth elements: Influence of transition elements, acidity and membrane stability, *Desalination* 430 (2018) 33–44. <https://doi.org/10.1016/j.desal.2017.12.033>.
- [244] J. López, M. Reig, E. Licon, C. Valderrama, O. Gibert, J.L. Cortina, Evaluating the integration of nanofiltration membranes in advanced water reclamation schemes using synthetic solutions: From phosphorous removal to phosphorous circularity, *Sep. Purif. Technol.* 290 (2022). <https://doi.org/10.1016/j.seppur.2022.120914>.
- [245] J. López, O. Gibert, J.L. Cortina, Evaluation of an extreme acid-resistant sulphonamide based nanofiltration membrane for the valorisation of copper acidic effluents, *Chem. Eng. J.* 405 (2021). <https://doi.org/10.1016/j.cej.2020.127015>.
- [246] J. Lopez, A. Yaroshchuk, M. Reig, O. Gibert, J.L. Cortina, An engineering model for solute transport in semi-aromatic polymeric nanofiltration membranes: Extension of Solution-Electro-Diffusion model to complex mixtures, *J. Environ. Chem. Eng.* 9 (2021). <https://doi.org/10.1016/j.jece.2021.105262>.
- [247] V. Nigro, R. Angelini, B. Rosi, M. Bertoldo, E. Buratti, S. Casciardi, S. Sennato, B. Ruzicka, Study of network composition in interpenetrating polymer networks of poly(N isopropylacrylamide) microgels: The role of poly(acrylic acid), *J. Colloid Interface Sci.* 545 (2019) 210–219. <https://doi.org/10.1016/j.jcis.2019.03.004>.
- [248] M. Fernández de Labastida, E.E. Licon Bernal, A. Yaroshchuk, Implications of inhomogeneous distribution of concentration polarization for interpretation of pressure-driven membrane measurements, *J. Memb. Sci.* 520 (2016) 693–698. <https://doi.org/10.1016/j.memsci.2016.08.040>.
- [249] M.S. Hall, D.R. Lloyd, V.M. Starov, Reverse osmosis of multicomponent electrolyte solutions Part II. Experimental verification, *J. Memb. Sci.* 128 (1997) 39–53.
- [250] O. Nir, N.F. Bishop, O. Lahav, V. Freger, Modeling pH variation in reverse osmosis, *Water Res.* 87 (2015) 328–335. <https://doi.org/10.1016/j.watres.2015.09.038>.
- [251] P. Vanýsek, Ionic conductivity and diffusion at infinite dilution, *CRC Handb. Chem. Phys.* 96 (1996) 5–98.
- [252] S. Bason, Y. Kaufman, V. Freger, Analysis of Ion Transport in Nanofiltration Using Phenomenological Coefficients and Structural Characteristics, *J. Phys. Chem.* (2010) 3510–3517. <https://doi.org/https://doi.org/10.1021/jp911615n>.
- [253] S. Bason, V. Freger, Phenomenological analysis of transport of mono- and divalent ions in nanofiltration, *J. Memb. Sci.* 360 (2010) 389–396. <https://doi.org/10.1016/j.memsci.2010.05.037>.
- [254] O. Coronell, B.J. Mariñas, D.G. Cahill, Depth heterogeneity of fully aromatic polyamide active layers in reverse osmosis and nanofiltration membranes, *Environ. Sci. Technol.* 45 (2011) 4513–4520. <https://doi.org/10.1021/es200007h>.
- [255] A.E. Yaroshchuk, Dielectric exclusion of ions from membranes, *Adv. Colloid*

- Interface Sci. 85 (2000) 193–230. [https://doi.org/10.1016/S0001-8686\(99\)00021-4](https://doi.org/10.1016/S0001-8686(99)00021-4).
- [256] A.E. Yaroshchuk, Rejection of single salts versus transmembrane volume flow in RO/NF: Thermodynamic properties, model of constant coefficients, and its modification, *J. Memb. Sci.* 198 (2002) 285–297. [https://doi.org/10.1016/S0376-7388\(01\)00668-8](https://doi.org/10.1016/S0376-7388(01)00668-8).
- [257] S. Sutijan, S.A. Darma, C.M. Hananto, V.S.H. Sujoto, F. Anggara, S.N.A. Jenie, W. Astuti, F.R. Mufakhir, S. Virdian, A.P. Utama, H.T.B.M. Petrus, Lithium Separation from Geothermal Brine to Develop Critical Energy Resources Using High-Pressure Nanofiltration Technology: Characterization and Optimization, *Membranes (Basel)*. 13 (2023) 1–15. <https://doi.org/10.3390/membranes13010086>.
- [258] T. Zhang, W. Zheng, Q. Wang, Z. Wu, Z. Wang, Designed strategies of nanofiltration technology for Mg²⁺/Li⁺ separation from salt-lake brine: A comprehensive review, *Desalination* 546 (2023). <https://doi.org/10.1016/j.desal.2022.116205>.
- [259] M. Turek, P. Dydo, R. Klimek, Salt production from coal-mine brine in NF - evaporation - crystallization system, *Desalination* 221 (2008) 238–243. <https://doi.org/10.1016/j.desal.2007.01.080>.
- [260] J. Tian, X. Zhao, S. Gao, X. Wang, R. Zhang, Progress in research and application of nanofiltration (Nf) technology for brackish water treatment, *Membranes (Basel)*. 11 (2021). <https://doi.org/10.3390/membranes11090662>.
- [261] M. Uyttebroek, P. Vandezande, M. Van Dael, S. Vloemans, B. Noten, B. Bongers, W. Porto-Carrero, M. Muñiz Unamunzaga, M. Bulut, B. Lemmens, Concentration of phenolic compounds from apple pomace extracts by nanofiltration at lab and pilot scale with a techno-economic assessment, *J. Food Process Eng.* 41 (2018) 1–10. <https://doi.org/10.1111/jfpe.12629>.
- [262] J. Yuan, J. Duan, C.P. Saint, D. Mulcahy, Removal of glyphosate and aminomethylphosphonic acid from synthetic water by nanofiltration, *Environ. Technol. (United Kingdom)* 39 (2018) 1384–1392. <https://doi.org/10.1080/09593330.2017.1329356>.
- [263] A. Premachandra, S. O'Brien, N. Perna, J. McGivern, R. LaRue, D.R. Latulippe, Treatment of complex multi-sourced industrial wastewater — New opportunities for nanofiltration membranes, *Chem. Eng. Res. Des.* 168 (2021) 499–509. <https://doi.org/10.1016/j.cherd.2021.01.005>.
- [264] A.S. Chugunov, V.A. Vinnitskii, Nanofiltration fractionation of radioactive solution components as a method for reducing the volume of wastes intended for permanent disposal, *Nucl. Energy Technol.* 5 (2019) 123–128. <https://doi.org/10.3897/nucet.5.35801>.
- [265] C. Morgante, J. Lopez Rodriguez, J.L. Cortina, A. Tamburini, Unlocking Seawater's Riches: A vast Comparative Study of Nanofiltration Membranes for Efficient Recovery of Major and Trace elements, *Under Rev. Sep. Purif. Technol.* (n.d.) 23.
- [266] B. Van Der Bruggen, K. Everaert, D. Wilms, C. Vandecasteele, Application of nanofiltration for removal of pesticides, nitrate and hardness from ground water: Rejection properties and economic evaluation, *J. Memb. Sci.* 193 (2001) 239–248. [https://doi.org/10.1016/S0376-7388\(01\)00517-8](https://doi.org/10.1016/S0376-7388(01)00517-8).
- [267] C. Maxwell, Cost indices, *Towering Ski.* (n.d.). <https://toweringskills.com/financial-analysis/cost-indices/>.
- [268] QYR Chemical & Material Research Center, Europe Magnesium Hydroxide Industry 2016 Market Research Report, (2016) 65.
- [269] J.V. Valh, B. Vončina, A. Lobnik, L.F. Zemljič, L. Škodič, S. Vajnhandl, Conversion of polyethylene terephthalate to high-quality terephthalic acid by hydrothermal hydrolysis: the study of process parameters, *Text. Res. J.* 90 (2020) 1446–1461.

- <https://doi.org/10.1177/0040517519893714>.
- [270] C.Y. Tang, Y.N. Kwon, J.O. Leckie, Effect of membrane chemistry and coating layer on physiochemical properties of thin film composite polyamide RO and NF membranes. I. FTIR and XPS characterization of polyamide and coating layer chemistry, *Desalination* 242 (2009) 149–167. <https://doi.org/10.1016/j.desal.2008.04.003>.
- [271] H. Zhu, B. Hu, F. Yang, Removal of sulfadiazine by polyamide nanofiltration membranes: Measurement, modeling, and mechanisms, *Membranes (Basel)*. 11 (2021). <https://doi.org/10.3390/membranes11020104>.
- [272] M. Figueira, D. Rodríguez-Jiménez, J. López, M. Reig, J.L. Cortina, C. Valderrama, Experimental and economic evaluation of nanofiltration as a pre-treatment for added-value elements recovery from seawater desalination brines, *Desalination* 549 (2023). <https://doi.org/10.1016/j.desal.2022.116321>.
- [273] G. Battaglia, M.A. Domina, R. Lo Brutto, J. Lopez Rodriguez, M. Fernandez de Labastida, J.L. Cortina, A. Pettignano, A. Cipollina, A. Tamburini, G. Micale, Evaluation of the Purity of Magnesium Hydroxide Recovered from Saltwork Bitterns, *Water (Switzerland)* 15 (2023) 1–22. <https://doi.org/10.3390/w15010029>.
- [274] W. Richard, Characterisation of nanofiltration membranes for predictive purposes - use of salts , uncharged solutes and atomic force microscopy, 126 (1997).
- [275] P. Dechadilok, W.M. Deen, Hindrance Factors for Diffusion and Convection in Pores, (2006) 6953–6959.
- [276] F.G. Donnan, Theory of membrane equilibria and membrane potentials in the presence of non-dialysing electrolytes . A contribution to physical-chemical physiology, 100 (1995) 45–55.
- [277] D.L. Parkhurst, C.A.J. Appelo, User’s Guide to PHREEQC (Version 2) A Computer Program for Speciation, Batch Reaction, One-Dimensional Transport, and Inverse Geochemical Calculations, n.d.
- [278] M. Born, Volumen und Hydratationswärme der Ionen., 1920.
- [279] M. Dina, Generalized Mass-Transfer Correction Factor for Nanofiltration and Reverse Osmosis, 52 (2006) 3353–3362. <https://doi.org/10.1002/aic>.
- [280] S. Senthilmurugan, A. Ahluwalia, S.K. Gupta, Modeling of a spiral-wound module and estimation of model parameters using numerical techniques, 173 (2005) 269–286.
- [281] R. Turton, R.C. Bailie, W.B. Whiting, Analysis, synthesis, and design of chemical processes, 1998. <https://doi.org/10.5860/choice.36-0974>.

LIST OF ISI PUBLICATIONS AND PRESENTATIONS AT INTERNATIONAL CONFERENCES

Publications/Patents

1. F. Vassallo, **C. Morgante**, G. Battaglia, D. La Corte, M. Micari, A. Cipollina, A. Tamburini, G. Micale, *A simulation tool for ion exchange membrane crystallization of magnesium hydroxide from waste brine*, Chem. Eng. Res. Des. 173 (2021) 193–205. doi:10.1016/j.cherd.2021.07.008.
2. **C. Morgante**, F. Vassallo, D. Xevgenos, A. Cipollina, M. Micari, A. Tamburini, G. Micale, *Valorisation of SWRO brines in a remote island through a circular approach: Techno-economic analysis and perspectives*, Desalination. 542 (2022). doi:10.1016/j.desal.2022.116005.
3. **C. Morgante**, F. Vassallo, G. Battaglia, A. Cipollina, F. Vicari, A. Tamburini, G. Micale, *Influence of Operational Strategies for the Recovery of Magnesium Hydroxide from Brines at a Pilot Scale*, Ind. Eng. Chem. Res. (2022). doi:10.1021/acs.iecr.2c02935.
4. **C. Morgante**, X. Ma, X. Chen, D. Wang, V. Boffa, V. Stathopoulos, J. Lopez, J. Cortina, A. Cipollina, A. Tamburini, G. Micale, *Metal-Organic-Framework-based nanofiltration membranes for selective multi-cationic recovery from seawater and brines*, Journal of Membrane Science (2023), doi: <https://doi.org/10.1016/j.memsci.2023.121941>.
5. **C. Morgante**, F. Vassallo, C. Cassaro, G. Virruso, D. Diamantidou, N. Van Linden, A. Trezzi, C. Xenogianni, R. Ktori, M. Rodriguez, G. Scelfo, S. Randazzo, A. Tamburini, A. Cipollina, G. Micale, D. Xevgenos, *Pioneering minimum liquid discharge desalination : A pilot study in Lampedusa Island*, Desalination 581 (2024) 117562. <https://doi.org/10.1016/j.desal.2024.117562>.
6. **C. Morgante**, J. Lopez, J. Cortina, A. Tamburini, *New generation of commercial nanofiltration membranes for seawater/brine mining: Experimental evaluation and modelling of membrane selectivity for major and trace elements*, Separation and Purification Technology (2024), doi: <https://doi.org/10.1016/j.seppur.2024.126758>.

7. **C. Morgante**, J. Lopez, T. Moghadamfar, J. Cortina, A. Tamburini, *Evaluation of enhanced nanofiltration membranes for improving magnesium recovery schemes from seawater / brine: Integrating experimental performing data with a techno-economic assessment*, J. Environ. Manage. 360 (2024) 121192. <https://doi.org/10.1016/j.jenvman.2024.121192>.
8. U.S. Provisional Patent CMZ Nanofiltration between **C. Morgante**, V. Boffa, J. Lopez, J.L. Cortina and ACWA POWER (in progress)

Presentations at national and international conferences

1. **C. Morgante**, F. Vassallo, A. Cipollina, A. Tamburini, G. Micale, *"Techno-economic analysis of a novel hybrid system for the valorisation of SWRO brines in a minor Sicilian island"*, 16th Conference on Sustainable Development of Energy, Water and Environment Systems (SDEWES), 10th-15th October 2021, Dubrovnik (Croatia)
2. **C. Morgante**, F. Vassallo, G. Battaglia, D. La Corte, M. Micari, A. Cipollina, A. Tamburini, G. Micale, *"Modelling of an innovative membrane crystallizer for the production of magnesium hydroxide from waste brine"*. EUROMEMBRANE 2021, 28th November – 2nd December 2021, Copenhagen (Denmark)
3. **C. Morgante**, F. Vassallo, A. Cipollina, A. Tamburini and G. Micale, *"A novel integrated technology to recover high valuable minerals from seawater through a circular economy approach"*, GRICU 2022, 3rd -9th July 2022, Ischia (Italy)
4. **C. Morgante**, F. Vassallo, G. Battaglia, F. Vicari, A. Cipollina, A. Tamburini, G. Micale, *"Operational analysis of a novel reactive crystallizer for the production of Magnesium Hydroxide from waste brines"*. BIWIC 2022 (the 27th International Workshop on Industrial Crystallization), 31st August – 2nd September 2022, Espoo (Finland)
5. F. Vassallo, **C. Morgante**, A. Cipollina, A. Tamburini and G. Micale, *"Effective magnesium recovery via seawater brines mining"*, BIWIC 2022 (27th International Workshop on Industrial Crystallization), 31st August – 2nd September 2022, Espoo (Finland)

6. **C. Morgante**, V. Boffa, X. Ma, J. Lopez, J. Cortina, A. Cipollina, A. Tamburini, G. Micale, "*Metal-organic-framework-based nanofiltration membranes for selective multi-cationic recovery from desalination brines*", European Desalination Society: Desalination for the Environment, Clean Water and Energy conference 2023, 22nd -26th May 2023, Limassol (Cyprus)
7. F. Vassallo, **C. Morgante**, F. Vicari, A. Cipollina, A. Tamburini, G. Micale, "*Influence of bicarbonate/carbonate removal on magnesium hydroxide slurry: A pilot study*", European Desalination Society: Desalination for the Environment, Clean Water and Energy conference 2023, 22nd -26th May 2023, Limassol (Cyprus)
8. F. Vassallo, **C. Morgante**, C. Cassaro, G. Virruso, D. Diamantidou, N. Van Linden, G. Scelfo, A. Tamburini, S. Randazzo, A. Trezzi, A. Cipollina, G. Micale, D. Xevgenos, "*Minimum Liquid Discharge desalination: a pilot study in Lampedusa island*", European Desalination Society: Desalination for the Environment, Clean Water and Energy conference 2023, 22nd -26th May 2023, Limassol (Cyprus)
9. **C. Morgante**, J. Lopez, J. Cortina, V. Boffa, "*Positively charged metal-organic-framework-based nanofiltration for selective multi-cationic recovery from seawater and brines*", ACWA Power Innovation Days 2nd edition, 23rd -25th January 2024, KAUST (Saudi Arabia).

AWARDS

1. **“Best Poster Award”** at Euromembrane 2021, Copenhagen (Denmark), *“Modelling of an innovative membrane crystallizer for the production of magnesium hydroxide from waste brine”*
2. **“First Miriam Balaban Innovation Award”** at EDS 2023, Limassol (Cyprus), *“Metal-organic-framework-based nanofiltration membranes for selective multi-cationic recovery from desalination brines”*



Figure 81: a) “Best Poster Award” at EUROMEMBRANE conference (Copenhagen, 2021); b) “The First Miriam Balaban Innovation Award” at European Desalination Society (EDS) conference (Limassol, 2023).